



**This electronic thesis or dissertation has been downloaded from the University of Bristol Research Portal, <http://research-information.bristol.ac.uk>**

*Author:*

**Mackenzie, G R**

*Title:*

**A Diamond Gammavoltaic Cell**

**General rights**

Access to the thesis is subject to the Creative Commons Attribution - NonCommercial-No Derivatives 4.0 International Public License. A copy of this may be found at <https://creativecommons.org/licenses/by-nc-nd/4.0/legalcode>. This license sets out your rights and the restrictions that apply to your access to the thesis so it is important you read this before proceeding.

**Take down policy**

Some pages of this thesis may have been removed for copyright restrictions prior to having it been deposited on the University of Bristol Research Portal. However, if you have discovered material within the thesis that you consider to be unlawful e.g. breaches of copyright (either yours or that of a third party) or any other law, including but not limited to those relating to patent, trademark, confidentiality, data protection, obscenity, defamation, libel, then please contact [collections-metadata@bristol.ac.uk](mailto:collections-metadata@bristol.ac.uk) and include the following information in your message:

- Your contact details
- Bibliographic details for the item, including a URL
- An outline nature of the complaint

Your claim will be investigated and, where appropriate, the item in question will be removed from public view as soon as possible.

---

---

# A Diamond Gammavoltaic Cell

---

---

By

GORDON ROBSON MACKENZIE



School of Physics  
UNIVERSITY OF BRISTOL

A thesis submitted to the University of Bristol in accordance with the requirements of the degree of DOCTOR OF PHILOSOPHY in the Interface Analysis Centre, School of Physics.

NOVEMBER 2022

Word count: 54,201



## ABSTRACT

This work presents a new design for a gammavoltaic cell, based on diamond and the surface transfer doping it exhibits. The design evolved from the observation of gammavoltism in a diamond dosimeter during previous work at the University of Bristol. The work first gives an overview of gammavoltaics in literature, highlighting the small size of the field as it currently stands, and the difficulty in comparing between previous works due to the range of approaches used both for conceiving gammavoltaic devices, and for testing them. As part of this overview, it draws attention to some other radiovoltaic work to illustrate where gammavoltaics sit in a wider context. It then discusses the processes by which high-energy photons are converted to conduction electrons within a device. Discussion is split into high-energy photon scattering processes, electron scattering processes (for hot electrons), and charge transport processes (for lower-energy electrons and their holes). As the presented gammavoltaic design is based on diamond, space is then given to the historical context of diamond research and of research into diamond devices under irradiation. Three device-specific aspects of diamond research are then covered in greater depth: the formation of high- and low- barrier electrical contacts on diamond, and the surface transfer doping effect. With this background given, the design for a gammavoltaic cell on which this work is based, is presented: a thick, insulating diamond with opposing, dissimilar contacts, covered on all surfaces with a certain coverage of hydrogen termination.

To marshal the lessons from existing gammavoltaic literature, and also to give clarity and structure to the experiments conducted for this work, five factors are introduced: comparability, accountability, capability, applicability and longevity. No gammavoltaic has yet seen a real-world deployment, to my knowledge. I assert here that each of these five factors has an important role to play in the conceptual development of the field and the progress it makes towards gammavoltaics becoming industrially useful. I define an energy range of 1 - 2000 keV, the Gamut, which I suggest contains all relevant photon energies for gammavoltaic purposes, both application and study. For similar reasons, I suggest a notation convention which lends itself to use for benchmarks in gammavoltaics, with two given directly:  $\frac{\text{Co-60}}{100}\mathfrak{P}$ , the volumetric maximum power-point density under a 100 Gy/h air KERMA dose rate of Co-60 radiation, in nW/cm<sup>3</sup>, and  $\frac{\text{Co-60}}{100}\mathfrak{p}$ , the analogous areal quantity, in nW/cm<sup>2</sup>.

A Theory chapter is included which gives a brief overview of the basic physics of traditional solar cells based on silicon *pn*-junctions, the equivalent circuit model which arises from this, and the use of the Lambert W function to derive an explicit *I-V* expression from the model. It then attempts to apply the same concepts to the diamond gammavoltaic cell presented in this work, although there are several elements which have not been included in the theoretical treatment at this time. An extended equivalent-circuit model based on opposing diodes, the opposing-diodes model, is derived from this circuit. Finally, the theory chapter discusses the fitting parameters space for both models, and the benefit of using orthogonal distance regression for radiovoltaic work, to account for the fact that uncertainty in the applied bias may be substantial as well as the measured current. There is also a Methods chapter which covers the computational aspects of the above as well as the

---

other experimental methods employed in the work.

The first set of results presented are for the purposes of capability and accountability. They seek to prove that the design presented here is capable of working, to a reasonable degree, as a gammavoltaic, and to verify that it works in the way intended. Due to the unusual method of hydrogen termination, required by the fact electrode contacts must be deposited prior to termination, an x-ray photoelectron spectroscopy study is presented which shows the enabling hydrogen termination to have consisted of approximately 0.3 monolayers.

The second set of results here goes further down the route of accountability, using a chain of synchrotron experiments and GEANT4 simulations to first attempt to validate the modelling approach used in this work, and then attempt to probe the operation of a diamond gammavoltaic cell under high fluxes of photons as the energy is varied between 50 keV - 150 keV, the region in which Compton scattering being to dominate over photoelectric absorption for diamond. Unlike in work published on the latter experiment, conclusions drawn are fairly limited due to uncertainties about the method that have arisen since publication.

The third set of results addresses the factors of comparability, applicability (to the gamma field in a nuclear waste store), and longevity (again, in the context of deploying in a nuclear waste store). Measurements are performed under irradiation from gamma rays from both Cs-137 and Co-60. In each case, air KERMA dose-rates of tens to thousands of Grays per hour are attained. An equivalent circuit model based on two opposing diodes is fitted to each curve in an attempt to extract quasi-physical parameters and observe their change with dose rate, to mixed success. For comparability, benchmark values are found of  ${}_{100}^{Co-60}p = 27 \text{ nW/cm}^2$  and  ${}_{100}^{Co-60}q = 179 \text{ nW/cm}^3$ . Longevity testing showed that the device design is promising for longevity. It suffered no catastrophic degradation after 800 kGy air KERMA of Cs-137, after an irradiation at 1,350 Gy/h air KERMA for over 3.5 wks. At most, degradation was around 16 %, but this is an overestimate due to temperature and humidity effects also playing a role. The longevity status of the gammavoltaic design presented here is promising but requires more study, over longer periods of irradiation.

The summary and conclusions of the work include avenues for improvement in the device, and early work that has been undertaken to address them. The thesis culminates with details of a demonstration in which a diamond gammavoltaic device powers a Bluetooth monitoring circuit, sufficiently to transmit a temperature and humidity measurement after charging from x-rays for 10 h. This is believed to be the first time a gammavoltaic has been used to power any kind of electronic device.

## AUTHOR'S DECLARATION

I declare that the work in this dissertation was carried out in accordance with the requirements of the University's Regulations and Code of Practice for Research Degree Programmes and that it has not been submitted for any other academic award. Except where indicated by specific reference in the text, the work is the candidate's own work. Work done in collaboration with, or with the assistance of, others, is indicated as such at the start of the relevant results chapters. Any views expressed in the dissertation are those of the author.

SIGNED: ..... DATE: .....



## DEDICATION AND ACKNOWLEDGEMENTS

It seems, from my perspective, that I have been unusually lucky in my life with the people I have fallen in with. I was raised by good people, I've consistently been befriended by good people, and likewise consistently been taught by good people.

Of teachers, mentors and supervisors, I would like to thank Professors Tom Scott and Neil Fox. Neil brought me into the world of diamond as an MSci student in 2015, whilst Tom has hurtled me rapidly around the world of nuclear, and indeed of industrial collaboration and business, since then. They are the masterminds behind my project, and often those who were more or less visibly pulling strings to allow my personal and professional development to occur. If it was the job of my teachers at school to restrain my youthful arrogance and tolerate it for the sake of my education, it has been Tom and Neil's job to encourage my self-respect to return after a healthy but horrifying brush with existential philosophy, and to do so whilst giving me the opportunities I needed to train as a scientist. Navigating the world of independent research can be very disorientating at first, and for help, particularly in the early years, with this navigation I owe deep and enduring debts to Dr. Hugo Dominguez Andrade and Dr. Chris Hutson. It is fair to say that Hugo turned me from a dependent researcher into an independent one (though my organisational spreadsheets will never match his), and that Chris chaperoned me vigilantly from following orders to asserting my own opinions (though "asserting" may be too strong a word for my brand of mercurial, Socratic faffing - the chalk to Chris' cheese). Towards the later stages of my PhD, Dr. Tomas Martin has increasingly featured in honing my writing skills and making free, frank and valuable efforts to guide me in my career development. He is a fine figure of a role model, and I owe many of my more intense periods of work to conversations had at my annual review meetings with him and Prof. Mike Uren. With choice of words, it's easy to destroy someone or to give them a free pass, but I imagine it is very difficult to walk the critical line and provide feedback that really helps a person to develop. For this I sincerely thank them both. Finally, of mentors, I would like to thank Ms Estelle Talfan-Davies, who I have learned a lot from by observation. It may seem strange to some people that I would acknowledge my supervisor's admin support as a mentor figure, given I am in a different line of work, but those people presumably have not met Estelle.

Of those in my personal life who contributed most materially to this work, I would like to acknowledge the substantial support, irreverent humour and vicarious experience of the world of rock n' roll afforded to me by Haz Wheaton. I remember when I first met Haz, I was knocked out by his exuberance, his raw power, and his punctuality. He hasn't let me down since. If he is lucky, he will never have to read this document - unlike several others he's proofread over the course of my studentship. I would like to thank my girlfriend Fiona Messer, whose science is gross, but who herself is a lovely person, and very tolerant. Fi's constancy and kindness is very valuable - I hope I can contribute to her PhD efforts as much as she has to mine. I suspect we're in it for the long haul now, though I haven't asked the question yet, and though I showed her a draft of these acknowledgements before inserting this sentence. I couldn't ask for better luck. I would like to thank my family, Colin, Gillian

---

and Jamie Mackenzie, for their support and guidance in traversing the social world of work, them all being far more adept at such things than I am. Also specifically my father Colin, for pitching in and transcribing interviews undertaken for a lecture course in nuclear ethics I created and delivered to the Nuclear MSc students this year, to free me up to work on my thesis when crunch time came. This was particularly helpful, as writing scripts and transcribing interviews for the lectures (podcasts due to the pandemic) was quite labour intensive, and it remains the case that the word count of the lecture course is actually greater than that of this thesis! As ever, anything I succeed in reflects my family's hard work. My failures, of course, are my own.

Finally, I would like to dedicate this work to the religion which has no name, and which I have attempted to honour on solitary days and nights with meaningless, ritual actions in the countryside. Here is one twang of the web, I hope it outperforms its counterfactuals.

*Update, November 2022:* It's been more than a year since I first submitted this work for examination, and nearly a year since I was examined for it *viva voce*. It has been a tough year involving most types of personal setback, so I would like to re-emphasize my thanks to my supervisors, my friends and my family for their support. I would like to extend new thanks the NHS for seeing to it that neither my father nor I will leave the scene earlier than we ought to. Finally, I would also like to thank my examiners for providing constructive feedback and a stimulating few hours of conversation. Fiona still hasn't got her ring - perhaps this is the year we'll manage to lay down roots of our own somewhere.

## TABLE OF CONTENTS

	Page
<b>Outputs</b>	<b>xi</b>
<b>Glossary</b>	<b>xiii</b>
<b>List of Tables</b>	<b>xxiii</b>
<b>List of Figures</b>	<b>xxv</b>
<b>1 Introduction</b>	<b>1</b>
1.1 Gammavoltaics: both radiovoltaics and photovoltaics . . . . .	3
1.2 Processes involved in the conversion of a high-energy photon to electron-hole pairs	7
1.2.1 High-energy photon scattering processes . . . . .	7
1.2.2 Electron scattering processes . . . . .	12
1.2.3 Charge transport processes . . . . .	14
1.3 Diamond as a device material: features, advantages and disadvantages . . . . .	16
1.3.1 The historical context of diamond research . . . . .	16
1.3.2 Diamond devices and radiation . . . . .	17
1.3.3 Electrical contacts to diamond devices . . . . .	19
1.3.3.1 Low-barrier contacts . . . . .	20
1.3.3.2 High-barrier contacts . . . . .	23
1.3.4 The surface transfer-doping effect . . . . .	24
1.4 Principles and design of the presented diamond gammavoltaic cell . . . . .	27
1.5 Research outline . . . . .	29
<b>2 Theory of photovoltaic modelling and curve fitting for the DGV</b>	<b>33</b>
2.1 <i>pn</i> -homojunction solar cells . . . . .	33
2.1.1 Forming a junction . . . . .	33
2.1.2 Applying a bias to a junction . . . . .	35
2.1.3 Illuminating a <i>pn</i> -junction . . . . .	37
2.1.4 The equivalent circuit of a solar cell . . . . .	41
2.1.5 Finding an explicit <i>I-V</i> relation for a photovoltaic with parasitic resistances .	45

TABLE OF CONTENTS

---

2.2	The opposing-diodes model . . . . .	51
2.3	Fitting and fit quality . . . . .	60
2.3.1	Orthogonal distance regression . . . . .	60
2.3.1.1	Background: ordinary least-squares regression . . . . .	60
2.3.1.2	Uncertainty in both variables: the need for ODR . . . . .	62
2.3.2	Assessing the quality of a fit . . . . .	63
2.3.2.1	The unsuitability of the reduced chi-squared statistic for the opposing-diodes model . . . . .	63
2.3.2.2	Residual inspection and non-parametric testing . . . . .	64
<b>3</b>	<b>Experimental and computational methods</b>	<b>69</b>
3.1	Cell and device fabrication . . . . .	69
3.2	X-ray photoelectron spectroscopy for termination stoichiometry . . . . .	72
3.2.1	Basic principles of XPS . . . . .	72
3.2.2	Experimental procedure . . . . .	73
3.3	Irradiation and electrical methods . . . . .	75
3.3.1	X-ray tomography microscope . . . . .	75
3.3.2	Synchrotrons . . . . .	76
3.3.2.1	The SPring-8 Synchrotron . . . . .	77
3.3.2.2	The Diamond Light Source synchrotron . . . . .	77
3.3.3	Co-60 Irradiation Cell . . . . .	78
3.3.4	Cs-137 Irradiator . . . . .	81
3.4	Computational Methods . . . . .	82
3.4.1	High-energy physics simulation with GEANT4 . . . . .	83
3.4.2	Computational use of Lambert's $W$ -function in the opposing-diodes model . . . . .	84
3.4.3	Calculation of the Lilliefors correction . . . . .	86
3.4.4	Fitting $I$ - $V$ data . . . . .	86
3.4.5	Miscellaneous tasks . . . . .	88
<b>4</b>	<b>The quantification of hydrogen coverage on the DGV, and its necessity for device function</b>	<b>91</b>
4.1	Quantification of surface termination via x-ray photoelectron spectroscopy . . . . .	92
4.1.1	Full survey scans . . . . .	92
4.1.2	O 1s and C 1s peak region scans . . . . .	92
4.1.3	Monolayer estimation . . . . .	93
4.2	The question of the efficacy of hydrogen termination . . . . .	96
<b>5</b>	<b>Synchrotron- and simulation- based studies of the physics of the diamond gammavoltaic cell</b>	<b>101</b>

5.1	GEANT4 simulation of a single-celled DGV irradiated with monoenergetic 1 - 2000 keV photons . . . . .	102
5.1.1	Simulation details . . . . .	102
5.1.2	Simulation Results . . . . .	103
5.2	Photoresponse mapping of a single-celled DGV at the SPring-8 synchrotron for simulation validation . . . . .	105
5.2.1	Simulation details . . . . .	105
5.2.2	Experimental details . . . . .	106
5.2.3	Results . . . . .	106
5.3	Probing an interaction crossover region at the Diamond Light Source synchrotron . .	109
5.3.1	GEANT4 simulation of a single-celled DGV irradiated by the DLS synchrotron	109
5.3.1.1	Simulation Details . . . . .	109
5.3.1.2	Simulation Results . . . . .	109
5.3.2	Current-voltage and power-voltage curves, power efficiencies and flux-normalised quantities . . . . .	111
5.3.2.1	Raw current-voltage and power-voltage curves with photon energy and flux varying . . . . .	111
5.3.2.2	Power efficiencies . . . . .	114
5.3.2.3	Flux normalised values . . . . .	116
<b>6</b>	<b>Isotope irradiation studies for more realistic performance assessment</b>	<b>119</b>
6.1	GEANT4 simulation of a triple-celled DGV irradiated with monoenergetic 1 -2000 keV photons . . . . .	120
6.1.1	Simulation details . . . . .	120
6.1.2	Simulation Results . . . . .	121
6.2	Irradiation of a triple-celled DGV with Cs-137 and Co-60 gamma rays . . . . .	123
6.3	Assessment of the durability of a single-celled DGV under Cs-137 gamma irradiation	150
6.3.1	<i>I-V</i> and <i>P-V</i> curves taken over 600 hours at 1,350 Gy/h Cs-137 irradiation. .	150
6.3.2	Parameter behaviour with irradiation time . . . . .	152
<b>7</b>	<b>Conclusions</b>	<b>157</b>
7.1	Summary of this work . . . . .	157
7.1.1	Capability and accountability: XRT and XPS experiments in Chapter 4 . . . .	158
7.1.2	Further accountability: synchrotron studies and validation of a GEANT4 model in Chapter 5 . . . . .	158
7.1.3	Comparability, applicability and longevity: Isotope irradiation experiments in Chapter 6 . . . . .	160
7.2	Avenues for future work . . . . .	162
7.2.1	Diamond type . . . . .	163

TABLE OF CONTENTS

---

7.2.2	Termination optimisation . . . . .	163
7.2.3	Mounting: Scatter shrouds and backplates . . . . .	164
7.3	A final demonstration . . . . .	167
<b>A</b>	<b>References for diamond-metal contacts</b>	<b>169</b>
<b>B</b>	<b><i>I-V</i> curves taken at the SPring-8 synchrotron in full</b>	<b>173</b>
<b>C</b>	<b>Towards mechanistic modelling of the long Cs-136 irradiation</b>	<b>177</b>
	<b>Bibliography</b>	<b>179</b>

## OUTPUTS

The work presented in this thesis has led to the following journal articles, formal presentations and miscellaneous outputs: -

### Journal Articles

#### *Available in print*

Mackenzie *et al*, "A diamond gammadvoltaic cell utilising surface conductivity and its response to different photon interaction mechanisms", *Materials Today Energy* **21** p.100688 (2021) - Reference [? ].

#### *In preparation*

Mackenzie *et al*, "A triple-celled diamond gammadvoltaic device tested for performance and longevity under irradiation from Cs-137 and Co-60 gamma rays".

### Presentations

#### *In reverse chronological order*

POSTER: "Towards Waste Monitoring, Powered by Waste", *Waste Management Symposium 2021*, virtual, normally Phoenix, Arizona, USA. 8th March 2021.

ORAL: "Micropower from Gamma Fields", *Institute of Physics Nuclear Series*, UK, virtual, 2nd June 2020.

ORAL: "Towards Gammadvoltaics for Energy Harvesting", *Nuclear Control and Instrumentation Engineering Workshop for the Scheme for Promotion of Academic and Research Collaboration*, National Institute of Technology, Tiruchirappalli, India, delivered virtually, 30th January 2020.

POSTER: "A gammadvoltaic diamond device for sensing and micropower generation", *Hasselt Diamond Workshop*, Hasselt, Netherlands, 13th March 2019.

POSTER: "Towards a gammadvoltaic device for low-powered sensors", *Nuclear Research Frontiers*, Bristol, UK, 15th January 2019.

ORAL: "Incorporated Graphitic Contacts for Gammadvoltaic Diamond Devices", *University of Bristol Postgraduate Conference*, 16th May 2018.

## **Miscellaneous**

PRIZE: Second place, *Young Generation Network regional speaking competition*, "Micropower from Gamma Fields", 16th July 2020.

*In preparation*

PATENT: "Diamond Gammavoltaic Cell", United States Patent number 17/674,384 pending.

## GLOSSARY

This glossary presents items split by classification (symbols, initialisms and acronyms, specialised terms) and then ordered alphabetically. The glossary omits certain symbols, terms *etc.* which are only used once and defined in place, or on the way to other concepts.

**N.B.** Elemental and material symbols are not given here, but follow the convention that symbols are used to denote atoms, whilst materials are named. For example, one may talk of the cross-sections of Si and C, but of the overall cross-section of a device made from silicon carbide, not SiC. However, I have tried to let readability and clarity take priority over consistency: conventional symbols have been used rather than material names to avoid ambiguity with radioisotopes (e.g. Co-60 is used rather than "radiocobalt"), and the established convention of using elements symbols, not names, to denote contact metal stacks has been used (thus a stack may be Au/Pt/Ti rather than "gold-platinum-titanium").

### Symbols

Each entry gives the measurement units used here for a quantity and its unit system. References to a given unit include use of scaled versions of that unit via exponentiation. Where a unit is not an SI unit, the relevant SI unit is also given.

- $A$  Cross-sectional area; the electrically-active cross-sectional area of a diode or voltaic cell, which may be equal to the area of the contacts. Square metre ( $\text{m}^2$ ), SI based unit.
- $\delta$  Fit residuals on the abscissa. Units depend on abscissa units.
- $E_c$  The energy of the conduction band minimum in a crystal. Electronvolt (eV), an SI-sanctioned non-SI unit; SI unit is the joule (J).
- $E_{\text{dep}}$  The energy deposited into a substance by incident radiation. Electronvolt (eV), an SI-sanctioned non-SI unit; SI unit is the joule (J).

- $E_F$  The Fermi level in a crystal; the energy at which there is a 50 % chance that carriers would fill the level if one existed there at thermal equilibrium. Electronvolt (eV), an SI-sanctioned non-SI unit; SI unit is the joule (J).
- $E_{F,n}$  The electron quasi-Fermi level in a crystal; the energy at which there is a 50 % chance that electrons would fill the level if one existed there when electrons are in equilibrium with each other but not with the hole population. Also known as the electron imref. Electronvolt (eV), an SI-sanctioned non-SI unit; SI unit is the joule (J).
- $E_{F,p}$  The hole quasi-Fermi level in a crystal; the energy at which there is a 50 % chance that holes would fill the level if one existed there when holes are in equilibrium with each other but not with the electron population. Also known as the hole imref. Electronvolt (eV), an SI-sanctioned non-SI unit; SI unit is the joule (J).
- $E_g$  The size in energy of the band gap in a crystal. Electronvolt (eV), an SI-sanctioned non-SI unit; SI unit is the joule (J).
- $E_\gamma$  Photon energy; the energy of either a single photon or a population of monoenergetic photons. Electronvolt (eV), an SI-sanctioned non-SI unit; SI unit is the joule (J).
- $E_v$  The energy of the valence band maximum in a crystal. Electronvolt (eV), an SI-sanctioned non-SI unit; SI unit is the joule (J).
- $\epsilon$  Fit residuals on the ordinate axis. Units depending on ordinate axis units.
- $FF$  Fill factor, treated as a symbol rather than an initialism by convention. A measure of quality for a voltaic device which compares its actual power output to the ideal power output; the ratio of the maximum power-point current to the theoretical or ideal maximum power. Unitless.
- $H$  Relative humidity. The fraction of water vapour actually in the air to the maximum that air could hold, with a view to the temperature and pressure of that air. Unitless, expressed as a percentage (%).
- $\eta$  Incident power efficiency. The ratio of the maximum power-point power to the incident photon/radiation power for a voltaic cell. Unitless.

---

$\eta_{\text{dep}}$	Deposited power efficiency. The ratio of the maximum power-point power to the deposited photon/radiation power for a voltaic cell. $\eta_{\text{dep}} \leq \eta$ . Unitless.
$I$	Current. Ampere (A), SI base unit.
$I_0$	The saturation current of a diode or voltaic cell; the current which the diode or voltaic cell allows through when biased in its blocking direction. May be further subscripted if more than one diode appears in a circuit. Ampere (A), SI base unit.
$I_{\text{diff}}$	Diffusion current; the current flowing through a diode or voltaic cell due to carrier diffusion. Ampere (A), SI base unit.
$I_{\text{MPP}}$	Maximum power-point current. The current flowing through a voltaic when it is generating its maximum possible output power under the extant conditions. Ampere (A), SI base unit.
$I_{\text{Ph}}$	Photocurrent. the current generated by incident light or other radiation in a voltaic cell. Ampere (A), SI base unit.
$I_{\text{SC}}$	Short-circuit current. The current a voltaic device produces when operating with no voltage across it (as if the device were shorted). Ampere (A), SI base unit.
$k_{\text{b}}$	The Boltzmann constant: $1.380649 \times 10^{-23} \text{ J.K}^{-1}$ . Joules per Kelvin, derived SI unit.
$n$	Used for two separate quantities: (1) Electron density of a semiconductor. Electrons per cubic centimetre ( $\text{cm}^{-3}$ ). (2) ideality factor of a diode or voltaic cell. Unitless.
$P_{\text{dep}}$	Deposited photon power; the power deposited into a volume by a stream of photons with a given flux and a given energy or range of energies. $P_{\text{dep}} \leq P_{\gamma}$ . Watt (W), SI derived unit.
$P_{\gamma}$	Incident photon power; the power delivered to an area or volume by a stream of photons with a given flux and a given energy or range of energies. Watt (W), SI derived unit.

- $P_{\text{MAX}}$  Theoretical or ideal maximum power. The output power a "perfect" device with the same short-circuit current and open-circuit voltage would produce under the extant conditions; the product of the short-circuit current and the open-circuit voltage. Watt (W), SI derived unit.
- $P_{\text{MPP}}$  Maximum power-point power. The maximum possible output power under the extant conditions. Watt (W), SI derived unit.
- $\wp$  Volumetric maximum power-point power density. The maximum power-point of a device divided by the volume of the device, always given with the radiation type in superscript and the air KERMA dose rate (in Gy/h) in subscript to the left, e.g.  $^{60}_{100}\text{Co}\wp$ . Nanowatts per cubic centimeter ( $\text{nW}/\text{cm}^3$ ), derived SI units.
- $p$  Areal maximum power-point power density. The maximum power-point of a device divided by the surface area of the device, always given with the radiation type in superscript and the air KERMA dose rate (in Gy/h) in subscript to the left, e.g.  $^{55}_{1}\text{Fe}p$ . Nanowatts per square centimeter ( $\text{nW}/\text{cm}^2$ ), derived SI units.
- $q$  Used for two separate quantities: (1) The number of electrons bound to an atom. In a neutral atom (i.e. not an ion),  $q = Z$ . Unitless. (2) the elementary charge,  $1.602176634 \times 10^{-19}$  C. Coulomb, derived SI unit.
- $R_{\text{S}}$  Series resistance. The resistance a current is subject to when travelling the intended path through a device. Ohm ( $\Omega$ ), derived SI unit.
- $R_{\text{Sh}}$  Shunt resistance. The resistance a current is subject to when travelling the unintended, or leakage, paths through a device. May be further subscripted if more than one shunt resistor appears in an equivalent circuit. Ohm ( $\Omega$ ), derived SI unit.
- $S$  Used in two separate contexts. (1) The aptly-named "S-parameter". The parameter which determines how well a semiconductor will obey the foundational or basic principles of the energy band-bending model of Schottky contacts. Unitless. (2) the letter used to label various regressors in curve-fitting. Unitless.
- $\sigma$  This symbol is used in two ways depending on context. For particle interactions with matter, see CROSS-SECTION in the Initialisms and Acronyms section. In all other cases it is a reference to the standard deviation of a set of measurements, and takes the unit of that measurement.

---

$T$	Temperature. Kelvin (K), base SI unit. Occasionally given in degrees Celsius ( $^{\circ}\text{C}$ ), miscellaneous non-SI unit. The scales are offset but equal in step size: $0^{\circ}\text{C} = 273.15\text{ K}$ .
$T_e$	The kinetic energy of an electron. Electronvolt (eV), an SI-sanctioned non-SI unit; SI unit is the joule (J).
$\theta$	Monolayer coverage. Always in subscript with the species forming the monolayer, e.g. $\theta_{\text{H}_2\text{O}}$ . Unitless, but always expressed in fractional terms rather than percentage terms.
$V$	Voltage. Volt (V), SI derived unit.
$V_D$	Diode voltage. The voltage across a diode when said diode is embedded in a wider circuit, meaning in general $V_D \neq V$ . May be further subscripted if more than one diode appears in a circuit. Volt (V), SI derived unit.
$V_{\text{MPP}}$	Maximum power-point voltage. The voltage over an operating voltaic when it is generating its maximum possible output power under the extant conditions. Volt (V), SI derived unit.
$V_{\text{OC}}$	Open-circuit voltage. The voltage that appears over an operating voltaic when no net current is flowing through it (as if the circuit were broken, or "open"). Volt (V), SI derived unit.
$V_T$	The thermal voltage; a quantity related to the energy charge carriers have due to a diode or voltaic cell being operated above absolute zero. $V_T = k_b T / q \approx 0.026\text{ V}$ at 300 K. Volt (V), SI derived unit.
$\phi_B$	Schottky barrier height. The potential barrier that forms naturally when a metal comes into electrical contact with a semiconductor. Units not used in this work, most commonly used with the electronvolt (eV), an SI-sanctioned non-SI unit; SI unit is the joule (J).
$X$	Electron affinity. The amount of energy released when a neutral atom attracts an electron, to become a negative ion. Units not used in this work, most commonly used with the electronvolt (eV), an SI-sanctioned non-SI unit; SI unit is the joule (J).

- $\chi_v^2$  Reduced chi-squared fit statistic. A fit statistic for assessing the likelihood that an unbounded linear fit is physical. Unitless.
- Z Atomic number. The number of protons in the nucleus of an atom. Unitless.

## Initialisms and acronyms

Some initialisms and acronyms represent quantities as symbols do. These follow the same convention as the symbol list for reporting unit information.

- CVD **C**hemical **V**apour **D**eposition. A material and device fabrication technique by which chemicals are first vapourised before mixing and then depositing onto a substrate. In this work, the type of CVD discussed is always microwave-enhanced CVD, a process by which the vapours are energised into a plasma with microwave radiation to grow diamond.
- DGV **D**iamond **G**amma**V**oltaic. May refer to either a device or a single cell, though usually this is specified rather than left to context where the distinction is important.
- DLS **D**iamond **L**ight **S**ource. A synchrotron in Oxfordshire, England, UK. Where this initialism is used in the text, it is normally to refer specifically to beamline I12 of said synchrotron.
- EQE **E**xternal **Q**uantum **E**fficiency. The average number of conduction electrons collected for every incident quantum of radiation. In the case of a gamma-voltaic, every gamma photon. Unitless.
- HPHT **H**igh-**P**ressure, **H**igh-**T**emperature. A method of diamond growth which operates by mimicking the high-pressure, high-temperature conditions in which diamonds form naturally.
- KS **K**olmogorov - **S**mirnov test, or statistic. A non-parametric test for normality, which in this work is used for testing residuals.
- NIST **N**ational **I**nstitute of **S**tandards and **T**echnology. A non-regulatory US government body specialising in metrology and standards.

---

ODR	<b>Orthogonal Distance Regression.</b> A method of fitting explicit or implicit linear or non-linear models to data with uncertainty in both the ordinate and abscissa variables.
OLS	<b>Ordinary Least Squares.</b> A method of fitting explicit linear or non-linear models to data with uncertainty in the ordinate variable.
SMA	<b>SubMiniature, version A.</b> A type of electrical connector.
SP8	<b>SPring-8.</b> A synchrotron in Harima Science Park City, Hyogo Prefecture, Japan. "SPring-8" is itself an acronym for <b>Super Photon ring - 8 GeV</b> .
KERMA	<b>Kinetic Energy Released in MAtter.</b> The sum of all the kinetic energies of the secondary charged particles liberated by ionising radiation. This is a material-dependent quantity. It is distinct from energy deposited, as secondary particles may escape the material with some of their kinetic energy remaining. Thus, KERMA deviates from energy deposited as incident energy increases. Grays (Gy), derived SI unit.
MPP	<b>Maximum Power-Point.</b> The maximum measurement on a $P$ - $V$ graph, or more properly a point which may reside between two measurements and which would have been the maximum had a measurement been made there. As $P$ - $V$ graphs are generally constructed from $I$ - $V$ graphs, the co-ordinates of this point can be said to comprise of the current, applied bias and power at that point.
XPS	<b>X-ray Photoelectron Spectroscopy.</b> A surface-sensitive analysis technique which uses x-rays to collect chemical information about samples such as elemental composition and the binding states of said elements.

## Specialised terms

Absorbed dose	The energy deposited into a substance by a given flux or field of radiation per unit mass. Gray (Gy), a derived SI unit. However, literature is quoted which uses the rad, a CGS unit. 1 rad = 0.01 Gy.
Alphavoltaic	A radiovoltaic for which the radiation in question is formed of alpha particles.

Betavoltaic	A radiovoltaic for which the radiation in question is formed of beta particles.
Bremsstrahlung	Photons radiated by high-energy charged particles as they slow down or change direction; a German loan word, from <i>bremsen Strahlung</i> , "breaking radiation". The term is also used as a shorthand for the physical processes that create bremsstrahlung.
Compton scattering	A process by which a photon interacts with an electron, being deflected and giving some of its energy to the electron (often enough to break the electron from atomic binding, where relevant).
Cross-section	An analogous quantity for the probability an interaction between two particles, or a particle and a device, will occur. This is discussed in both a qualitative and a quantitative sense in this work. Where it is quantitative, the unit used in the miscellaneous non-SI unit, the barn (b); the SI unit is the square meter (m <sup>2</sup> ).
Equivalent dose	A measure of the projected stochastic health effects of radiation on the body. Occasionally found in gammavoltaic literature depending on the experimental setup used. Sievert (Sv), derived SI unit. For gamma rays, the equivalent dose is equal in value to the absorbed dose in tissue; an absorbed dose of 1 Gy creates an equivalent dose of 1 Sv. For diamond, due to approximate tissue equivalence, a rough approximation means this can be extended back in the other direction: a 1 Sv/h flux may deposit 1 Gy/h of absorbed dose in diamond. Occasionally seen in literature in terms of Roentgen Equivalent Man/Men (rem), a deprecated non-SI unit. 1 rem = 0.01 Sv.
Exposure dose	Referenced obliquely in the text, a deprecated measure of irradiation which is a measure of the total charge of particles ionised in air by x-rays or gamma rays. Roentgen (R), non-SI and deprecated unit. Of use insofar as 1 R translates to 0.009 Gy of absorbed dose in air (although they are not measures of the same quantity).

---

Gammavoltaic	A term used as both an adjective and a noun to describe a device which converts gamma radiation into electricity directly or, at least, without recourse to heat; a photovoltaic which operates for photons with energies higher than those of visible photons, usually much higher; a radiovoltaic for which the radiation in question is formed of gamma rays.
Gamut, the	The photon energy range from 1 - 2000 keV which this work argues is the window relevant to gammavoltaic research. Name chosen from the contemporary meaning of the phrase "run the gamut" (display the complete range of something), and in relation to the origin of that phrase, <i>gamma ut</i> , the Latin phrase for the range of notes (hence wave energies) starting at bass G, and due to its chiming well with the word "gammavoltaic" itself.
GEANT4	Strictly speaking an acronym ( <b>GE</b> ometry <b>ANd</b> <b>T</b> racking 4), but in practice a proper noun; the name of the high energy physics simulation software used in this work.
Pair production	A process by which a photon with 1022 keV of energy or more spontaneously materialises into an electron and a positron. In this work, this is only considered in the nuclear field of an atom. Any excess energy the photon possesses is shared as kinetic energy by the electron and positron.
Photoelectric absorption	A process by which a photon gives all of its energy to an electron bound to an atom, either promoting or ionising it.
Photovoltaic	A term used as both an adjective and a noun to describe a device which converts photons into electricity directly, or at least without recourse to heat. In common parlance synonymous with the solar photovoltaic, which does the above for predominantly visible photons.
Radiovoltaic	A term used as both and adjective and a noun to describe a a device which converts radiation - quanta emitted by radioisotopes - into electricity, either directly, or at least without recourse to heat.

Rayleigh scattering	A process by which a photon interacts with an atom, being deflected by it but keeping all its energy (i.e. an elastic process).
Scatter shroud	Material or materials placed in front of a gammavoltaic to catch gamma rays and direct their scatter products into the gammavoltaic, for the purposes of higher energy collection.
Surface transfer-doping	A process by which conductivity may be created or enhanced on a solid surface by the adsorption of a chemical species, which leads to the creation of a two-dimensional charge carrier gas.
Terminator, the	A modified sputter coater now used to strike direct-current plasmas, used for the termination of diamond surfaces with different atomic species.
Voltaic	An informal description or loose classification of devices; any device which generates electricity by use of some physical principle which appears direct.
XRT	Strictly an initialism ( <b>X-Ray Tomography</b> ), in practice used as a noun to refer to the XRT microscope used as an irradiation method.

## LIST OF TABLES

<b>TABLE</b>	<b>Page</b>
1.1 An illustrative comparison between three fictional gammavoltaic devices. . . . .	30
3.1 Comparison of quantities known for the various irradiation methods. . . . .	75
3.2 Hardware specifications for the computer that ran the simulations. . . . .	83
6.1 <i>p</i> -values from the two-sample Kolmogorov-Smirnov test between residuals from fits to <i>I-V</i> curves taken under different dose rates of Cs-137 gamma rays . . . . .	124
7.1 Simulated energy deposition for diamonds placed side-on to radiation . . . . .	166
A.1 References for Schottky contact barrier heights, Ag to Cr. . . . .	170
A.2 References for Schottky contact barrier heights, Cu to Ni. . . . .	171
A.3 References for Schottky contact barrier heights, Pb to Zr. . . . .	172



## LIST OF FIGURES

FIGURE	Page
1.1 The Gamut; the range of photon energies between 1 - 2000 keV for which almost all gammavoltaics are intended. . . . .	8
1.2 Prevalence for different photon interaction mechanisms for various atoms. . . . .	11
1.3 Total stopping power as a percentage of incident electron kinetic energy, and radiative stopping as a percentage of total stopping, against incident electron kinetic energy. . . . .	12
1.4 A Venn diagram of a sample of metals which have been investigated in the literature for use as low-barrier and high-barrier contacts . . . . .	19
1.5 Barrier heights attained for a range of metals and terminations with Schottky contacts in literature . . . . .	24
1.6 A band diagram of the surface transfer doping effect of hydrogen-terminated diamond in air	26
1.7 An image detailing three DGV design philosophies . . . . .	28
2.1 A band diagram of $p$ - and $n$ -type silicon being brought into contact to form a $pn$ -junction.	35
2.2 Band diagrams of a $pn$ -junction under positive and negative biases . . . . .	36
2.3 Band diagrams of a $pn$ -junction under illumination under open-circuit and short-circuit conditions . . . . .	38
2.4 Band diagrams showing four types of recombination in silicon . . . . .	39
2.5 The most commonly-encountered equivalent circuit model for a photovoltaic cell, including parasitic resistances. . . . .	41
2.6 A plot of the photovoltaic model equation without parasitic resistances showing the definition of the Fill Factor $FF$ . . . . .	42
2.7 The effect of varying parameters in the PV equivalent circuit without parasitic resistances	44
2.8 The parameter space in the region of the true parameters for simulated $I$ - $V$ data without parasitic resistances . . . . .	46
2.9 Portions of the two real-valued branches of Lambert's $W$ -function . . . . .	47
2.10 The effect of varying the parasitic resistances in the PV equivalent circuit . . . . .	49
2.11 A low-resolution image of the five-dimensional parameter space of the photovoltaic model including parasitic resistances . . . . .	50

LIST OF FIGURES

---

2.12	The subspace of non-resistance parameters for a photovoltaic cell with parasitic resistances, at the true resistance values . . . . .	51
2.13	Band diagrams for the route through the bulk of an unterminated diamond with dissimilar contacts, and around the surface of a terminated diamond with the same contacts. . . . .	53
2.14	A concept band diagram for the DGV . . . . .	54
2.15	Equivalent circuits for the diamond gammavoltaic as two opposing Schottky junction solar cells . . . . .	57
2.16	$I$ - $V$ curves shows the affect of varying the additional parameters from the opposing-diodes model . . . . .	59
2.17	The (empirical -) cumulative density functions for a normal distribution and two random samples drawn from that distributions, to illustrate the Kolmogorov-Smirnov statistic . . . . .	66
3.1	Schematics of the modified equipment used for cell fabrication . . . . .	70
3.2	A render of a single-celled DGV device . . . . .	71
3.3	A schematic of the XPS section of the NanoESCA II . . . . .	74
3.4	A schematic of the x-ray tomography microscope . . . . .	76
3.5	A photograph of the x-ray tomography microscope . . . . .	79
3.6	A schematic diagram of the Co-60 irradiation cell . . . . .	80
3.7	A schematic diagram of the Cs-137 irradiator . . . . .	81
3.8	A flow diagram describing the algorithm used to choose between different implementations of Lambert W calculation . . . . .	87
3.9	A screen-shot of the reactive notebook used to simulate $I$ - $V$ curves against real data to find start-points for fitting procedures . . . . .	89
4.1	Full spectral surveys for various O:H termination ratios on diamond . . . . .	93
4.2	O1s and C1s regions of the x-ray photo-emission spectra for various O:H surface termination ratios on diamond . . . . .	94
4.3	The oxygen monolayer calibration from peak area ratios, for various durations of oxygen termination of a diamond sample . . . . .	95
4.4	$I$ - $V$ curves taken in the XRT both with and without a hydrogen termination on the device . . . . .	97
5.1	The simulation geometry used in simulations of single-celled DGVs . . . . .	103
5.2	GEANT4 simulation data of the number of hits, the energy deposited per hit, and the energy deposited in total for a single-celled DGV with 500,000 incident primary gamma rays, across a range of energies. 10 million gamma rays were spread out over 20 threads. . . . .	104
5.3	Simulation and measurement results for the homogeneous mapping experiment at the SP8 synchrotron . . . . .	107
5.4	GEANT4 simulation data of the number of hits, the energy deposited per hit, and the energy deposited in total for a single-celled DGV with 500,000 incident primary gamma rays, with the energy profiles used at the DLS synchrotron . . . . .	110

---

5.5	Raw DLS I-V and P-V data . . . . .	112
5.6	Key device parameters extracted from the Diamond Light Source experiment . . . . .	113
5.7	Comparison of the power deposited into the device as simulated with GEANT4, to the power output by the single-celled DGV, leading to power conversion efficiencies. . . . .	115
5.8	Flux normalised values of short-circuit current and maximum power-point power of a single-celled DGD at DLS . . . . .	117
6.1	The simulation geometry used in simulations of triple-celled DGVs . . . . .	120
6.2	The total energy deposited into each of the cells of a triple-celled DGV simulated under 500,000 monoenergetic gamma rays at various energies. . . . .	121
6.3	<i>I-V</i> and <i>P-V</i> data from a triple-celled DGV irradiated with dose rates between 15 Gy/h and 3200 Gy/h air KERMA of Cs-137 gamma rays . . . . .	126
6.4	<i>I-V</i> data from a triple-celled DGV irradiated with 15 Gy/h air KERMA of Cs-137 gamma rays, fitted with the opposing-diodes model . . . . .	127
6.5	<i>I-V</i> data from a triple-celled DGV irradiated with 95 Gy/h air KERMA of Cs-137 gamma rays, fitted with the opposing-diodes model . . . . .	128
6.6	<i>I-V</i> data from a triple-celled DGV irradiated with 273 Gy/h air KERMA of Cs-137 gamma rays, fitted with the opposing-diodes model . . . . .	129
6.7	<i>I-V</i> data from a triple-celled DGV irradiated with 520 Gy/h air KERMA of Cs-137 gamma rays, fitted with the opposing-diodes model . . . . .	130
6.8	<i>I-V</i> data from a triple-celled DGV irradiated with 1070 Gy/h air KERMA of Cs-137 gamma rays, fitted with the opposing-diodes model . . . . .	131
6.9	<i>I-V</i> data from a triple-celled DGV irradiated with 3200 Gy/h air KERMA of Cs-137 gamma rays, fitted with the opposing-diodes model . . . . .	132
6.10	<i>I-V</i> and <i>P-V</i> data from a triple-celled DGV irradiated with dose rates between 13 Gy/h and 2900 Gy/h air KERMA of Cs-137 gamma rays . . . . .	133
6.11	<i>I-V</i> data from a triple-celled DGV irradiated with 13 Gy/h air KERMA of Co-60 gamma rays, fitted with the opposing-diodes model . . . . .	134
6.12	<i>I-V</i> data from a triple-celled DGV irradiated with 17 Gy/h air KERMA of Co-60 gamma rays, fitted with the opposing-diodes model . . . . .	135
6.13	<i>I-V</i> data from a triple-celled DGV irradiated with 24 Gy/h air KERMA of Co-60 gamma rays, fitted with the opposing-diodes model . . . . .	136
6.14	<i>I-V</i> data from a triple-celled DGV irradiated with 72 Gy/h air KERMA of Co-60 gamma rays, fitted with the opposing-diodes model . . . . .	137
6.15	<i>I-V</i> data from a triple-celled DGV irradiated with 100 Gy/h air KERMA of Co-60 gamma rays, fitted with the opposing-diodes model . . . . .	138
6.16	<i>I-V</i> data from a triple-celled DGV irradiated with 130 Gy/h air KERMA of Co-60 gamma rays, fitted with the opposing-diodes model . . . . .	139

LIST OF FIGURES

---

6.17	<i>I-V</i> data from a triple-celled DGV irradiated with 149 Gy/h air KERMA of Co-60 gamma rays, fitted with the opposing-diodes model . . . . .	140
6.18	<i>I-V</i> data from a triple-celled DGV irradiated with 241 Gy/h air KERMA of Co-60 gamma rays, fitted with the opposing-diodes model . . . . .	141
6.19	<i>I-V</i> data from a triple-celled DGV irradiated with 374 Gy/h air KERMA of Co-60 gamma rays, fitted with the opposing-diodes model . . . . .	142
6.20	<i>I-V</i> data from a triple-celled DGV irradiated with 743 Gy/h air KERMA of Co-60 gamma rays, fitted with the opposing-diodes model . . . . .	143
6.21	<i>I-V</i> data from a triple-celled DGV irradiated with 902 Gy/h air KERMA of Co-60 gamma rays, fitted with the opposing-diodes model . . . . .	144
6.22	<i>I-V</i> data from a triple-celled DGV irradiated with 2900 Gy/h air KERMA of Co-60 gamma rays, fitted with the opposing-diodes model . . . . .	145
6.23	$I_{SC}$ , $V_{OC}$ , $P_{MPP}$ and $FF$ for the Cs-137 data from Figure ?? and the Co-60 data from Figure 6.10 . . . . .	146
6.24	Fitting parameter values for the opposing-diodes model, as fit to the data in Figures 6.4 to 6.22 . . . . .	148
6.25	3,192 <i>I-V</i> and <i>P-V</i> curves taken under constant irradiation at 1,350 Gy/h air KERMA of Cs-137 gamma irradiation over the course of 600 h. . . . .	151
6.26	$P_{MPP}$ , $I_{SC}$ , $V_{OC}$ , $H$ and $T$ with irradiation time and dose . . . . .	153
7.1	The normalised total energy deposited into a single-celled DGV in various configurations. . . . .	165
7.2	The <i>I-V</i> curve of the triple-celled DGV under irradiation in the XRT. . . . .	166
7.3	The circuit attached to the triple-celled DGV for demonstration purposes. . . . .	167
B.1	The full <i>I-V</i> curves from the SP8 mapping experiment. . . . .	174

## INTRODUCTION

During his doctoral studies, Dr. Hutson of the University of Bristol developed a package of gamma dosimetry equipment based around a diamond dosimeter, showing that it could reliably measure dose rates up to at least 3,600 Gy/h without degradation [1]. One question was raised during that work which could not be pursued at the time, but which spawned this work. During one experiment, the dosimeter appeared to be producing currents around a thousand times weaker than previous experiments suggested it should: picoampere currents in a device which normally produced, by a convenient rule-of-thumb, 1 nA for every 1 Gy/h of air KERMA dose rate. The dosimeter, based on a 0.5 mm thick piece of highly pure, single crystal diamond, required a bias of 300 V to operate. As it transpired (and in a turn of events with which every experimentalist can empathise), the currents had dropped so low not due to degradation, nor some broken component in the wider electronic circuits, but because the bias had been left switched off, accidentally. From the perspective of that work, the obvious course of action was to chalk the episode up to experience and continue with the existing research plan. However, it was not missed that the dosimeter had acted as a source of electricity - as a gammavoltaic. This was unusual for at least two reasons. Firstly, pure diamond is highly insulating [2], and with no external bias, let alone a bias approaching the 300 V operating voltage of the crystal, this diamond should have acted as if it were a break in the circuit, with a resistance on the order of  $10\text{ T}\Omega$  in the dark (thought substantially less at very high dose rates [3]). Secondly, the device was symmetric, at least nominally. The contacts were the same on either side, and designed to create as low a potential barrier as possible. So, the device should not have generated a current in either direction when turned off, due to the low barriers. Then, any current that *was* generated, due to the fact that a low barrier is not *no* barrier, should have been cancelled out by an equal and opposing barrier at the other contact. It seemed that any current that escaped this cancellation, likely due to random variation in the contact deposition process, should have been

even more vanishingly small.

A programme of research was conceived to try to explain the observation, both for reasons of scientific curiosity, and also because gammavoltaics is a nascent field, to which further research into this effect could prove useful. It would be a new approach. Immediate progress towards a "useful" gammavoltaic - one which could surpass previous attempts by achieving an actual deployment - was envisioned with, and supported by, Sellafield Ltd., who had an interest in any device which may be able to power long-deployment environmental monitoring devices for their waste stores. However, this was an ambitious goal. The difference between the power observed in the dosimeter and the power required by the lowest-power energy harvesting chip then on the market <sup>1</sup>, was a factor of six million. Scientific intuition prevailed against numerical doubt, and I was brought onto the project to carry things forward. This work presents the beginning of a programme of work to develop an industrially usable device.

Semiconductor device development does not normally follow this pattern. A mixture of scientific enquiry and engineering, it is by now a fairly well-oiled process in which the golden rules are to simulate far more than one fabricates, and fabricate far more than one investigates. This saves time and resources, lends theoretical context to results, and emphasises process reliability. To a certain extent, however, gammavoltaic development is not like the development of other semiconductor devices. The field is immature, and arguably pre-paradigmatic: several different approaches have been considered for gammavoltaic energy harvesting, which diverge quite strongly in their particulars, with none having yet "won out" in the sense of having created a device that could be deployed and used. What is more, there is no commercial software package capable of simulating the entire process of a semiconductor device converting a flux of gamma rays into a time-dependent current, although in the cases of most designs, the physics of all the steps is well known. For this reason this thesis has elected to follow a lead that has presented itself - a dosimeter producing power when it seemed it should not.

This introduction will first survey what little literature there is on gammavoltaics, highlighting the difficulty of comparison between previous works (through no fault of previous researchers) and the diversity of approaches considered. Following that, an account will be given of the physical processes through which energy must go to be converted from an incident gamma ray into a conduction electron in a device, which will go some of the way to explaining why no software package yet exists that is capable of simulating the whole picture. It will then discuss the use of diamond as a device material. The use of diamond was of course decided at first by circumstance, but eventually it showed itself to be indispensable for the gammavoltaic device design chosen, so this part is not just an exercise in *post hoc* justification. Finally, the introduction will end with a description of the device design pursued in this work, and the series of conceptual steps which led to it from the anomalous dosimeter results. In this final part, an explanation will be given of the experiments performed using this device design and the rationale behind them. This will include a framework I have used to

---

<sup>1</sup>the EH300 by Advanced Linear Devices [4].

understand previous research and to describe this work.

## 1.1 Gammavoltaics: both radiovoltaics and photovoltaics

In the years since the first rooftop solar array was installed in the mid-1880s [5], the solar cell has transformed from an experimental device of roughly 1% efficiency, more suitable for light detection than power generation, to the subject of an international industry. As a field, photovoltaics remains essentially synonymous with solar photovoltaics. However, the same effect is produced for photon energies outside of the visible, and research has sporadically appeared to investigate the potential of photovoltaics for much higher photon energies: gammavoltaics. Gammavoltaics additionally belong to the class of devices known as radiovoltaics, which also include alphavoltaics and betavoltaics<sup>2</sup>. Betavoltaics have been designed, simulated, and/or made out of a fairly wide variety of materials, such as gallium nitride [7, 8], gallium arsenide [9, 10], indium gallium phosphide [11], silicon carbide [12, 13] and most prominently silicon [14–18]. Silicon, along with a tritium source, is the basis of the City Labs/Betacel device lineage, which are not just sold commercially, but have been used to power pacemakers in patients for several decades [19, 20]. In the quest for longer lifetimes and higher power outputs, researchers have looked at using isotopes such as Ni-63 with diamond, most successfully the Moscow team who published a string of articles in the mid-to-late 2010s, culminating in a 200-cell prototype device capable of generating just under 1  $\mu\text{W}$  continuously [21–23]. Further information on the present state of betavoltaic development can be found in a recent and thorough review article by Krasnov and Legotin [24]. Alphavoltaics have received less attention, despite producing more power than betavoltaics as a rule, because the issue of radiation damage has presented itself quite severely in even radiation-hard voltaics [25–27].

Alphavoltaics and betavoltaics are, in general, intended for use as portable micropower sources (whether that be for consumer, military or space use). With a few exceptions [28–32], the case for gammavoltaics has been made differently, as the shielding requirements of gamma isotopes are much greater. Gammavoltaic devices are better suited to deployment into existing and problematic gamma fields. Whilst this limits the applicability of gammavoltaics compared to other radiovoltaics, it also provides an advantage, in that no radioisotope sourcing, handling or processing is necessary in the creation of devices. Furthermore, the amount of energy present in a stationary gamma field can be much greater than that attainable in a compact source intended for self-contained radiovoltaics. It has also, historically, allowed commercial solar photovoltaics to be used directly as gammavoltaics, in various setups. There are several settings in which such gamma fields exist, usually tied to the nuclear industry. In waste stores, ambient air KERMA dose rates are around 100 Gy/h and canister surface dose rates can be 1,200 Gy/h<sup>3</sup>. In these locations, the danger posed by radiation precludes worker access, and information about the interior is sparse. Simple measurements of dose rate, temperature,

---

<sup>2</sup>There is also some evidence of researchers having considered "neutronvoltaics" in the 2000s [6], though this term appears to have been used in reference to powered neutron detectors.

<sup>3</sup>Private communication, Sellafield, 2020. Similar values can be found in [33].

and humidity, if made often, would increase the safety of the stores. Batteries have limited lifespans and retrieval is not feasible, thus using the gamma field itself as a power source is attractive.

In 1960, Scharf tested the suitability of a standard silicon *pn*-junction for x- and gamma-ray dosimetry, echoing the initial application of photovoltaics as light detectors. Using a  $7.9 \text{ cm}^2$  cell of 0.7 mm thickness, under Co-60 irradiation (1.17 MeV and 1.33 MeV), the cell produced a short-circuit current  $I_{SC} \approx 35 \text{ nA}$  and an open-circuit voltage  $V_{OC} \approx 73 \text{ mV}$  at a dose rate of 4 Gy/h [34]. The cell performed better under a more intense irradiation from an unfiltered 50 kV x-ray source, producing an  $I_{SC} \approx 85 \text{ mA}$  and a  $V_{OC} \approx 65 \text{ mV}$  at 1.08 MGy/h. Although the power to dose rate ratio was low, development may have continued from here were it not for the terminal susceptibility of silicon to radiation damage, acknowledged by Scharf. Scharf observed that the cells "*showed considerable decay with time*" at an exposure dose rate of 0.6 Mr/h (6 kGy/h).

More recent attempts, by Horiuchi *et al* in 1997 [35] and White *et al* in 2005 [33] have focused on the use of a tandem device comprising a scintillator and a solar photovoltaic. The former produces the visible light photons, upon irradiation, for which the latter is optimised. White *et al* found that power output degraded with total dose, as did series resistance and shunt resistance. The best voltaic, which had a surface area of  $45 \text{ cm}^2$ , initially achieved an  $I_{SC} = 4.6 \text{ }\mu\text{A}$  and a  $V_{OC} = 0.2 \text{ V}$ , under a Co-60 air absorbed dose rate of 1,224 Gy/h. In 1997, Horiuchi *et al* exposed silicon solar cells to Co-60 gamma rays with the explicit intention of assessing them for power generation from spent nuclear fuel waste [35]. This work was particularly thorough, and assessed amorphous, monocrystalline and polycrystalline solar cells, each both with and without scintillators, and with multiple scintillators assessed. Importantly, this work also recognised and made use of the fact that the penetrating nature of gamma rays allows gammavoltaics to be arranged stackwise as well as arranged panelwise, with the latter being the manner conventional to solar photovoltaics. Results for single cells were reported in terms of conversion efficiency between power produced and an exposure dose of 7950 R/h, with units of  $\text{mW}/\text{cm}^2/\text{R}/\text{h}$ .  $1 \text{ R} = 2.58 \times 10^{-4} \text{ C}/\text{kg}$  of air. Comparison of this to absorbed dose measurements is difficult, as the conversion is material and energy dependent. However, one can look at air KERMA, for which  $1 \text{ Gy} \approx 0.009 \text{ R}$  [36]. The best single-cell performance was  $1.7 \times 10^{-8} \text{ mW}/\text{cm}^2/\text{R}/\text{h}$ , for a  $38 \text{ cm}^2$  monocrystalline cell with a caesium iodide scintillator. For triple-cell stackwise experiments, results were reported in terms of a conversion rate between the induced current density in  $\text{A}/\text{cm}^2$  for each cell. Here, both monocrystalline and polycrystalline cells without scintillators behaved similarly, with conversion rates around  $6.5 \times 10^{-13} \text{ A}/\text{cm}^2/\text{R}/\text{h}$ . Degradation of induced current was found to proceed at a rate of  $6.69 \times 10^{-6} \text{ \%}/\text{R}$  ( $\sim 0.7 \text{ \%}/\text{kGy}$ ) under irradiation at 105 R/h ( $\sim 0.9 \text{ kGy}/\text{h}$ ). Extrapolating this in a linear fashion would give an estimated time to total failure of around 160 h, i.e. just under one week. Of course, linear degradation cannot be assumed, and it is possible the device may have failed far sooner, or lasted far longer. Degradation under gamma irradiation is treated with greater detail in Section 1.3.2, with a focus on diamond.

In 2005, Horiuchi and co-workers developed their work further [37], using a combination of a  $35.2 \text{ cm}^2$  amorphous silicon solar cell and caesium iodide scintillator. This attained an induced current of

approximately 10  $\mu\text{A}$ , and an induced voltage of approximately 2.3 V at a distance of 40 cm from an 18.8 TBq Co-60 source. It is likely in the context that the induced current and induced voltage are equivalent to the  $I_{\text{SC}}$  and  $V_{\text{OC}}$ . Ancillary to the main presented results was a report of a degradation experiment, which noted that after being irradiated for 25 h at an equivalent dose of 791 Sv/h, the power output was "*not completely reduced*" (presumably meaning there was no catastrophic failure but that degradation of some sort had occurred). For the basis of comparison, it should be noted that an equivalent dose of 1 Sv is generated by an absorbed dose of 1 Gy of gamma rays [36], and that diamond is roughly tissue-equivalent [3], so 1 Sv can be treated as equivalent to an absorbed dose of 1 Gy when comparing to diamond gammavoltaics.

Hashizume *et al* reported in 2010 on a set of in-house silicon voltaics which were tested under an absorbed dose rate of 200 Gy/h of Co-60 radiation [38]. These silicon voltaics were tested alongside a commercial silicon solar cell of substantially lower resistance, and interestingly, power output was up to two orders of magnitude greater for the higher-resistance, in-house voltaics. The best device produced 20 nW/cm<sup>2</sup> and 400 nW/cm<sup>3</sup>. However, after 6 months at this dose rate (i.e. a total absorbed dose between 800 and 900 kGy), performance had dropped over 90 %.

The most similar of existing and established devices to a gammavoltaic is the gamma dosimeter or detector, and mention has already been made to the gammavoltaic effect seen in Dr. Hutson's dosimeter. This has also been reported on by Almazov *et al* in a single crystal detector created in 2008 [39], which could operate in a gammavoltaic mode for the purpose of *in vivo* dosimetry and which, when irradiated at an absorbed dose of 180 Gy/h of 10 MV bremsstrahlung photons, produced an  $I_{\text{SC}} = 48$  pA, a  $V_{\text{OC}} = 1.3$  V, and a maximum power-point power  $P_{\text{MPP}} \approx 34$  pW<sup>4</sup>. The diamond device was 4 × 4 mm in area, and made on a commercial substrate fabricated by the high-pressure, high-temperature (HPHT) method, so likely 0.5 mm thick. Section 1.3.1 gives more detail on diamond fabrication techniques. In 2010, Almazov led further research, this time employing a similar device and measuring its responsivity (current collected for power imparted, A/W) between 6 - 20 keV of monochromatic photons at the Diamond Light Source synchrotron [40]. The diamond current (presumably equivalent to the  $I_{\text{SC}}$  of the device) was also measured as a function of photon flux at 17.5 keV, with linear behaviour found for fluxes between 0 -  $2.5 \times 10^{11}$   $\gamma \cdot \text{s}^{-1}$ , and a maximum measured value of approximately 27 nA at approximately  $2.3 \times 10^{11}$   $\gamma \cdot \text{s}^{-1}$ . This device was also a single crystal and also 4 × 4 × 0.5 mm<sup>3</sup> in size. Other researchers have taken a different approach, using single crystal methylammonium lead triiodide [41–44]. Degradation has been observed, but devices have withstood equivalent dose rates of 100 Sv/h during a test of several hours. Being composed of a lead-containing perovskite, these devices are particularly elegant in being highly-absorbing direct conversion devices. However, at time of writing, they still require the application of a DC bias and are in that sense not standalone voltaics, but detectors still.

Finally, some attention should be given to attempts to make portable gammavoltaics, in the mould of other radiovoltaic devices. Liakos, along with a theoretical treatment of scintillator-based

---

<sup>4</sup>These values were obtained by digitisation of the  $I$ - $V$  plot in the article.

gammavoltaics for Co-60 [28, 30], has also modelled the effectiveness of using Th-229, which emits gamma rays with very low (near visible) energies [45], as a safe in-built radioisotope [29]. The low emission energies are the key, in that concept, to sidestepping the shielding requirements normally encumbering portable gammavoltaics. To my knowledge, however, the devices were never made. Butera *et al* reported in 2016 on an aluminium indium phosphide-based gammavoltaic which incorporated an Fe-55 source [31]. Fe-55 emits at a few different energies in the 5-6 keV range [46] and therefore is easy to shield, but does still require a shield, unlike Th-229. The Butera cell operated best at -20 °C, producing a  $P_{MPP} = 1.2$  pW. Small though this is, it should be noted that it represented a very high power conversion efficiency, of 22 %. To my knowledge this is the highest reported conversion efficiency of any radiovoltaic, with other recent references to high conversion efficiencies being on the order of a few percent for both alphavoltaics and betavoltaics. Becquerel for Becquerel, it is otherwise normally to be assumed that gammavoltaics will be less efficient than other types of radiovoltaic, due to the much more penetrating nature of gamma rays. Indeed, all of the above examples of gammavoltaics have involved thin active regions (sensitive volumes) where charge may be collected. This is a natural result of using solar cells in some cases (optimised for much less penetrating radiation) or, in the case of Almaguer *et al*, because the focus of the work was on self-powered beam profiling, so thin volume was directly required for higher spatial resolution, and power output was a secondary concern. This is in stark contrast to the diamond dosimeter found to act as a gammavoltaic by Dr. Hutson, the 0.5 mm thickness of which was around 500 times greater than other reported gammavoltaics - presuming that the entire diamond, being homogeneous, was acting as the sensitive volume. This presumption is tested in this work.

Beyond the simple statement that gamma rays are highly penetrating, the manner by which they interact with a gammavoltaic is an important consideration on the conceptual level (although its specifics are left to simulation software) and sets gammavoltaics apart from other radiovoltaics and photovoltaics. Indeed, it sets some types of gammavoltaics apart from other types, too. This topic will be treated next.

## 1.2 Processes involved in the conversion of a high-energy photon to electron-hole pairs

In all voltaics energy must, ultimately, be converted into a number of low-energy conduction electrons and holes that are collected at the contacts of the device, and so become device current. The form which that energy initially takes defines the processes which must take place for conversion to occur. For gammavoltaics, the processes pertain to how high-energy photons are converted first to intermediary particles, and those intermediary particles are then converted into a larger number of conduction electrons. Of course, gammavoltaics which rely on scintillators have a different set of intermediary processes to those which do not. Only the latter will be considered here. Common to *all* voltaic devices is the set of considerations for how conduction electrons are successfully brought through the device to the contacts, and the sources of inefficiency and energy loss inherent in that journey.

### 1.2.1 High-energy photon scattering processes

With the exception of the concept devices of Liakos, photon energies relevant to gammavoltaics are comfortably bounded by the range 1 - 2000 keV. The portable gammavoltaic candidate Fe-55 undergoes electron capture to Mn-55, emitting x-rays around 6 keV due to internal bremsstrahlung [46]. X-ray tubes and hard x-ray synchrotron beamlines tend to produce photons in the range of 10 - 300 keV. Am-241, which builds up inside plutonium-based thermoelectric devices in space applications, decays to an excited state of Np-237 before emitting a gamma photon at 60 keV [47, 48]. The U-235\* fission delayed-gamma spectrum, which Náfrádi *et al* pointed out could be a source of power in emergency reactor shut-downs [42], sits mostly between 0 - 450 keV, with a broad set of peaks between 50 - 250 keV [49]. Cs-137, the most prominent and troublesome nuclear waste isotope, emits a gamma at 662 keV [50]. Finally, Co-60, which is widely distributed around the world in medical equipment and also a prominent waste isotope, emits two gammas at 1170 and 1340 keV [51]. The range 1 - 2000 keV brackets all these energies nicely on both linear and logarithmic scales, for the sake of study. This range and the important energies within it are shown in Figure 1.1. I have taken to calling this range the Gamut, on the basis of both the contemporary meaning of the word, and its etymology<sup>5</sup>. To my knowledge there is no way of testing a gammavoltaic that runs the full Gamut in a way which is self-consistent, making a piecemeal approach necessary. Of course, simulation studies are not so bound. Over the Gamut, there are four photon-matter interactions of importance. These are Rayleigh scattering, photoelectric absorption, Compton scattering, and pair production in the nuclear field. Of these, all but Rayleigh scattering are inelastic.

Rayleigh scattering will take place when the scattering centres are smaller than the wavelength of the incident photon [53]. This locates the Rayleigh scattering region in the lower end of the Gamut. A 1 keV photon has a wavelength of about 1.2 nm, whilst the lattice parameter of diamond is 3.6 Å[54].

---

<sup>5</sup>Originally from the phrase *gamma ut*, the musical scale (hence range of wavelengths) starting at gamma, the low G.

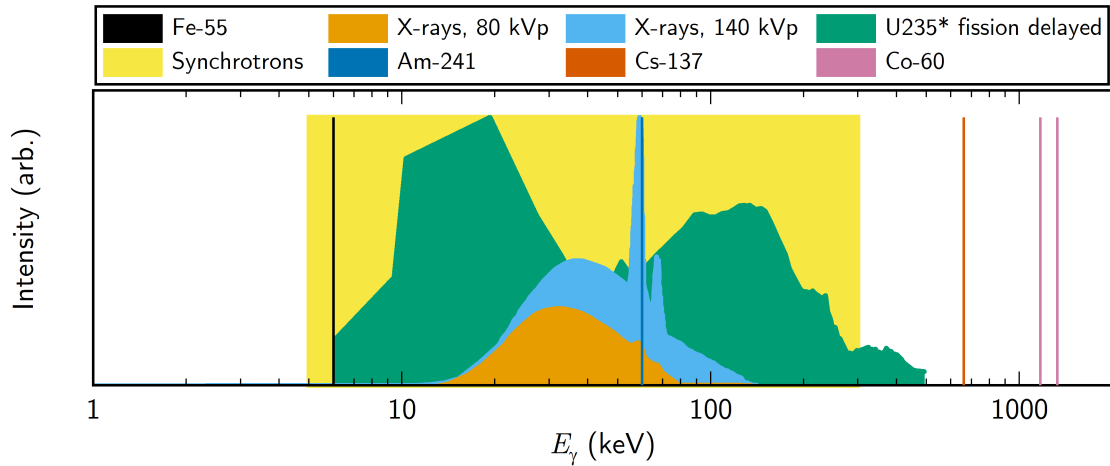


FIGURE 1.1. The Gamut; the range of photon energies between 1 - 2000 keV for which almost all gammavoltaics are intended. Shown in the figure are normalised energy spectra for various relevant isotopes; the range in which hard x-ray beamlines at synchrotrons operate; two example spectra from a tungsten x-ray tube operating at different source voltages, digitised and adapted from [52]; and, the U235\* fission delayed gamma spectrum, digitised and adapted from [49]. Note that the original data was on a linear scale, so resolution is poorer at lower energies due to the logarithmic scale in this figure.

When interacting via Rayleigh scattering, a photon is effectively absorbed and re-emitted by an atom, leading to no overall energy deposition. Rayleigh scattering may lead to emission in any direction, but there are emission maxima parallel and anti-parallel to the direction of travel of the incident photon <sup>6</sup>.

In photoelectric absorption, a photon gives the entirety of its energy to an atomic electron, and is destroyed [56]. Depending on the energy of the photon, the generated electron - the photoelectron - may either be promoted to an excited state but remain bound to the lattice, or it may escape its binding. Taking the former case, the photoelectric effect is the mechanism by which conventional photovoltaics convert the energy in photons into electrons. Taking the latter, the photoelectric effect is the mechanism upon which x-ray photoelectron spectroscopy is based (see Section 3.2). When considering photons with higher energies such as x-rays and gamma rays, the absorption of all this energy by an electron will not directly create a charge-carrying electron as in a conventional photovoltaic, but rather a "hot" electron, which travels through the lattice ballistically. This is a beta particle in all but origin, and the device effectively becomes a betavoltaic from an energy perspective once a photon has been converted in this way. For gammavoltaics which are intended as portable devices, Rayleigh scattering and photoelectric absorption are the only two processes

<sup>6</sup>The equation for scattered irradiance has two terms, one of which is proportional to  $\cos^2(\theta)$  where  $\theta$  is the scattering angle relative to the incident direction [55].

needing consideration, as the comparatively low emission energies of the sources used do not break through to the next regime - that of Compton scattering.

In Compton scattering, a photon can either be said to give part of its energy to an electron, or equivalently to be destroyed and to give part of its energy to a secondary photon and part to a secondary electron [57]. Whereas photoelectric absorption conceivably involves the interaction of a photon with an entire atom, Compton scattering is associated only with the electrons themselves. The photoelectric cross-section has a complicated but direct relationship to the material's average  $Z$ , whilst Compton scattering is linearly related to  $q$ , the number of electrons per atom [58]. For neutral atoms,  $q = Z$ , so this distinction does not matter much. However, it is worth noting that for light elements, the addition or removal of even one electron per atom can cause  $q$  to deviate significantly from  $Z$ . For carbon,  $Z = 6$ . To ionise by the loss of one electron thus reduces the Compton scattering cross-section of a carbon atom by  $\sim 18\%$ . Compton scattering takes place at higher energies than photoelectric absorption, with there being a crossover region in which both interactions are present. The reasoning for how a Compton electron must then be treated is the same to how a photoelectron must be treated - effectively a beta particle. Additionally, and depending on the energy of the incident photon, the Compton photon may *itself* go on to interact with the material via either Compton scattering or photoelectric absorption.

Finally, in pair production in the nuclear field, a photon passing within a certain distance of a nucleus may spontaneously convert into an electron and a positron [59]. At the energies considered, the proximity to a nucleus is required by conservation of momentum; the nucleus recoils slightly as the electron and positron are produced [59]. The threshold photon energy for this process, to first approximation, is 1022 keV. That is, the combined rest mass energies of the electron and positron,  $2m_e c^2 = 2 \times 511$  keV. Any additional photon energy is converted into kinetic energy for the electron and positron. The corollary for this is that while pair production above 1022 keV will create hot electrons and hot positrons (which behave much the same as hot electrons, albeit with slightly shorter attenuation paths [60]), electrons and positrons produced from a photon at or near the 1022 keV threshold are quite likely to annihilate, unless external factors such as an electric field are present to sweep the particles apart. Annihilation leads normally to the production of two photons, each on average now having approximately half the energy of the incident photon. Little has been deposited except recoil, and from an energy harvesting perspective, one higher-energy photon has effectively converted itself into two or more lower energy photons, likely to deposit energy by other mechanisms, if at all. If annihilation does not occur in such threshold cases, however, some uncertainties arise. Kinetically the positron ought to behave much as any electron of reasonably low energy would inside a material, but to my knowledge, it is not known whether under favourable conditions it would act as a true charge carrier - for example, if it were created in the depletion region of a voltaic <sup>7</sup>. The behaviour of positrons in materials, including semiconductors and diamond specifically, has been

---

<sup>7</sup>One may well ask: if an incident photon with an energy of 1022.01 keV undergoes pair production in the nuclear field of an atom in the depletion region of a voltaic, is the result truly a loose low-energy positron and a 5 eV electron, effectively just a conduction electron?

studied and is the basis of techniques such as positron annihilation spectroscopy [61]. However, to my knowledge, all such research is aimed at material characterisation and not the study of how positrons may act as charge carriers in an active device. After typically less than 120 ps in a high-quality diamond [62], and up to 1 ns in a diamond with sufficient internal vacancy space [63], such positrons will annihilate regardless, and may produce one photon rather than two or more if the electron involved is tightly bound to an atom.

The National Institute of Standards and Technology in the USA provides a program, XCOM, for calculating the cross sections for the various photon interaction mechanisms for most elements [64]. Figure 1.2 shows mechanism prevalences based on these plotted over the Gamut for five atoms. The atoms, C, Si, Fe, Ag and Au, are chosen for their wide range in  $Z$  and their relevance to this work and others. All elements but silicon form major parts of the DGV and test mounting used in this work, whilst silicon is a good typical case for a semiconductor and is the main material in several of the works mentioned previously. In all cases, Compton scattering is the main photon interaction mechanism and dominates for most energies. Pair production only becomes significant at higher photon energies and higher  $Z$ , its prevalence reaching around 10 % in Au at 2000 keV. Gold itself, as a metal, would not be used for the bulk of a gammavoltaic. However, it forms a major part of electrical contacts and is likely to be present in appreciable quantities in device housings. Scatter products may be scattered into the device from its enshrouding housing, and the prevalence values support the notion that at Co-60 photon energies, gold in contacts and housing may supply small but notable quantities of positrons to a diamond device. Also notable along these lines is the Rayleigh scattering prevalence. Rayleigh scattering is an elastic process, and so for the purposes of power generation, is broadly a detractive effect within the device itself and enhanceive in the device housing. It is therefore encouraging that the Rayleigh scattering prevalence in C is always small, and becomes more so rapidly as photon energy increases. Doubly encouraging is that for the heavier, housing elements, it remains comparatively large up to around 500 keV. Whilst the most prominent gamma emitters emit gamma rays at energies higher than this, the photons produced via Compton scattering and bremsstrahlung are largely in this range. It can be envisioned that a Compton photon caused by a 662 keV Cs-137 gamma might escape the device, only to be bounced back in by Rayleigh scattering from adjacent gold and thence be absorbed.

The crossover between photoelectric absorption-dominant and Compton scattering-dominant regimes occurs at higher energies for higher  $Z$ . On the face of it this is a bad thing for carbon-based gammavoltaics, as the part of the interaction energy embodied in the Compton photon is more liable to escape the device than when all the energy is bound up in a secondary electron, as in photoelectric absorption. This would favour higher- $Z$  semiconductors for gammavoltaic work in which this crossover is relevant. In this example, one might favour a silicon or silicon-based semiconductor for gammavoltaic devices operating with photon energies below about 100 keV, provided they can avoid radiation damage. However, as is explored in Reference [65] and Chapter 5, this may not be true in an unqualified sense when the effect of photon interaction on semiconductor electrical properties is

1.2. PROCESSES INVOLVED IN THE CONVERSION OF A HIGH-ENERGY PHOTON TO ELECTRON-HOLE PAIRS

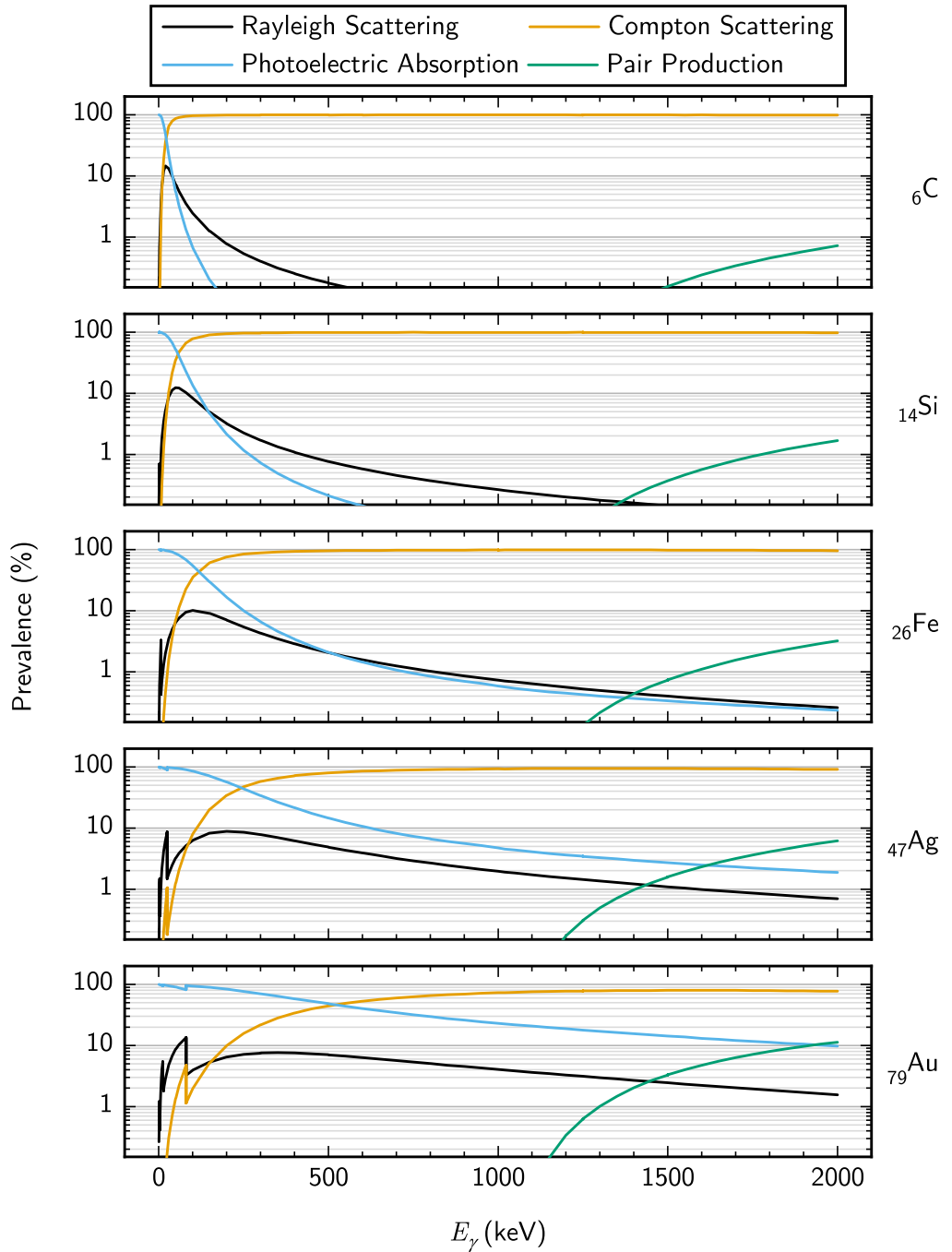


FIGURE 1.2. Prevalence for different photon interaction mechanisms for various atoms. Pair production is in the nuclear field only.

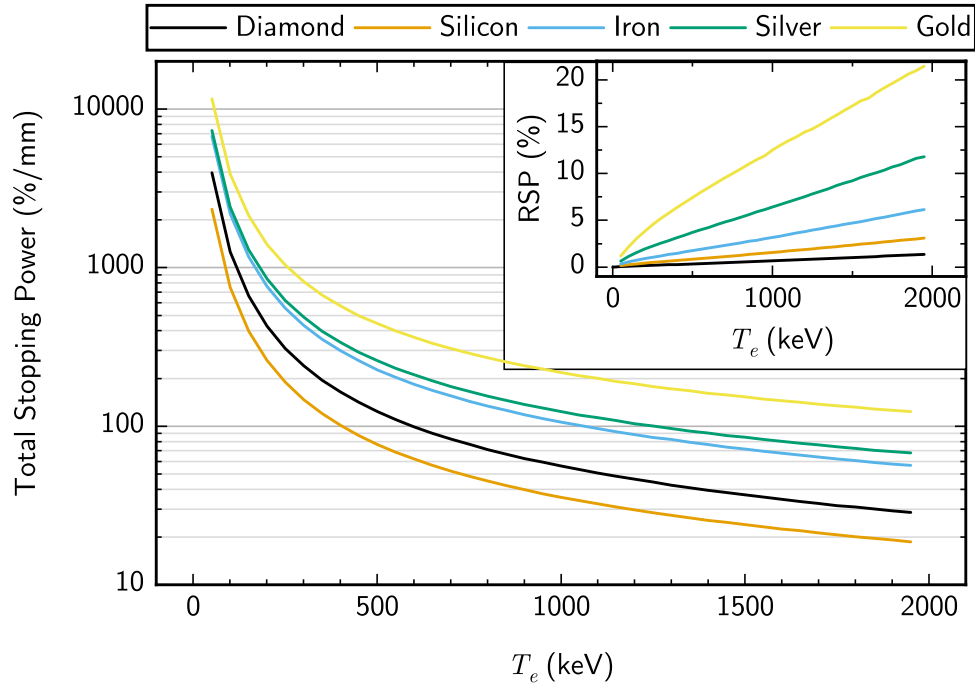


FIGURE 1.3. Total stopping power as a percentage of incident electron kinetic energy, and (inset) radiative stopping as a percentage of total stopping, against incident electron kinetic energy.

considered.

For Ag and Au, which are atoms with higher  $Z$ , edges begin to show prominently in the photo-electron absorption behaviour. Whilst this is unlikely to contribute significantly to power output in devices which are not optimised to exploit the effect, the abrupt nature of absorption edges does suggest itself as a tool for greater qualitative understanding when devices are tested. Measurements made either side of an absorption edge may be used to investigate the contribution of enshrouding metal to power output, or else used as a position of maximum contrast for degradation testing as in Chapter 5.3.

### 1.2.2 Electron scattering processes

Of the photon interaction mechanisms, all but Rayleigh scattering produce a secondary electron. The magnitude of the photon energies considered means that this electron cannot be considered "promoted" in the conventional photovoltaic sense. Rather, it interacts with the device first as a high energy particle - like a beta particle in a betavoltaic - before either escaping the device or gradually losing its energy and becoming a conduction electron. One implication of this relates to

the external quantum efficiency (EQE), which is the ratio of incident photons to collected electrons. In a gammavoltaic the EQE may be, and indeed really ought to be, greater than 1. In a conventional photovoltaic, this is never the case, as a photon may promote at most one electron. For a solar photovoltaic, the EQE is equivalent to the probability that an incident photon will cause an electron to be collected [66, p. 7].

Taking high-energy, massive, charged particles in general, interaction mechanisms in solids - referred to as types of "stopping" due to their retarding effect on the particles - are Coulomb (or collision) stopping, nuclear stopping, and radiative stopping [60].

Coulomb stopping is the process by which charged particles interact with the electrons in a solid. The incident particle scatters from atomic electrons, promoting or ejecting them and thus losing energy in the process [67].

Nuclear stopping, also referred to as Non-Ionizing Energy Loss (NIEL), is a process by which charged particles lose energy by scattering from nuclei rather than electrons. This may result only in phonons being generated at the lattice site, or in the atom becoming displaced [68]. Although nuclear stopping is a dominant degradation mechanism for devices subjected to radiation (for example, solar cells in space [69]), the contribution to the energy being deposited in any given moment is negligible compared to that of Coulomb stopping [68]. More attention to damage is given in Section 1.3.2.

Radiative stopping refers to bremsstrahlung, and may occur either when an electron is deflected by a nucleus (conventional bremsstrahlung), or by an electron (ee-bremsstrahlung) [70]. The radiative loss experienced by an electron is proportional to the square of the charge of a scattering centre, be that centre a nucleus or an electron. This means that ee-bremsstrahlung scales linearly with  $Z$  as the number of electrons (i.e.  $q = 1$  scattering centres) per atom increases, whilst conventional bremsstrahlung increases with  $Z^2$ , as the charge of the nucleus of each atom, a single scattering site, increases [71]. As such, ee-bremsstrahlung is often disregarded, as the effect of conventional bremsstrahlung quickly dominates. However, this is not appropriate for low- $Z$  materials such as diamond [60], where the effect of the two is more comparable.

To get a top-level understanding of what happens to electrons which are generated by photon interactions in the materials in Figure 1.2, another database tool from NIST, ESTAR [72], is useful. Figure 1.3 shows the total electron stopping, as a percentage of initial electron kinetic energy. It also shows the portion of stopping attributable to radiative stopping (both conventional and ee-bremsstrahlung), as a percentage of total stopping. As atomic density is taken into account in stopping calculations, unlike the atomic cross-section-based prevalence calculations presented for photon interactions in Figure 1.2, the diamond form of carbon is specified for electron stopping. This density consideration is important, because the density of diamond is significantly higher than graphite ( $3.5 \text{ g/cm}^3$  vs  $2.2 \text{ g/cm}^3$  [73]) and indeed silicon ( $2.33 \text{ g/cm}^3$  [73]), with silicon carbide, a radiation-hard gammavoltaic candidate material, falling in-between as would be expected ( $3.2 \text{ g/cm}^3$  [74]). The stopping power of diamond therefore hovers at around twice that of silicon over the energy range considered. Diamond punches above its weight - or perhaps punches above its  $Z$  - for gamma

capture.

Of the two "device" materials considered, both have stopping power significantly below 100 %/mm for 1000 keV electrons. However, it should be noted that the actual range will be shorter than this number suggests: the path length requires integrating the stopping power between the initial energy and the energy at which the electron is considered absorbed, and energies below 1 keV are not calculable with the methods used in ESTAR to reasonable accuracy [72]. Furthermore, the actual range will not be the same as the path length, but rather less, due to the fact that the electron will take a non-linear path through the lattice.

The broad conclusion that may be drawn is that any gammavoltaic device is likely to experience quite significant losses. Most of these will be out of the faces of the device, given semiconductor devices tend to be constructed on wafers of about 0.5 mm, and almost always less than 1 mm in thickness. However, an appreciable quantity of secondary electrons will also escape out of the sides of the device. One potential solution to this is to arrange devices stackwise rather than panelwise, as Horiuchi *et al* did, to catch escaped secondary electrons from one set of faces, contrary to how solar cells are arranged into a panel. This will feature in this work.

Conversely, of the "housing" materials, Figure 1.3 gives some idea of how significant the contribution of scatter electrons will be from within the housing: the most adjacent 1 or 2 mm will contribute almost all of the secondary electron flux into the device; electrons generated elsewhere in the housing will be re-absorbed by the housing itself.

Radiative stopping is lowest in diamond, being at most 2 %, despite the density of diamond being larger than silicon. Within the device this is a good thing, as the radiation generated in radiative stopping is more penetrating than electrons, and is more likely to carry energy out of the device, leading to inefficiency. Importantly, the energy in radiative stopping is not wholly converted to radiation; most energy remains with the electron. Thus, in both device materials, the losses from escaped radiation generated in radiative stopping is small. The proportion of stopping attributable to radiative stopping is much higher for the "housing" materials.

Ultimately, whilst considerations of the fundamental photon and electron scattering mechanisms are important for a good understanding of what is going on inside a gammavoltaic whilst it is operating, a detailed calculation of quantities like energy deposition, which account for exact electron paths and quantified contributions from device housing, must rely on more sophisticated simulation techniques. These techniques must simulate the paths of individual incident photons and their secondary electrons. The simulation technique used is discussed in Section 3.4.1.

### 1.2.3 Charge transport processes

Once a high-energy photon has interacted (provided it has interacted at all), spawned numerous interactions where secondary photons and electrons go on to interact themselves, and finally some portion of its original energy has been absorbed, the end result is that a high-energy photon will have been converted into many low-energy electrons. This is as far as high-energy physics simulation

programs will normally go, with the resultant total energy of these low energy electrons being referred to as the energy deposition,  $E_{\text{dep}}$ . A threshold energy value is picked, below which electrons are considered to have been absorbed. However, for these electrons to actually contribute to power produced in the device, they must be collected as current. Unlike the processes of high-energy photon and electron scattering, the transport of electrons through voltaics is a key part of conventional photovoltaic research, as electrons generated individually by many low-energy visible photons are no different to electrons generated *en masse* by a smaller number of high-energy gamma photons. The holes left behind by promoted electrons also act as charge carriers, and have similar but distinct transport properties to electrons [75].

However, as will be made clear in Section 1.4, there are important differences between the design of the voltaic presented here and traditional voltaics, or indeed other well-understood devices such as Schottky diodes or MOSFETs. For this reason, and because the simulations used here do not extend to it, discussion of charge transport processes will be brief and qualitative here in the introduction, with a more in-depth treatment given in Chapter 2. They can be grouped thematically into those processes which inhibit the movement of charge carriers, and those which cause movement. Processes which inhibit movement are various forms of scattering, such as from impurities, lattice defects, and phonons [76, pp. 28-30], and recombination, which goes beyond inhibiting motion to stopping it entirely via annihilation of an electron and hole [76, pp. 40 - 45]. Processes which cause charge-carriers to move are diffusion and drift [77].

Drift is the process by which charge carriers move in a semiconductor device due to a device-scale electric field [77] (most commonly due to a bias being applied across the contacts of a device). Holes move in the direction of an applied electric field whereas electrons move in the opposite direction. However, as the two types of charge carrier have opposite charges, the effect on the current magnitude is additive, rather than the two cancelling one another out [77]. For voltaics, the velocity with which carriers drift is linearly related to the strength of the external electric field, but when this field is much stronger (for example, the  $\sim 1$  kV/cm used in Dr. Hutson's diamond dosimeter), the relationship will deviate from linear [76, pp. 35-36]. So-called built-in voltages, where contact between dissimilar materials results in a potential barrier, may supply an electric field, and this is one possible basis of separating electrons and holes such that they do not recombine in a voltaic, thus producing current [66, p. 36].

Diffusion, meanwhile, is the process by which charge carriers move from inhomogeneous spatial distributions towards homogeneous ones due to the repulsive interactions of their own electric fields [77]. Hence, diffusion is a self-limiting process; diffusion of carriers tends towards an equilibrium state. For voltaics, the most obvious situation which may lead to a large amount of sustained diffusion is localised illumination, wherein only a fraction of the surface area of a cell is illuminated whilst the rest is deliberately shadowed, such as in photoresponse mapping [78]. The creation of a dense region of carriers leads those carriers to diffuse into regions with fewer carriers [77]. However, for radiovoltaics in particular, there is another important consideration with diffusion current, and that

is the penetration depth of various radiations. For example, where entire betavoltaics have been created, as opposed to voltaic structures being investigated under electron guns, they have a fixed beta source, such as the Ni-63 electrodes used by Bormashov *et al* [21]. Beta particles, undergoing the stopping processes described above, will have a finite range, and will tend to deposit most of that energy near the end of their journey through the material [60]. As such, betavoltaics will tend to have perpetually re-enforced, inhomogeneous carrier distributions, meaning diffusion will remain a particularly relevant process. For gammavoltaics, which may be used to harvest energy from photons of a range of different energies depending on the application, we have to contend with the fact that the location of carrier-dense regions will change. Lower energy photons will tend to deposit most of their energy towards the side of the device facing the radiation, and as photon energy increases, this deposition location will broaden, before eventually concentrating on the far side of the device.

In the formation of built-in voltages, diffusion opposes drift, and the voltage stabilises as a result of a dynamic equilibrium between the two processes [66, p. 146]. Because both have a time dependency, the difficulty of extending high-energy physics simulations to device physics is increased. Certain aspects of device physics could, in principle, be brought under existing high energy physics simulations. For example, one could introduce a static electric field to influence secondary electrons, to mimic the built-in voltage of a contact. Time-dependant features such as drift currents, or Compton scattering cross-sections changing due to ionisation, are incompatible with Monte Carlo high-energy physics codes, which are timeless.

The above interaction processes are one half of the gammavoltaic picture. Diamond, the device material, is the next.

## **1.3 Diamond as a device material: features, advantages and disadvantages**

### **1.3.1 The historical context of diamond research**

Diamond has of course been known as a gemstone since ancient times, with its identity as a carbon allotrope guessed obliquely by Newton, who supposed it was "*probably an unctuous substance coagulated*" - that is, some solid form of an oil which we would today know to be a hydrocarbon. This and other interesting facts about the history of diamond in general, from the doubtful translation status of Biblical passages mentioning diamond to the state of diamond synthesis as it was in 1984, *via* contributions made to the field of diamond science by figures such as Lavoisier and Einstein, can be found in the broad and engaging *Diamond* by Gordon Davies of King's College London [79]. Diamond synthesis was a goal pursued for centuries, which finally became possible in 1955 with reports of the development of the HPHT process by Bundy *et al* [80]<sup>8</sup>. HPHT essentially recreates the intense conditions by which diamonds are created naturally. For much of its history, HPHT diamond

---

<sup>8</sup>It should be noted, however, that the first diamond actually synthesized was the result of work in 1953 by ASEA - but this was not reported [81].

suffered from unavoidable nitrogen contamination, much like the majority of natural diamond, although this has in more recent times been remedied by more advanced versions of the process [81]. Nitrogen is a deep donor dopant in diamond, which limited the usefulness of synthetic diamonds for devices whilst HPHT was the only option. In 1984, for example, Burgemeister investigated diamond as a gamma dosimeter material, and to do so, had to find a suitable natural diamond - one which was very pure - from a collection of several thousand stones which had already been vetted for the clear colour and other properties associated with a minimal nitrogen and boron content [3]. Additionally, though HPHT can create diamonds which may then be used as substrates for devices, it is not capable of film-like growth for additional diamond layers, and is too harsh a process for the purposes of growing diamond onto other semiconductors out of which devices are already made. Chemical vapour deposition (CVD) of diamond is the alternative. Although some work preceded it, the advent of CVD as a viable diamond growth mechanism is generally held to be the 1982 work of Matsumoto *et al*, who obtained reasonable growth rates and crystal qualities together for the first time [82]. The commercialisation of the process from that point took several years, with Element Six producing their first line of commercially-available CVD diamond by 1989 [83]. With CVD came the ability to grow diamond epilayers for device fabrication, as well as to ensure minimal impurities, and hence the quality necessary for biased radiation detectors. Thus, although the history of diamond research stretches very far back, its use as a device material is much newer, and far less developed than that of several other materials, especially silicon. With this relative lack of development comes a number of drawbacks, such as its cost and the small attainable wafer sizes.

#### 1.3.2 Diamond devices and radiation

Due to the strength of the C-C bond in diamond (3.8 eV, vs. 2.0 eV for silicon [84]), as well as the low  $Z$  of C atoms, diamond is very radiation hard [85] - one of several superlative material properties cited regularly in diamond literature. Diamond also has a wide, indirect band gap of  $\sim 5.5$  eV [86], which improves the charge collection distance within a device relative to other semiconductors [85]. It is for these reasons that, as previously mentioned, diamond has already been used for alpha- and beta- voltaics [21, 25], as well as for gamma/X-ray dosimeters and detectors [3, 87, 88], including the aforementioned Almaviva devices, which form part of the extensive research on diamond detectors which has been undertaken at University of Rome *Tor Vergata* [39, 40, 89–92]. Researchers there have tested their dosimeters under a wide range of radiation types both with, and without, an applied bias. However, as the spatial measurement resolution of dosimeters is important, the *Tor Vergata* group have tended towards thinner sensitive volumes. Their dosimeter has been successfully commercialised [93, 94]. A lineage of diamond detector research has also been produced by the RD42 Collaboration [95], which is a collaboration intended to make use of, and serve, the Large Hadron Collider. Most notably, recent work from the RD42 Collaboration has focused on the use of polycrystalline diamond [96, 97], as has work from others in the past two decades [98–100]. In one case, a detector nearly 5 cm in diameter was created [98]. This is significant, as the difference in cost

between electronic grade single crystal and polycrystalline diamond is great. Also, large-area growth is far easier for polycrystalline diamond, with the upper limit for polycrystalline diamond being fixed at around 100 mm by the physical properties of a microwave growth plasma [101], whereas single crystals still tend only to be found in sizes of a few square millimetres. Development in this area for detectors may facilitate polycrystalline diamond gammavoltaic cells in future, in a manner analogous to how polycrystalline solar cells offer a cheaper, if less efficient, alternative to those which are monocrystalline [102].

Although diamond is radiation hard, it is not immune to radiation damage. In fact, damage of diamond by radiation is of interest to at least three groups of researchers: -

1. those using diamond for devices such as the present gammavoltaic cells, for whom damage is undesirable;
2. those involved in or associated with gemmology, wherein irradiation often increases the value of diamonds, particularly in those rare cases where it has happened naturally<sup>9</sup>, and;
3. those studying fundamental quantum physics, for whom radiation-induced nitrogen vacancies in diamond have proved fruitful objects of study [105].

Early studies into diamond radiation damage faced difficulties with gamma rays: out of a sample of 52 diamonds, Clark, Ditchburn and Dyer found in 1956 that they could only subject one to gamma radiation in a comparative study. This was because in the time they had allocated for the work, and with the apparatus available to them, there was time to damage only one diamond with gamma rays to the point where colouration was observed. In this time, they were able to colour all other diamonds with either alpha or beta radiation [106]. The gamma rays employed were Co-60 gamma rays. Since then, Collins has noted that although the Co-60 treatment remains an effective way of achieving a homogeneous colouration of diamond - unlike other radiation types which form only coloured "skins" - the fact that the process takes several months even with the most powerful sources available means that other techniques are favoured [107]. This is partly because the gamma rays themselves are not responsible for damage in the main, but rather the Compton electrons produced when gamma rays scatter [108]. These may knock C atoms out of their lattice sites *via* the mechanism of nuclear stopping discussed in Section 1.2.2, but being lower in energy than the incident gamma ray, are less likely to do so than beta or alpha particles of the same energy as said gamma ray. Beta particles/hot electrons with less than 180 keV in energy are incapable of causing any damage to the diamond lattice at all [109], and it may be shown that an incoming gamma ray must have at least 324 keV itself before it may generate Compton electrons of 180 keV or more [57]. Such damage is also often not permanent; with the combination of energy provided from the initial impact and

---

<sup>9</sup>The famous Dresden Green diamond is just such a stone: an appreciable size of 41 ct [103] conspired with its rare colour to afford it such a great value that shortly after purchasing it in 1741, Augustus II, King of Poland, was unable to finance artillery for the siege of Brünn [104]. Naturally irradiated, green diamonds are rare, but the Dresden Green has the particular distinction of an almost homogeneous colour throughout. This, rather than colour in patches around the surface, is likely to indicate gamma irradiation specifically.

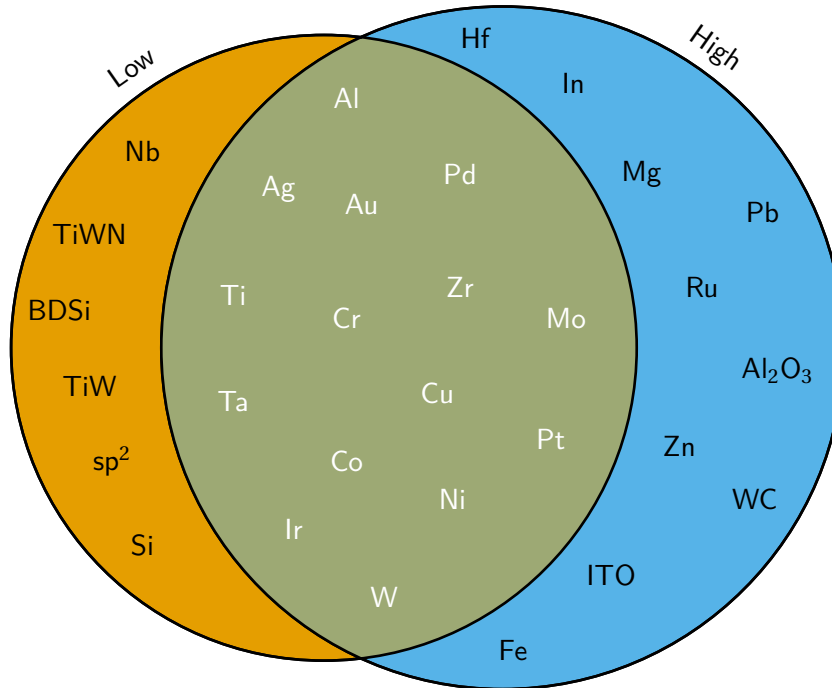


FIGURE 1.4. A Venn diagram of a sample of metals which have been investigated in the literature for use as low-barrier [110–134] (orange) and high-barrier [21, 22, 25, 131, 135–155] (blue) contacts to diamond. "BDSi" here refers to B-doped Si, and  $sp^2$  to controlled damage which converts diamond  $sp^3$  bonds to graphitic  $sp^2$  bonds. A table of references for contacts and their properties can be found in Appendix A.

thermal energy from the environment, C atoms which have been knocked out may migrate back to their lattice sites [108]. Of course, this resistance to damage and colouration is a good thing from the perspective of attempting to create a gammavoltaic device. One final distinction which must be made is that, although the changing colour of a diamond is directly caused by lattice damage, optical change and electrical change are not necessarily linked in a straightforward manner, and it is the latter that is of importance.

### 1.3.3 Electrical contacts to diamond devices

Every device must have electrical contacts, and often the precise properties of these contacts are crucial in determining the capabilities of that device, even though those properties may be decided by less than ten atomic layers where the device material meets the metal. At this interface, the energy levels of the two materials must meet to maintain the conservation of energy, and the charge redistribution that happens near the surface to facilitate this is conceptualised as those energy bands bending. Where the bands bend, a potential barrier - a barrier to charge carriers - is formed. Whether or not this is good or bad is dependent on what role the contact is intended to perform.

According to fundamental or early semiconductor theory [156], the height of the potential barrier (Schottky barrier height,  $\phi_B$ ) created at the interface between a metal and a semiconductor should depend solely on the choice of metal, or more specifically, the electron affinity  $X_M$  of that metal. An explanation of this theory is usually given in textbooks (see, for example, Sze [76, p. 135-139]). However, as discussed for example in the in-depth 2014 review by Tung [157], there is a significant discrepancy between this fundamental theory, which is based purely on the physics of energy bands within materials, and the measured reality, which may be perturbed from the ideal case or even deviate entirely from it. This may be due to physical reasons such as interface states caused by the abrupt breaking of crystal symmetry at the surface, or surface roughness. It may also be due to distinctly chemical reasons, such as solid-state reactions between the semiconductor and the metal, or reactions with terminating species that may be present on the order of a few atomic layers, picked up by contact with ambient air or laid down intentionally by researchers. Experimental work has allowed the definition of the parameter  $S$ , according to

$$(1.1) \quad S \equiv \frac{d\phi_{B0}}{dX_M},$$

where  $\phi_{B0}$  is the Schottky barrier height measured at 0 V bias [76, p. 144]. For the ideal case,  $S = 1$ . By measuring the same semiconductor with different metal contacts on it,  $S$  can be determined for that semiconductor. Whilst for some semiconductors,  $S \approx 1$  and the ideal theory holds, for many semiconductors, it has been found that  $S \approx 0$ , meaning that the ideal theory barely applies at all [158]. Ultimately this was found to be related to the covalency of a given semiconductor, which can be presented in terms of the difference in electron affinities,  $\Delta X$ , of the various atomic species in the semiconductor. Higher  $\Delta X$  means the bonding in the semiconductor is more ionic, whereas a lower  $\Delta X$  means the bonding is less so, with  $\Delta X = 0$  indicating the semiconductor only contains a single element, such as Si or diamond, and the bonding is purely covalent. A sample of relevant literature, in which groups have been looking to either minimise or maximise the  $\phi_B$  of contacts on diamond, is shown in Figure 1.4. The group of metals which has been tried for both low- and high-barrier contacts is larger than either group alone, as might be expected in light of the  $S$  parameter for diamond.

### 1.3.3.1 Low-barrier contacts

There is a fairly large number of parameters now known to be important when investigating metal-semiconductor contacts. Papers which use a metal for a high-barrier contact will tend to focus directly on measuring barrier height, whereas papers investigating metals for low-barrier contacts will tend to focus instead on the contact resistivity. This is because a low-barrier contact will often be intended as an ohmic contact - a contact which has a linear  $I$ - $V$  relationship and which behaves as though there is no interfacial potential barrier. That said, a low-barrier contact need not necessarily be ohmic to do jobs usually delegated to ohmic contacts. Often, as long as a contact allows enough charge carriers to the rest of the device for it to function effectively, whilst avoiding creating a built-in voltage

great enough that it disrupts the effects of *intentional* built-in voltages elsewhere in the device, that is enough [159, p. 99]. Literature would suggest that approaches to creating low-barrier contacts on diamond can be broadly split into the following typology: *carbide-based*, *damage-based*, *solvating*, and *hydrogen-based*.

The ohmic contact technology which is most generally used for diamond, and capable of achieving the lowest contact resistances, is the annealed carbide-based ohmic contact. These contacts contain anywhere from one to three metals. The diamond-facing metal must be chosen such that it reacts with the diamond at the interface when annealed, to form a carbide. The other layers, should they be used, perform functions to protect the functioning of the first layer as an electrical contact. By far the most common example of a carbide-based ohmic contact is the Au/Ti contact [111–113, 117, 120, 121, 124]. The titanium layer is usually between 10-50 nm thick, and the gold layer 100 nm or thicker. The literature reports widely varying gold thicknesses, which to my knowledge go as high as 1200 nm [124], but the main consideration for this choice is the thickness required for subsequent tests. If the barrier height is to be probed by tools such as x-ray photoelectron spectroscopy, the gold layer must be as thin as possible, so that photoelectrons can escape to the spectrometer. For experiments conducted purely to establish a contact resistivity, thicker layers are required, but they need only be thick enough to withstand the mechanical stress of scratching by probes during testing. For device fabrication, the layer must often be thicker to accommodate gold wire bonding. In any case, the primary function of the gold layer is to form an inert seal around the titanium to prevent a titanium oxide layer forming on the side opposite the diamond. The layers must be deposited without breaking vacuum. Using this method, contact resistivities of the order of  $10^{-7} \Omega \text{ cm}^2$  have been achieved [121, 126]. This type of contact has been under investigation since at least the 1980s, when Moazed *et al* reported quasi-ohmic behaviour for it [129, 160]. As well as gold, contacts are sometimes fabricated with a platinum layer between 10-50 nm thick, in an Au/Pt/Ti configuration [110, 114, 118, 119, 125, 126]. When used, platinum serves as a diffusion barrier; annealing or operating at high temperatures can otherwise cause titanium to migrate through the gold [117], leading to greater contact resistivities and lesser ohmic behaviour.

It is also fairly common for researchers to test contacts that rely on other carbide-forming metals. Work has been undertaken on molybdenum [111, 112, 115, 116, 130], which tends to approach titanium in effectiveness, by achieving contact resistivities as low as  $10^{-6} \Omega \text{ cm}^2$ . Tantalum-based contacts have been reported with resistivities of the order of  $10^{-5} \Omega \text{ cm}^2$  and higher [125, 128], as have alloys of titanium with tungsten [112, 124]. The general impression that these results give is that, provided a carbide layer forms, the particular carbide-forming element is not so important. Molybdenum and tungsten are both often used to make deposition equipment and so are less suitable than titanium, the latter having a lower melting point. Vanadium, another logical option, has both a high melting temperature and is relatively untested. As such, titanium remains the metal of choice for carbide-based ohmic contacts. A 1994 paper by Nakanishi *et al* [115] included an in-depth study which, among other things, investigated the effect of annealing status on contact resistivity

in titanium- and molybdenum-based contacts. The study corroborated the suggestion that it is the carbide layer, and not the specific metal, that allows annealed contacts to work; after annealing, molybdenum and titanium contacts behaved, to all intents and purposes, identically.

Damage-based contacts are contacts made by inducing some of the diamond  $sp^3$  bonds at the surface to break, whether by chemical or physical means. Two papers by Tachibana, Williams and Glass in 1992 [122, 123], investigated the dependence of contact resistance on interface damage. The first focused on gold as an ohmic contact, and the second on titanium. The distinction being made was that gold and titanium sit at opposite ends of the spectrum in terms of carbide formation. Gold is extremely unreactive, being bound to the surface only by Van der Waals forces [127]. Gold contacts were rectifying, regardless of annealing. Titanium, on the other hand, forms a carbide fairly easily: annealing temperatures as low as 200°C have been qualified [125]. Tachibana, Williams and Glass used x-ray photo electron spectroscopy to show convincingly that the gradual approach to ohmic behaviour with annealing temperature was directly related to the formation of a titanium carbide interface layer. However, they also showed that *in-situ* cleaning with argon-ion sputtering could also create ohmic behaviour. The onset of titanium carbide formation was also lowered, from over 400°C to 140°C, and provided only minimal improvement in the  $I$ - $V$  behaviour of the contact when the surface was pre-damaged in this way. Interestingly, when gold deposition was preceded by a sputter-cleaning step, this also allowed ohmic contacts to be formed. As gold does not form a carbide, this further isolated the sputtering damage as a route to ohmic behaviour. The caveat, however, was that annealing these gold contacts led to them reverting to rectifying behaviour, suggesting that the contacts were unstable. The suggestion from these papers is that, although carbide-based contacts are the most important class of ohmic contact for diamond, they may actually be a subset of contacts based on damage formation, with the carbide layer acting more as a type of chemically-induced surface damage than as true interlayer - that it is not the electrical properties of the titanium carbide itself, say, that matters. Diamond detectors have occasionally employed damage-based contacts, with the natural diamond dosimeter of Burgemeister's study using graphitised edges as contacts. This technique is increasingly of importance with the advent of laser-induced pillar contacts, which may be created throughout the thickness of a diamond by altering the focus depth of a laser [161–163], or even, most recently, in a highly-controlled mesh pattern by vertical and horizontal control of the laser [164].

Solvating contacts are not a large class of diamond contacts. Similar to how carbide-based contacts appear to operate through very localised disruption to the diamond lattice, solvating contacts operate through the use of the small number of materials which may dissolve in diamond in solid state reactions. By dissolving slightly into the diamond lattice, they induce localised disruption. Pd and Co were both tested alongside carbide-based contacts by Yokoba *et al* in 1997 [116], and found to be passable ohmic contacts, but not on a par with carbide-based contacts. Others have found much lower resistivities since by combining Pd with a hydrogen termination [133, 165].

Hydrogen-based contacts, in some sense, take the opposite approach to carbide-based contacts.

They more or less only rely on physical, not chemical, principles. A hydrogen-terminated diamond surface has a negative electron affinity (NEA) [153, 166–168], which is to say that it is energetically favourable for conduction electrons to be emitted from the surface. By the deposition of a noble metal, or at least an unreactive metal, directly onto the hydrogen termination, hydrogen-based contacts aim to preserve this NEA and use it to create a contact with either a low or no barrier [120, 134], or even a negative barrier [132, 133, 165, 169].

Hydrogen-based contacts have several things to recommend them: they are capable of low resistivities and may even add to, rather than subtract from, the potential created by the high-barrier contact; they are a relatively simple system; they require no annealing; they involve no direct reaction with, or into the diamond surface itself, leaving the crystal less damaged than carbide based contacts for recycling purposes. However, they have a fatal flaw: the adhesion of hydrogen-based contacts is poor [127, 128], probably due to the fact that no reaction with the diamond surface takes place. Just as with other diamond surface configurations, between the gold and hydrogen atoms, there are only Van der Waals forces, which may be more easily overcome by mechanical forces than the chemical bonds in a diamond-TiC-Ti interlayer system.

#### 1.3.3.2 High-barrier contacts

Where work has sought to create high-barrier contacts on diamond, it is typically the case that researchers are looking to create Schottky diodes, in which a device may be optimised to increase rectification whilst decreasing resistance and voltage drop. It is not necessarily the case that a perfect Schottky diode (e.g. of high quality according to some metric like Baliga's Figure of Merit (BFOM) [170]) will create a perfect radiovoltaic, as voltage drop and in-built voltage are related and may be essentially the same quantity. Increasing the built-in voltage may therefore dominate the design process of a radiovoltaic, rather than rectification. However, as a rule of thumb, contacts successfully employed in Schottky diodes can be expected to work well as high-barrier contacts in a radiovoltaic, much as ohmic contacts relate to low-barrier contacts.

Although many of the same considerations prevail for the creation of Schottky contacts as for ohmic contacts, the process of choosing a contact recipe is significantly eased by an inspection of the literature. Figure 1.5 shows literature barrier heights achieved with different contact metals and surface terminations. Dopant concentration under the contact, not shown in the plot, changed by orders of magnitude across the literature. It is clear that surface termination is the primary determinant of the barrier height on diamond for high-barrier contacts. Hydrogen-terminated substrates yield the lowest barrier heights, as is expected from the discussion of ohmic/low barrier contacts. Oxygen-terminated surfaces will tend to create contacts with barriers with a fairly broad spread around 1.2 eV, and fluorine- and nitrogen-terminated surfaces, whilst less represented in literature, appear to populate a rank of contacts with barriers higher than oxygen. Those designing Schottky diodes are more constrained in their choice of metal from this point, as surface chemistry must be taken into account to allow further processing to reduce the built-in voltage [135]. However,

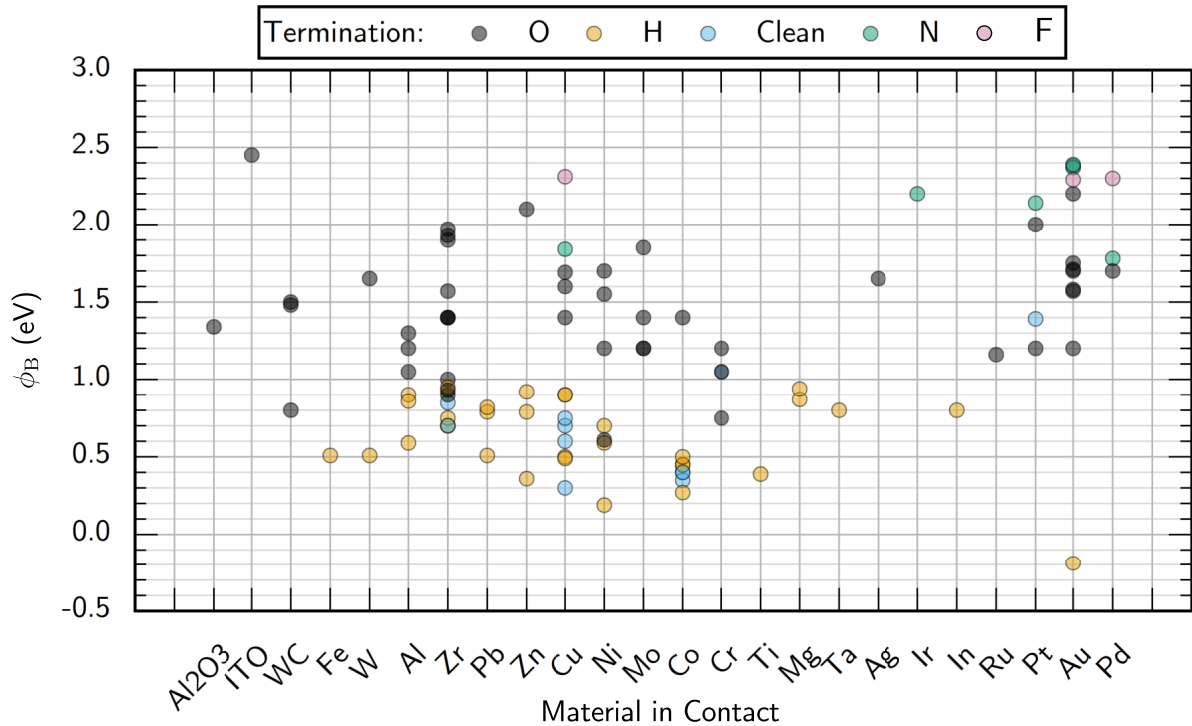


FIGURE 1.5. Barrier heights attained for a range of metals and terminations with Schottky contacts in literature [21, 22, 25, 131, 135–155]. A table of references for contacts and their properties can be found in Appendix A. "Clean" in this context refers to surfaces not intentionally terminated.

for radiovoltaic design, a metal and termination combination can be chosen solely on the basis of external factors such as cost, availability, and environmental impact.

### 1.3.4 The surface transfer-doping effect

A final - but for the purposes of this work, crucial - property of diamond, is its ability to exhibit surface transfer doping. As a phenomenon, surface transfer-doping is best-known in diamond, although similar effects have been seen in gallium nitride [171], another wide-bandgap material. It is also exploited for other carbon-heavy materials such as graphene [172–174] and organic semiconductors [172, 175]. The most basic form of surface transfer doping in diamond was seen first in natural diamonds [176] and then synthetic diamonds [177] in 1989 by Landstrass and Ravi, but the mechanism by which it occurred remained controversial for at least the next decade [178]. A bare, hydrogen-terminated diamond surface is conductive in air, with a resistance that varies with the coverage of terminating hydrogen,  $\theta_H$ , and of the adsorbed layer of water vapour,  $\theta_{H_2O}$ , which activates the hydrogen sites [179] - although recent studies have suggested that more complex chemical mechanisms mediated

by adsorbed water are responsible, and not the water vapour alone [178]. This creates a low-resistivity two-dimensional hole gas (2DHG) [167, 178, 179]. That is, with a full hydrogen coverage and in suitable circumstances, holes form at the diamond sub-surface and become delocalised in the two dimensions parallel to the surface, whilst remaining tightly localised, to within a few nm, in the dimension perpendicular to it [178, 180]. A band diagram illustrating this process is shown in Figure 1.6, adapted from [178]. The electrons removed into the adsorbed molecules are, if not static, then much less mobile. The surface transfer doping effect is made possible by the negative electron affinity of diamond because, as the band gap is constant, the diamond conduction band minimum  $E_C$  being so far above the vacuum energy  $E_{vac}$  leads the diamond valence band maximum  $E_V$  to also be unusually high in energy. Specifically, higher in energy than the chemical potential of the air,  $\mu_{air}$ . Thus, when the adsorbates from the air and the surface of the diamond exchange charge to reach equilibrium, the Fermi level of the diamond,  $E_F$ , is below  $E_V$  at the surface. It should be noted that the precise location of  $E_F$  within the band gap, although well-defined in doped diamond, becomes a bit more questionable in very pure diamond, which is an insulator at room temperature. On the other hand, states exist at the surface which do not exist in the bulk. It remains the case that the surface transfer-doping mechanism is found on pure diamond. The small region of the valence band above  $E_F$  becomes conductive in the two dimensions parallel to the surface.

Although adsorbed water vapour was the first adsorbate studied for hydrogen-terminated diamond - largely because its presence was not at first understood to be relevant - any adsorbate may in principle be used, provided the energy of its lowest unoccupied molecular orbital is below the valence band maximum energy of the hydrogen-terminated diamond [172]. This has led to successful surface transfer doping of diamond with other materials, with fluoro-/fullerenes being well represented in both theoretical [181–183] and experimental studies [184, 185], as well as various gaseous environments [186], most prominently those of nitrogen dioxide [187] and nitrogen [187–189]. To my knowledge, these latter options have shown the highest sheet conductivities of any with hydrogen-terminated diamond. However, as surrounding devices with gases is not always a practical solution, solid-state alternatives have been sought in the form of transition metal oxides. High-electron affinity metals such as tungsten trioxide [190], vanadium pentoxide [191], molybdenum trioxide [192, 193] and rhenium trioxide [190] have all been shown to replace the need for water vapour in the triggering of surface transfer doping whilst simultaneously granting much greater stability, with thermal stability extending to several hundred degrees Celsius. All of these oxides bar that of rhenium were compared, along with niobium pentoxide, in a 2016 work by Verona *et al* [194], which showed that the work function of these oxides was linearly related to sheet hole concentration, and thus directly to sheet conductivity, with higher work function oxides allowing greater conductivity.

Surface transfer doping, despite its increasing study in other materials, remains particularly of interest in diamond because of its dramatic nature: the conductivity of the surface may readily be increased by ten orders of magnitude by a full hydrogen termination in air, and in tandem with the aforementioned nitrogen dioxide environment, increased a further three orders of magnitude.

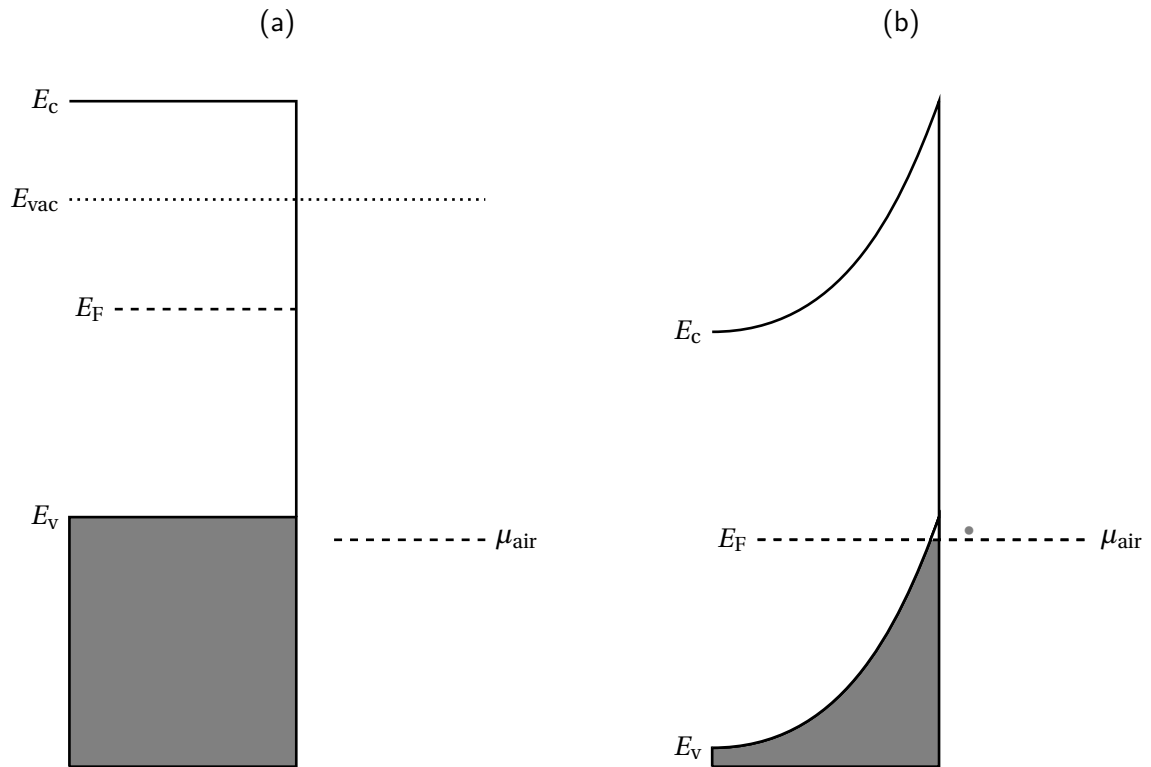


FIGURE 1.6. A band diagram of the surface transfer doping effect of hydrogen-terminated diamond in air, adapted from [178]. In (a), the energy bands are shown as idealised values as if prior to an instantaneous adsorption of atmospheric water. Adsorption leads to (b), in which the 2DHG forms where the valence band is pulled over the Fermi level by electron transfer, due to the chemical potential of the surface adsorbates. The 2DHG has its longest dimension perpendicular to the page, which corresponds to the two directions parallel to the surface. The diagram is to scale in energy. Regarding thickness, the 2DHG is a few nanometers thick.

Further information on surface transfer doping in diamond can be found in the 2021 review by Crawford *et al* [178].

With the peculiarities of diamond discussed, as well as the various mechanisms that lead a gamma ray to become a population of collected conduction electrons in a gammavoltaic, I will turn now to how these principles were used to adapt Dr. Hutson's dosimeter into what was hoped to be a more potent and practical gammavoltaic cell.

## 1.4 Principles and design of the presented diamond gammavoltaic cell

A fundamental problem in the design of a DGV is the correlation between gamma ray capture cross-section,  $\sigma$ , and series resistance  $R_S$ . Gamma photons are very penetrating, and diamond is highly insulating [86, 195]. In a pseudo-vertical Schottky diode structure, such as those used in other diamond radiovoltaics and in the Tor Vergata detectors, increasing the sensitive volume in order to capture enough gamma photons to power external circuitry would lead to unacceptable device resistance, and hence also prevent the device from generating enough power. Dr. Hutson's dosimeter showed that this thickness concern was maybe not so important as it would seem at first for electronic-grade diamond, whether that be due to radiation-based resistance decrease, large diffusion lengths due to crystal quality, or small quantities of surface hydrogen contamination, but it remained the case that the device was producing only a small amount of power under intense radiation. A novel solution to this problem, presented here and in published work by myself and colleagues [65], is to further reduce the coupling of thickness and device resistance *via* exploitation of the surface transfer doping effect. The thickness, radiation hardness and collection distance of the bulk is used to capture gamma rays and scatter showers of lower-energy electrons and photons towards the surface. Of these, those which are captured create even lower-energy conduction electrons and holes. Holes which reach the surface, and hence the 2DHG, are collected as current. The majority of the current is expected to flow around the surface rather than through the bulk although, as previously mentioned, there was a hypothesis that greater hydrogen termination may act as a greater catalyst for resistance reduction in the bulk, too. The problematic coupling between capture cross section and series resistance is thus reduced. Figure 1.7 shows the principles of this solution, by comparison to the two other possible candidates. For this first iteration, the crystal type was kept the same as in the dosimeter: detector grade, ultra-pure, 0.5 mm thick single crystal. This was for three reasons: to keep the gammavoltaic reasonably close to the dosimeter design in order to trace the benefits of any alterations made, to retain the good charge transport properties of such detector grade crystal, and to keep the parameter space for device design small. Detector grade diamond is about as close as it is possible to get to an idealised diamond crystal, and so its use minimises the relevance of parameters like dopant concentration, defect density and (poly-) crystallinity that would otherwise need to be controlled for. The use of this type of crystal did come with some difficulties, however (in addition to cost per sample). The good charge transport properties are to some extent too good: they match those of the diamond dosimeter, but being grown by proprietary means by a company who are expert in diamond growth, the charge transport properties exceed those which might be expected from a research group growing devices themselves. The Element Six electronic grade diamond is specified to have a carrier lifetimes of around 2000 ns and carrier mobilities in excess of 2000 cm<sup>2</sup> V<sup>-1</sup> s<sup>-1</sup>, meaning carrier diffusion lengths in excess of 100  $\mu\text{m}$ . This value is significant compared to the 500  $\mu\text{m}$  thickness of a DGV cell<sup>10</sup>, and some contributions to the current from the DGV acting in a

<sup>10</sup>It should be noted that diffusion lengths of this size are not always found in diamond devices even when single crystal is used - c.f. a 2016 report of 34 [196] and a 2010 report of 2  $\mu\text{m}$  [197].

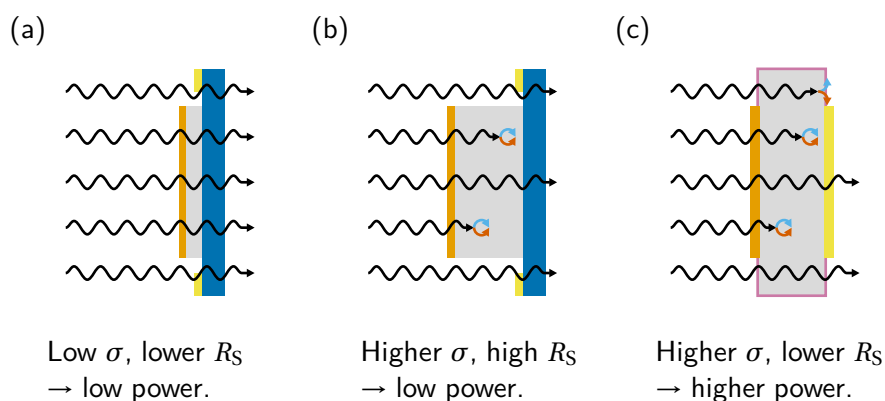


FIGURE 1.7. Three possible designs for a DGV device, in which boron-doped diamond is represented as blue, intrinsic or low-doped diamond in beige, electrons and holes as blue and red arrows respectively, ohmic or low-barrier contacts as yellow, high-barrier contacts as orange, and a hydrogen-terminated surface as pink. (a) is a standard pseudo-vertical Schottky diode, such as is suitable for diamond alpha- and beta-voltaics, (b) is a similar device with a much thicker intrinsic region. (c) is the design tested in this paper, in which the resistance of a thick capture volume is bypassed by allowing current to travel around the surface of the device.

conventional sense - i.e. as it would without hydrogen termination - may therefore not be negligible. I did not give proper weight to this when undertaking this work, and only compared devices with and without partial hydrogen termination in one experiment (see Chapter 4). This experiment appeared to me to confirm the design choice at the time, but the reader should note this issue nonetheless. The influence of the surface treatment can also be seen in Chapter 6, in which ambient humidity changed over the course of the experiment and was measured.

Surface encapsulation, such as with the transition metal oxides, was not attempted in this work, though it is anticipated that it will form an important part of future development.

Figure 1.7 also makes reference to high-barrier and low-barrier contacts. By using different contact recipes to introduce a larger potential barrier mismatch, an intentional in-built field could be created. This was a natural choice, as Schottky-contact-based voltaics are very common. The choice of contacts had to be made on the basis of several factors. The disadvantage of carbide-based, damage-based, and solvating contacts is that, by their very nature, they damage - or at least alter - the diamond surface they are formed on. If the DGV concept involved cheap, thermal-grade polycrystalline diamond, this would not be a problem, as each substrate could be treated as single-use. However, there are only so many detector-grade diamonds that can be obtained before financial concerns make themselves apparent. The option to return crystals to their prior state so they could be re-used was needed. A hydrogen-based low-barrier contact would have met this criterion, but the adhesion issues ruled this option out. With the four reviewed contact types all suffering in one

way or another from attributes that made them unsuitable for their use in cell development, an alternative was needed. 80/20 nichrome was suggested<sup>11</sup>, as a common alloy of nickel which has been shown to display ohmic behaviour [121] but which suffers poor adhesion [111], and chromium, which does not suffer from adhesion issues but which is more liable to form high-barrier, rectifying contacts [116, 136, 148, 150]. It should be noted that the literature is not unequivocal on this issue, with at least one paper suggesting both metals can attain good adhesion and that in fact, chromium forms a lower barrier, with poorer adhesion, than nickel [154]. Nevertheless, in a simple two-pad *I-V* measurement on a home-grown boron-doped epilayer, 80/20 nichrome on an oxygen-terminated surface was found to produce an ohmic contact with good adhesion and no need for annealing. As the metal was bonding to the surface oxygen rather than the diamond, contact removal could be accomplished with ease with commercial etchant solutions, and the diamond returned so far as possible to its original state.

For the high-barrier contact, an oxygen-terminated contact recipe was chosen for the following reasons: oxygen-terminated Schottky contacts are well-attested in literature whereas nitrogen and fluorine terminated contacts are less so; the comparative difficulty of striking a nitrogen plasma in the equipment available (see Section 3.1), and; the possible environmental damage which may be caused by failing to properly control a sulfur hexafluoride plasma for fluorine termination in said equipment<sup>12</sup>. From this point, the obvious metal choice was aluminium, which is both well-attested due to having been investigated for betavoltaics [22], cheap, and abundant.

## 1.5 Research outline

In this introduction I have outlined the existing literature on gammavoltaic devices, the processes by which gamma rays are converted to conduction electrons and hence power, diamond as a device material, and the principles and design of the DGV presented in this work. As context for the DGV design, I have provided some history to explain why the cell in this work is so unlike a normal voltaic in its structure.

What emerges from a survey of the existing gammavoltaic literature, in combination with an understanding of the various applications gammavoltaics have been envisaged for, is that for any gammavoltaic to move beyond the lab and become a successful piece of technology, it must move through three phases. To aid research efforts both within and between research groups, it must also address two ancillary topics. Together, these five factors form the framework that I use in this work

---

<sup>11</sup>Prof. Neil Fox, private communication

<sup>12</sup>Sulfur hexafluoride has a global warming potential 23,900 times greater than carbon dioxide over a 100-year period and 32,600 times greater over a 500-year period [198]. Based on Government data [199], a good rule of thumb is that each 1 sccm of sulfur hexafluoride leaked or vented has the same global warming potential as the emissions of an average 2021 UK petrol car over 1 km. With oxygen available as a quite serviceable alternative, a standard flow rate of 10 sccm being used (see Section 3.1), and normal lab work invariably involving aborted runs, vented chambers, leaks and the like, I did not consider the use of the SF<sub>6</sub> option justified for this first iteration of the cell.

	<b>Device 1</b>	<b>Device 2</b>	<b>Device 3</b>
Performance	Induced current 1 $\mu\text{A}$	$P_{\text{MPP}} = 30 \text{ nW}$	$P_{\text{MAX}}$ density = 3 $\text{pW}/\text{cm}^2$
Irradiation	10 cm from an x-ray tube	750 Gy/h Si KERMA, 30 keV	100 rem Co-60
Cell dimensions	$5 \times 5 \times 0.5 \text{ mm}$	$25 \text{ cm}^2$ + scintillator	irregular
Degradation	Not measured	0.03 %/Gy	Some after six weeks

TABLE 1.1. The reported properties of three fictional gammavoltaic devices, inspired by the literature, to illustrate the difficulty of comparison.

to clarify things. The ancillary topics are **comparability** and **accountability**. The three phases are **capability**, **applicability**, and **longevity**.

**Comparability** is to do with the wider experiments and the way they are reported, as much as it is to do with devices themselves. It is the ease with which the performance of a device may be compared against others in the literature. There is no standard of comparison for gammavoltaics, and finding precedent in the literature is hard. This is not at all to do with the quality of research, but a natural result of experimental and social circumstances, such as the mixture of old and new radiation units, occasional lack of reported device dimensions or ambiguity thereof (is a scintillator part of a device for power density purposes?), the different types of dose, and the fact that the environment in which a cell is tested is normally not mentioned. For illustration, consider the fictional comparison in Table 1.1. In this work, for the sake of comparability, one set of measurements was made over a range of dose rates of Co-60, with those dose rates measured in air KERMA. Co-60 was used as it appears to be the isotope with the best balance of availability to other researchers, and similarity to the gamma makeup of a waste store. Air KERMA was chosen because it is not specific to the device material and may be readily converted to the old unit of Roentgens. It is also the measure suggested by the International Atomic Energy Agency for referencing in photon fields [200]. Because both volumetric and areal power output density are important for gammavoltaics, I suggest two figures-of-merit that may be of use to gammavoltaic researchers going forwards:  $\frac{\text{Co-60}}{100} \text{p}$ , the volumetric maximum power-point density under a 100 Gy/h air KERMA dose rate of Co-60 radiation, in  $\text{nW}/\text{cm}^3$ , and  $\frac{\text{Co-60}}{100} \text{p}$ , the analogous areal quantity, in  $\text{nW}/\text{cm}^2$ . These figures-of-merit are intended to allow comparison between devices in experiments that are physically comparable to deployment conditions without placing unrealistic demands on researchers, as Co-60 sources are among the more readily available and 100 Gy/h is both a reasonable and accessible dose rate. Where the same Fraktur notation is used in the work, it is always intended that the dose-rate number be in Gy/h air KERMA and the power in question be the  $P_{\text{MPP}}$ , not the  $P_{\text{MAX}}$ . The notation may still be of use to future researchers even if the comparability standard is not, for example if lower-energy portable gammavoltaics attracted more attention and a figure-of-merit like  $\frac{\text{Fe-55}}{1} \text{p}$  became more useful.

**Accountability** is the degree to which the performance of a device is understood. At least in

principle, this may sit anywhere from the top-level assertion that a device has produced electricity in a gamma field because of its voltaic structure, through semi-quantitative conclusions about scattering mechanisms and internal reflection, all the way to a precise match between a simulated  $I$ - $V$  curve and a measured one. As previously mentioned, to my knowledge there is currently no software available that could bring accountability to the highest level of precision and accuracy. This work started on the back foot in terms of accountability because the gammavoltism exhibited by the dosimeter which the device was based on was not understood. GEANT4 simulations were used to provide accountability so far as high-energy physics was concerned; device modelling was not attempted due to a lack of information about specific, important electrical properties in the device. Experiments reported in Chapters 4 and 5 were undertaken to increase accountability.

The two ancillary factors are relevant at each of the three phases. The three phases seem, usually, to arrange themselves in the same order.

**Capability** is the first phase. A device must prove that it has the capability to act as a gammavoltaic. Obviously, all devices which appear in the literature so far have acted as a gammavoltaic in some capacity, and so at time of writing it could be said the publication bias for this factor is at or near 100 %. The difficulty is usually in the comparison of capability and the setting of a threshold. To my knowledge, no work on gammavoltaics has set a goal against which to measure parameters like  $I_{MPP}$ ,  $V_{MPP}$  and  $P_{MPP}$  (see Section 2.1.4 for descriptions of these parameters) as they relate to requirements in real circuits. In this work, the values of 4 V and 200 nA, from the EH300 Linear Device energy harvesting chip [4], were used, on the understanding that suitable circuitry can convert voltage to current and *vice versa* at need, and that devices could be combined in series or parallel if the performance of a single cell did not fall too far short of these values. Devices therefore had their capability measured against an 800 nW capability benchmark.

**Applicability** moves from the question of whether the gammavoltaic can be induced to produce a given output at all, to whether it is capable of producing that power output in circumstances applicable to its intended application. For example, a device may produce far more power under a 50 kV x-ray tube than under the mix of 662, 1170 and 1340 keV gamma rays it is intended to work with in a waste store. Experiments reported in Chapter 6 address applicability using a wide range of dose rates from Co-60 and Cs-137 gamma rays. The quantities  $\frac{Cs-137}{1000} \beta$  and  $\frac{Cs-137}{1000} p$  are of interest here as benchmark values for the waste store application this work is aimed at.

**Longevity**, finally, is the ability of a gammavoltaic cell to withstand the radiation it is placed in. Ultimately, the best longevity tests are done in the same circumstances used for the applicability test. In short, it must be able to withstand the strains of its intended application. Longevity is a particularly strenuous hurdle, because gammavoltaics may be intended for deployments that last many years and involve high dose rates. Longevity is addressed by an experiment in Chapter 6, using a dose rate of 1,350 Gy/h Cs-137 gamma rays for several weeks, to a total dose of 800 kGy.

So, to summarise the above in the order they will appear, the next two chapters will be devoted to a more in-depth discussion of some pertinent theory and of experimental methods. After that, the

three results chapters report on the following research questions: -

- Chapter 4 is a **capability** and **accountability** chapter, which will test a single-celled DGV both with and without a hydrogen termination under irradiation from an x-ray tube, to test the principles of the design and to get a first handle on the power generating capabilities of such a cell. It also includes an x-ray photoelectron spectroscopy study, performed to measure the hydrogen coverage attained by the fabrication methods used. The research questions are: Can a hydrogen termination truly perform the role envisaged, of allowing a design like the present one to work? If so, given standard hydrogen termination processes cannot be used in this design, how much hydrogen has been successfully laid down on a device that proves itself?
- Chapter 5 is a pure **accountability** chapter, in which two synchrotron studies are presented. One study is paired with a high-energy physics simulation in order to attempt to validate that simulation, so that it can be used with some confidence in later experiments to separate high-energy effects from electrical effects. The second probes the photon energy region in which photoelectric absorption cedes dominance to Compton scattering, to investigate what effect, if any, that has on the electrical properties and performance of the DGV. The results are compared to what the simulation predicted. The research questions are: What effect might changing photon interaction mechanisms have on a DGV, given Compton scattering is unique to gammavoltaics? How far can we get towards simulating the system, looking only at particle physics simulation?
- Finally, Chapter 6 is all about isotope experiments for addressing **comparability**, **applicability** and **longevity**. For this chapter, except for the longevity experiment, a triple-celled DGV was used instead of a single-celled one for the sake of higher power outputs. The longevity experiment kept the single-celled DGV design of previous chapters in order to keep the parameter space as small as possible. The research questions are: How much power can be produced under realistic dose rates, of realistic photon energies, with an early, multicell prototype? How does changing the dose rate over several orders of magnitude affect device performance? Finally, how long might a single cell last under such conditions?

## THEORY OF PHOTOVOLTAIC MODELLING AND CURVE FITTING FOR THE DGV

This work draws on several sub-disciplines, and unfortunately this breadth has necessarily been achieved at the cost of some depth in each. This chapter is an attempt to give a better underpinning from a photovoltaic theory perspective. It will first give an overview of the band theory of a silicon  $pn$ -junction based solar cell under illumination for visible photons, before covering the equivalent circuit of the same. It will then cover Jain and Kapoor's [201] use of the Lambert W function to derive an explicit  $I$ - $V$  relation for such an equivalent circuit when parasitic resistances are included. Following this, it will provide a concept band diagram for the DGV based on measured parameters from the literature which, whilst not fully developed, is sufficient to construct an equivalent circuit for the DGV called the opposing-diodes model. Some derivation will then be presented which uses the Lambert W function to find a single implicit  $I$ - $V$  fitting function for this model, as well as an explicit  $V$ - $I$  function. Turning to the fitting process itself, the chapter will discuss the theory of orthogonal distance regression and why it was used instead of ordinary least squares. Finally, it will discuss the theory of the Kolmogorov-Smirnov test used to assess fit quality, and why it was used instead of the reduced chi-squared fit statistic. As a theory chapter, this chapter heavily references certain longer works by page(s): Nelson's *The Physics of Solar Cells* [66], Sze's *Physics of Semiconductor Devices* [76], and the work of Boggs [202, 203] and Zwolak [204] on orthogonal distance regression.

### 2.1 $pn$ -homojunction solar cells

#### 2.1.1 Forming a junction

The energy band diagram of a  $pn$ -junction is often presented with the  $p$ - and  $n$ -type layers first artificially separated in space, such that they may be considered as distinct, electrically isolated

crystals, with the energy bands taking their bulk values. In the case of the two layers being formed of the same material (a homojunction), this means the two crystals will have the same electron affinity, and as such that their valence and conduction bands will be aligned in energy. The Fermi level - the energy at which half of the allowed states in the crystal are occupied for a finite temperature - will, however, be different. The acceptor dopant atoms in the  $p$ -type crystal will create an energy band at an energy  $E_a$  slightly above the valence band, and the greater the number of acceptors, the greater the number of holes in that band, which will drag the Fermi level lower in energy. For the  $n$ -type material, the donor dopant atoms will create an energy band at an energy  $E_d$  slightly below the conduction band, and this will drag the Fermi level upwards in energy. Mathematically, assuming the crystals are separately both at thermal equilibrium [76, p. 21],

$$(2.1) \quad E_F \approx E_V + \frac{E_g}{2} - k_b T \ln \left( \frac{p}{n_i} \right), \text{ and}$$

$$(2.2) \quad E_F \approx E_C - \frac{E_g}{2} + k_b T \ln \left( \frac{n}{n_i} \right),$$

for the  $p$ - and  $n$ -type crystals respectively.  $E_V$  and  $E_C$  are the energies of the top of the valence band and the bottom of the conduction band,  $p$  and  $n$  are the densities of holes and electrons respectively, and  $n_i$  is the density of conduction electrons in a pure crystal of the same semiconductor, promoted due to thermal energy. The manner in which  $p$  and  $n$  relate to the acceptor and dopant concentrations  $N_a$  and  $N_d$  respectively are material dependant, like  $n_i$ . Figure 2.1(a) shows a separated band diagram of this type. The band diagram of the  $pn$ -junction is then arrived at by imagining the two crystals joining and being allowed to reach thermal equilibrium, at which point by definition their Fermi levels align. Diagrammatically this leads to the intuitive picture of Figure 2.1(b), wherein the valence and conduction bands, and the vacuum level  $E_{vac}$ , bend to allow this Fermi level alignment, leading to an built-in potential difference  $V_{bi} = \frac{1}{q} \Delta E_{vac}$ . The physical process underlying this is the flow of surplus electrons, due to donor dopants, on the  $n$  side, diffusing across to the acceptor dopants with a paucity of electrons on the  $p$  side. In doing so, they built up negative charge on the  $p$  side which opposes the further flow of electrons until there is no more net flow. The analogous process happens for holes from the  $p$  side, which flow to the  $n$  side and build up there a positive charge. The diffusion current of electrons/holes is the process minimising the statistical potential energy of the electrons/holes, whilst the drift currents flow the opposite way to their respective diffusion currents to minimise the electrostatic potential energy [66, p. 73]. The equilibrium band-bending is the electrostatic field which leads to the drift currents cancelling the diffusion currents [66, p. 146], with the region where the bands bend being called the space-charge region. It is this kind of "traditional" band-bending approach which was referenced as unsuitable for metal-diamond contacts in Section 1.3.3, but it works in silicon  $pn$ -junctions because, among other reasons, the interface is between two silicon layers grown continuously, and so there are no surface states.

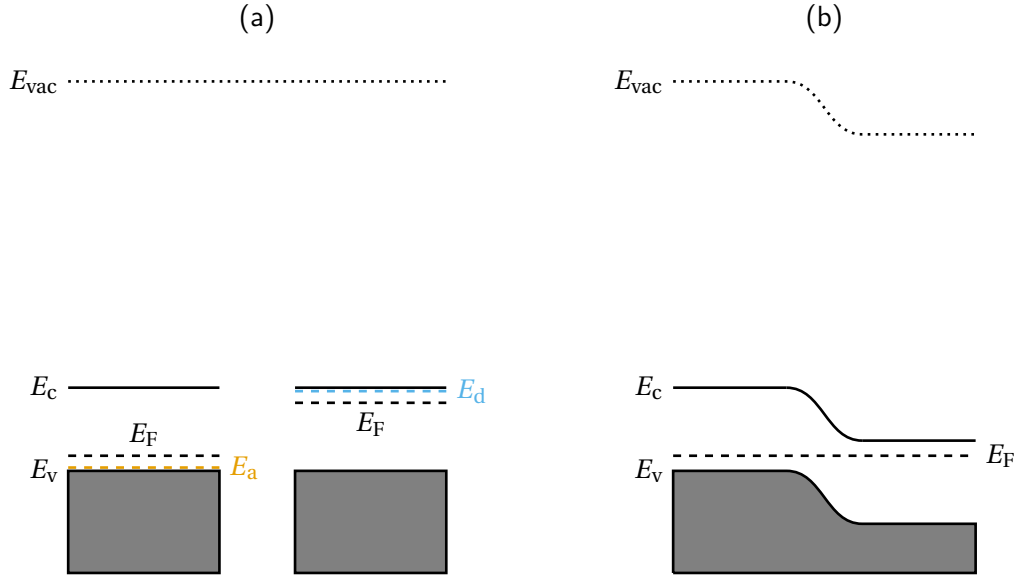


FIGURE 2.1. Band diagrams of *p*- and *n*-type silicon, when (a) spatially separated and electrically isolated, and (b) brought into contact and equilibrium. In each case the *p* side is on the left. The energy differences are approximately to scale for a silicon *pn*-homojunction, with  $E_a$  based on boron and  $E_d$  on phosphorous, both in silicon [76, p. 23], and the respective  $E_F$  values both based on acceptor/donor concentrations of  $10^{16} \text{ cm}^{-3}$ .

### 2.1.2 Applying a bias to a junction

When a bias  $V$  is applied to a *pn*-junction, thermal equilibrium is disrupted, but the electron and hole populations are said to be separately still in quasi-thermal equilibrium, having separate quasi-Fermi levels<sup>1</sup>. The definitions for these are analogous to the Equations 2.1 and 2.2 for the Fermi level at thermal equilibrium: -

$$(2.3) \quad E_{F,p} \approx E_v + \frac{E_g}{2} - k_b T \ln\left(\frac{p}{n_i}\right), \text{ and}$$

$$(2.4) \quad E_{F,n} \approx E_c - \frac{E_g}{2} + k_b T \ln\left(\frac{n}{n_i}\right).$$

Sufficiently far into the *p* side, the population of electrons will disappear as they recombine with the much more numerous holes, meaning there will again be a single definable Fermi level,  $E_F = E_{F,p}$ . Similarly, far enough into the *n* side,  $E_F = E_{F,n}$ . This implies that the maximum separation of  $E_{F,p}$  and  $E_{F,n}$  is  $qV$ . Under the commonly-used depletion approximation, it is assumed that all dopants within the space charge region are ionised. So, within said region  $p = N_a$  is a constant, as is  $n = N_d$ . Thus in the space charge region all the terms in Equations 2.3 and 2.4 are constant, and  $qV = E_{F,n} - E_{F,p}$ . This is illustrated for positive and negative biases in Figure 2.2. Upon the application of a bias and the splitting of the Fermi level, several different processes occur which generate net currents,

<sup>1</sup>Also known as imrefs. That is, "Fermi" spelled backwards.

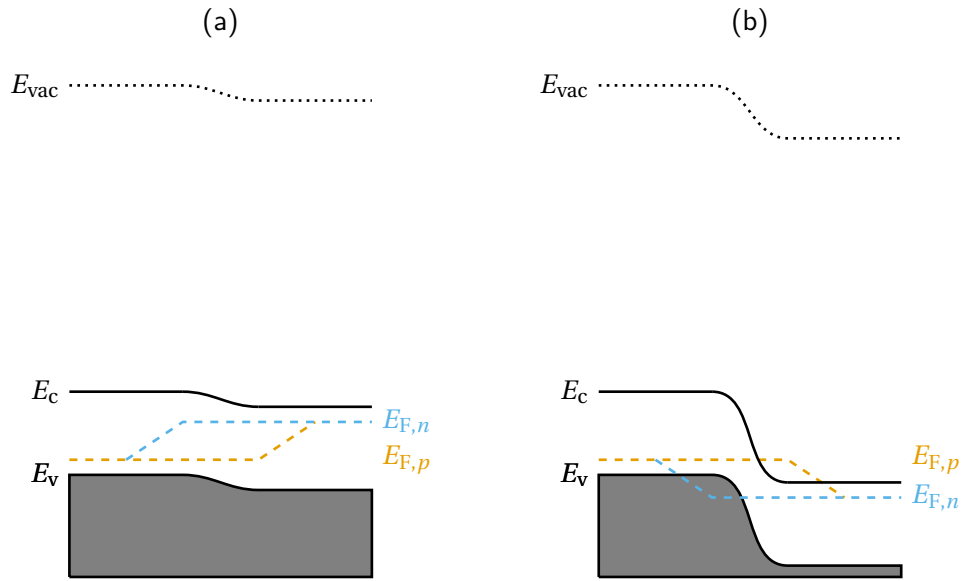


FIGURE 2.2. Band diagrams of the  $pn$ -junction from Figure 2.1(b), now under a bias of (a)  $V = 0.5$  V, and (b)  $V = -0.5$  V, showing the Fermi level splitting into quasi-Fermi levels separated by  $qV$ .

which dominate to differing degrees in different materials. Wagner showed in 1931<sup>2</sup> that the best rectification possible with a device which used charge carriers of charge  $q$  gave an  $I$ - $V$  relation of the form

$$(2.5) \quad I = I_0 \left( \exp\left(\frac{V}{V_T}\right) - 1 \right),$$

where  $I_0$  is a reverse saturation current (the current that leaks through the diode when it is in blocking mode) and

$$(2.6) \quad V_T = \frac{k_b T}{q} \approx 0.026 \text{ V} \Big|_{T=300 \text{ K}}$$

is the thermal voltage, related to the energy in the system due to ambient heat. Shockley, in his landmark long-form article of 1949 [209], re-derived this to give an equation of the same form in which  $I_0$  was given explicitly in terms of diffusion currents. He showed that the diffusion current [66, p. 163],

$$(2.7) \quad I_{\text{diff}} = Aqn_i^2 \left( \frac{D_n}{N_a L_n} + \frac{D_p}{N_d L_p} \right) \left( \exp\left(\frac{V}{V_T}\right) - 1 \right),$$

<sup>2</sup>Shockley cited Wagner, but the article was published in *Physikalische Zeitschrift*, which ceased publishing in 1945. The article is cited here from completeness [205], but is still under copyright at time of writing and not available online. It is due to be made available by HathiTrust in 2027 [206]. A similar situation presents itself for the work of B. Davydov, who was said by Moll [207] to have published work similar to Shockley's approach, if less complete, which appeared in English in 1938 but was largely ignored. I have been unable to find a copy of Davydov's work, online or otherwise, but for completeness the reference is [208].

where  $A$  is the area of the diode in the plane perpendicular to current flow,  $D_n$  and  $D_p$  are the so-called Einstein diffusion constants for the electrons and holes respectively, and  $L_n$  and  $L_p$  are measures of the average distance an electron/hole will diffuse in the  $p/n$ -side before recombining [66, p. 115].

In conventional silicon  $pn$ -junctions, the diffusion current dominates and the total current can be approximated by Equation 2.7. However, if  $L_n$  and  $L_p$  are short compared to the width of the space charge region, then recombination may happen within the space charge region. The equation for current caused by recombination in the space charge region is [66, p. 163]

$$(2.8) \quad I_{\text{scr}} = \frac{Aqn_i(w_n + w_p)}{\sqrt{\tau_p\tau_n}} \left( \exp\left(\frac{V}{2V_T}\right) - 1 \right),$$

where  $w_n$  and  $w_p$  are the widths of the space charge region measured from the centre of the junction, which are equal for a homojunction with symmetrical doping  $N_a = N_d$  [66, p. 151], and  $\tau_n$  and  $\tau_p$  are measures of the lifetimes of electrons and holes before they recombine within the space charge region. Notably, the argument to the exponential has a factor of 2 in the denominator not present in the equation for  $I_{\text{diff}}$ . There are additional processes which contribute to the current (see the discussion of recombination mechanisms in the next subsection), but to a good first approximation they can be disregarded for silicon  $pn$ -junctions [66, p. 164]. The  $I$ - $V$  relation of the diode can thus be written

$$(2.9) \quad I = I_{\text{diff},0} \left( \exp\left(\frac{V}{V_T}\right) - 1 \right) + I_{\text{scr},0} \left( \exp\left(\frac{V}{2V_T}\right) - 1 \right),$$

where  $I_{\text{diff},0}$  and  $I_{\text{scr},0}$  have been defined from the prefactors in Equations 2.7 and 2.8. This can then be approximated as the final form

$$(2.10) \quad I = I_0 \left( \exp\left(\frac{V}{nV_T}\right) - 1 \right),$$

where  $n$  is the "ideality factor" - not to be confused with the previous use of  $n$  to refer to the electron carrier density - which acts as a measure of the relative dominance of diffusion and space charge recombination currents. Physically,  $n$  changes with  $V$ , but is often treated as a constant, especially for the purposes of simulating circuits or fitting data. The exponential  $I$ - $V$  relationship renders a  $pn$ -junction a diode.

### 2.1.3 Illuminating a $pn$ -junction

When a  $pn$ -junction diode is formed in such a way that light can penetrate though it as far as the junction, the photons may promote electrons from the valence band into the conduction band. To do so, a photon must have at least as much energy as the band gap. For silicon, which has a band gap of approximately 1.1 eV, the minimum photon energy is in the infrared region of the spectrum. For comparison, the band gap of diamond being 5.5 eV means the minimum photon energy is in the "hard UV" or UV-C range, and in principle a diamond photovoltaic could be constructed for

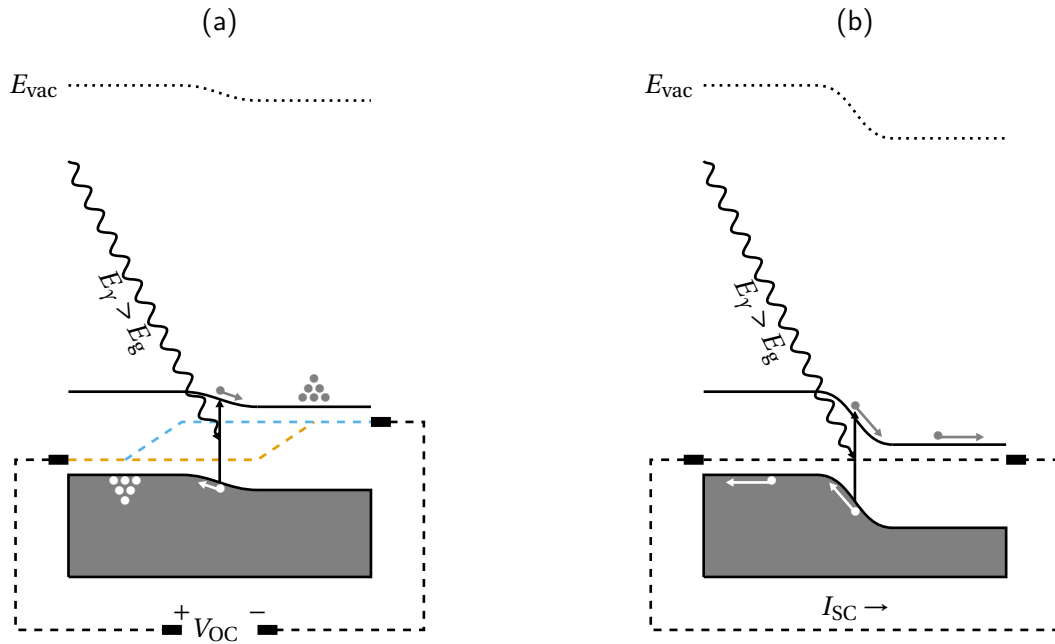


FIGURE 2.3. Band diagrams of the  $pn$ -junction from Figure 2.1(b), now under illumination from photons of energy  $E_\gamma$  with (a) open circuit conditions, where a photovoltage  $V = V_{Ph} = V_{OC}$  develops and no net current flows, and (b) short circuit conditions, where a photocurrent  $I = I_{Ph} = I_{SC}$  flows so as to eliminate any voltage. In the case where a finite load is used instead, a mix of the two will prevail with a voltage  $V < V_{OC}$  and a current  $I > I_{SC}$ , the latter because the currents have negative signs.

photons with energy greater than this with structures similar to those used in silicon for visible light. What happens to the energy levels and currents in the junction then depend on whether, or how, the diode is connected to any external circuit. Photogenerated electrons and the holes they leave behind will drift under the influence of the prevailing electrostatic field, with the electrons drifting from the  $p$  side into the  $n$  side and the holes drifting from the  $n$  side to the  $p$  side. If there is no external circuit, or an open circuit, then the illumination will bring the electron and hole populations out of equilibrium with one another, creating a photovoltage. If the diode is shorted so that the hole and electron populations are forced to remain in equilibrium with one another, then the mechanism by which this equilibrium is achieved is by a photocurrent. These two circumstances are shown in Figure 2.3.

If the diode is connected to a circuit which is neither open nor shorted but instead presents a load, then a situation between the two extremes will prevail and, there being both a (smaller) current and a (smaller) voltage generated at the same time, the diode will generate power. This is the most basic form a model for a  $pn$ -junction solar cell can be and is the basis for the equivalent circuit model without parasitic resistances, discussion in the next Section.

Opposing the photocurrent are the diode dark currents and their recombination mechanisms,

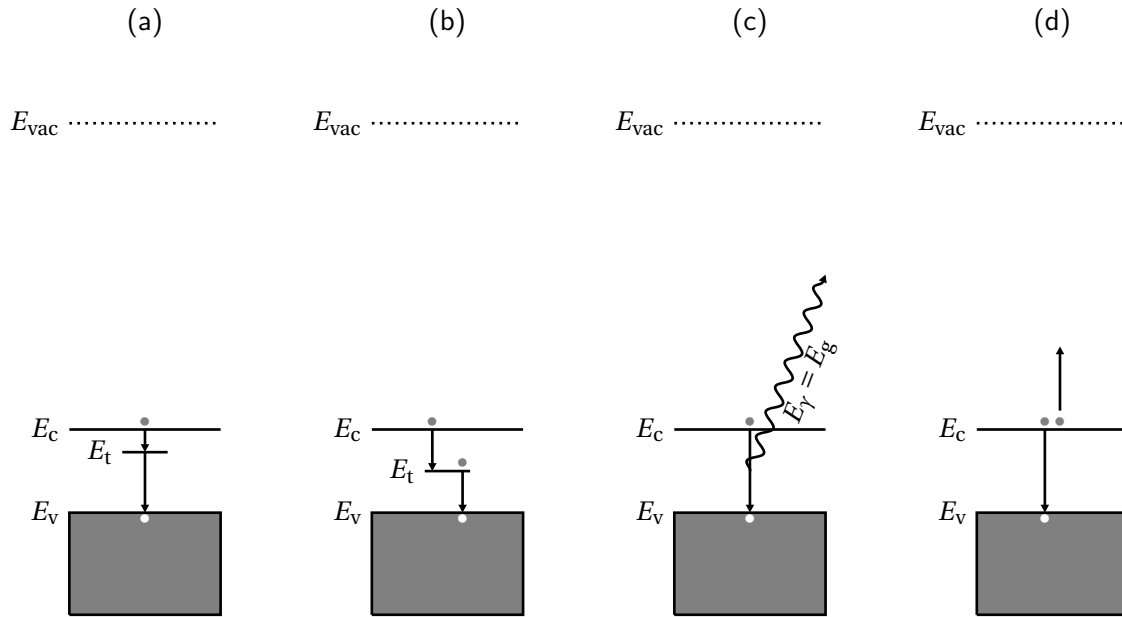


FIGURE 2.4. Band diagrams showing four types of recombination in silicon. **(a)** shows recombination mediated by a trap state. **(b)** shows recombination at a recombination centre. **(c)** shows radiative recombination. **(d)** shows Auger recombination. Additionally, Auger recombination can occur when one electron is at a trap level, too, and there is an analogous form of Auger recombination in which there are two holes and one electron, rather than two electrons and one hole [66, p. 106].

often termed recombination losses. Band diagrams describing four types of recombination are given in Figure 2.4. The recombination underpinning  $I_{diff}$  and  $I_{scr}$  in the dark current (Equation 2.10) will tend to be dominated in real junctions by Shockley-Read-Hall (SRH) recombination, which is recombination mediated by spatially localised intra-band gap states brought about by material defects [66, pp. 106-107]. These states may be traps, which preferentially trap one type of carrier before releasing them further due to thermal excitation, allowing them to recombine in the valence or conduction band. Or, they may be recombination centres, which trap both carriers and allow them to recombine at the state itself. When recombination occurs directly between the conduction and valence bands instead, it is referred to as radiative recombination because a photon is emitted at the energy of the band gap, although it is not the only recombination mechanism in which a photon may be emitted [66, p 105]. Indeed, SRH recombination may also emit photons in materials with larger band gaps, this being a method of creating single-photon emission sources in diamond [210]. Radiative recombination is generally only a small concern in indirect band gap materials such as silicon [66, p. 164] and diamond unless the device structure has been specifically tailored to work as a light-emitting diode (LED). Finally, Auger recombination involves an electron in the conduction band interacting with another promoted electron - in either the conduction band or a trap state - leading the first electron to lose energy to the second and thus recombine with a nearby hole. This

process may also occur with two holes and one electron [66, pp. 105 - 106]. The energy lost to the second electron/hole causes it to be promoted in energy, but this energy is then usually lost to the lattice as thermal energy. The Auger recombination rate is proportional to the square of the density of the carrier of which two are involved, and linearly proportional to the density of the carrier of which there is one. This means that the purity of the semiconductor (due to intentional or unintentional doping) has a strong influence on the prevalence of Auger recombination. Auger recombination may still dominate radiative recombination in indirect band gap semiconductors, however, as the latter is more strongly suppressed [66, pp. 106].

Recombination and generation mechanisms oppose one another, but are two sides of the same coin. The recombination mechanism diagrams in Figure 2.4 may each have their arrows reversed to describe a generation mechanism. The most obvious pairing from a photovoltaics perspective is that radiative recombination is the reverse of generation of a photocurrent. For SRH recombination, except in the cases mentioned above where photons are involved, the energy of the recombining electron is carried away as thermal energy in the lattice *via* phonons. The generative reverse of this is thermal generation of carriers. This is always present to some degree in devices at room temperature, but is specifically harnessed in thermionic energy converters which use high temperatures to generate currents [166, 211]. It is also targeted by the similar, but more recent and distinct, class of devices known as *phono*-voltaics, which aim to create materials in which there is a significant population of phonons higher in energy than the band gap [212, 213]. That said, it should be noted that these devices do not aim specifically for a kind of thermal generation that mimics SRH recombination in reverse, but band-to-band carrier generation, equivalent in its effects to photogeneration. Finally, the generative reverse process to Auger recombination is impact ionisation, in which an electron with at least twice the band gap energy promotes a second electron from the valence band to the conduction band whilst remaining in the conduction band itself - or the equivalent for two holes. Impact ionisation has been targeted alongside photogeneration in hot carrier solar cells [66, pp. 318-323], and is also - perhaps most directly - the primary generation method intended by betavoltaics.

To make a brief interjection on radiovoltaics amid this discussion on conventional silicon photovoltaics: whilst not all of the high-energy processes described in Sections 1.2.1 and 1.2.2 are accounted for among the generation mechanisms just discussed, many are<sup>3</sup>. Photoelectric absorption is straightforwardly the same process as photogeneration, but at photon energies high enough that the photoelectron may escape the material entirely if created sufficiently close to its surface. Coulomb stopping is, likewise, impact ionisation, except the high-energy electron has possibly hundreds of thousands of times the band gap energy, meaning the number of electrons it may promote from the valence band is very large. NIEL, particularly in the case when the nucleus involved is not permanently displaced, generates phonons which may effect carriers. The high-energy physics processes not represented by analogous semiconductor physics generation processes are those in which

---

<sup>3</sup>I have so far been unable to discern whether the distinct nomenclature is used on purpose, to distinguish between the energy regimes involved, or is a social result of high-energy physics and semiconductor physics being different sub-disciplines with differing foci and histories. At time of writing, the impression I get is the latter.

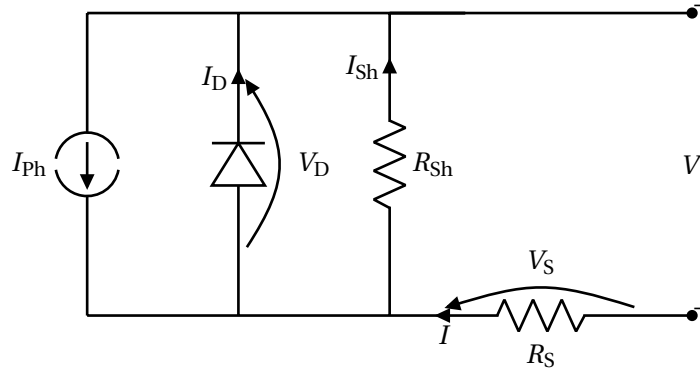


Figure 2.5: The most commonly-encountered equivalent circuit model for a photovoltaic cell, including parasitic resistances.

energy is released from the incident particle through means instead of, or in addition to, the lattice or the sub-conduction band electrons. In Compton scattering and both types of bremsstrahlung, this additional energy is lost from the primary photon as a secondary photon. In pair production, energy is lost in the creation of a new electron-positron pair. The products of each of these processes, however, may go on to interact by other mechanisms within the device.

#### 2.1.4 The equivalent circuit of a solar cell

The most commonly-encountered model for a single solar cell is the equivalent circuit shown in Figure 2.1.4.

The current source and diode in parallel represent the  $I$ - $V$  behaviour of an illuminated  $pn$ -junction of the type discussed in the previous subsection. Added to this are resistors to account for things not represented in the band diagram: a shunt resistor representing leakage paths around or through the device, for example hopping conduction between intra-band gap defect states, and a series resistor which accounts for the resistance the total current experiences when travelling through bottlenecks in the circuit, such as contact resistances between the junction and the rest of the circuit, and wire resistances hitherto ignored. The series and shunt resistances,  $R_s$  and  $R_{sh}$ , are termed parasitic resistances<sup>4</sup>. When a load is connected to the terminals, allowing current to flow, Kirchoff's current law (KCL)<sup>5</sup> stipulates that  $I = I_D + I_{Sh} - I_{Ph}$ . The simplest version of this model occurs for high-quality cells where the series and shunt resistances can be considered negligible and infinite respectively, so  $V_D = V$  and  $I_{Sh} = 0$ , yielding the current-voltage relation

$$(2.11) \quad I = I_0 \left( \exp \left( \frac{V}{nV_T} \right) - 1 \right) - I_{Ph}.$$

<sup>4</sup>Because it is preferable for the shunt resistance to be as high as possible, and the series resistance to be as low as possible, the shunt resistance is sometimes referred to as a shunt conductance,  $G_{sh}$ , so that both parameters are optimised in the same direction, i.e. minimised. In this work, the resistance convention is followed.

<sup>5</sup>Elaboration of which can be found online or in undergraduate physics texts, for example [214].

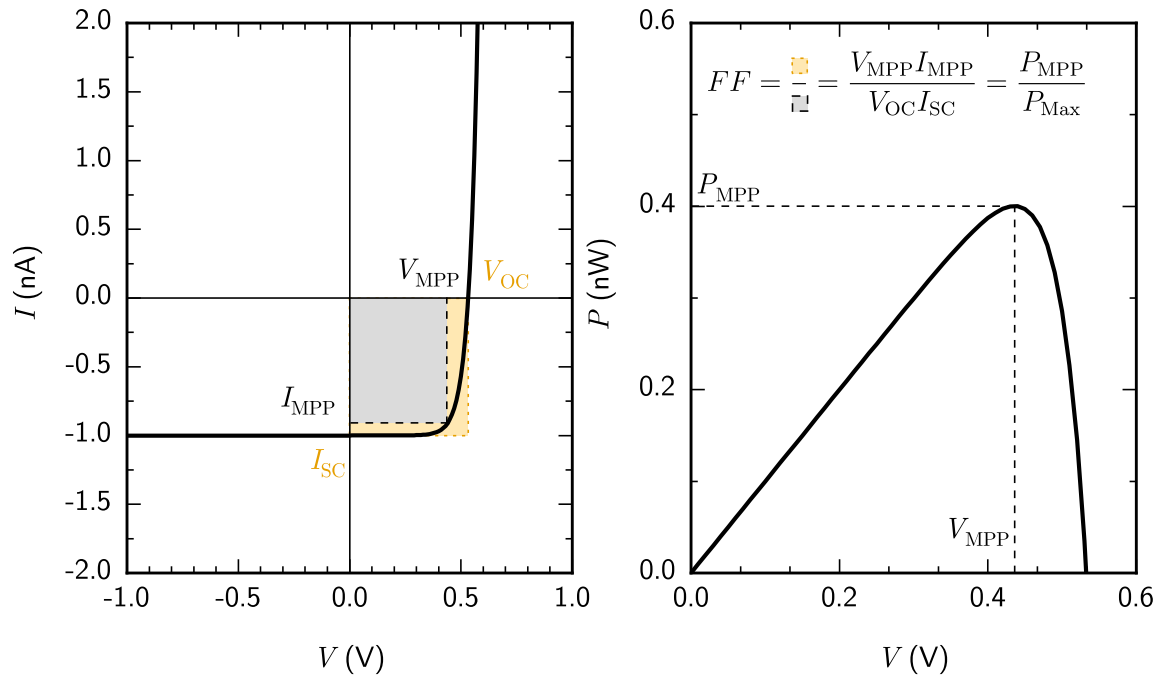


FIGURE 2.6. A plot of the photovoltaic model  $I$ - $V$  and  $P$ - $V$  curves, without parasitic resistances, showing also the definition of the Fill Factor  $FF$ , a measure of cell efficiency. Mathematically  $FF$  is described by the equation in the figure (Equation 2.12), and graphically as the ratio of areas between the orange and black rectangles in the figure.

A plot of this function is shown in Figure 2.6 with realistic values for radiovoltaics, namely  $I_{ph} = 1$  nA,  $n = 1.5$  and  $I_0 = 1$  fA. A plot of the resultant  $P$ - $V$  curve is also shown in Figure 2.6. Finally, the definition of the Fill Factor  $FF$  is also shown graphically, which is a measure of cell efficiency which increases as the curve's "squareness" increases. Mathematically,  $FF$  is defined as

$$(2.12) \quad FF = \frac{I_{MPP} V_{MPP}}{I_{SC} V_{OC}} = \frac{P_{MPP}}{P_{Max}}.$$

It is one of several conceivable power-based figures of merit. Another common one is the maximum power efficiency,

$$(2.13) \quad \eta = \frac{P_{MPP}}{P_\gamma} = \frac{P_{MPP}}{E_\gamma \Phi},$$

where  $P_\gamma$  is the power of the incident photons,  $E_\gamma$  is their energy and  $\Phi$  their areal flux. When the radiation is not monochromatic (such as sunlight), the latter two may be replaced with a suitable integration over photon energies greater than the bandgap.  $\eta$  is in a sense the most natural figure of merit for a conventional solar cell which is, to all intents and purposes, opaque to sunlight, as it answers the question of how much power one gets out for the power put in.

As per the discussion in the previous section,  $n$  will take a value close to 1 when space charge recombination current dominates, and will move closer to 2 when diffusion or radiative recombination current dominates [66, pp. 163-164]. When tunnelling currents are present however, such as when *pn*-junctions are formed from heterojunctions rather than homojunctions, or when Schottky junctions are used, they can give rise to values of  $n$  greater than 2. In particular, where wide-bandgap materials are used, the values of  $n$  reported in the literature are notably higher. For example, GaN *pn*-homojunctions with  $n = 6.9$  [215], p-AlGaIn/GaN *pn*-heterojunctions with  $n = 4.0$  [215], n-ZnO/p-diamond *pn*-heterojunctions with  $n = 6.0$  [216], and finally BN/ZnO heterojunctions with "apparently giant ideality factors" of  $n \approx 100 - 200$  attributed to Frenkel-Poole conduction [217]. That is, conduction of carriers between trap states in an otherwise more resistive bulk [76, p. 358].

Figure 2.7 shows calculated photovoltaic  $I$ - $V$  and  $P$ - $V$  curves in which the parameters  $I_{Ph}$ ,  $n$  and  $I_0$  are varied around the set of values used for Figure 2.6. In the range considered, the photocurrent  $I_{Ph}$  exerts the most influence over the short-circuit current  $I_{SC}$ , as without parasitic resistances,  $I_{SC} = -I_{Ph}$ . For solar cells operating under one-sun conditions at standard temperature, the photocurrent is linear with the light intensity, and thus so is the short-circuit current [66, p. 266]. However, if the light begins to heat the cell sufficiently, the effective band gap is reduced and, although this increases the photocurrent, it increases the dark current more. As these compete, the overall effect of increasing the temperature is to reduce the efficiency of the cell [66, p. 270], which puts a limit on how much light a conventional photovoltaic cell can efficiently convert. Additional sources of non-linearity between incident light intensity and short-circuit current can occur when the incident flux becomes great enough that the population of phonons required to thermalise carriers is depleted in the doing, leaving fewer left to thermalise those charge carriers that are generated later (the hot carrier effect, [66, p. 317]) or when the incident light is energetic enough that impact ionisation occurs, competing with recombination processes and causing a similar effect [66, p. 323]. Additionally, the increase in flux and attendant increase in current density may begin to cause a sufficient series resistance increase that the latter can no longer be ignored. The effect of series resistance is discussed in Section 2.1.5.

In the case of non-concentrated fluxes and standard temperatures, the influence of  $I_{Ph}$  on  $V_{OC}$  is logarithmic in the absence of parasitic resistances [66, p. 10], as can be seen by re-arranging Equation 2.11 with  $I = 0$ : -

$$(2.14) \quad V_{OC} = nV_T \ln \left( \frac{I_{Ph}}{I_0} + 1 \right).$$

By inspection of Equation 2.14 it can also be seen that the  $V_{OC}$  rises linearly with  $n$  (though only within the limited range over which  $n$  can vary), and conversely that  $V_{OC}$  decreases linearly with the order of magnitude of the saturation current  $I_0$ . In fact, as can be seen from the graphs in which  $n$  and  $I_0$  are varied in Figure 2.7, it is possible to achieve very similar curves by varying one or the other appropriately. This is a problem when fitting curves to data. As discussed in Section 2.3.1 below, fitting proceeds by finding the curve which has the minimum difference between its data and the measured data, so having covariant parameters causes the risk of a fitting procedure finding a fit

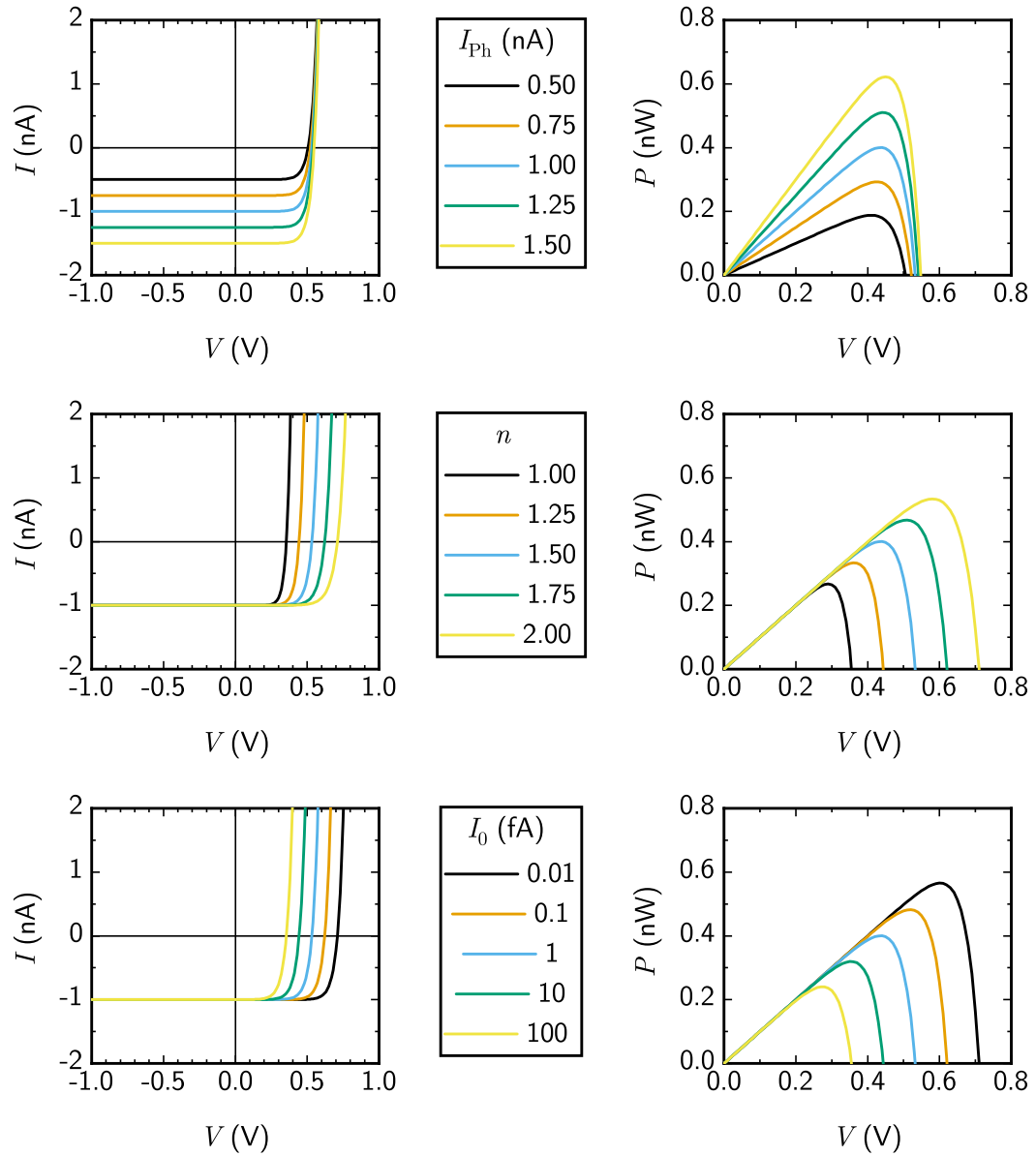


FIGURE 2.7. The effect on the  $I$ - $V$  and  $P$ - $V$  curves of varying parameters in the PV equivalent circuit without parasitic resistances. The blue line is the same in each case and corresponds to  $I_{ph} = 1$  nA,  $n = 1.5$  and  $I_0 = 1$  fA.

which, whilst very close to the measured data, is in the wrong region of the parameter space. This issue is compounded for radiovoltaics by the fact that currents are much smaller and as such will tend to be more vulnerable to noise. Figure 2.8 shows some data simulated by generating an  $I$ - $V$  curve according to the parameters used so far (with  $I_{\text{ph}} = 1$  nA,  $n = 1.5$  and  $I_0 = 1$  fA), and adding some error terms drawn from the same normal distribution as one another (i.e. the uncertainty for each point is the same). Alongside that, it shows the base-10 logarithm of the sum of squared residuals, mapped across the parameter space in the region already used. The projection is a minimum intensity projection, which is to say that the viewer sees the point corresponding to the best fit when looking into the page at the parameter space, not any points of worse fit which may reside between it and the viewer.

In Figure 2.8, there is a prominent line of well-fitting points at the correct value of  $n$  and  $I_0$  which, when the threshold for the colourmap is varied can also be shown to slope towards the best fit value for the correct value of  $I_{\text{ph}}$ . This latter manipulation is not shown because the point is barely visible at the resolution used for the parameter space, which is to say that the locality of the global minimum is very steep and there are many points in the minimum line which have similar fit qualities despite having different values of  $I_{\text{ph}}$ . However, what can also be seen is that there are parallel lines of values which, although orders of magnitude worse than the fits for the main line of minima, are still themselves orders of magnitude better than the regions of the parameter space around them. Because fitting algorithms will tend to rely to some extent on gradient descent, these lines represent possible traps in which a fit may be found which is very reasonable to the eye but which actually sits at erroneous values, particularly of  $n$  and  $I_0$ .

When parasitic resistances cannot be ignored, application of both KCL and Kirchoff's voltage law (KVL), i.e.  $V = V_D + V_S$ , to the equivalent circuit in Figure 2.1.4 yields

$$(2.15) \quad I = I_0 \left[ \exp\left(\frac{V - IR_s}{nV_T}\right) - 1 \right] + \frac{V - IR_s}{R_{\text{sh}}} - I_{\text{ph}}.$$

Essentially, the total voltage is now shared between the the diode and shunt resistance on the one hand and the series resistor on the other, whilst the total current must now take account of the flow through the shunt resistor as well as those through the current source and diode. The entire current flows through the series resistor, meaning the voltage over it depends on  $I$ , and thus so does the voltage over the diode  $V_D$ . This renders the equation implicit in  $I$ . However, the existence of only a single exponential term allows it to be made explicit by recourse to a tool which, seemingly by historical accident, is beyond normal algebraic manipulation: the Lambert W function.

### 2.1.5 Finding an explicit $I$ - $V$ relation for a photovoltaic with parasitic resistances

Equation 2.15 is implicit, which adds a layer of complexity when attempting to manipulate it, plot, it, or fit it to data. All are possible, but tend to require additional steps, such as for example when plotting the  $I$ - $V$  curve for a given set of parameters, having to iteratively solve the equation for  $I$  at each value of  $V$ . Use of the Lambert W function can remedy this.

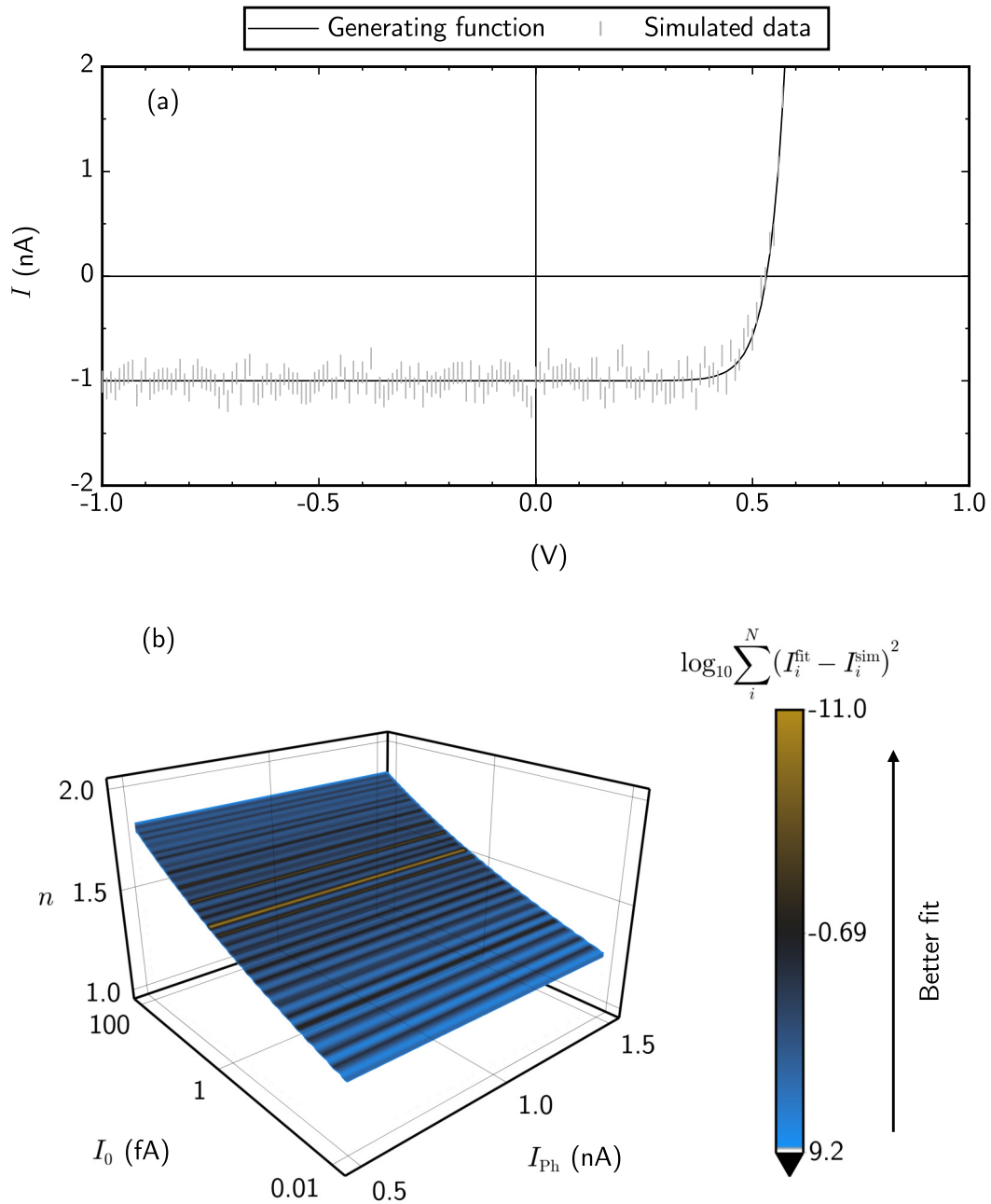


FIGURE 2.8. (a) some simulated data, generated by adding errors randomly drawn from a normal distribution to a model  $I$ - $V$  curve with  $I_{ph} = 1$  nA,  $n = 1.5$  and  $I_0 = 1$  fA, and (b) the parameter space for the fit quality in the region of the true parameters, where each point has had the logarithmic of the sum-of-squares of the attempted fit mapped in a minimum intensity projection. The logarithm has been used to aid clarity. The bounds of the parameter space correspond to the ranges used in the curves plotted in Figure 2.7.

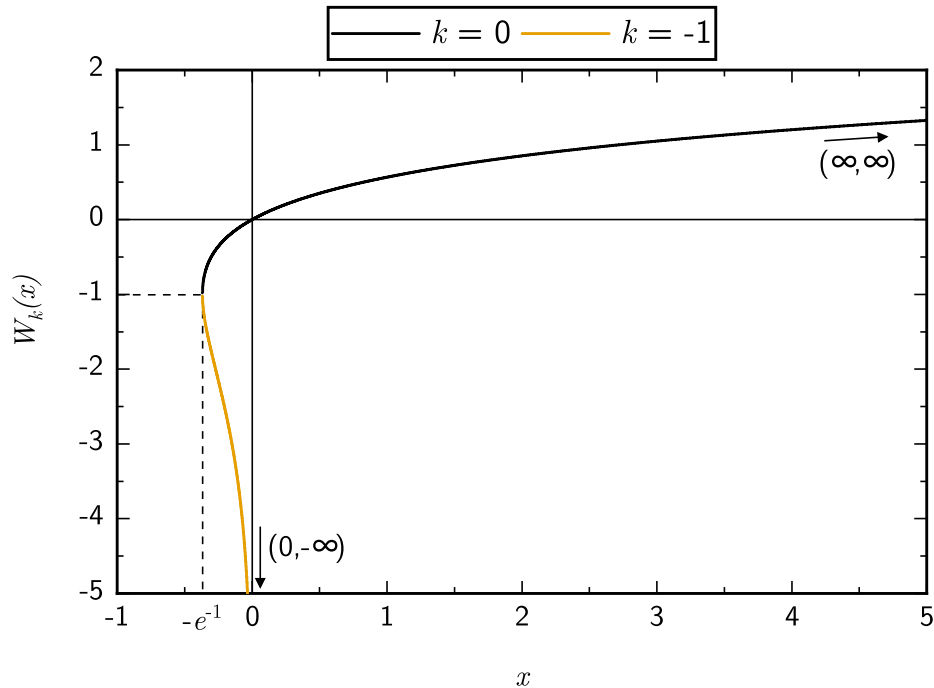


FIGURE 2.9. Portions of the two real-valued branches of the Lambert W function.

The Lambert W function, developed in correspondence between Lambert and Euler<sup>6</sup> is defined as the function  $W_k$  which solves the equation

$$(2.16) \quad W_k(x)e^{W_k(x)} = x.$$

where  $k \in \mathbb{Z}$ , reflecting the fact that there are a countably infinite number of branches of the function.  $W_k(x)$  cannot be expressed in terms of elementary functions [223]<sup>7</sup>. For every  $k$ ,  $W_k: X \in \mathbb{C} \rightarrow Y \in \mathbb{C}$ . However, only two branches have real ranges within their codomains, and each of those real ranges has a real domain. When  $k = 0$ , the domain is  $[-e^{-1}, \infty)$  and the range is  $[-1, \infty)$ . When  $k = -1$ , the domain is  $[-e^{-1}, 0)$  and the range is  $[-1, -\infty)$ . Portions of these branches are shown in Figure 2.9.

In general [222], if an implicit equation can be manipulated into the form

$$(2.17) \quad x = a + be^{cx},$$

where  $a$ ,  $b$  and  $c$  are constants, then the Lambert W function can be used to find an explicit equation

<sup>6</sup>The correspondence lead to publications in the late eighteenth century, the original citations for which are [218] for Lambert and [219, 220] for Euler. As both are in Latin however, more use may be found in the translation of Euler's work in reference [221], or in a more recent discussion [222].

<sup>7</sup>Technically the reference gives a proof that  $W_k(x)$  cannot be expressed in terms of Louvillian functions. As elementary functions are a subset of Louvillian functions, the point remains.

according to

$$(2.18) \quad x = a - \frac{1}{c} W(-bce^{ac}).$$

It appears to have been Banwell and Jayakumar who first applied the use of the Lambert  $W$  function to diodes in 2000 [224], with Jain and Kapoor [201] then applying it to the model for a solar cell with parasitic resistances, Equation 2.15, in 2004. Jain and Kapoor used the other major convention for displaying photovoltaic  $I$ - $V$  data in which the power-producing quadrant of the graph is set to the top right. For the convention used in this work, the coefficients are

$$a = \frac{V - R_{Sh}(I_{Ph} + I_0)}{R_{Sh} + R_S}, \quad b = \frac{I_0 R_{Sh}}{R_{Sh} + R_S} \exp\left(\frac{V}{nV_T}\right), \quad \text{and } c = \frac{-R_S}{nV_T}.$$

Feeding these back into the form of Equation 2.18 then gives

$$(2.19) \quad I = \frac{V - (I_{Ph} + I_0) R_{Sh}}{R_{Sh} + R_S} + \frac{nV_T}{R_S} W_0 \left[ \frac{I_0 R_{Sh} R_S}{nV_T (R_{Sh} + R_S)} \exp\left(\frac{R_{Sh}(V + (I_{Ph} + I_0) R_S)}{nV_T (R_{Sh} + R_S)}\right) \right],$$

in which some additional re-arranging has been done to combine the exponential term from  $b$  with that residing in the form of Equation 2.18 itself. It is worth noting also that unlike in Equation 2.18, Equation 2.19 specifies use of the principal branch of  $W$ . Whilst this would have perhaps been the natural choice anyway, Equation 2.19 gives us physical reasons to specify the principal branch. All of the parameters are physically constrained to be real and positive, as is the output. Only  $W_0$  produces real outputs from positive, real arguments. Additionally, it is a requirement that the model without parasitic resistances be recoverable from this one; allowing  $R_S \rightarrow 0$  means the branch of  $W$  used must be defined at 0, and the principal branch is the only branch for which this is true.

The effects of  $R_S$  and  $R_{Sh}$  on Equation 2.19 are explored in Figure 2.10 in the same manner as the effects of  $I_{Ph}$ ,  $n$  and  $I_0$  on Equation 2.11 were explored in Figure 2.7. Instead of varying in either direction however, they are varied in the direction of increasing deviation from the previous model;  $R_S$  increases and  $R_{Sh}$  decreases. As before, the values used for the other parameters are  $I_{Ph} = 1$  nA,  $n = 1.5$  and  $I_0 = 1$  fA. As would be expected, Figure 2.10 shows that if  $R_S$  gets too high, it dominates the forward  $I$ - $V$  behaviour of the diode to the point that it becomes linear, like a resistor. Conversely if  $R_{Sh}$  gets too low, the same happens - but this time because the shunt resistor is allowing the majority of the current through it, bypassing the diode. The exact dependence of the  $I_{SC}$  and  $V_{OC}$  on the two resistances is not simple, but as the figure shows,  $R_S$  will tend to exert an influence on the  $I_{SC}$  whilst leaving the  $V_{OC}$  relatively untouched, whereas the opposite is true for  $R_{Sh}$ . What is true of both of them is that their influence drags the maximum power-point and fill factor lower *via* action on both the current and voltage. In the limits where the  $I$ - $V$  curve becomes linear due to one or both resistances, the  $P$ - $V$  curve becomes symmetrical about the maximum power-point and the poorest cell efficiency is attained, with a fill factor  $FF = 0.25$ .

Visualising the parameter space of the model with parasitic resistances is somewhat more difficult than in the case without, due to the parameter space having five dimensions rather than three. An attempt has been made in Figure 2.11, in which the three-dimensional parameter space of the model

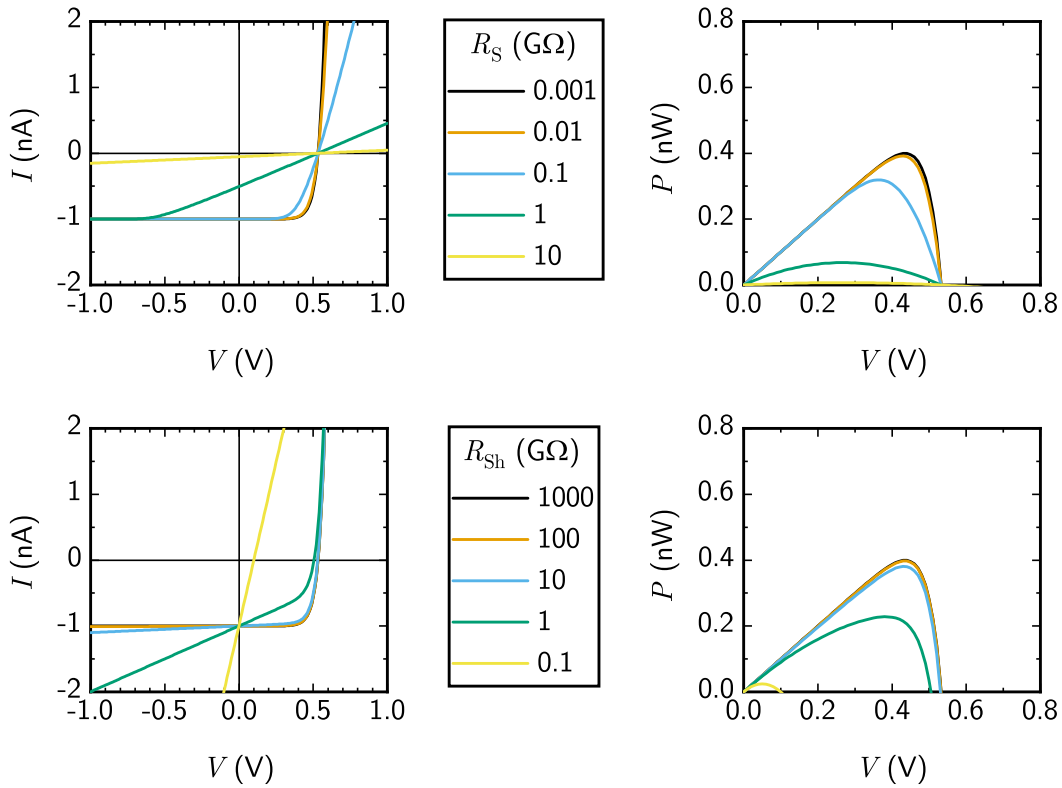


FIGURE 2.10. The effect on the  $I$ - $V$  and  $P$ - $V$  curves of varying the parasitic resistances in the PV equivalent circuit. As in the blue curves of Figure 2.7,  $I_{ph} = 1$  nA,  $n = 1.5$  and  $I_0 = 1$  fA, so the black curves in this figure most closely approximate the blue curves in Figure 2.7.

without parasitic resistances is plotted at logarithmic intervals along two axes for  $R_S$  and  $R_{Sh}$ , with the intervals corresponding to the values used in the traces in Figure 2.10.

The fit values in the parameter space are comparisons against simulated data, generated with the same uncertainties and errors as before and the same values of  $I_{ph} = 1$  nA,  $n = 1.5$  and  $I_0 = 1$  fA, but now additionally with  $R_S = 0.1$  GΩ and  $R_{Sh} = 10$  GΩ. Only so much can be determined from a plot with such low resolution in two of the dimensions, but it can be seen that there is a strong linear minimum corresponding to the correct value of  $R_S$ , and what appears to be either a patch or a line of poorer fits values for  $R_{Sh} = 1$  GΩ, suggesting there *may* be false minima present in  $R_{Sh}$ . The inclusion of parasitic resistances has also made the parameter space around the true value of  $I_{ph}$  steeper, so that it will in fact be easier to fit than before. Figure 2.12 shows this sub-plot at greater magnification and with a different threshold to show that the many false minima in  $n$  and  $I_0$  still exist, despite this.

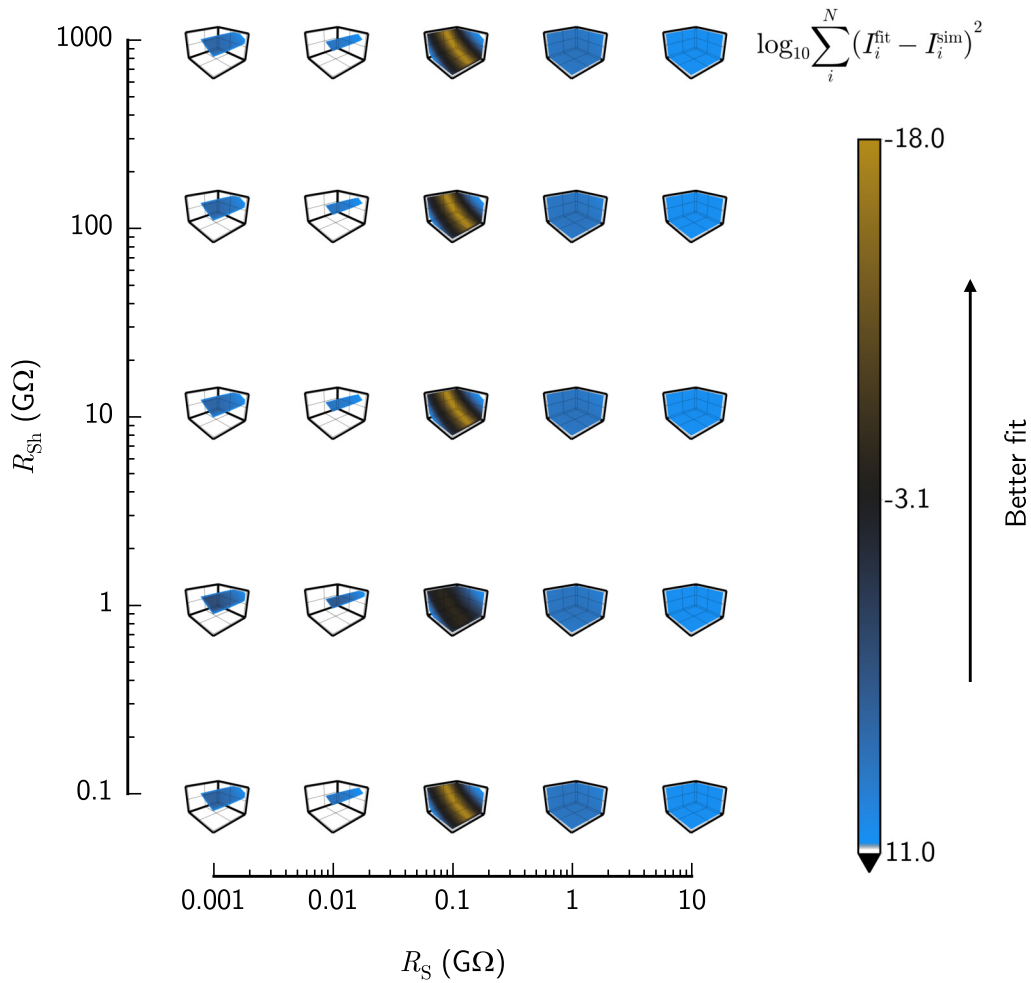


FIGURE 2.11. A low-resolution image of the five-dimensional parameter space of the photovoltaic model including parasitic resistances. Each sub-plot is the three-dimensional parameter space, with the same axis ranges, as used in Figure 2.8. The central sub-plot corresponds to the values of  $R_S$  and  $R_{Sh}$  used to generate the simulated data.

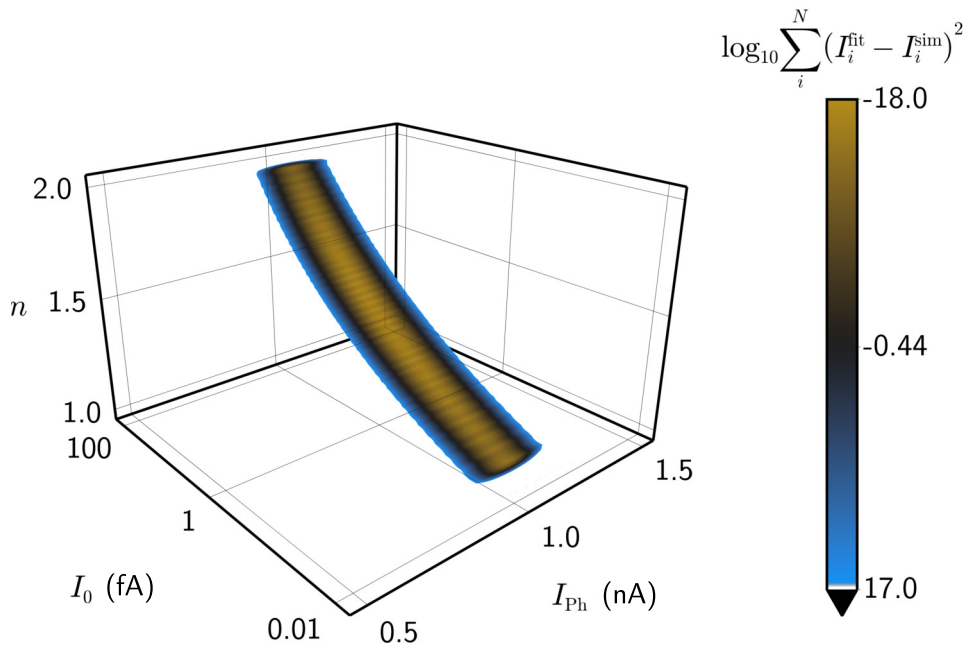


FIGURE 2.12. The subspace of non-resistive parameters for a photovoltaic cell with parasitic resistances, around the true resistance values.

The picture painted by the above cannot be too general because it is restricted to a certain set of simulated data. However, it does illustrate how the five parameters of the photovoltaic cell model with parasitic resistances may interact, and how when fitting data, false minima may exist in some parameters but not others which mean any extracted value deserves caution.

The structure of the DGV is quite different to a standard silicon photovoltaic, and so whilst the photovoltaic mode with parasitic resistances may be fruitfully used for a certain part of the DGV  $I$ - $V$  curve, a more representative model would be an improvement. For this work, that is the opposing-diode model.

## 2.2 The opposing-diodes model

Although the power-generating part of the DGV  $I$ - $V$  curve can be modelled in the same way as a conventional photovoltaic cell, the wider  $I$ - $V$  curve deviates. This reflects the structure of the device, which is more akin to a metal-insulator-metal (MiM) diode. Although MiM and MSM (metal-semiconductor-metal) diodes may have similar theoretical tools applied to them as  $pn$ -junctions, empirical fitting of MiM  $I$ - $V$  data seems to also be popular in the literature, with Pelz, Belkadi and Modelle commenting that prior to 2018 "*it [had] become common practice*" to analyse MiM diode  $I$ - $V$

data with polynomial fitting [225]. Pelz, Belkadi and Moddel suggested a more physically-inspired model, of the form

$$(2.20) \quad I = I_0 (\exp(bV) - \exp(-dV))$$

where  $b$  and  $d$  are fitting constants and  $I_0$ , whilst referred to as a scaling factor, plays the part of a saturation current of sorts. In particular, they mention the case when  $b = 1/nV_T$  and  $d = 0$ , where the equation reverts back to the Shockley diode equation and  $I_0$  takes on its conventional meaning.

The form proposed by Pelz, Belkadi and Moddel does not account for parasitic resistances, which are assumed to exert a noticeable influence on the presented gammavoltaic. For that reason, this work has pursued an equivalent circuit model which combines features mentioned so far. A fully-featured band diagram of the DGV, particularly under irradiation from gamma rays generating hot carriers, has so far proved beyond me, but below a working model is presented. First, considering a thick, pure diamond with no hydrogen surface termination and dissimilar contacts, the band diagram at short circuit will look like Figure 2.13(a). Provided contacts are chosen appropriately, Fermi-level pinning will pin the Fermi level of one contact to around 1.2 eV above  $E_v$  and the other to a lesser, but unknown, distance in energy. Under irradiation by photons with  $E_\gamma > E_G = 5.5$  eV, electron promotion will occur, but the chances that charge separation will occur and that the charges will stay separated long enough to be collected at the contacts is relatively low. The average path length is expected to reach the width of the diamond only at several hundred volts, so the small electric field created by the contacts will generate only a small current. If the diamond is fully hydrogen terminated except under the contacts, then the band diagram around the surface may look something like Figure 2.13(b). Whilst the contacts will stay pinned to the same distances from the diamond valence band, the uncontacted surface will undergo surface transfer-doping and the valence band maximum of the diamond over the rest of the surface will be pulled up over the Fermi level. The energy difference between the Fermi level and valence band maximum will be about 0.1 - 0.3 eV [178] and the depth into the surface for which this effect will hold true over will be about 1 - 5 nm [178]. Although there will be potential barriers near the contacts where hydrogen-terminated diamond meets oxygen-terminated diamond, these will be on the order of a few atoms thick and so mostly transparent to charge carriers. There will otherwise be no built-in electric field over the surface as it will act like a short, meaning electrons promoted by incident photons will have no preferred direction of travel and net charge separation will not occur. Furthermore, the depletion of electrons from the valence band in the region above the Fermi level will add 0.1 - 0.3 eV to the minimum energy required of a photon to promote an electron, and the device will conduct in the dark to a far greater extent than has been observed.

To come up with a concept band diagram for a surface which is only partially hydrogen terminated, it is necessary to give some thought to how hydrogen atoms are distributed on a partially-terminated surface. When hydrogen termination is performed on a diamond surface by the (high-temperature) MWCVD technique, the hydrogen will tend not to diffuse across the surface once it has cooled: surface diffusion is a thermal process and the thermal energy required to activate it in

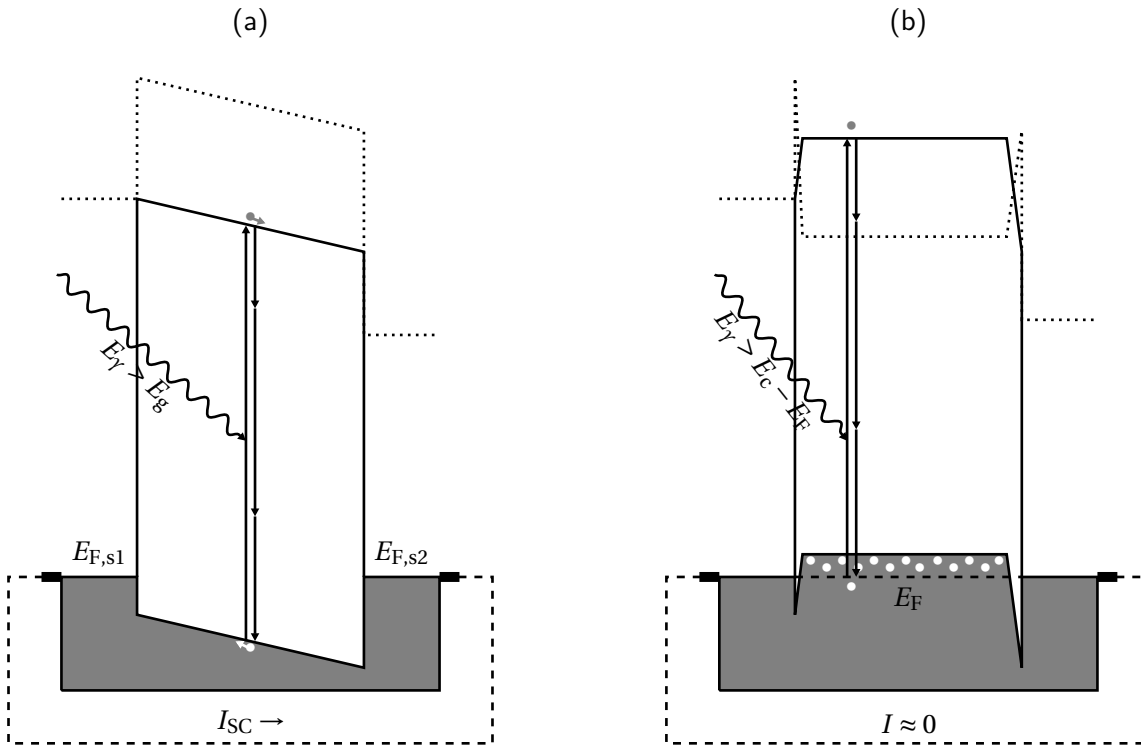


FIGURE 2.13. Band diagrams for (a) the route through the bulk of an unterminated diamond with dissimilar contacts, and (b) around the surface of a terminated diamond also with the same dissimilar contacts. One contact (on the right of each subfigure) is pinned at  $E_{F,s2} = 1.2$  eV above the diamond valence band, the other is shown pinned at an arbitrary smaller value of  $E_{F,s1} = 0.5$  eV.

the case of hydrogen on diamond is nearly as high as the thermal energy required for desorption [226]. As an example, desorption begins at around 900 K when the diamond is increased in temperature at a rate of 1 K/s [227]. As the termination process used in this work is a room-temperature process, it is here assumed that the surface populates without diffusion, with hydrogen atoms during the termination process adsorbing and desorbing at some differing rates but not moving laterally whilst adsorbed. It is known that some sites on the diamond surface are more reactive to hydrogen termination than others, with work by Geis *et al.* [228] having found anisotropic resistance across the surface of samples terminated at high temperature, consistent with hydrogen concentrating along the parallel steps that form to minimise surface energy when thermal conditions permit. By contrast, they found low-temperature termination led to isotropic surface resistance. Wade *et al.* [187] found that deliberate roughening prior to hydrogen termination can be used to further increase the surface conductivity. The variability of the electric field due to the distribution of surface hydrogen being inhomogenous at the nanometer scale is believed to limit the mobility of the holes in the 2DHG [229]. But in our case, a variable electric field is desirable to separate charge. Even without such effects as differing roughness concentrating hydrogen in some sites over others, however, in the absence of

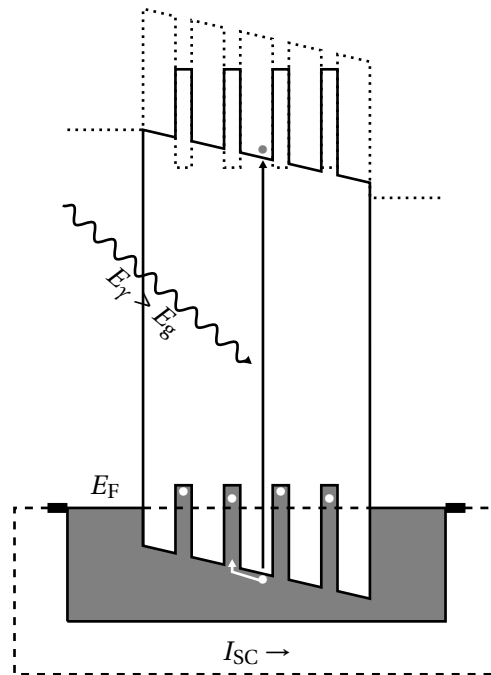


FIGURE 2.14. A concept band diagram for the DGV, neglecting the interaction between the bulk and surface and treating the device as though the electrical activity is concentrated around the surface. Patches of hydrogen-terminated diamond bring the diamond valence band over the Fermi level in places on the surface but are interspersed with areas where no hydrogen termination is present, creating a variable potential on the surface which is capable of separating charge. The contacts are still on oxygen-terminated diamond and so subject to Fermi-level pinning, which sets up the in-built bias.

diffusion it seems a statistical requirement that a partial hydrogen termination will lead to patches of greater and lesser concentration of hydrogen on the surface at the nanometer scale<sup>8</sup>. So, if it can be assumed that at relatively low partial coverages there are patches of highly hydrogen terminated diamond across a surface which otherwise more closely resembles the surface with no hydrogen termination, the band structure may look something like Figure 2.14. In the figure, four hydrogen-terminated patches are shown schematically between the contacts - the real number is expected to be far higher. In this concept, charge separation happens due to hole drift, with some contribution from electron drift depending on where in the band structure the photon strikes. Conduction over the barriers is expected to occur due to diffusion after drift leads to pile-up of charge carriers. The built-in electric field is provided by the dissimilarity of the contacts, but the charge separation occurs due to the patchy termination. Under this model there will be some photocurrent flowing in the

<sup>8</sup>As a quick demonstration: a computation was performed in which a square grid of one million elements had its elements filled at random with a probability of 0.5, representing a square surface which has been partially hydrogen terminated to 0.5 ML. Repeating this ten thousand times suggested that the mean number of populated elements with all eight adjacent elements also populated was  $1950 \pm 50$ , or about 0.2 % of the elements.

wrong direction, especially if the barriers are not as abrupt as drawn but instead vary more smoothly.

There are still several limitations to the model in addition to the question of whether or not the assumptions used to create it are valid. Particularly, it has not been developed far enough to account for how the bulk interacts with the surface and assumes that the electrical activity primarily occurs around the surface. This interaction may become significant under high doses of more penetrating radiation, when charge injection throughout the crystal will be significant. From comparison to the diamond detector, it is not believed that gamma rays in the dose rates and energies available will cause much impact, but synchrotron x-ray beams might. Furthermore, it does not consider the negative electron affinity in the hydrogen-terminated patches past the fact that hydrogen termination induces surface transfer-doping - for example, how promoted electrons may behave in relation to this surface. Finally, the band diagrams in Figures 2.13 and 2.14 go as far as photon energies just greater than the band gap, whereas a gammavoltaic will operate with incident photons hundreds of thousands of times higher in energy, meaning impact ionisation will be the norm. Indeed, impact ionisation in solar cells seems like one of the places where gammavoltaic theory could most fruitfully look to bridge the gap into high-energy/nuclear physics. But, this work is not sufficiently developed to attempt to bridge that gap. It seems likely that a lot of the theoretical work for this will have been done and will be somewhere in the literature for semiconductor radiation detectors, but incorporating this has had to be left for future work. One practical matter which has been accounted for in this work is that gamma photon energies are high enough that gammavoltaic devices, unlike conventional solar photovoltaic devices, are in general not opaque to the incident radiation. The relationship which gamma photons have to their environment is also different, with the various scattering processes discussed in Section 1.2.1 taking the place of reflection, meaning there is not always a feasible way to define the quality, energy and direction of incident radiation on a gammavoltaic cell. Whilst there is still a lot of value in talking about the conventional maximum power efficiency  $\eta$  (Equation 2.13), as there will tend to be a primary radiation field which can be described by some mathematical simplification, it also becomes useful to talk of the maximum deposited power efficiency,

$$(2.21) \quad \eta_{\text{dep}} = \frac{P_{\text{MPP}}}{P_{\text{dep}}}.$$

$P_{\text{dep}}$  is the power deposited into the cell or device. It will be expected that  $\eta_{\text{dep}} \leq \eta$ , with the two being closer in value for smaller photon energies as  $P_{\text{dep}} \rightarrow P_{\gamma}$ . As discussed in Sections 1.2.1 and 1.2.2,  $P_{\text{dep}}$  may come from a range of photon energies besides those which would traditionally be considered the incident radiation, due to inelastic scattering processes in the locality of the cell or device, and for the same reason there may be an additional contribution from other high energy particles, particularly electrons. Except in very tightly controlled experimental setups it seems therefore that values of  $P_{\text{dep}}$  must be arrived at with simulation.

There is an additional constraint upon the incident photon energy, imposed by the hydrogen termination: the band gap of diamond being in the UV means that the minimum photon energy coincides quite closely with the energies at which hydrogen desorbs strongly from diamond, with UV

illumination in the presence of oxygen actually being an established method of oxygen termination [168]. So whilst the DGV might be expected to act as a photovoltaic for UV radiation, the electrical behaviour of the device might be expected to change substantially as the hydrogen coverage decays. Nevertheless, for pure, relatively defect-free diamond, even photons near the band gap in energy penetrate a long way through diamond, and so charge generation away from the surface is always a consideration. For example, Nesládek et al measured an absorption coefficient of around  $40 \text{ cm}^{-1}$  for 5.5 eV photons [230], corresponding to an absorption length of around  $252 \mu\text{m}$ . Illuminating the DGV with hard UV would be considerably safer than the gamma and x-ray experiments presented in this work and has been suggested for future work as a way to gather more information about the device<sup>9</sup>.

In setting up an equivalent circuit, we note that the gammavoltaic band structure in Figure 2.14 is structured such that it resembles two sets of Schottky junction photovoltaic cells, opposing one another and generating opposite and unequal photocurrents. If these can be represented by two opposing Schottky diodes, they may be joined by surface and bulk resistors between them as in Figure 2.2(a). In doing so the model could also apply to either of the band structures in Figure 2.13, so it is resistant to some degree to any flawed understanding that may have gone into the band structures containing hydrogen termination, but also cannot be used directly to differentiate between the band structure models. A possible exception to this might be the appearance of giant ideality factors linked to Frenkel-Poole conduction as mentioned above [217]. As the goal is to create a model which can be fit to data, it is apparent that the current sources in Figure 2.2 will be entirely covariate and therefore not available for individual extraction from an  $I$ - $V$  curve. Likewise, the surface and bulk resistors<sup>10</sup>. This leads to a simplified model as in Figure 2.2(b). Applying KCL to node A, we get the first of two equations for the total current: -

$$(2.22) \quad \begin{aligned} I &= I_{\text{Sh1}} - I_{\text{D1}}, \\ &= \frac{V_{\text{D1}}}{R_{\text{Sh1}}} - I_{01} \left( \exp \left( \frac{-V_{\text{D1}}}{n_1 V_T} \right) - 1 \right). \end{aligned}$$

Notably,  $V_{\text{D1}}$  is defined as being in the same direction as  $V$ , so its sign must be reversed in the exponential term. Applying KCL and KVL to node B gives the second equation for  $I$ , which is a similar equation to that for the conventional solar cell circuit, except  $V_{\text{D1}}$  must now also be taken into account when determining the voltage over the diode and shunt resistor: -

$$(2.23) \quad \begin{aligned} I &= I_{\text{D2}} + I_{\text{Sh2}} - I_{\text{Ph}} \\ &= I_{02} \left( \exp \left( \frac{V - IR_S - V_{\text{D1}}}{n_2 V_T} \right) - 1 \right) + \frac{V - IR_S - V_{\text{D1}}}{R_{\text{Sh2}}} - I_{\text{Ph}} \end{aligned}$$

Unlike the other parameters which may be approximated as constant with  $I$  and  $V$  for the purposes of a fitting a curve,  $V_{\text{D1}}$  changes substantially over the curve. It may be arbitrarily assumed

<sup>9</sup>Prof. J. Nelson, Imperial College London, private communication.

<sup>10</sup>An experiment may be conceived where different durations of surface treatment are used on the same cell to parse the surface and bulk resistances from one another, but this is left to future work.

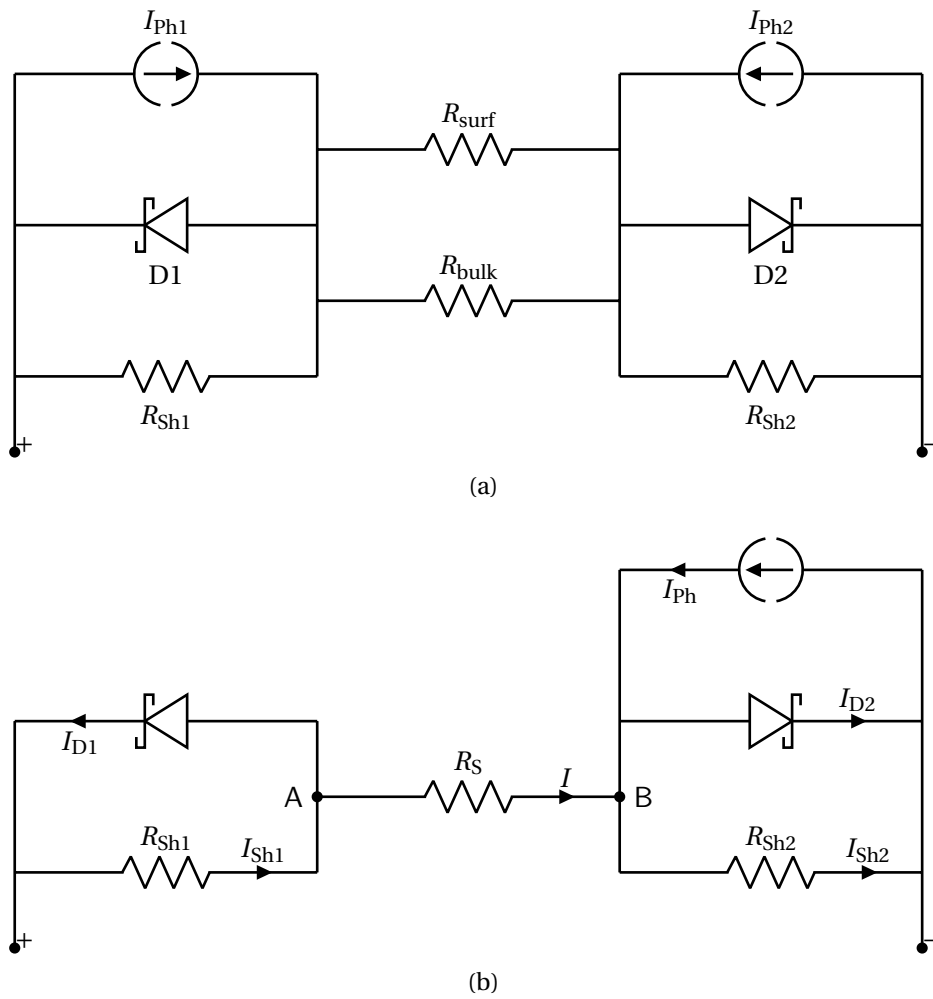


FIGURE 2.15. Equivalent circuits for the diamond gammavoltaic as two opposing Schottky junction solar cells, showing (a) a physical conceptualisation including current being generated at each contact and passing through both the bulk and surface, and (b) an alternative in which directly covariate parameters/circuit elements have been lumped to allow fitting. In (b), nodes A and B can be used to apply KCL and KVL.

that the negative side of the applied bias is at ground, in which case  $V_{D1}$  is very small for negative  $V$ , when diode 1 is forward-biased and so node A is at a similar voltage to the ground. It grows substantially when  $V$  is positive, and diode 1 is reverse biased, leading a voltage to develop over shunt resistor 1.  $V_{D1}$  would not make a good fitting parameter for this reason. However, the Lambert  $W$  function can be used to find an equation for  $V_{D1}$  that allows a single, implicit fitting function to be found, solely in terms of static fitting parameters. First, Equation 2.22 can be re-arranged into the pre-Lambert  $W$  form of Equation 2.17, with the coefficients

$$a = (I - I_{01})R_{Sh1}, \quad b = -I_{01}R_{Sh1}, \quad \text{and } c = \frac{-1}{n_1 V_T}.$$

Performing the Lambert  $W$  re-arrangement then gives

$$(2.24) \quad V_{D1} = (I - I_{01})R_{Sh1} + n_1 V_T W_0 \left[ \frac{I_{01} R_{Sh1}}{n_1 V_T} \exp \left( \frac{R_{Sh1} (I_{01} - I)}{n_1 V_T} \right) \right].$$

As previously, the choice of  $W_0$  is justified by the fact that the argument to  $W$  is constrained to be positive and the output is constrained to be real. Substituting Equation 2.24 into Equation 2.23 finally gives us the opposing-diodes model for a single cell,

$$(2.25) \quad I = I_{02} \left( \exp \left( \frac{V - IR_S - (I - I_{01})R_{Sh1} + n_1 V_T W_0 \left[ \frac{I_{01} R_{Sh1}}{n_1 V_T} \exp \left( \frac{R_{Sh1} (I_{01} - I)}{n_1 V_T} \right) \right]}{n_2 V_T} \right) - 1 \right) \\ + \frac{V - IR_S - (I - I_{01})R_{Sh1} + n_1 V_T W_0 \left[ \frac{I_{01} R_{Sh1}}{n_1 V_T} \exp \left( \frac{R_{Sh1} (I_{01} - I)}{n_1 V_T} \right) \right]}{R_{Sh2}} \\ - I_{Ph}.$$

Although it is implicit fitting of  $I$  that is used in this work, it is of note that there is an explicit equation for  $V$  which may be attained by subjecting Equation 2.25 to a further Lambert  $W$  transformation, this time with

$$a = (I + I_{02} + I_{Ph})R_{Sh2} + IR_S + V_{D1}, \quad b = -I_{01}R_{Sh2} \exp \left( \frac{-IR_S + V_{D1}}{n_2 V_T} \right), \quad \text{and } c = \frac{1}{n_2 V_T}.$$

This leads to

$$(2.26) \quad V = (I + I_{02} + I_{Ph})R_{Sh2} + (I - I_{01})R_{Sh1} + IR_S \\ + n_1 V_T W_0 \left[ \frac{I_{01} R_{Sh1}}{n_1 V_T} \exp \left( \frac{R_{Sh1} (I_{01} - I)}{n_1 V_T} \right) \right] \\ - n_2 V_T W_0 \left[ \frac{I_{02} R_{Sh2}}{n_2 V_T} \exp \left( \frac{R_{Sh2} (I + I_{02} + I_{Ph})}{n_2 V_T} \right) \right],$$

from which it may be discerned that there is an expression for the voltage over the second diode,  $V_{D2}$ , which is similar in form that that for  $V_{D1}$ ,

$$(2.27) \quad V_{D2} = (I + I_{02} + I_{Ph})R_{Sh2} + n_2 V_T W_0 \left[ \frac{I_{02} R_{Sh2}}{n_2 V_T} \exp \left( \frac{R_{Sh2} (I + I_{02} + I_{Ph})}{n_2 V_T} \right) \right].$$

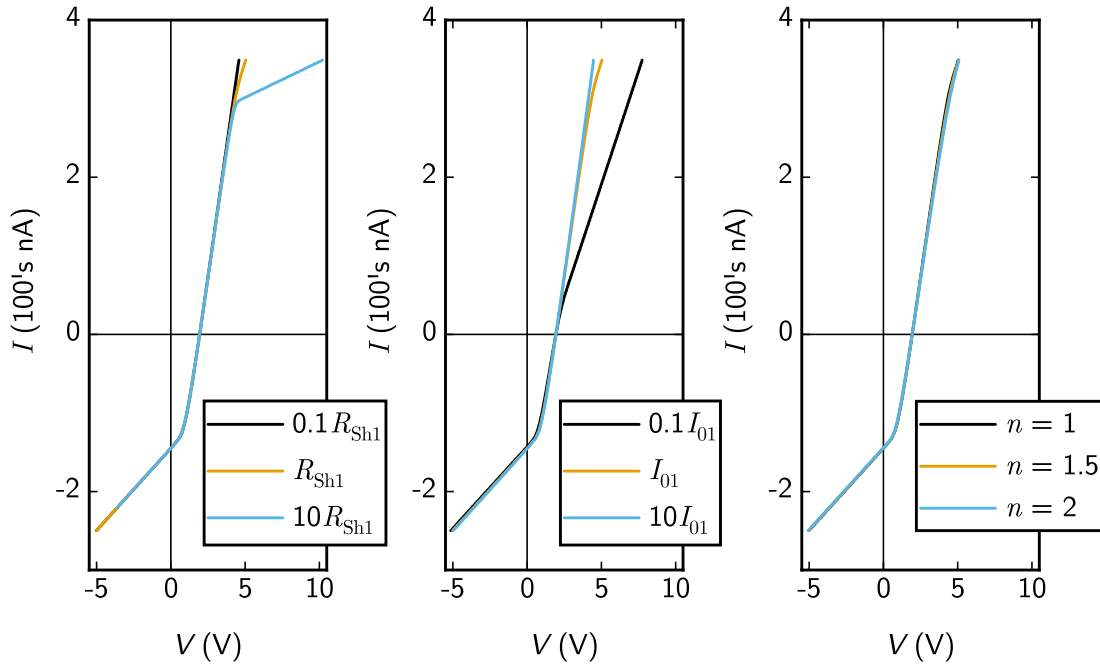


FIGURE 2.16.  $I$ - $V$  curves shows the affect of varying the additional parameters from the opposing-diodes model, and how the model deviates from the standard photovoltaic cell model with parasitic resistances.

Setting  $I = 0$  in this equation, or Equations 2.26 or 2.24, shows that under open-circuit conditions, the series resistor and diode 1, and by extension shunt resistor 1, are unbiased. Using some fit parameters from later in the work as an example, Figure 2.16 shows how  $I_{01}$ ,  $R_{Sh1}$  and  $n_1$  affect the shape of an  $I$ - $V$  curve. In the example given none of them change sufficiently to noticeably change the curve behaviour in the power-producing region, but this is possible and it also means that values for the original photovoltaic model parameters will be different for the same data.

When multiple cells are connected in series, then an initial attempt at apply KVL shows

$$(2.28) \quad V = \sum_{i=1}^M V_{D1,i} + IR_{S,i} + V_{D2,i},$$

where  $M$  is the number of cells and there is a correspondingly greater number of fitting parameters. The single-cell model already contains a relatively large number of fitting parameters, so including too many cells in series in the model runs the risk of allowing the number of fitting parameters to rise too high relative to the number of data in a given curve. So, it is both expedient and arguably necessary to treat each cell as identical. This approach, although often not reflective of reality, does allow the fitting procedure to generate an average value for each parameter, provided the curve

does not include features such as steps in the power-producing region which would indicate vastly different operating conditions or cell qualities between cells. In this case, Equation 2.28 simplifies to

$$(2.29) \quad V = M(V_{D1} + IR_S + V_{D2}),$$

and thus the only modification necessary to adapt Equation 2.25 to the series-cell case is to replace  $V$  with  $V/M$ . In terms of the equivalent circuit, the model can either contain  $M$  identical cells, or can contain a single cell with lumped parameters, such that any parameter  $\beta$ , for a single cell which is not a current, is set to  $\beta \rightarrow M\beta$ . This work has used the former convention, such that quoted parameter values are always for a single cell even if multiple cells were used.

## 2.3 Fitting and fit quality

The combination of model and experimental details in this work led to specific choices regarding fitting procedure and the assessment of fit quality. Namely, fitting was performed using implicit, bounded orthogonal distance regression with normalised instrumental weighting, and fit quality was assessed using the Kolmogorov-Smirnov test for residuals. Some detail will be given in this section on each. Where possible this will leave methodological details to be covered in Section 3.4, but it will be necessary to mention some here.

### 2.3.1 Orthogonal distance regression

The choice to use orthogonal distance regression (ODR) was due to the specifications of the multimeter, which entail that the relative uncertainty in the applied bias could have been of a similar size to that of the measured current. More common approaches to fitting assume that the latter is sufficiently small compared to the former that it may be safely disregarded. The algorithm used to perform ODR was first published in 1987 [202, 203], and updated to accept bounds on fitting parameters in 2006 [204, 231]. The following discussion will outline the theory presented in the papers and manuals associated with the algorithm.

#### 2.3.1.1 Background: ordinary least-squares regression

Most commonly, non-linear curve fitting is performed using explicit ordinary least squares (OLS) regression, which may be either unweighted, or weighted. Assuming a graph where the independent variable is on the abscissa and the dependent variable is on the ordinate, OLS seeks to minimise the sum of vertical distances between the data and the fitted curve. Mathematically, we assume that

$$(2.30) \quad y_i = f(x_i, \boldsymbol{\beta}^*) + \epsilon_i^*, \quad i = 1, \dots, N,$$

where  $(x_i, y_i)$  is a point from the data  $(\mathbf{x}, \mathbf{y})$  which is  $N$  points long;  $x_i$  has been used in place of the true value  $x_i^*$  because they are equal (there is no horizontal error);  $f$  is the model;  $\boldsymbol{\beta}^*$  is a vector of

true parameters; and  $\epsilon_i^*$  is a value from the true values of physical error,  $\epsilon^*$ . For example, in the case of an  $I$ - $V$  measurement of an ideal diode without a Faraday cage for very low voltages and currents, we would have  $\mathbf{x} = \mathbf{V}$ ,  $\mathbf{y} = \mathbf{I}$ ,  $f$  as the Shockley diode equation,  $\boldsymbol{\beta}^* = (I_0, n, V_T)$  where the latter take their true values, and  $\epsilon^*$  may be largely made up of electrical interference from other apparatus nearby. Fitting the curve by minimising the vertical distances therefore entails finding the values in  $\boldsymbol{\beta}$  which minimise the sum-of-squares parameter  $S$ , where the latter is defined as [202, 203]

$$(2.31) \quad S \equiv \sum_{i=1}^N \epsilon_i^2 = \sum_{i=1}^N (f(x_i, \boldsymbol{\beta}) - y_i)^2$$

Note that it was the logarithm of this quantity which was used in the projections of the fitting parameter spaces in Figures 2.8, 2.11 and 2.12. It is assumed that the values for  $\boldsymbol{\beta}$  which minimise  $S$  satisfy  $\boldsymbol{\beta} = \boldsymbol{\beta}^*$ . Thus, the output curve will reproduce the true values for the independent variable,  $\mathbf{y}^*$ , and the vertical distances between the output curve and the data will be  $\epsilon = \epsilon^*$ . The extent to which  $\epsilon = \epsilon^*$  is actually true upon minimisation of  $S$  is the basis for assessment of the fit quality in physical terms, discussed later.

When an attempt has been made to quantify the uncertainties  $\sigma_y$  in  $\mathbf{y}$ , this information may be used to give greater influence in the fit to those points which are believed to have greater certainty. This is known as instrumental weighting, where a weight for each point is defined as

$$(2.32) \quad w_i = \frac{1}{\sigma_{y,i}}.$$

Then, the definition for  $S$  becomes

$$(2.33) \quad S \equiv \sum_{i=1}^N w_i^2 \epsilon_i^2 = \sum_{i=1}^N w_i^2 (f(x_i, \boldsymbol{\beta}) - y_i)^2.$$

This expression may also be used to employ weighting methods other than instrumental weighting, notably such as setting some weights to zero if outliers are detected, or setting all weights to 1, in which case  $S$  reverts to its previous definition. Furthermore, the same minimisation result on  $S$  is produced if all weights are equal to each other as if all the weights are set to 1. In the example of the ideal diode measurement, weights might be calculated by taking multiple current measurements at each applied bias, and using the mean as  $y_i$  and the standard deviation as  $\sigma_{y,i}$ . Weighting would not be required if it were reasonable to assume the electrical interference did not change over the course of the  $I$ - $V$  measurement and the standard deviations were thus more or less the same for each point. If, however, it was believed certain points may have been compromised due to things such as passing colleagues knocking the bench, large equipment being turned on or off nearby, and so forth, then instrumental weighting could be used to lower the influence of these less certain measurements on the fit, and thus increase the chances of finding the true value of the curve and

$(I_0, n, V_T)$ <sup>11</sup>. Instrumental weighting may also suggest itself simply if the uncertainty margins on the data are visibly different when it is plotted with error bars, even if the reason for this is unknown.

Mathematically, adding bounds only entails writing that whichever version of  $S$  is used (Equation 2.31 or 2.33), the minimisation is subject to  $L_i \leq \beta_i \leq U_i$ ,  $i = 1, \dots, m$ , where  $m$  is the number of fitting parameters, and  $\mathbf{L}$  and  $\mathbf{U}$  are vectors containing the lower and upper bounds on each of the parameters. If the uncertainties are large enough or poorly estimated, or the parameters highly covariant, adding bounds can avoid the minimisation procedure finding minima which correspond to physically prohibited parameter values, such as  $n < 1$  in the diode example.

### 2.3.1.2 Uncertainty in both variables: the need for ODR

The move from OLS to ODR when there is sufficient uncertainties in  $\mathbf{x}$ , labelled  $\sigma_{\mathbf{x}}$ , that it cannot be assumed that  $\mathbf{x} = \mathbf{x}^*$ , but instead that

$$(2.34) \quad x_i = x_i^* + \delta_i^*, \quad i = 1, \dots, N,$$

where  $\boldsymbol{\delta}^*$  is a vector of true error values analogous to  $\boldsymbol{\epsilon}^*$ . Put another way, when seeking to measure the true values of a point  $(x^*, y^*)$ , we instead are measuring  $(x, y) = (x^* + \delta^*, y^* + \epsilon^*)$ . So instead of Equation 2.30, we have [204, p. 5][231]

$$(2.35) \quad y_i = f(x_i + \delta_i^*, \boldsymbol{\beta}^*) + \epsilon_i^*, \quad i = 1, \dots, N.$$

For fitting, rather than minimising the vertical distance between the fitting curve and the data, we now need to minimise a distance for each point which is at some unknown angle to the curve. A right-angle is chosen as an approximation, to allow the distance to be defined as

$$(2.36) \quad r_i = \sqrt{\epsilon_i^2 + \delta_i^2}, \quad i = 1, \dots, N.$$

This is the orthogonal distance for which ODR is named. Substituting for  $\epsilon_i$  from Equation 2.35, this leads to a definition for  $S$  in the unweighted case:

$$(2.37) \quad S \equiv \sum_{i=1}^N \epsilon_i^2 + \delta_i^2 = \sum_{i=1}^N (f(x_i + \delta_i, \boldsymbol{\beta}) - y_i)^2 + \delta_i^2,$$

which must be minimised by manipulating the values of both  $\boldsymbol{\beta}$  and  $\boldsymbol{\delta}$ . Indeed, it could in principle be viewed as equivalent to an OLS problem where the length of  $\boldsymbol{\beta}$  is  $m + N$ . However, actually treating it this way would lead to a very flexible model with a very large risk of over-fitting, not to mention a huge parameter space with a dimensionality that varied with the number of data. Weighting may be

<sup>11</sup>Of course in the circumstances described in the example it is much more likely that the measurement would simply be re-run with steps taken to prevent the re-occurrence of the unforeseen interference, it being preferable to take higher-quality data than post-process poorer data. However, there are situations when re-runs are not feasible or easy - controlled access to gamma irradiation sources and time on synchrotron beamlines being pertinent cases.

accomplished in a similar fashion to the OLS case, with weights for the abscissa,  $\mathbf{d}$ , now also being included, so that  $S$  becomes<sup>12</sup>

$$(2.38) \quad S \equiv \sum_{i=1}^N w_i^2 \epsilon_i^2 + d_i^2 \delta_i^2 = \sum_{i=1}^N w_i^2 (f(x_i + \delta_i, \boldsymbol{\beta}) - y_i)^2 + d_i^2 \delta_i^2.$$

The use of bounds is then the same as for OLS - specified bounds are not used for  $\delta$ .

Finally, although the concept of ODR for fitting implicit functions is the same as for explicit functions, the method is not. This is because if a function is implicit in  $y$ , it is also implicit in  $\epsilon$ , and thus the latter cannot be substituted out of the definition of the orthogonal distance. This means, in effect, that it must also be manipulated to minimise a final definition of  $S$ ,

$$(2.39) \quad S \equiv \sum_{i=1}^n w_i^2 (f(x_i + \delta_i, y_i + \epsilon_i, \boldsymbol{\beta}) - y_i)^2 + d_i^2 \delta_i^2.$$

It is this minimisation over  $\boldsymbol{\beta}$ ,  $\boldsymbol{\delta}$  and  $\boldsymbol{\epsilon}$  that was performed in this work by ODR to fit the opposing-diodes model, Equation 2.25. The bounded version of the algorithm, ODRPACK95 [204], was employed. Details of the implementation are given in the Methods section, Section 3.4.4.

### 2.3.2 Assessing the quality of a fit

Various methods of assessing the quality of a fit exist, with the choice between them depending on whether, if one is forced to choose, one is looking to most accurately reproduce data, or to extract physical values from a model with the most accuracy. For the reproduction of data, the best fit is the fit that minimises the difference between the fit curve and the data. This may in principle be done with an arbitrarily flexible model such as the polynomials mentioned previously as having been in use for analysing MiM diodes [225] - the model need have no physical underpinning. For the extraction of physical values from a model, the best fit is the one which (a) best reproduces the "true" parameter values, and which, as such, is (b) based on a model which is true enough for one's purposes. It will use only fitting parameters which have physical underpinnings and this parsimony may lead the best fit to nevertheless fail to completely reproduce the data. The reduced chi-squared statistic is often used to strike a balance between these two, but it is not suitable for the opposing-diodes model.

#### 2.3.2.1 The unsuitability of the reduced chi-squared statistic for the opposing-diodes model

Using the nomenclature established in the discussion of OLS and ODR, the (non-reduced) chi-square statistic is defined for OLS as

$$(2.40) \quad \chi^2 = \sum_{i=1}^N \left( \frac{\epsilon_i}{\sigma_{y,i}} \right)^2.$$

<sup>12</sup>The manner of stating this expression in Boggs *et al* [202] is slightly different to Equation 2.39, but the paper makes clear just below the problem statement that the expression is intended as equivalent to how it is expressed here.

If instrumental weights were used, the summands may also be expressed as  $(w_i \epsilon_i)^2$ , making it identical to the definition of  $S$  for weighted OLS. The reduced chi-squared statistic is then defined as

$$(2.41) \quad \chi_v^2 = \frac{\chi^2}{\nu},$$

where  $\nu$  is the degrees of freedom of the model. It is commonly held that  $\nu = N - m$ , that is, the number of data minus the number of fitting parameters, as this is the case for linear models with unbounded parameters. However, as was pointed out by Andrae, Schulze-Hartung and Melchior in 2010 [232], the concept of degrees of freedom cannot be so easily applied to bounded linear models or non-linear models, with non-linear models often subject to changes in degree of freedom depending on the values taken by the parameters. For comparison: a linear model  $y_i = \beta_1 x_i + \beta_2$ ,  $i = 1, \dots, N$  will always have  $N - 2$  degrees of freedom because  $\beta_1$  will always determine the gradient and  $\beta_2$  will always determine the ordinate intercept. On the other hand, the opposing-diodes model is actually designed to collapse into the conventional solar cell model when  $R_{Sh1} \rightarrow 0$ , so the ability of  $n_1$  and  $I_{01}$  to affect the shape of the curve will diminish as  $R_{Sh1}$  decreases. For this reason, and following the advice of Andrae, Schulze-Hartung and Melchior, an alternative method is used in this work: residual inspection with non-parametric testing.

### 2.3.2.2 Residual inspection and non-parametric testing

Whilst the opposing-diodes model is physically inspired, it is both complicated and involves a relatively large number of fitting parameters with non-trivial influences on one another. The ODR process stops when either of three conditions are met: parameter convergence, sum-of-squares convergence, or an iteration limit. As such, the combination of ODR with the opposing-diodes model is liable to over-fit data. Over-fitting is not necessarily all bad, as over-fit data will faithfully represent the device within its characterised voltage range if the equivalent circuit is used by an engineer. But, it reduces the physical reliability of the extracted parameters - insofar as they are physical themselves. With  $\chi_v^2$  not defined for the model, graphical inspection of the residuals is a less quantitative but potentially more instructive tool. It may be backed up - to some extent, and with caution - with quantitative results from non-parametric testing. Graphical inspection of residuals may be done with histograms. In the ideal case in which a true model is correctly fit to high-quality data, the histogram of instrumentally-weighted residuals will describe a normal distribution  $\mathcal{N}(0, 1)$ , that is to say having mean  $\mu_{we} = 0$  and variance  $\sigma_{we}^2 = 1$ . It is expected that for the ODR case, both the current and voltage instrumentally-weighted residuals should be normally distributed in this way, and it is easier and more instructive to analyse them separately than to apply the algebra of random variables and analyse the distribution of the instrumentally-weighted orthogonal residuals. Instrumentally-weighted residuals being perfectly normal with  $\mu_{we} = 0$  and  $\sigma_{we}^2 = 1$  in practise will not happen with  $I$ - $V$  curves of only  $N = 100$  to  $200$  points even if the model is physical and the fit is not an over-fit, but graphical inspection can quickly give qualitative information on how close to the ideal the fit is.

As we expect ODR to be liable to over-fitting, but perhaps to different degrees for different datasets, it is helpful to have some quantitative measure of how severe the departure from normality is. Non-parametric tests are useful for this, and the Kolmogorov-Smirnov (KS) test is used here. There are more powerful and generally more recommended alternatives such as the Anderson-Darling (AD) [233] and Shapiro-Wilk (SW) [234] tests, but the KS test is used here because it is powerful enough to confirm and compare cases of over-fitting (if the KS test detects a departure from normality, so will the AD and SW tests), and is comparatively simple. There being only limited utility in statistical analysis of the residuals of an over-fit equivalent circuit model which reproduces the data well, a balance has been struck in how far down the statistical path it is worthwhile to travel.

The Kolmogorov-Smirnov (KS) test <sup>13</sup> is a method of doing either of two things: (1) testing whether a sample of data are drawn from a specified distribution, or, (2) testing whether two samples of data are drawn from the same, unspecified, distribution. Using the OLS fitting as an example, the Kolmogorov-Smirnov statistic for testing scaled residuals of one sample (1S) of  $N$  data against a normal distribution is

$$(2.42) \quad {}^1S D_N = \sup_{w\epsilon} |F(w\epsilon) - \Phi(w\epsilon; \mu_{w\epsilon}, \sigma_{w\epsilon}^2)|,$$

where sup is the sumpremum function, indicating the choice of the lowest upper bound (in this context effectively the maximum) of its argument, and  $\Phi$  is the cumulative distribution function of a normal distribution  $\mathcal{N}(w\epsilon; \mu_{w\epsilon}, \sigma_{w\epsilon}^2)$  which is given by

$$(2.43) \quad \Phi(w\epsilon; \mu_{w\epsilon}, \sigma_{w\epsilon}^2) = \frac{1}{2} \left( 1 + \operatorname{erf} \left( w\epsilon - \frac{\mu_{w\epsilon}}{\sigma_{w\epsilon} \sqrt{2}} \right) \right).$$

$\Phi$  returns the probability that a value  $w_i \epsilon_i$  randomly chosen from that normal distribution will be less than  $w\epsilon$ .  $F$  is the empirical cumulative distribution function of the instrumentally-weighted residuals and returns an analogous value, but is defined directly from said residuals by first ordering them, and then for each  $w_i \epsilon_i$ , calculating how many scaled residuals with values less than that there actually are in the data. As such, it is a stepwise function with a number of steps equal to the number of data  $N$ .

When comparing two sets of  $N$  instrumentally-weighted residuals to ascertain whether they are from the same, unspecified distribution, the two-sample (2S) Kolmogorov-Smirnov statistic is defined similarly as

$$(2.44) \quad {}^2S D_N = \sup_{w\epsilon} |F_1(w\epsilon) - F_2(w\epsilon)|,$$

where  $F_1$  and  $F_2$  are the empirical cumulative density functions of the two sets of instrumentally-weighted residuals. The two cases are more clearly expressed graphically, as in Figure 2.17. The figure shows the empirical cumulative density functions of two sets of random numbers drawn from the same distribution  $\mathcal{N}(x, 0, 1)$ , and also shows  $\Phi(x, 0, 1)$ , to show how  ${}^1S D_N$  and  ${}^2S D_N$  are defined. In

<sup>13</sup>Original references: Kolmogorov [235], Smirnov [236]. For a discussion in English on testing for normality and why the KS test has been superseded, see the commentary by D'Agostino, Belanger and D'Agostino [237].

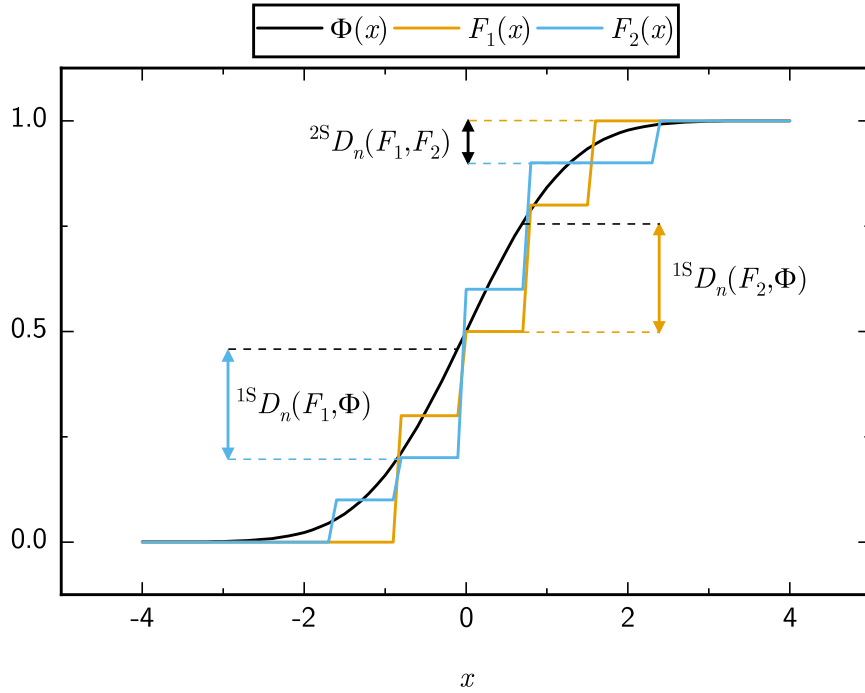


FIGURE 2.17. The cumulative density function  $\Phi$  for a normal distribution  $\mathcal{N}(0, 1)$ , with two empirical cumulative distribution functions  $F_1$  and  $F_2$  for two ten-value samples taken from the same distribution. The values of the test statistics  $1^S D_N$  for the one-sample KS test for both samples against  $\mathcal{N}$  are shown, as well as the two-sample KS test statistic  $2^S D_N$  of the two samples against each other.

short, the smaller the value of the KS statistic in either case, the more likely the empirical-/cumulative density functions were generated from the same distribution. Because the number of instrumentally-weighted residuals is finite, there must be some deviation from the perfect case of  $D_N = 0$ , and so the KS test produces a  $p$ -value like other statistical tests. The null hypothesis is that the residuals *are* drawn from either the specified distribution (in the one sample case) or from the same distribution (in the two sample case). A threshold,  $\alpha$ , is chosen for  $p$  to have statistical significance, such that if  $p < \alpha$  the null hypothesis is rejected. Commonly,  $\alpha = 0.05$  is used, being the threshold below which there is a less than a one-in-twenty chance of the data producing the KS test statistic as great as or greater than that it did, in the case that the null hypothesis is true. This is the value of  $\alpha$  used in this work. The use of  $p$ -values has itself come under some criticism [238], but it is here taken as generally safe to use a  $p$ -value if it falls clear enough of  $\alpha$  in either direction, as it should do for a substantial over-fit. The test cannot provide certainty in the other direction, so when  $p > \alpha$ , it is said that the test fails to give reason to reject the null hypothesis. When the  $p$ -value for  $\mu_{w\epsilon} = 0$  and  $\sigma_{w\epsilon}^2 = 1$  is substantially below  $\alpha$ , but higher than  $\alpha$  when  $\mu_{w\epsilon}$  and/or  $\sigma_{w\epsilon}^2$  take different values, this can also be

of interest, as it may suggest that there is something physical that may be salvaged from the fit. For example if only  $\sigma$  differs from the ideal value, this may suggest that the estimates for the measurement uncertainty are the wrong size but that the model is otherwise correct. If  $\mu$  deviates, then there is a chance that the fit has fallen into a false minimum and that a better fit may be found with an offset on the axis to which the residuals pertain. The secondary use the KS test may be put to in fitting is to determine whether two fits have converged in a similar way, if their instrumentally-weighted residuals are not distributed normally but the test has failed to reject the hypothesis that the two sets of residuals are drawn from the same distribution. In a parameter fitting space with one or more local minima in addition to the global minimum, this may give information on whether the fitting procedure has ended in analogous minima between fits. The method of calculation of a  $p$ -value from a KS test statistic depends on whether the test is for one sample or two, and in the case of one sample, whether  $\mu$  and  $\sigma$  have been specified *a priori*, or have been estimated *a posteriori* from the data themselves. The reason for this latter point is that by estimating  $\mu$  and  $\sigma$  from the data, the normal distribution to test against has been made artificially more similar to the data being tested. Thus were  $p$ -values to be calculated in the same way as when  $\mu$  and  $\sigma$  are specified, they would be more prone to falsely suggesting normality. In a one sample test where  $\mu$  and  $\sigma$  have been specified, or in a two-sample test,

$$(2.45) \quad p \approx 2 \sum_{k=1}^{\infty} (-1)^{k-1} \exp(-2k^2 D_N^2 N),$$

provided  $N$  is large enough (the  $I$ - $V$  curves to which the KS test is applied in this work provides large enough  $N$ ). For a one-sample test where  $\mu$  and  $\sigma$  are estimated, there is no convenient analytical solution that covers all possible values of  $p$ , but Monte Carlo methods have been used to generate corrections. The correction for this case is known as the Lilliefors correction [239]. The implementation of the Lilliefors correction used in this work is based on fourth-order polynomials and is detailed in Section 3.4.3.



## EXPERIMENTAL AND COMPUTATIONAL METHODS

This chapter explains the methods used in this work. The techniques used to fabricate DGV cells, and from there DGV devices, are first covered. Because the rationale and much of the theory of the DGV design was laid out in the previous chapters, the material in this chapter is restricted to the specifics of the fabrication methods. Following that, a section is devoted to the basic principles of x-ray photoelectron spectroscopy and the specifics of its use in this work. A section is then given to methods by which devices were electrically tested under irradiation, and the methods used for that irradiation. Because these methods most closely match experiments on gammavoltaics in the literature, particular emphasis is placed on how these methods do (or do not) contribute to knowledge about the factors of **comparability**, **accountability**, **capability**, **applicability**, and **longevity**, which were highlighted in the first chapter as being of particular concern for gammavoltaic research. Finally, computational methods are discussed. These are the methods by which simulations were constructed to compare to experiment, results were analysed, and various other miscellaneous project tasks were accomplished.

### 3.1 Cell and device fabrication

In common with standard leakage-mode detectors, and Dr. Hutson's dosimeter, the core of each gammavoltaic cell was an electronic-grade, single crystal diamond, with dimensions  $4.5 \times 4.5 \times 0.5\text{mm}$  (i.e. a surface area of  $0.205\text{ cm}^2$ ). "Electronic grade" is a diamond industry term indicating the high purities needed for radiation detectors, quantum optics experiments, and other electronic uses. In this case, the electronic grade specification referred to B impurities less than 1 ppb and N impurities less than 5 ppb equivalent to  $\sim 10^{14}\text{ cm}^{-3}$  [240]. These diamonds were purchased from Element Six Ltd of Oxfordshire, UK (product code: 145-500-0390). The crystal orientation was [100]. The diamond was washed for 2 h in aqua regia at  $65\text{ }^\circ\text{C}$ , to remove any environmental contaminants and metal

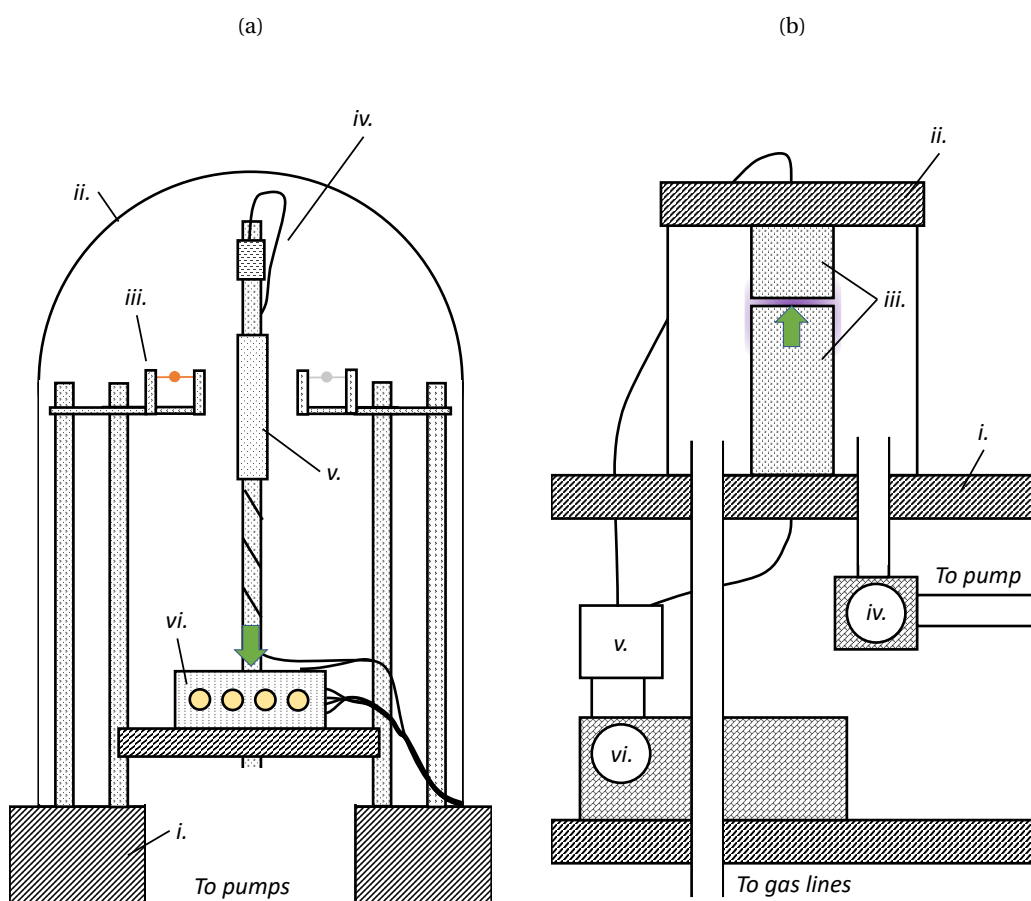


FIGURE 3.1. Schematics of the equipment used to fabricate a DGV cell. **(a)** The thermal evaporator, showing *i.* the bell jar and chamber base, *ii.* the bell jar, *iii.* the dual metal filaments and their electrode posts, *iv.* the quartz crystal microbalance, *v.* the contamination shield between the two sources, and *vi.* the heating stage and thermocouple. **(b)** shows the Terminator, including *i.* the base housing, *ii.* the electrode and chamber top, *iii.* the electrodes within the chamber, *iv.* the manual pump valve used to fix chamber pressure, *v.* the timer switch, and *vi.* the variac-style voltage control and supply. In each sub-figure, green arrows show where the sample is placed.

residues from prior use. This process was also used as an under-contact oxygen termination step, in line with established method [195].  $3.5 \times 3.5$  mm contacts, centrally located on opposing faces, were deposited. Both the nichrome and aluminium were capped with gold under the same vacuum, to avoid oxidation. Metals were deposited using resistive thermal evaporation, through shadow masks, in an Edwards 306 Thermal Evaporator. The base pressure was  $\sim 6 \times 10^{-6}$  mbar, and substrates were heated to  $250$  °C during deposition and for one hour beforehand. Using a modified sputter coater (the "Terminator"), a DC oxygen plasma was struck at  $\sim 3$  kV and 1 Torr for 30 s, to further clean the device. Schematic diagrams of the evaporator and Terminator are shown in Figure 3.1. These were all the steps necessary to create a fully oxygen-terminated device. For partial hydrogen termination, the chamber was then re-pumped and then a hydrogen plasma struck using the same voltage, and duration. Whether using hydrogen or oxygen, the gas flow into the coater system chamber was 10 sccm. The standard method of producing a hydrogen termination on diamond is to treat a substrate to a microwave-enhanced hydrogen plasma. This was not suitable for this application due to the need for the contacts to be deposited prior to termination; the conditions of a microwave plasma are too harsh for metal contacts, which will anneal and laterally diffuse. To assess the actual hydrogen coverage attained by the coater system, x-ray photoelectron spectroscopy was employed, as discussed in Section 3.2. Three cells were fabricated in this way, labeled samples E6\_ELSC\_2, E6\_ELSC\_3 and E6\_ELSC\_5. One or more cells were mounted on an altered subminiature version A (SMA) connector head to create a device, with the central pin connected to the low-barrier contact and the high-barrier contact being connected to the external housing of the SMA pin with silver epoxy paint and a twisted set of copper wires. A single-celled DGV device made in this fashion is rendered in Figure 3.2.

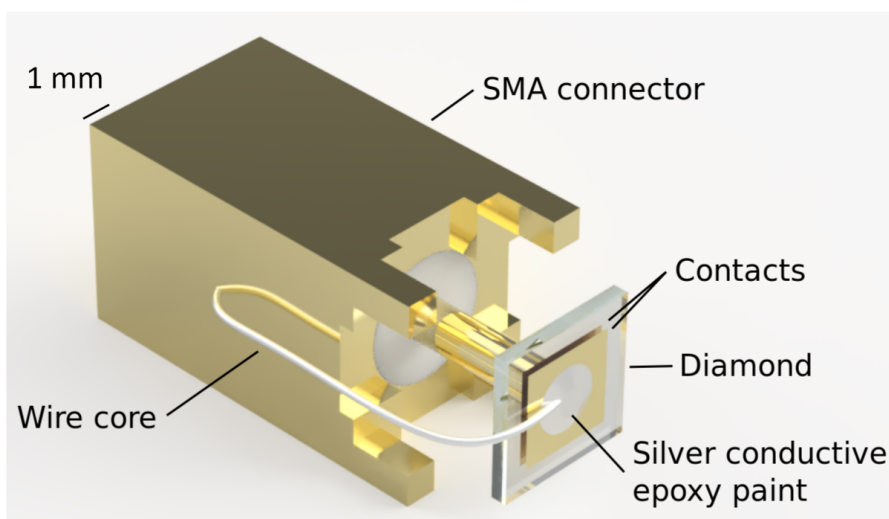


FIGURE 3.2. A render of a single-celled DGV device.

## 3.2 X-ray photoelectron spectroscopy for termination stoichiometry

X-ray photoelectron spectroscopy (XPS) was used to estimate the surface coverage of hydrogen achieved by the coater system during a standard cell fabrication. In this section, a brief and basic overview of XPS as a technique will be given, followed by specific details of the XPS equipment and process used to estimate coverage.

### 3.2.1 Basic principles of XPS

Photoelectron spectroscopy, of which XPS is one type, is an analytical technique widely used for its ability to assess both the atomic composition of the near-surface region of a sample and its adsorbates, and the chemical states of the atoms present [241]. Fundamental to it is the photoelectric effect of Einstein, whereby [56]

$$(3.1) \quad T_e = h\nu - E_b^{\text{vac}},$$

where  $h$  is Planck's constant,  $\nu$  is the frequency of an incident photon,  $E_b^{\text{vac}}$  is the vacuum binding energy of an electron prior to the impact of the photon, and  $T_e$  is the kinetic energy of that electron (the photoelectron) once it has been liberated by the impact of the photon. It is the measurement of  $T_e$  that is the goal of photoelectron spectroscopy. There is an energy cost for the escape of the photoelectron, even from atoms at the very surface of a sample, due to electrostatic force. Likewise, the spectrometer used to measure the kinetic energy of the photoelectron will have an associated work function. This means that in practice, for measurements [242],

$$(3.2) \quad T'_e = h\nu - \phi_{\text{spec}} - E_b^{\text{f}},$$

where  $T'_e$  is the kinetic energy of the photoelectron as actually measured,  $\phi_{\text{spec}}$  is the work function of the spectrometer, and  $E_b^{\text{f}}$  is the binding energy of the electron relative to the Fermi energy of the sample. There are a wide range of techniques that employ this basic principle to different ends, with the classic distinction being between the two techniques of ultraviolet photoelectron spectroscopy (UPS) and XPS [243]. The range of x-ray energies used in XPS is such that core electron energies may be probed [244]. These energies are unique to a given atom species, and may be shifted by the chemical binding the atom is subject to [244], hence the analytical capabilities of XPS for quantifying the elements present at a surface and also determining their binding states.

To measure the kinetic energies of photoelectrons, they are commonly passed through a slit, and then through a magnetic field, before hitting a detector. The slit creates a beam of photoelectrons, which the magnetic field then spreads out: photoelectrons with greater kinetic energy have their trajectories bent less by the field [245].

XPS measurements may be performed in two different modes, which are often used in tandem. Full survey measurements scan the entire energy range of the spectrometer, at a reasonable resolution but not so high as to render the scan time unworkable. Such a survey will show several or many peaks,

and can be used to identify the approximate elemental composition of the near-surface region and its adsorbates. Once this is achieved, one or more peak scans can be performed. These focus on an individual peak or peak region (where two or more peaks overlap) and are performed at much higher resolution. Peak scans can be used to determine chemical information, as the shape, width and precise position of an elemental peak is related to the chemical bonding of that element in the sample. There are two particular difficulties with performing XPS measurements which require mentioning, one specific to carbon-based samples such as diamonds, and one a generally-reported problem in the field.

The first problem is to do with techniques used to account for sample charging using the C 1s peak of adventitious carbon. Samples which are not fully-fledged conductors, and in particular strong insulators, will charge when photoelectrons are removed by the measurement process. Charging gradually leads to distortions of the measurement itself due to the increasing attractive force the substrate exerts on liberated photoelectrons [246]. To account for this effect, and others with similar results, experimentalists often make use of charge referencing [247]. Charge referencing is the procedure by which a peak is chosen for its known location in near-ideal situations, and its measured location is then used to establish the energy offset in all other peaks. Because carbon-containing compounds ("adventitious carbon") adsorb on all surfaces exposed to air [248], the C 1s peak from these compounds is a widely-used charge reference, although doubts have been raised about some aspects of the process [249]. For diamond, a material made entirely of carbon, the issue is obvious: the surface atoms themselves, and their peak shifts due to chemical bonding, produce signals in the same region as the adventitious carbon signal. XPS measurements of diamond must therefore use a less common charge reference, or must be restricted to conducting diamond films. This second approach has been used in this work.

The second problem is with analysing chemical information from XPS data. The curve-fitting by which backgrounds and peaks are fitted to XPS data is among the more challenging class of data analysis procedures: the class by which a correct-seeming result is relatively simple to achieve, whilst an actually-correct result is far harder. Because any peak-like data may be fitted to arbitrary precision if one allows oneself an arbitrary number of peaks [250], caution has been called for among XPS specialists when fitting data [250, 251]. This work employs an intellectually conservative approach to XPS data analysis.

### **3.2.2 Experimental procedure**

XPS was used to estimate the hydrogen monolayer coverage attained using the coater system. Hydrogen cannot be detected directly by XPS in a normal laboratory [244], due to the low interaction cross-section of hydrogen for x-rays, which necessitates the high flux capability of synchrotron XPS [252]. Despite the use of two synchrotrons in this work, synchrotron XPS was not practicable due to the need for a quantification standard, which meant the need for multiple re-terminations of a sample. As such, hydrogen coverage was inferred from the oxygen-to-carbon ratio on an initially

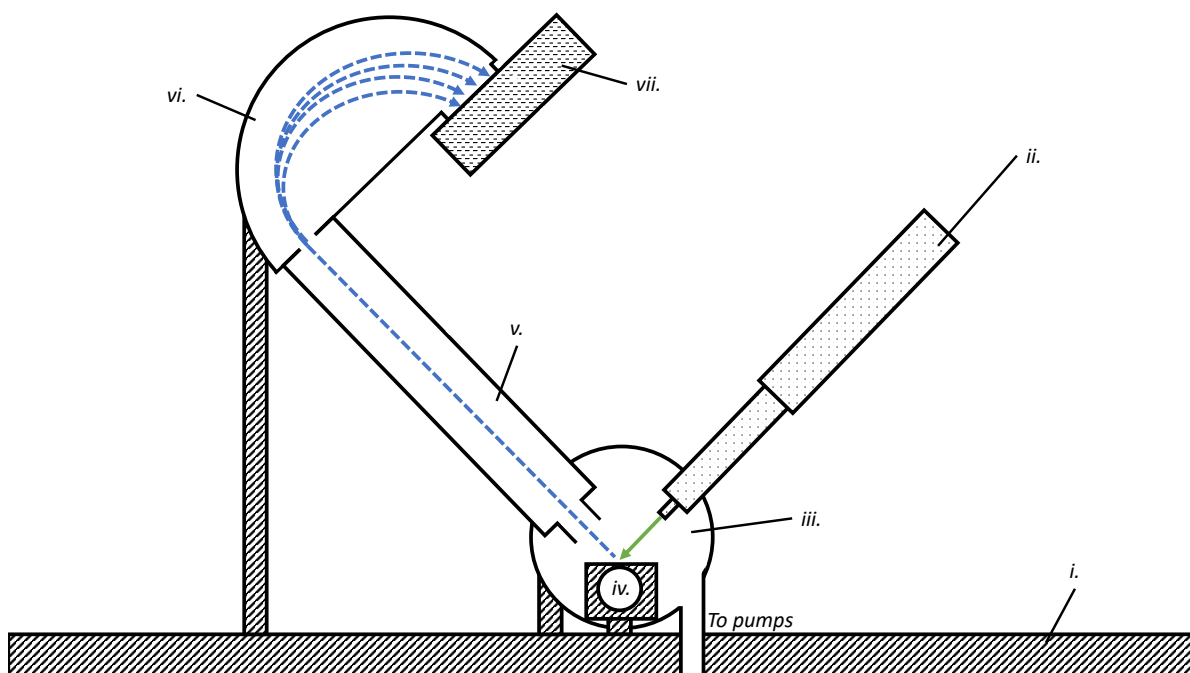


FIGURE 3.3. A schematic of the XPS section of the NanoESCA II, showing *i.* the inertial base, on a concrete cube floated on an air cushion, *ii.* the x-ray gun, *iii.* the main chamber, *iv.* the sample manipulator and stage, *v.* the electron collimator (in reality full of electron optics), *vi.* the hemispherical analyser, separating the electrons out by energy, and *vii.* the detector, converting hit position to energy.

hydrogen-terminated surface, as the oxygen coverage was incremented towards saturation. The saturation of the oxygen to carbon ratio was taken to indicate a total oxygen monolayer coverage, and the hydrogen coverage calibrated from this. A DGV was not used for XPS measurements, due to the small surface area presented around the contacts and the insulating nature of the crystal. Instead, the sample used was a [100] diamond used by Wan *et al* for a similar calibration [168], with a conductive boron-doped top layer that prevented charging. Because this sample was single crystal and the same orientation as the crystals used for the DGV cells, and the boron doping still made up a very small portion of the surface atoms, this sample was considered a suitable stand-in for a DGV for XPS purposes. XPS was performed in a Scienta Omicron NanoESCA II [253, 254] at the Bristol Ultra Quiet NanoESCA Laboratory (BrUNEL) [255], using a monochromatic Al  $k\alpha$  source (1486.7 eV) and a 45° analyser angle. The use of monochromatic x-rays was important to prevent degradation of the hydrogen-terminated surface regions during the scan, which is known to happen particularly when a diamond is heated in vacuum [256], as would occur under a non-monochromatic source [257]. A schematic of the XPS portion of the NanoESCA is shown in Figure 3.3. Both peak and survey scans were performed. For peak O 1s and C 1s scans, a pass energy of 20 eV was used, and the overall energy resolution was 600 meV. For the full survey scan, a pass energy of 50 eV was used. The sample

was initially fully hydrogen terminated using a microwave plasma. After the spectra were taken for the sample in this state, as a baseline, the sample surface was oxygen-terminated in 1 s increments in the Terminator. XPS analysis was interleaved with the termination. Termination continued until the raw O:C peak area ratio in the XPS spectra saturated. The sample was then subjected to the partial hydrogenation recipe used for the DGV, including a de-ionised water rinse and an initial 30 s oxygen plasma treatment. The survey scan was then used to find peak areas for relevant regions, to calculate a contaminant-controlled O:C peak area ratio and estimate the partial hydrogen coverage for the DGV. The results of this experiment are discussed in Section 4.1.

### 3.3 Irradiation and electrical methods

A variety of irradiation methods were employed in this work, each with complementary strengths and weaknesses. In each case, the method by which the electrical properties and performance of the device were analysed was by taking the current-voltage characteristic curves ( $I$ - $V$  curves), whether that be curves taken for changing photon energy or flux. This section will first discuss  $I$ - $V$  curves in more detail, before describing the various irradiation methods used. Because of the difficulty of comparing between irradiation methods, mentioned in Section 1.5, Table 3.1 makes explicit what information was known and not known for each method.

Irradiation method	Activity	Flux	Absorbed dose	Air KERMA dose
XRT	N/A	Y	N	N
SP8	N/A	Y	Y	N
DLS	N/A	Y	Y	N
Co-60	Y	N	N	Y
Cs-137	Y	N	N	Y

TABLE 3.1. Comparison of quantities known for the various irradiation methods.

#### 3.3.1 X-ray tomography microscope

A Zeiss Xradia Versa 520 x-ray tomography microscope (XRT), a schematic of which is shown in Figure 3.4, was used to test the difference between operation with an unterminated and partially terminated surface. For these tests, the x-ray source was set to 160 kV accelerating voltage and 9 W power. The characteristic emission lines of tungsten, the x-ray source material, in this range are  $K\alpha_2 \approx 58.0$  keV and  $K\alpha_1 \approx 59.3$  keV [258]. The predominant benefits of using the XRT were convenience and power. Being a fully-interlocked instrument in a group-owned lab, the XRT presented few of the administrative hurdles associated with the other irradiation techniques, and allowed a quick method of testing the basic concept of the presented cell design. That is to say, of the factors mentioned in the Introduction, the XRT was used predominantly to test **capability** and **accountability**, by flooding

a cell with a high flux of mostly soft x-rays, for high energy deposition. Photon flux could, in principle, be estimated from the source current. However, as the energy spectrum of the source is not known by the manufacturer except in a qualitative sense, there was not much that could be gained by knowing the photon flux other than to be confident it was quite high. By extension, the dose and dose rate, both in terms of air KERMA dose and absorbed dose, were unknown for the XRT experiment. As such the XRT could not be used for tests of **applicability** or **longevity**.

Because the cell design presented here is novel, the XRT was used to check that introducing surface hydrogen to a diamond crystal with dis-similar contacts would indeed turn it into a functioning gammavoltaic device. A cell was fabricated up to the point before hydrogen termination and then irradiated in the XRT whilst an  $I$ - $V$  curve was taken. It was then terminated with hydrogen, and irradiated again whilst another  $I$ - $V$  curve was taken.  $I$ - $V$  curves were taken in air, with a Keithley 6517A multimeter both applying the bias and measuring the current. The bias was increased in increments of 0.05 V. The bias ranges used were -50 to 50 V for both dark measurements, -0.1 to 0.55 V for the illuminated unterminated measurement, and -0.5 to 1 V for the illuminated partially terminated measurement. 10 measurements were taken per increment. A 0.1 s dwell time was employed at the start of each increment to allow capacitive effects to settle. The results of this experiment are discussed in Section 4.2.

### 3.3.2 Synchrotrons

Synchrotron irradiation experiments can be thought of as the "big science" equivalent of the in-house XRT irradiation. The emphasis of the synchrotron irradiation experiments in this work was still on the factors of **capability** and **accountability**, but some progress into **applicability** and **longevity**

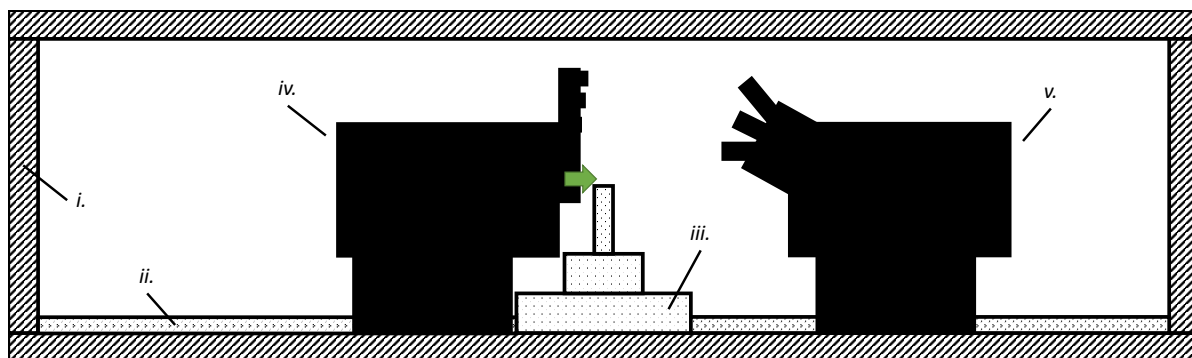


FIGURE 3.4. A schematic of the XRT, showing *i.* the interlocked chamber shielding, *ii.* the runners on which the x-ray gun and detector could be moved, *iii.* the sample clip and actuator stack, capable of linear motion in three dimensions and horizontal rotation, *iv.* the x-ray gun and filter selection (the source was left unfiltered in this work), and *v.* the detector and focal selector, not used. The green arrow shows the device mounting position.

could also be made. The primary focus of the synchrotron irradiation experiments was to probe **accountability**, as the high brightness, known energy, and estimable flux allowed a greater degree of comparison to simulation than the other irradiation methods. Dose and dose rate were not immediately known quantities in the synchrotron experiments, but unlike in the case of the XRT, absorbed dose could be estimated by comparison with a GEANT4 model, provided that model were accurate. Validating the model was the basis of one of the experiments. Dose and dose rate in terms of air KERMA remained unknown. Two synchrotrons were used: the SPring-8 synchrotron and the Diamond Light Source synchrotron.

### 3.3.2.1 The SPring-8 Synchrotron

SPring-8 (SP8) houses what is, at time of writing, the world's most powerful synchrotron, at the Harima Science Park City of Hyogo Prefecture, Japan [259].  $I$ - $V$  curves were taken in air, using a Keithley 2400 Source-Measure Unit (SMU). The SMU was configured to take 100 measurements between -1 and 1 V, with one measurement taken per bias step<sup>1</sup>. Irradiation was performed with quasi-monochromatic x-rays at 182.6 keV, at the BL08W beamline over a 24 h period. The flux was estimated at approximately  $1.5 \times 10^{10} \text{ } \gamma \cdot \text{s}^{-1}$  using a measurement with an air-filled ion chamber. The SP8 experiment was a photoresponse mapping experiment, very similar to those used for conventional photovoltaics, at least in concept [78]. The beam was constrained to a  $1 \times 1 \text{ mm}^2$  square cross section, and moved around the presented surface of a single-celled DGV, with an  $I$ - $V$  curve being taken at each position. This was an **accountability** experiment, in that it sought to tie the photoresponse map directly to a GEANT4 simulation of energy deposition. By keeping photon energy and flux constant, it was hoped that relevant physics would be kept to that which GEANT4 is designed for, rather than risking the involvement of device physics. By testing the GEANT4 model in this way, the aim was to support the model's validity in other experiments where factors such as photon energy and flux were changed. The criterion for validating the model was chosen such that the model was considered valid if there was a linear relationship between simulated energy deposited, and measured current extracted at a given voltage. The  $I_{\text{SC}}$  was chosen for convenience. Sample positioning within the beam was performed using a stage with micromanipulator screws, with the edge of the sample being located by the lack of device response when the beam was positioned beyond the edge. The mapping was performed over two perpendicular lines, in 0.5 mm steps. The results of this experiment are discussed in Section 5.2.

### 3.3.2.2 The Diamond Light Source synchrotron

The Diamond Light Source (DLS) is the national synchrotron facility of the UK, located at the Harwell Science and Innovation Campus in Oxfordshire [261].  $I$ - $V$  curves were taken in air, using

<sup>1</sup>This electrical test setup was different from that used for other irradiation experiments. This was due to the fact that the experiment was kindly carried out remotely, by SP8 staff using locally available equipment, under the COVID-19 remote participation regime in place at the time [260].

monochromatic x-rays, over two 8-hour shifts on the I12 beamline [262]. The synchrotron beam current was 250 mA, rather than the 300 mA which is normal for the facility. The beamline does not operate in the energy regime of prominent waste isotopes such as Cs-137 or Co-60, but can provide very precise energies between around 50-150 keV. This range is of interest, as it covers several gamma emission energies, most prominently Am-241 [47, 48] and a significant portion of the U-235\* fission delayed-gamma spectrum [49], and in that sense allowed an **applicability** assessment. However, this range is equally of interest because it is the region over which photon-electron interactions transition from photoelectric (PE) dominant to Compton scattering (CS) dominant [263]. This was the primary focus of the experiment - an **accountability** experiment - which was undertaken to better understand the effect of the photon interaction mechanism on the electrical properties of a single-celled DGV. 12 photon energies were used between 50 - 150 keV. Before exposing the cell to each incident wavelength, the energy of the beam was measured with the monochromator crystals unbent, using x-ray diffraction from a NIST Standard Reference Material® 674b CeO<sub>2</sub> powder sample. The photon flux of the beam at each photon energy employed is shown in Figure 3.5. The beamline has controllable flux; however, this is achieved through aperture size. Because it was desirable to keep the irradiated surface area constant, the flux was allowed to vary with the energy.

### 3.3.3 Co-60 Irradiation Cell

Co-60 irradiation was performed at a location containing several cells, holding sources of varying strengths, externally shielded by their subterranean installation and internally shielded by lead bricks and chicane architecture. The cells are room-sized, with four individually-retractable and interlocked Co-60 sources. The size of the cells permit a wide range of dose-rates to be achieved geometrically, without shielding, and thus without the complications arising from in-beam inelastic scattering. That is to say, all of those gamma rays incident on samples in the cell are of 1.17 MeV and 1.34 MeV, the emission energies of Co-60 [51], except a very small fraction scattered by the copper pipes into which the sources are fed. A schematic diagram of the region of the cell containing the sources can be found in Figure 3.6. Dosimetry located the maximum possible dose rate in the cell as 2,900 Gy/h air KERMA, when the dosimeter was placed directly above the middle of the four sources. At the time, the four sources comprised of two 6.4 TBq sources and two 7 TBq sources, for a total of 26.8 TBq. The minimum achievable dose rate was below the 1 Gy/h air KERMA threshold of the dosimeter, which occurred just over 1 m from the centre of the sources. Thus, *I-V* curves could be taken at dose rates reliably measured over three orders of magnitude. In addition, because the four sources were individually retractable, fifteen distinct dose rates were possible at each irradiation position via permutation (neglecting the OUT/OUT/OUT/OUT source permutation, which of course gave no dose). In practice, the sources were of sufficiently similar activity and location that fewer permutations were used. This capability allowed consistent measurements to be taken that avoided positioning errors between the dosimeter and the diamond gammadivoltaic. This uncertainty became important at higher dose rates, where the irradiation position was closer to the sources, as dose rate decay is geometric. The

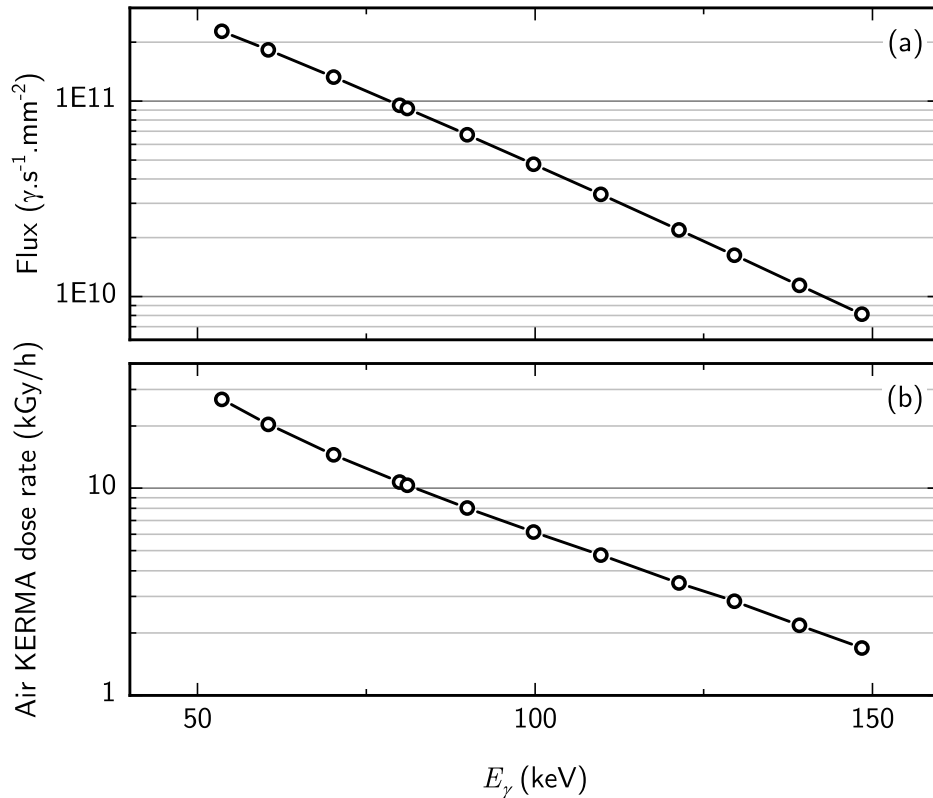


FIGURE 3.5. **(a)** The DLS synchrotron flux, calculated for the incident photon energies used when taking  $I$ - $V$  curves for the DGV, and **(b)** the resultant air KERMA dose rate, as calculated using the approximation in Reference [264].

experiment primarily concerned **comparability**, as Co-60 is among the better-represented sources used for gammavoltaic research in the literature. However, as Co-60 is often used as a stand-in for Cs-137, for which there appear to be many fewer irradiation facilities, the Co-60 irradiation also acted as an **applicability** test for the wide range of dose rates employed - analogous to the position a DGV could occupy in a waste store - and also of **accountability**, as Co-60 results could be combined with Cs-137 results (see Section 3.3.4) for comparison with a GEANT4 model that assessed both cases. For the Co-60 experiments, air KERMA dose rate was known, and total air KERMA dose would have been measurable but was not used, due to the short duration of the experiment. Photon energy was known but flux was not, and as such, absorbed dose and dose rate, which was not known by other means, was not calculable with a simulation. A phenomenological conversion equation between air KERMA and flux does exist [264], but it assumes photons are incident through a single surface, which seemed a valid approximation for the synchrotron experiments (flux to air KERMA), but not for the isotope irradiation experiments (air KERMA to flux). Quantitative comparison to simulation was therefore not possible for the Co-60 energy alone. However, the difference between Co-60 and Cs-137 cases

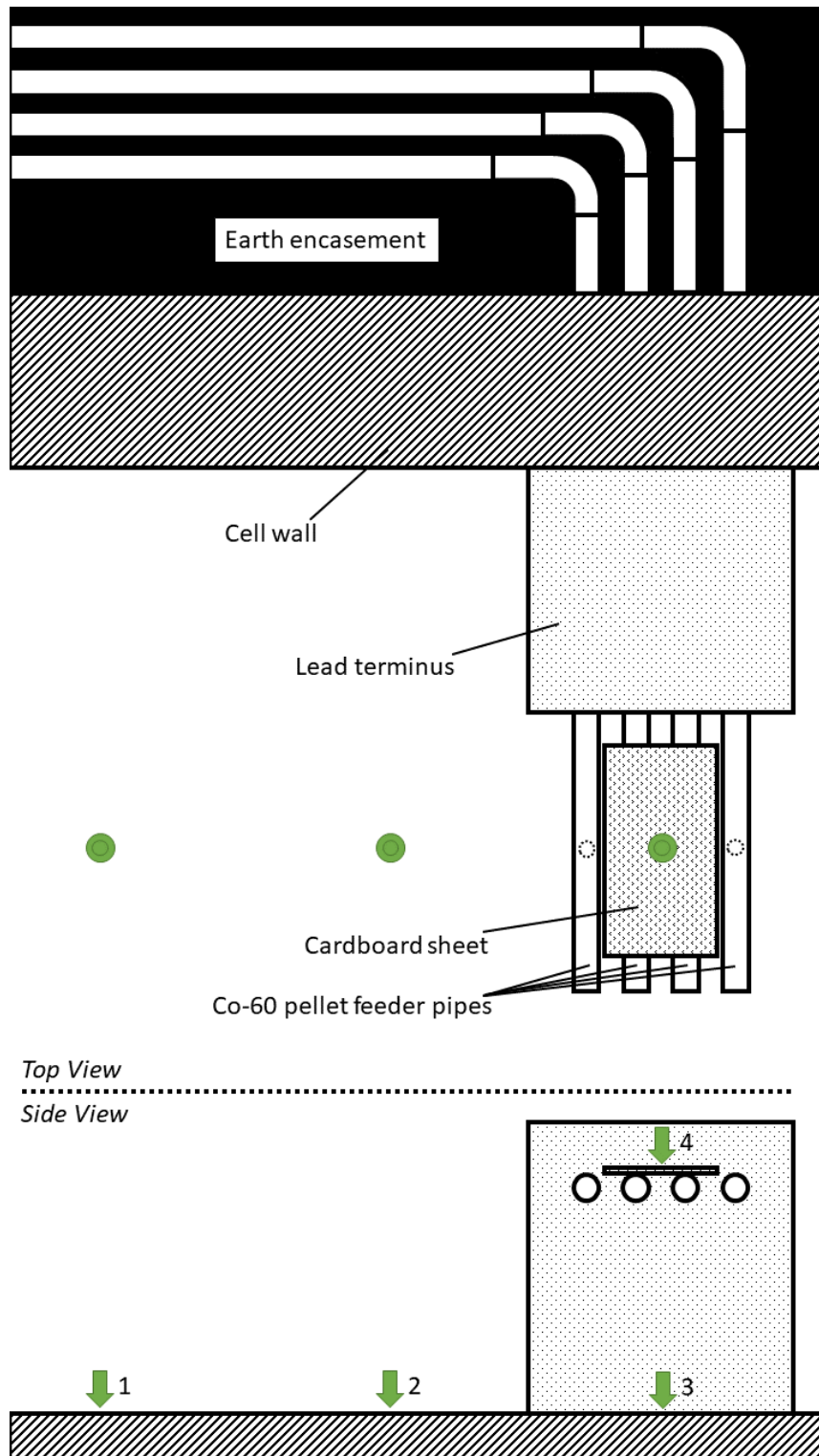


FIGURE 3.6. A schematic diagram of the Co-60 irradiation cell, not to scale. Green arrows correspond to positions at which the dosimetry and gammavoltaic  $I$ - $V$  measurements were made. Dotted circles show source positions.

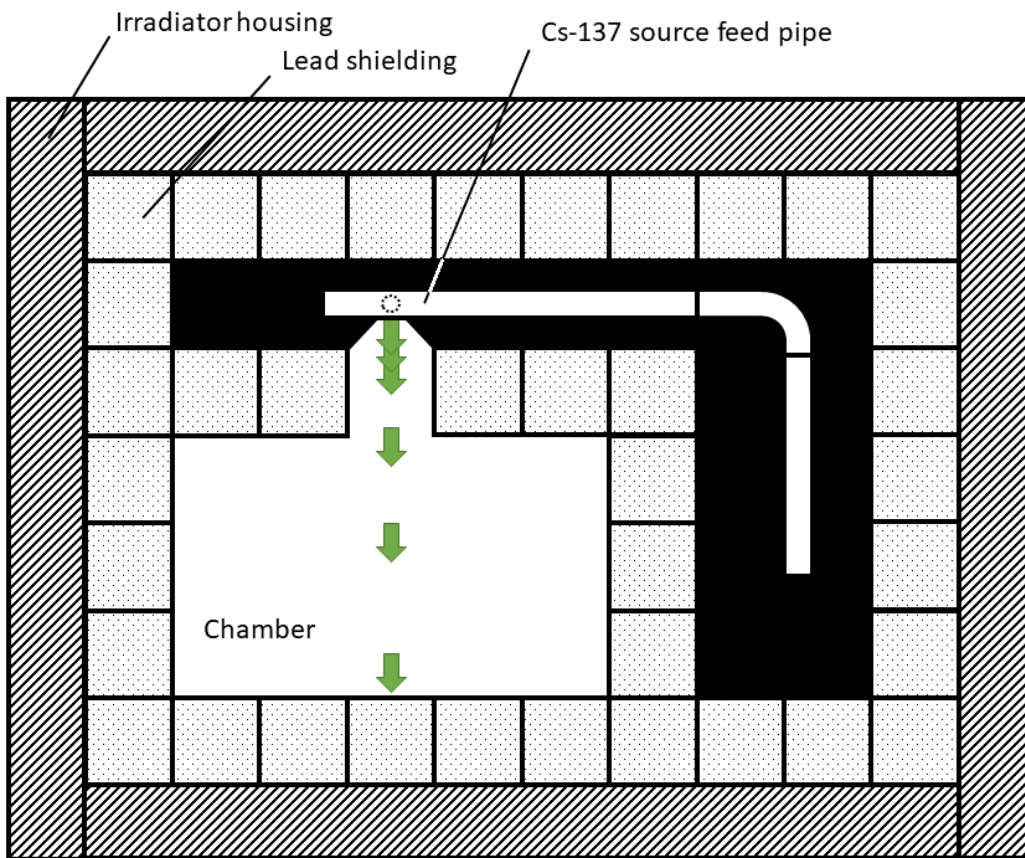


FIGURE 3.7. A schematic diagram of the Cs-137 irradiator, not to scale. Green arrows correspond to positions at which the dosimetry and gammavoltaic  $I$ - $V$  measurements were made. The dotted circle shows the source position.

could be both simulated and measured, and so this difference was the object of comparison.  $I$ - $V$  curves were taken in air, between -5 and 5 V, using 0.05 V steps, using the Keithley 6517A. Because of the focus on **applicability**, the device used for the Co-60 experiment was a triple-celled DGV. This was very similar to the single-celled DGVs used elsewhere, but for the fact that it was built using all three cells fabricated, glued together stackwise using silver epoxy paint. The results of the Co-60 experiment are discussed in Section 6.2.

### 3.3.4 Cs-137 Irradiator

A Cs-137 irradiator also became available for irradiation. The location and activity of the source cannot be disclosed <sup>2</sup>. The irradiator was housed in a sealed, secure vault and provided a single, retractable source and chamber, with different dose rates achieved by sample positions. A schematic

<sup>2</sup>A condition of use, due to the risk Cs-137 poses were it to get into the wrong hands.

diagram is provided in Figure 3.7. The maximum dose rate was approximately 3,200 Gy/h air KERMA, the minimum was below the 1 Gy/h air KERMA measurement threshold of the dosimeter. As such, the Cs-137 irradiator permitted measurements over the same three orders of magnitude as were available in the Harwell Co-60 cell. *I-V* curves were performed in the same way as for the Co-60 experiment. Two experiments were performed in the Cs-137 irradiator. The first experiment performed with the Cs-137 irradiator was a complementary experiment to that performed in the Co-60 cell at Harwell: *I-V* curves were taken over the full range of dose rates available. This was to assess, with more validity than the Co-60 experiment, **applicability** to a waste store deployment. As previously mentioned, this also allowed a comparison between simulation and measurement for the difference caused in performance by using Co-60 and Cs-137 radiation. The results of this experiment, as for the Co-60 experiment, are discussed in Section 6.2.

The second was a **longevity** test and employed a single-celled DGV, built using sample E6\_ELSC\_2. During this experiment, the DGV was irradiated at 1,350 Gy/h air KERMA for over 3.5 wks, for a total air KERMA dose of over 800 kGy. This is just higher than the dose rates expected at the canister surfaces in a nuclear waste store, as previously mentioned. Opportunities to perform this sort of experiment are rare; outside of waste stores themselves, Cs-137 sources capable of generating this sort of dose rate seem to be thin on the ground. Sources which do exist tend to be used for sterilising biological samples, and as such are frequently and routinely used by the institutions that house them. To have uninterrupted use of one for such a long period was therefore a valuable opportunity. Because the building in which the irradiator was housed was to be closed down almost completely over the duration of the experiment <sup>3</sup>, with the exception of security visits to the vault, a temperature and humidity logger was used to track these quantities. Both temperature and humidity are known to affect the conductivity of hydrogen-terminated diamond surfaces when varied drastically [256, 265], and the effect of the building closure on both quantities could not be predicted ahead of time. The results of this longevity experiment are discussed in Sections 6.3.1 and 6.3.2.

### 3.4 Computational Methods

A number of computational methods were employed, both for simulation and for data analysis: GEANT4 was used to simulate experiments carried out on the DGV from a particle physics perspective, Python scripts were created for electrical measurement automation, and analysis of experimental data employed techniques such as ordinary least-squares regression and orthogonal distance regression performed with Python and Julia scripts.

A number of computers were used throughout the course of the work, and were largely interchangeable in terms of their use for data analysis and programming. However, for numerical

---

<sup>3</sup>The building was to be closed for an extended duration due to the intersection of the Christmas holidays with a COVID-19 lockdown. This enabled an experiment of this type to occur in the first place, as it created a long window when the normally heavily-used irradiator would be vacant, but caused the potential for greater-than-normal changes in temperature and humidity.

simulation, hardware was important. They were transferred to a more powerful server-like computer for running. The specifications of the this computer can be found in Table 3.2.

### 3.4.1 High-energy physics simulation with GEANT4

GEANT4 (**Ge**ometry **and** **T**racking) was developed under the auspices of the RD44 collaboration at CERN and is an open-source software toolkit, designed to simulate "*the passage of particles through matter*" [266]. It was written by such a large and international group of collaborators that it has been said to act "*as a repository that incorporates a large part of all that is known about particle interactions*" [266]. As it is a software toolkit, rather than a simulation application, individual problems often require applications to be built from scratch. This is a significant undertaking, particularly in more complex cases which may, *in extremis*, involve creating the digital twin of equipment such as the Compact Muon Solenoid experiment at CERN [267]. GEANT4 is also written in C++, which has many benefits, such as speed, power and relatively homogeneous coding style between users due to being an ISO standard language [268], but which is also known as difficult for those without significant experience in the language. Based on these reasons, and the relatively small subset of GEANT4 functionality necessary for simulating a gammavoltaic, other options such as using more tailored codes (e.g. PENELOPE [269]), or writing bespoke software, might appear more sensible. However, as GEANT4 is open-source, it provides a more efficient route than building an application from scratch under certain circumstances: if a GEANT4 application already exists which closely resembles the problem at hand, it may be adapted. In 2012, Davis *et al* created a GEANT4 application for simulating diamond radiation detectors for radioprotection applications in space [270]. The application contains all physical processes necessary to describe the interaction of gamma rays with diamond and various metals, and so was relatively easy to adapt to the needs of this work. The application is, additionally, capable of event-level parallelism (as opposed to process-level parallelism). This latter feature was added to the GEANT4 toolkit after the initial release, in order to improve memory footprint [271]. In common with the GEANT4 vernacular, an *event* here means the physical processes directly

Operating system (OS)	Ubuntu 20.04.2 LTS (codename: focal) operating within Windows Subsystem For Linux, version 2 (WSL2), running on Windows 10 Home version 10.0.19041.
System type	x64
Processor	Intel Core i9-10850K, CPU @ 3.60 GHz, 10 Cores, 20 logical processors.
Motherboard	ASUSTek Computer Inc., TUF Gaming B460-PLUS
Installed/total available physical memory (RAM)	16.0 GB / 15.8 GB DDR4, 2400 MHz

TABLE 3.2. Hardware specifications for the computer that ran the simulations.

resultant from the life-cycle of a single incident particle: its initial interaction, the interaction of any secondary particles, etc. Each event is computationally independent. A *process* here means a single running instance of the GEANT4 application. Event-level parallelism therefore allows the simulation written by Davis *et al* to restrict parallel memory usage only to that which is needed to differentiate events. The alternative would be to also hold a copy in memory, for each process, of things common to all events, such as the detector geometry. Adapting the code of Davis *et al* involved changing the geometry and materials involved in the simulation, and the particles used, but otherwise the application stayed largely the same. The GEANT4 simulations were computationally heavy, and as such were run on the more powerful computer mentioned above. Scripts to handle the batching (i.e. changing of parameters) and data were written in both the Python and Bash languages. Additionally, the application was altered to output data in CSV format rather than ROOT. The code for each simulation was version-controlled with a Git repository, and can be viewed on the repository hosting service Bitbucket. Links to each repository are given in the relevant sections.

Although individual simulations differed, the core concept in each was to simulate the energy deposited into some region of a DGV by photons of a given energy which were incident upon it. As mentioned in section 1.2, GEANT4 is not capable of semiconductor electrical simulations; energy deposited into the device may be calculated with a high degree of certainty - at least so far as the faithfulness of the physical model allows - but how that deposited energy is then harvested is not simulated. Although the event-level parallelism was beneficial for computational speed, it implied no time dependent simulation was possible. For example, a carbon atom ionised by a previous gamma ray would not present a lower Compton scattering cross section to subsequent gamma rays.

Validation of the GEANT4 model was attempted by comparison to the SP8 results discussed in Section 5.2. Simulations were also compared to the DLS experiment in Section 5.1 (using a single-celled model) and the Co-60 and Cs-137 applicability experiments, in Section 6.1 (using a triple-celled model). Details of the models can be found in those relevant sections.

### 3.4.2 Computational use of Lambert's $W$ -function in the opposing-diodes model

The Lambert  $W$  function cannot be expressed in terms of the elementary functions which programming languages natively support<sup>4</sup>. Furthermore, the nature of fitting models to data means that sometimes, sets of parameter values may be tried which, although within the physical bounds set on those parameters individually, create an argument to the Lambert  $W$  function which cannot be computed due to the size of the exponential term in the argument. As a simplified example, the term  $750 \exp(750)$  is beyond computable size on the computer this document is being written on, so even though by definition  $W_0[750 \exp(750)] = 750$ , a program will fail to process this argument. For these reasons I have found it convenient to use the approximation method developed by Iacono and Boyd [272] for the principal branch, with additional adaptations for very small and very large arguments.

---

<sup>4</sup>Although higher-level languages will often have easily-accessible packages to compute the function, such as SciPy's special functions section for Python, and LambertW.jl for Julia.

This is a very short iterative procedure which uses a set number of iterations - three - to arrive at an approximation of  $W_0(x)$ . It calculates  $W_0(x)$  by first creating a new variable  $y$ , defined as

$$(3.3) \quad y = \sqrt{1 + xe^1},$$

then generates a first guess for  $w \approx W_0(x)$  according to

$$(3.4) \quad w_0 = 2.036 \ln \left( \frac{1 + 1.14956131y}{1 + 0.45495740 \ln(1 + y)} \right) - 1.$$

This starting point can then be iterated by applying

$$(3.5) \quad w_{n+1} = \frac{w_n}{1 + w_n} \left( 1 + \ln \left( \frac{x}{w_n} \right) \right)$$

The reason this process stops after three iterations (i.e. setting  $W_0(x) = w_3$ ) is that this is the point Iacono and Boyd found that the relative error of the approximation came within machine precision. The small number of iterations makes this a good candidate for loop unrolling, that is, hard coding each of the iterations rather than using a loop, which can lead to performance improvements too.

There is an issue with the Iacono and Boyd approximation which they do not appear to have noticed, which is that for very small values of  $x$ , the iterative scheme fails because it will attempt to evaluate a logarithm with a negative argument. However this is easily remedied by noting that for very small  $x$ ,  $W_0(x) \approx x$ .

When  $x$  is very large due to containing a large argument to an exponential, Iacono and Boyd's method can be adapted to bypass the evaluation of  $x$  due to its use of logarithms. For this, a function is defined as  $L_W(\ln(x)) \approx W_0(x)$ . Separating the logarithmic term in Equation 3.4 gives

$$(3.6) \quad w_0 = 2.036 (\ln(1 + 1.14956131y) - \ln(1 + 0.45495740 \ln(1 + y))).$$

Due to the size of  $x$ , and hence  $y$ , in problematic cases, we can make the approximations that

$$(3.7) \quad 1 + 1.14956131y \approx 1.14956131y$$

and

$$(3.8) \quad 1 + 0.45495740 \ln(1 + y) \approx 0.45495740 \ln(y),$$

giving

$$(3.9) \quad w_0 = 2.036 (\ln(1.14956131y) - \ln(0.45495740 \ln(y))).$$

Separating the logarithmic terms and collecting the resultant constants then gives

$$(3.10) \quad w_0 = 2.036 (\ln(y) - \ln(\ln(y))) + 0.8872333297094248.$$

By the same logic as before, for very large  $x$ ,  $y \approx \sqrt{x \exp(1)}$ , allowing the final form for  $w_0$  to be

$$(3.11) \quad w_0 = 2.036 \left( \frac{1}{2} \ln(x) - \ln(\ln(x)) \right) + 3.3164809893294738.$$

The adaptation of the iterative scheme from that point requires no approximations, just the re-arrangement of  $w_{n+1}$  as

$$(3.12) \quad w_{n+1} = \frac{w_n}{1 + w_n} (1 + \ln(x) + \ln(w_n)).$$

We then set  $L_W(\ln(x)) = W_0(x) = w_3$  as before. For the opposing-diodes model,

$$(3.13) \quad \ln(x) = \ln\left(\frac{I_{01}R_{Sh1}}{n_1V_T}\right) + \frac{(I_{01} - I)R_{Sh1}}{n_1V_T}.$$

There are discontinuities in  $V_{D1}$  where the calculation of the Lambert W term moves between the three methods, but comparison to circuit behaviour simulated with ngspice [273] for the model suggest these discontinuities are minor when the case structure in Figure 3.4.2

### 3.4.3 Calculation of the Lilliefors correction

As mentioned in Section 2.3.2, the Lilliefors correction has no analytical form at present, and so its calculation must be based on numerical approximation. Different software packages use different approximations, and the Lilliefors correction to the KS test is also sometimes packaged separately from the KS test as the "Lilliefors Test". The one used here is that provided by DescTools [274] using fourth-order polynomials: first, let

$$(3.14) \quad z_n = D_n \left( \sqrt{n} - 0.01 + \frac{0.85}{\sqrt{n}} \right).$$

Then,

$$(3.15) \quad p \approx \begin{cases} 1 & z_n \leq 0.302 \\ 2.76773 - 19.828315z_n + 80.709644z_n^2 - 138.55152z_n^3 + 81.218052z_n^4 & 0.302 < z_n \leq 0.5 \\ -4.901232 + 40.662806z_n - 97.490286z_n^2 + 94.029866z_n^3 - 32.355711z_n^4 & 0.5 < z_n \leq 0.9 \\ 6.198765 - 19.558097z_n + 23.186922z_n^2 - 12.234627z_n^3 + 2.423045z_n^4 & 0.9 < z_n \leq 1.31 \\ 0 & 1.31 < z_n \end{cases}$$

Note therefore that below a certain probability  $\ll \alpha = 0.05$ , the use of the approximation of the Lilliefors correction will return  $p = 0$  in cases where the uncorrected KS test will return smaller and smaller values, with prevents the rough comparison of fits which both return residuals very unlikely to be normally distributed.

### 3.4.4 Fitting $I$ - $V$ data

In line with the theoretical considerations discussed in Section 2.3, orthogonal distance regression was chosen as the algorithm to perform the fitting of  $I$ - $V$  data on account of its ability to take into consideration uncertainty in both axes when fitting non-linear models, and the Kolmogorov-Smirnov non-parametric test was used to supplement visual inspection of the fit residuals. ODR is provided

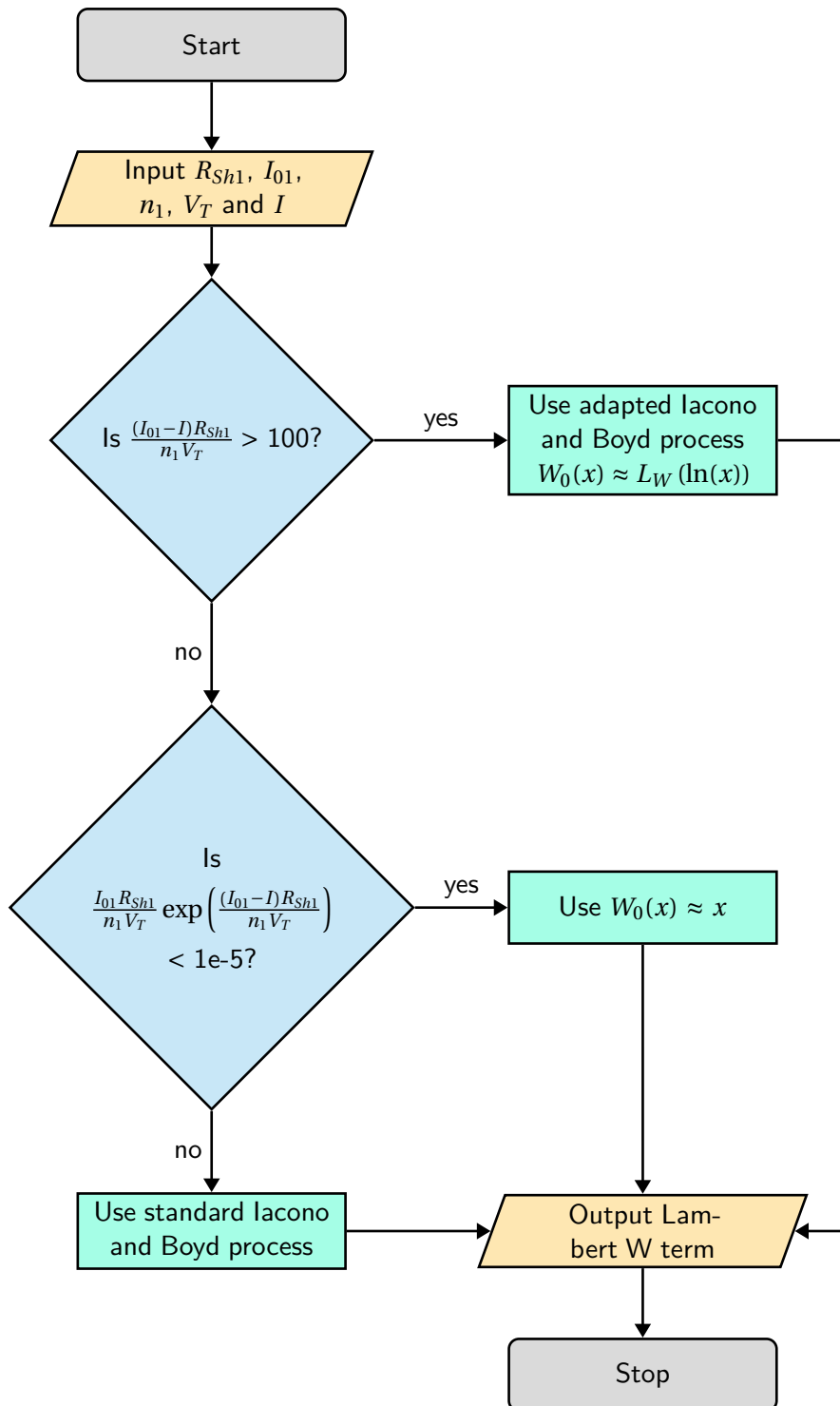


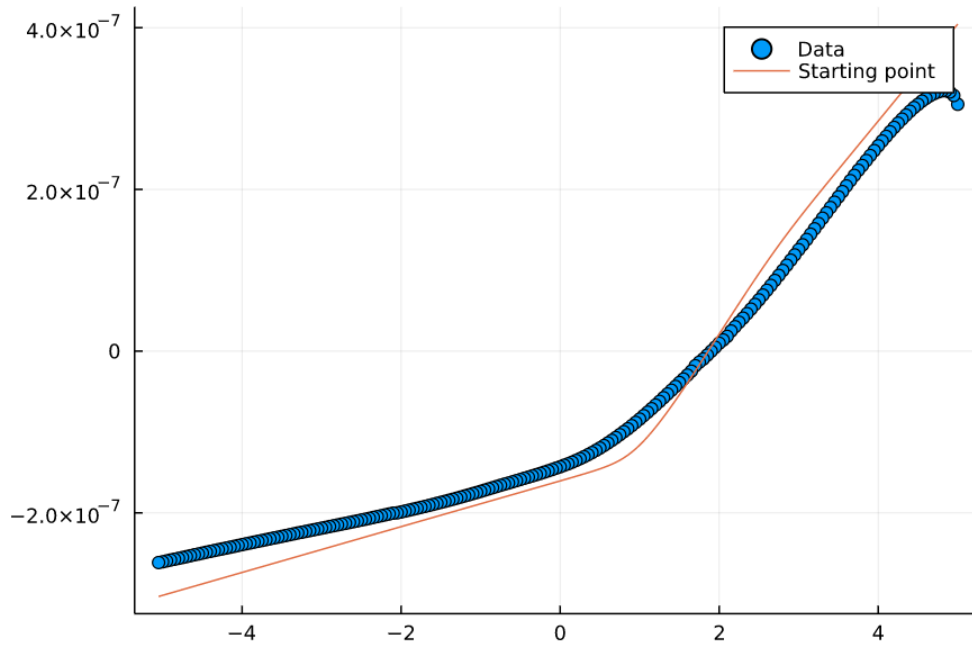
FIGURE 3.8. A flow diagram showing how the Lambert W function was calculated depending on the values taken by the opposing-diodes model parameters during fitting.

with bounds under the name ODRPACK95 [231] as a Fortran 95/77 file which may be built by the user using a compiler such as gfortran [275]. The user must write a Fortran file of their own which calls the ODRPACK95 routines. There are easier ways to use it under some circumstances: the scientific computing package for Python, SciPy, has an interface to the unbounded version of ODR released in the 1980s [276], but discussion on its community boards suggest that the move to the bounded version was never made because the volunteer developers did not feel that the licensing conditions of the bounded version were sufficiently clear to permit it. On the other end of the scale, the proprietary data analysis/scientific software OriginLab uses ODRPACK underneath its own software to supply ODR in its premium version, OriginPro [277]. I did not make use of the SciPy offering due to the need for bounds. Having tried to use the Origin offering, I found that the number of iterations needed, and the sensitivity of the fit to starting position, made the constraints imposed by the Origin GUI to be too cumbersome. As such, I reverted to writing a Fortran file of my own, as the authors of ODRPACK95 originally instructed. This Fortran file included a function to implement the Iacono and Boyd iteration scheme for the Lambert W function, as well as the modifications I made for small and large arguments, as discussed in Section 3.4.2. Failing parameter convergence or sum-of-squares convergence, it allowed a maximum of one hundred thousand iterations. For data handling and performing the Kolmogorov-Smirnov tests, I used Julia [278] with the HypothesisTests.jl package [279]. The Lilliefors correction I implemented in Julia myself, but the code was taken almost verbatim from the R code in the DescTools package [274].

It was found that the fitting algorithm had difficulty converging to reasonable values - or sometimes even converging at all - if the start point for the fit was not chosen with sufficient care. As such, start values were chosen visually by simulating data and comparing it to the data to be fitted, using a reactive Julia-based notebook built with Pluto.jl [280]. A screen-shot of the notebook is shown in Figure 3.9. This allowed parameter values to be quickly changed with both fine and coarse controls. The fits were performed subsequent to my having derived the implicit  $I$ - $V$  relation (Equation 2.25) but before I had appreciated that the explicit  $V$ - $I$  relation could be derived (Equation 2.26). As such, starting values were found via SPICE simulation and updated in real time as the parameter controls were changed. The spice simulator used was ngspice [273]. A quicker, simpler and easier method to use in future would be to use the explicit  $V$ - $I$  equation directly.

### 3.4.5 Miscellaneous tasks

In addition to the above, several miscellaneous tasks were handled with computational methods. Figure creation for data presentation, as well as some basic data analysis such as  $V_{OC}$  extraction of small datasets, was performed in Origin [277]. Machine control, of the Keithley 6517A multimeter for  $I$ - $V$  curve acquisition, was performed using a Python script that used the PyVISA package [281] to communicate via a USB to RS232 serial cable. For the long Cs-137 irradiation discussed in Section 3.3.4, this included bundling the script into a Linux-compatible executable, complete with simple GUI, such that it could be run from a Raspberry Pi microcomputer [282], and controlled and checked



## Measurement Information

File	data/Co-60_2900Gy_full.cs		
Number of cells	3	$T$ (Celsius)	20.3

1x10 Matrix{Float64}:  
 1.0e6 1.0e7 1.7e6 1.9e-7 1.0 1.5 1.0e-7 1.0e-14 0.0252971 3.0

## Parameter Controls

$R_{sh1}$	1.0	E 6	$R_{sh2}$	1.0	E 7
$R_s$	1.7	E 6	$I_{ph}$	1.9	E -7
$n_1$	1.0		$n_2$	1.5	
$I_{01}$	1.0	E -7	$I_{02}$	1.0	E -14

FIGURE 3.9. A screen-shot of the reactive notebook used to simulate  $I$ - $V$  curves against real data to find start-points for fitting procedures. Where parameters may change over orders of magnitude between datasets, controls have both fine and coarse controls manipulated by mouse click. The figure shows  $R_{sh1}$  being changed at the fine scale. The notebook runs a SPICE simulation of the opposing-diodes model using ngspice for each change of parameter values.

remotely using VNC Connect [283]. For some data operations, Julia [278] was used. This was particularly useful for handling large datasets such as the long Cs-137 irradiation, wherein, for example,  $V_{OC}$  values had to be found by interpolation for over 3,000  $I$ - $V$  curves, as well as those  $I$ - $V$  data themselves requiring manipulation for such things as figure creation in Origin. The relative ease of composition of Julia, combined with its speed, aided this work. Finally, typesetting and some figure creation was done with software under the TeX umbrella: pdfLaTeX via Overleaf [284] for overall typesetting, TikZ [285] for band diagrams, and its extension CircuiTikZ [286] for circuit diagrams. The template used as a basis for this document was written by Víctor F. Breña-Medina and made available on Overleaf.

## THE QUANTIFICATION OF HYDROGEN COVERAGE ON THE DGV, AND ITS NECESSITY FOR DEVICE FUNCTION

One of the defining features of the DGV cell design presented in this work is the use of a surface hydrogen termination to create a deliberate leakage path around the outside of the device. The results in this chapter are concerned entirely with this concept and aim to answer three questions. Firstly, given the use of an altered coater system is an improvised termination method, to what extent does it successfully hydrogen-terminate the surface? Secondly, does the design work? Finally, if the design does work, how significant is the hydrogen termination in allowing the device to work? In the language of the Introduction to this work, this chapter deals with **accountability** and **capability**. Those with a background in diamond surface science will naturally also ask to what extent the hydrogen termination can survive irradiation. As this is likely to be dependent on the radiation energy and strength, this question is addressed in Section 6.3, where isotopic gamma rays are employed to assess **applicability** and **longevity**.

The work in this chapter is adapted from the work presented in *A diamond gammavoltaic cell utilizing surface conductivity and its response to different photon interaction mechanisms*, Mackenzie *et al* [65]. The x-ray photoelectron spectroscopy study was conceived of between myself and Dr. Hugo Dominguez-Andrade of the University of Bristol, and undertaken with the consultation, direction and physical assistance of Dr. Mattia Cattelan, then Manager of the Bristol Ultra Quiet NanoESCA Laboratory at the University of Bristol but now of the Elettra Sincrotrone Trieste, Italy. The irradiation experiment, I undertook alone.

## 4.1 Quantification of surface termination via x-ray photoelectron spectroscopy

XPS was employed, *via* the techniques discussed in Section 3.2, to estimate the hydrogen surface termination. Surface terminations are given in fractional quantities (i.e. a full monolayer of a species is given as  $\theta = 1$ ).

### 4.1.1 Full survey scans

Figure 4.1 shows the full survey scans for each plasma treatment. As well as the expected carbon and oxygen signals, there are very clear sodium peaks in several of the scans, as well as a minor fluorine peak. There is also a very small peak in a region associated with molybdenum. If anything, this is likely a slight misalignment signal from the molybdenum sample mounting, though it is too weak to analyse with any confidence.

The sodium and fluorine signals are believed to originate in elements of the coater system chamber construction. As no significant chlorine signal was seen, it is likely that the sodium contamination came from pre-existing sodium oxide rather than any salts from manual handling. The chamber of the coater system is made from borosilicate glass, in which sodium oxide is used as a flux. It is therefore considered likely that some chamber etching took place during oxygen termination. It is noteworthy that no such sodium signal was present after the hydrogen termination step, suggesting that no sodium oxide contamination is present on the DGV to interfere with expected electrical behaviour. The small fluorine signal is likewise expected to come from Fomblin® grease used in a nearby chamber seal. The existence of sodium in the calibration terminations had implications for the monolayer estimation, which is discussed further in Section 4.1.3.

### 4.1.2 O 1s and C 1s peak region scans

The O 1s and C 1s regional XPS scans are shown in Figure 4.2. In a qualitative sense the spectra follow the expected behaviour, with the oxygen signal becoming stronger with increasing oxygen termination duration and the carbon signal, visible through the undetectable hydrogen, reducing as an oxygen monolayer establishes itself in place of that hydrogen. The form of the O 1s signal in particular made it difficult to deconvolute into single, chemically-shifted components. The shoulder around 530 eV in several of the spectra suggests metal oxide contamination [287], as indeed would be expected, as these are the same scans for which sodium was found to be present. These same scans likewise showed an increased signal in the areas expected for sodium Auger peaks: 535 eV [288–291] and 500 eV [290]. It is likely that the O 1s region contains, at least, signals from various carbon-oxygen bond types, e.g. the C-O and C=O bonds at 532 eV and 533 eV respectively [291, 292]. It was decided that a fit generated for the region would be too arbitrary. The region around 287 eV in the C 1s scan may indicate a transition of carbon-oxygen bonding type, which is consistent with the O 1s scan region. Moreover, we can observe a clear C 1s shift to higher binding energy with increasing

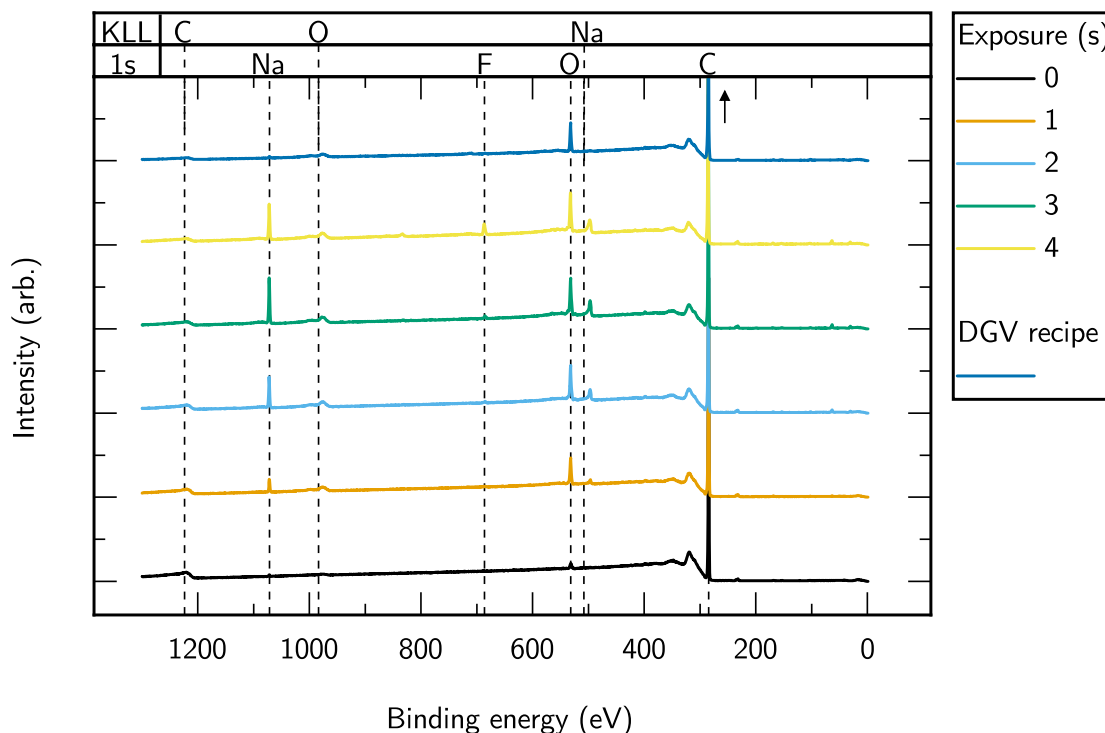


FIGURE 4.1. Full XPS spectra for the calibration sample for each plasma treatment, with five datasets given for seconds of oxygen plasma exposure after a full hydrogen termination, and a sixth given for the DGV recipe of 30 s oxygen plasma exposure followed by 30 s hydrogen plasma exposure. As well as the expected oxygen and carbon peaks, additional peaks corresponding to sodium and fluorine are present, as well as a small signal at 232 eV believed to be a molybdenum  $3d_{1/2}$  peak. The top of the C 1s peak has been cut for clarity.

oxygen content, as found by Wan et al [168]. Overall, the lack of confidence in attributing specific chemical states to the peak scans meant that less information was gathered in this measurement than might have been possible with a less contaminating termination procedure. The peak scans did not generate much more quantitative information than the survey scans, although the qualitative hints it provided were instructive in a broader sense.

#### 4.1.3 Monolayer estimation

Due to the presence of sodium on the sample surface, as seen in the survey scans, and the relative lack of extra quantitative information provided by the peak scans, the survey scans rather than the peak scans were used for coverage estimation. To determine an accurate O:C peak area ratio related to the diamond, an oxygen signal corresponding to  $\text{Na}_2\text{O}$  was linked to the sodium peak area, and subtracted from the total oxygen peak area ratio once photoemission cross sections and

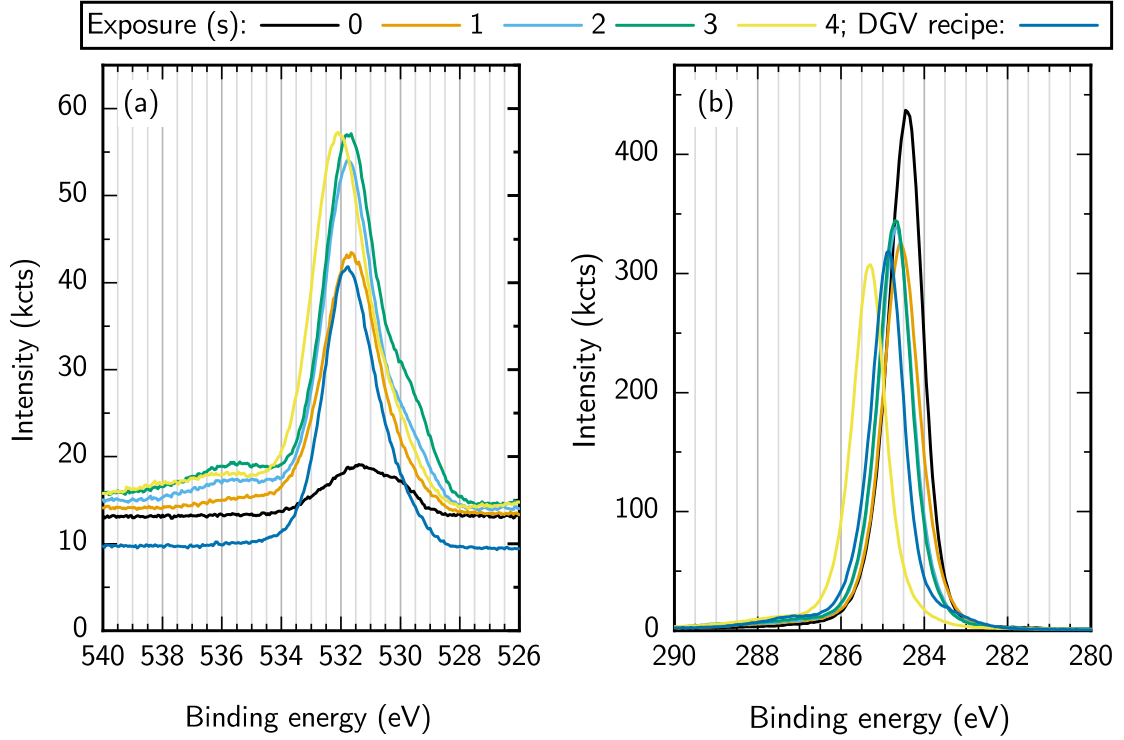


FIGURE 4.2. **(a)** The O 1s and **(b)** C 1s regions of the XPS calibration sample, scanned at a higher energy resolution.

stoichiometry were taken into account. This oxide form was chosen because it is the most stable in the highly oxidising environment that the sample had been subjected to. The remaining oxygen was assumed to be a terminating surface layer. The O:C ratios are shown in Figure 4.3. The saturation of this quantity allowed an estimate of full monolayer coverage, also shown in the figure. Saturation was modelled with an exponential fitting curve, given by

$$(4.1) \quad T_{\text{MAX}} \left( 1 - e^{-\frac{t}{\tau}} \right) + T_0,$$

where  $T_{\text{MAX}} = 8.2 \pm 0.7 \%$  is the maximal addition to the O:C ratio deliverable by the termination process,  $\tau = 1.3 \pm 0.3 \text{ s}$  is an exposure time constant for the surface monolayer formation, and  $T_0 = 1.3 \pm 0.5 \%$  is the contribution of pre-termination surface oxygen to the O:C ratio. For this fit,  $R^2 > 0.98$ . This generates an estimate for the O:C ratio expected for a total oxygen monolayer as

$$(4.2) \quad T_{\text{SAT}} = T_{\text{MAX}} + T_0 \approx 9.5\%.$$

Propagating uncertainty through this equation, by the normal methods, is likely to lead to a deceptively tight margin of error. In reality, the process of transporting the sample between the coater system and the XPS equipment will have introduced adventitious hydrocarbon surface contaminants,

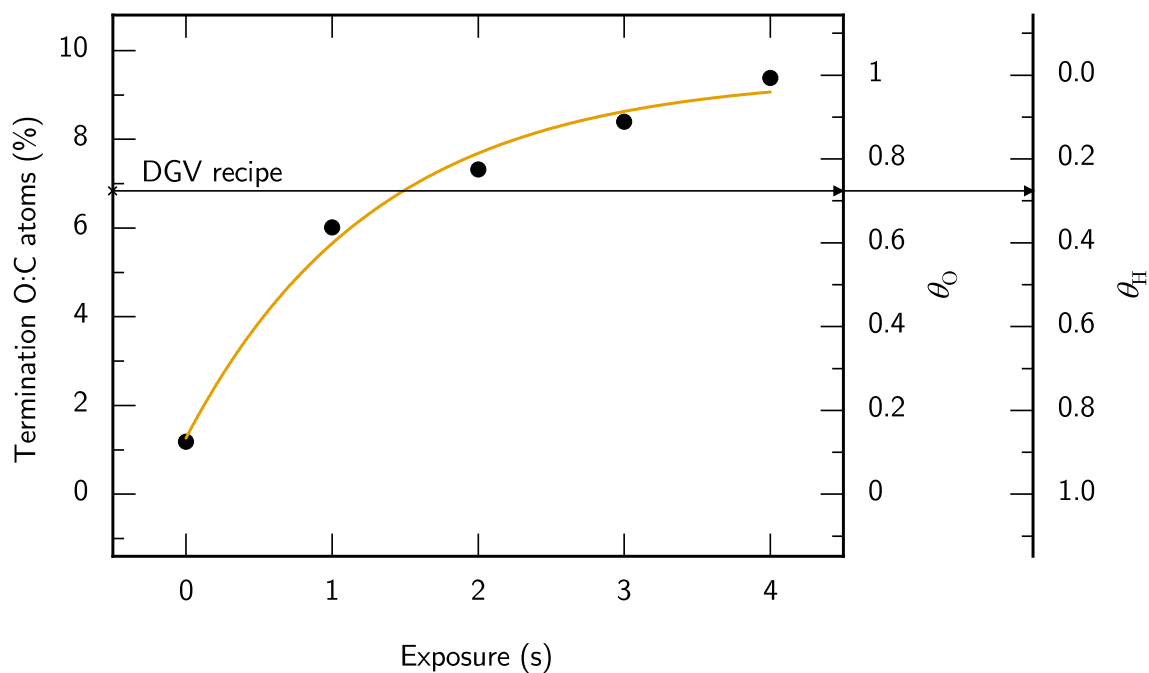


FIGURE 4.3. **(Left ordinate)** the ratio of O:C atoms on the surface of the diamond calibration sample, after starting from a full hydrogen termination and exposing incrementally to a DC oxygen plasma. The oxygen signal is controlled to account for contaminating  $\text{Na}_2\text{O}$ . The ratio was determined by XPS. **(Right ordinates)** the calculated corresponding oxygen and hydrogen monolayers,  $\theta_{\text{O}}$  and  $\theta_{\text{H}}$ . The hydrogen proportion can be taken as the only other species on the surface. The reference arrow shows the signal obtained from the sample after it was subjected to the partial hydrogen termination recipe used for the DGV, and the corresponding monolayer values. The orange line is a fitted exponential saturation curve, described in 4.1, for which  $R^2 > 0.98$ .

capable of causing more systematic uncertainty than that random uncertainty inherent in the measurement. As such, the more cautious approach is to treat the value of  $T_{\text{SAT}}$  as wholly approximate rather than bounded by a calculated uncertainty margin.

Measurements of the O:C ratio after the partial hydrogen termination gave a value of 6.84 %, corresponding to a calibrated oxygen monolayer coverage  $\theta_{\text{O}} \approx 0.7$ , assuming total coverage for the 4 s exposure. As the sample started off with a full hydrogen termination, it is assumed that the partial hydrogen coverage after termination was  $\theta_{\text{H}} \approx 0.3$ . The approximate nature of  $T_{\text{SAT}}$  of course confers the same level of uncertainty on  $\theta_{\text{O}}$ , and hence  $\theta_{\text{H}}$ .

The XPS data provided a fair calibration of the partial hydrogen termination process, despite the sodium contamination.

## 4.2 The question of the efficacy of hydrogen termination

To answer the questions of whether the presented design worked as a gammavoltaic, and if so, to what extent the surface hydrogen termination played a role, a single-celled DGV fabricated using sample E6\_ELSC\_5 was irradiated using a laboratory XRT, as outlined in Section 3.3.1. Figure 4.4 shows dark  $I$ - $V$  data taken between -50 to 50 V, and illuminated  $I$ - $V$  data taken at voltages within a margin of the power-producing quadrant, from the device with no hydrogen coverage ( $\theta_{\text{H}} = 0.0$ ) and after partial hydrogen coverage ( $\theta_{\text{H}} \approx 0.3$ ).  $P$ - $V$  curves are also given for the illuminated cases. In the dark, the unterminated device acted as an ohmic resistor with a very high resistance of around 3 T $\Omega$ , as would be expected, with a small ingress into the power-producing curve which, in the absence of illumination or significant temperature, seems most likely to be due to systematic error in the measurement apparatus. With a partial hydrogen termination the dark  $I$ - $V$  curve over the same voltage range is rectifying in nature, with a smaller ingress into the power-producing quadrant which again seems most likely to have come from systematic measurement error. The differential resistance of the sample when partially terminated is otherwise mostly greater in the dark than prior to termination - an unexpected state of affairs for which the reason is not clear. Turning to the curves under illumination, the device produced only a small gammavoltaic effect with no hydrogen coverage, generating currents of the order of 10 pA. The curve is at the limits of the multimeter resolution, but there does appear to be a jump around -0.2 nA, which based on similar effects in later measurements may have been due to auto-ranging error in the multimeter. Unfortunately, auto-ranging error was not identified as the culprit of these jumps until later work in the project, and is generally responsible for jumps in  $I$ - $V$  data when they occur near currents with first significant figures near 2 at certain orders of magnitude. The  $FF$  was not considered sensibly calculable, due to the form of the  $P$ - $V$  curve. When the partial hydrogen termination was applied, the device showed a clear gammavoltaic effect, with a short-circuit current  $I_{\text{SC}} = 400$  nA, four orders of magnitude greater than when no termination was present, a  $V_{\text{OC}} = 0.8$  V and an  $FF = 0.43 \pm 0.01$ . Comparison may be drawn to work by Conte et al [293], in which MESFETS based on hydrogen-terminated diamond were triggered by UV pulses,

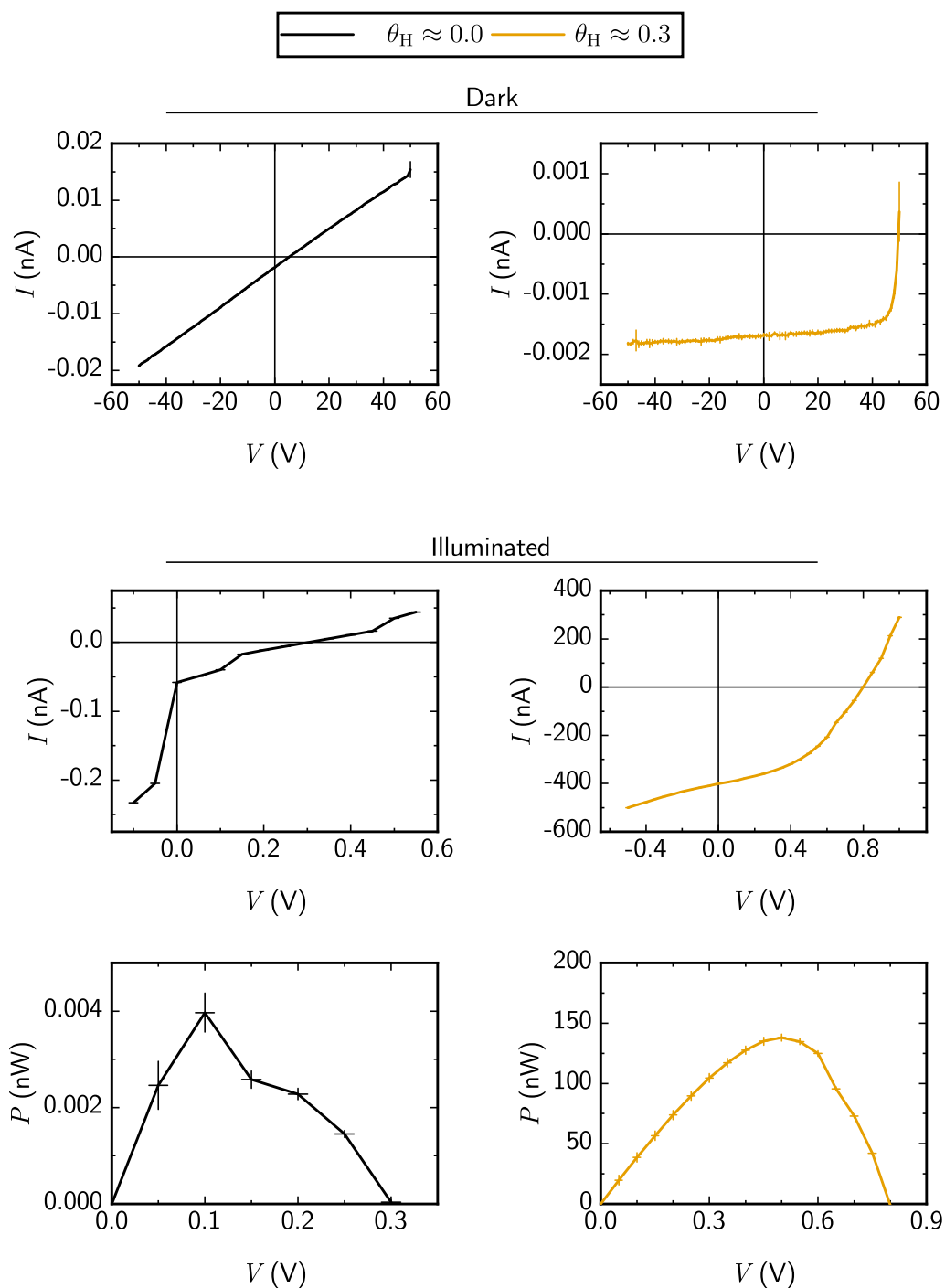


FIGURE 4.4.  $I$ - $V$  curves taken with the device and the related  $P$ - $V$  curves, first with no hydrogen coverage, and then with  $\theta_H \approx 0.3$  as estimated with XPS. The devices were driven with broadband X-rays from the XRT. Uncertainty in the hydrogen-terminated  $I$ - $V$  case was  $< 10$  nA.

which turned the devices on via photogenerated holes. There appears to be an auto-ranging error in this  $I$ - $V$  data also, visible near -200 nA, which due to its position in voltage, appears in the  $P$ - $V$  curve too. The transition in the  $I$ - $V$  behaviour from the dark to the illuminated cases for the device when it was partially hydrogen terminated is not the same as is expected from the conventional photovoltaic model; the dark  $I$ - $V$  curve cannot be transformed into the illuminated  $I$ - $V$  curve by adding a constant current offset, such as would be the case if the equivalent circuit were to solely have  $I_{ph}$  altered as in Figure 2.7.

This test showed that the presented design is **capable** of acting as a gammavoltaic, and suggests that the partial hydrogen termination was necessary (though perhaps not sufficient) to **account** for that level of gammavoltism. This supports the design principle put forward in this work, suggesting that creating a conductive surface does indeed capture scattered secondary particles from photons interacting with the bulk. As the hydrogen termination is a single atomic layer, the capture cross section would be too low for this output to come solely from photons interacting at the surface. However, it remains unknown whether the entire bulk is takes part in the mechanism, or whether a shallower sub-surface region is responsible. An attempt to address this question is given in Section 5.2. Also, whilst in published work [65] I and co-workers<sup>1</sup> used the above result as justification for using a hydrogen termination in all circumstances, it does not account for dose rate. Whilst the hydrogen termination does appear to have played a significant and necessary role in allowing the DGV to function when irradiating it with the XRT, at sufficiently high dose rates, charge injection throughout the device may become so substantial that a hydrogen terminated layer is not necessary, and to some extent this oversight is perpetuated in the work presented in Section 5.2.

The fill factor was quite low - contemporary solar cells can reach  $FF > 0.8$  [294, 295]. This is likely due to both shunt and series device resistances, visible in the gradual slopes of the trace, in contrast to the ideal step shape. Both quantities are expected to be influenced by the hydrogen coverage. The hydrogen coverage, 0.3, was relatively low, and is not optimised. As the 2DHG resistivity can change by orders of magnitude with different adsorbate coverages [256] it is likely that this parameter will significantly affect device performance and act as an avenue for improvement. It is not certain that as high a coverage as possible would be optimal; a coverage too high may short the device, or reduce the ability of the surface to collect charge carriers. I expect, at present, that a medium-low hydrogen coverage may be optimal for this type of device, with the surface hydrogen acting similarly to a dopant in a conventional semiconductor junction: high enough in concentration to allow current to flow, but low enough that the built-in electric field may vary over the surface, and hence separate charge. It may be that this view is mistaken, and that in fact, as high a hydrogen coverage as possible is desirable. In this case, a stable and reproducible bulk counterpart to the surface termination would be graphite pillar electrodes. These are increasingly prevalent in diamond detectors [96, 163, 296–300], but also have the distinction of having worked well in an energy device: the diamond photon-enhanced thermionic energy converter of Girolami et al [162]. Laser processing might also be prove useful in a

---

<sup>1</sup>The oversight was solely mine.

more typical sense, in that excising a regular array of trenches from the bare areas of diamond prior to hydrogen termination could increase the surface area available to collect charge. This would of course require optimisation, as the deeper such trenches got in order to increase surface area to collect charge, the smaller the volume there would be available to interact with gamma rays in the first place. A systematic study along these lines might fruitfully look at plasma-based diamond etch methods first for controllable, iterative diamond removal [301] before moving on to faster but more aggressive laser processing.



## SYNCHROTRON- AND SIMULATION- BASED STUDIES OF THE PHYSICS OF THE DIAMOND GAMMAVOLTAIC CELL

This chapter presents results from an investigation into the performance of a single-celled DGV, built using E6\_ELSC\_5, under irradiation at the SP8 and DLS synchrotrons. Firstly, a GEANT4 simulation of energy deposited into the device over the Gamut, with a 1 keV resolution, is presented. Secondly, the photoresponse mapping experiment carried out at the SP8 synchrotron, and its associated GEANT4 simulations, are presented in an attempt to validate the GEANT4 model geometry being used throughout this work. The validation is based on the idea that there should be a linear relationship between deposited energy  $E_{\text{dep}}$  and short-circuit current  $I_{\text{SC}}$  when the flux and photon energy are held constant, and the validation is not entirely successful. A similar simulation is then presented where the photon energies and energy spectra are modelled on the beam energies and spectra used at the DLS synchrotron.  $I$ - $V$  curves measured under irradiation from these energies are then presented, with  $I_{\text{SC}}$ ,  $V_{\text{OC}}$ ,  $P_{\text{MPP}}$  and  $FF$  extracted or calculated from the data as relevant. Because the synchrotron flux changed with photon energy, these quantities are first plotted against both variables. The  $P_{\text{MPP}}$  and incident power  $P_{\gamma}$  values are used to calculate  $\eta$  values for each curve. The GEANT4 simulation is used to supply estimates for the deposited power  $P_{\text{dep}}$  to allow  $\eta_{\text{dep}}$  to be estimated for each curve. In an attempt to isolate any effects caused purely by the photon energy, and on the proviso that the  $V_{\text{OC}}$  is fairly stable across all curves, the  $I_{\text{SC}}$  and  $P_{\text{MPP}}$  values are then normalised according to the flux the synchrotron delivered for each curve. The studies in this chapter are mainly for the purposes of **accountability**, but it should be noted that the photon energies in the synchrotron studies cover the Am-241 emission energy and a large part of the U235\* fission delayed-gamma spectrum. As such,  $\beta$  and  $\rho$  values are given for Am-241, but they are for very high dose rates and therefore unlikely to be of much practical use.

Some of the work in this chapter, the Diamond Light Source experiment, is adapted from the

work presented in *A diamond gammavoltaic cell utilizing surface conductivity and its response to different photon interaction mechanisms*, Mackenzie *et al* [65]. It benefited from the consultation and physical assistance of Dr. Thomas Connolley, Principle Beamline Scientist of Beamline I12 at the Diamond Light Source, who also performed the photon energy measurements. It also benefited from the administrative and physical aid of Dr. Peter G Martin of the University of Bristol. The presentation differs in this work from that in the paper predominantly in the removal of a method used in the paper to extract series resistance from the flux-normalised  $I-V$  curves, which was an extension of a method taken from Schröder's *Semiconductor Material and Device Characterisation* [159, p. 157][302]. I am no longer sufficiently confident that it is valid to present it here, having had the benefit of critical feedback on top of the normal peer review process when this work was examined *viva voce*<sup>1</sup>. Similarly for flux normalisation of  $I_{SC}$  and  $P_{MPP}$ : this procedure was deemed valid by peer reviewers and also when this work was examined, but it is presented below in addition to, rather than instead of, the raw  $I-V$  curves in case flux normalisation should later be found to be invalid due to non-linearity between current and flux under these experimental circumstances.

At the time of writing, the SPring-8 data are being prepared for an article titled *A triple-celled diamond gammavoltaic device tested for performance and longevity under irradiation from Cs-137 and Co-60 gamma rays*. Due to global events, they were taken using samples I prepared under the auspices of my experimental design, but otherwise at the hands of collaborators Dr. Yukihiro Satou, Dr. Takahisa Shobu, Dr. Tatsuo Fukuda, Dr. Tsuyoshi Yaita, and Dr. Kenji Yoshii of the Japan Atomic Energy Agency, and Dr. Naruki Truji of the Japan Synchrotron Radiation Institute. These colleagues also consulted on experimental design. The simulations I undertook alone.

## 5.1 GEANT4 simulation of a single-celled DGV irradiated with monoenergetic 1 - 2000 keV photons

### 5.1.1 Simulation details

The simulation geometry used for single-celled DGVs can be seen in Figure 5.1.

The silver conductive epoxy paint, which in reality had a blob shape due to being applied with a paint brush, was approximated by a truncated cone. The copper wire strands, twisted together and used to connect the cell to the SMA outer housing, were approximated by five strands set parallel in front of the device in section. The low-barrier and high-barrier contacts were approximated as 100 nm thick and pure gold. The SMA connector pin was modelled according to specifications: a steel-303 pin coated with approximately 2  $\mu\text{m}$  of gold. The geometry was surrounded by air at 40 % relative humidity. Photons were fired from a planar source directly at the device, the planar dimensions of

---

<sup>1</sup>The resistance extraction method was used in the paper to support the idea of resistance decrease being tied to an increase in the proportion of Compton scattering events, so work is ongoing to understand whether the record may need to be corrected in some way such as by corrigendum. Any fault in the use of the method lies with me and not the other authors on the paper.

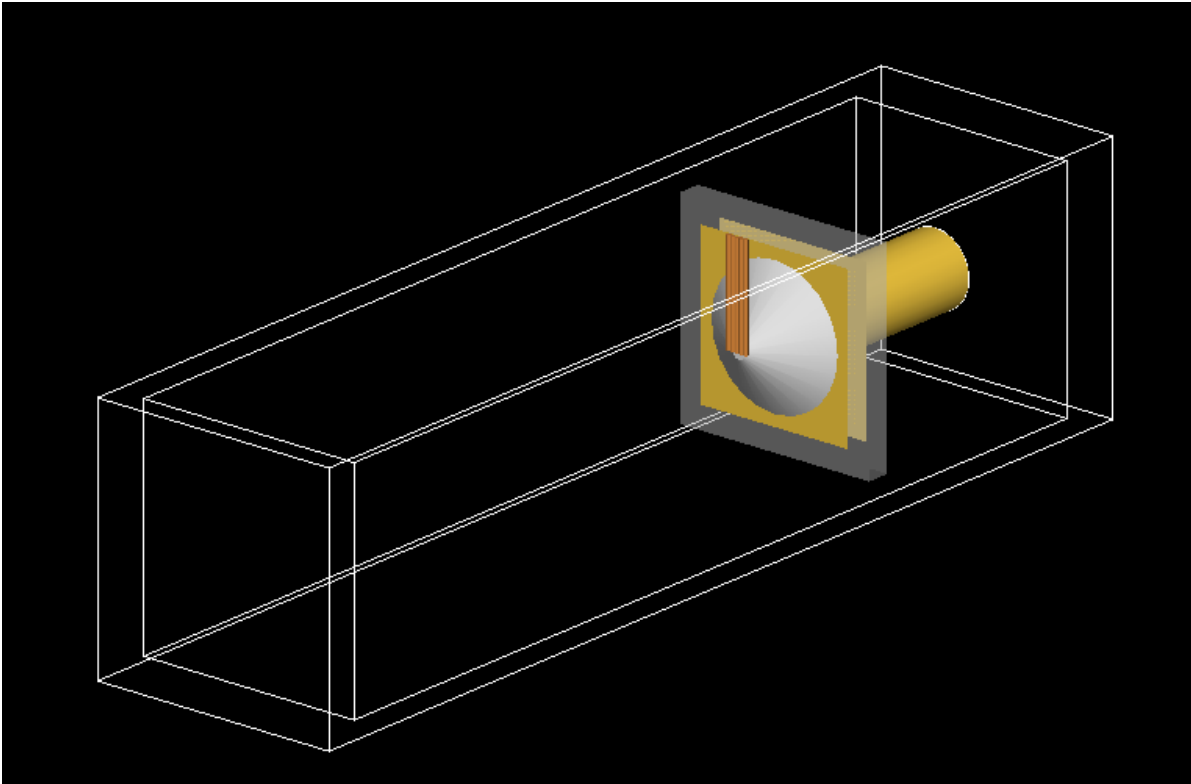


FIGURE 5.1. The GEANT4 geometry used for simulating single-celled DGVs. Gamma rays originated at randomly-generated positions in a planar square region the same size as the cell cross-section on the left-hand side of the simulation cuboid. The silver epoxy is modelled as a truncated cone, and the twisted copper wire as five repeated straight sections in front of the device. The whole diamond was treated as a sensitive volume.

the source matching those of the diamond. The sensitive volume of the diamond (i.e. the volume in which energy was counted as collected if it was deposited there) was assumed to be the whole diamond. This assumption is tested in the next section.

The Git repository for this simulation can be found at

<https://bitbucket.org/RobbieMackenzie/singlecellmono/src/main/>

### 5.1.2 Simulation Results

The quantities collected by the simulation were the number of hits (i.e. the number of primary gamma photons which deposited energy into the diamond), the energy deposited ( $E_{\text{dep}}$ ) per hit, and the total  $E_{\text{dep}}$  in the run. The simulation having had 20 threads and ten million primary gamma photons, the number of hits and the total  $E_{\text{dep}}$  should be read as having been for 500,000 primary gamma photons. These quantities are shown in Figure 5.2. Absorption (i.e. the number of hits) starts out as effectively total for 1 keV photons - complete attenuation. It is constrained geometrically by the existence of

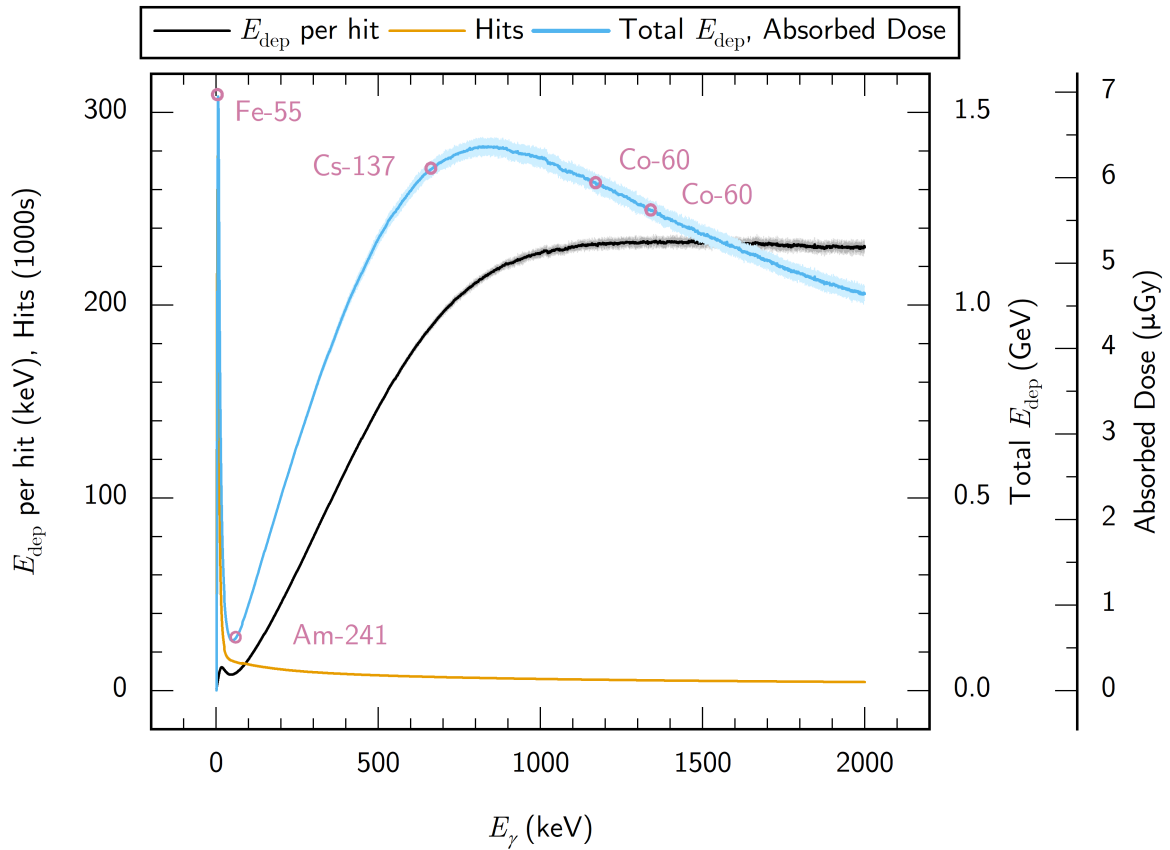


FIGURE 5.2. GEANT4 simulation data of the number of hits, the energy deposited per hit, and the energy deposited in total for a single-celled DGV with 500,000 incident primary gamma rays, across a range of energies. 10 million gamma rays were spread out over 20 threads. An additional ordinate is provided to convert between total energy deposited in GeV and absorbed dose in  $\mu\text{Gy}$ , taking the mass of the diamond into account. Pink circles show the emission energies of isotopes which are important for gammavoltaics.

silver epoxy in front of the diamond, rather than energetically by the probability of the photons being absorbed once they get to the diamond. This drops abruptly towards about 20 keV and then more gradually from there to 2000 keV.  $E_{\text{dep}}$  per hit conversely starts low, because the photons do not start with much energy, comparatively speaking. There is an initial peak due to the opposing influences of photon energy rising whilst the absorption falls, these influences reversing in their strength until just after 20 keV, where the absorption starts to drop more gradually and thus, the continuing linear increase in photon energy starts to dominate. This effect eventually saturates at around 1000 keV. Finally, the total  $E_{\text{dep}}$ , which is theoretically the product of the two previous quantities, has a sharp peak in the lowest energies, coincidentally matching precisely with the emission energy of Fe-55, despite portable gammavoltaics not being the focus of this work. Conversely, the same quantity has a very distinct local minimum which coincides with similar precision to the Am-241 emission energy. Ultimately the total  $E_{\text{dep}}$  shows its broadest peak - the range at which the DGV is most effective for a given flux - at higher energies. The isotopic emission energies of Cs-137 and Co-60 are both near the top of this peak and at similar heights, albeit on opposite sides of the peak. Conversion between total  $E_{\text{dep}}$  and absorbed dose, using the known dimensions and density of the diamond, show that 500,000 gamma rays over this energy range will tend to lead to an absorbed dose of a few Gy.

GEANT4 events (the computation associated with each primary gamma photon) are independent, which means the results can be linearly scaled for hits, total  $E_{\text{dep}}$  and absorbed dose.

## 5.2 Photoresponse mapping of a single-celled DGV at the Spring-8 synchrotron for simulation validation

This section presents a photoresponse mapping experiment undertaken at the SP8 synchrotron. The experiment was performed with a quasi-monochromatic 182 keV beam with a square cross-section, dimensions of  $1 \times 1 \text{ mm}^2$ . Sample E6\_ELSC\_5 was mounted as a DGV and the beam was moved around the surface, to investigate the contribution made to the current output by different regions of the cell and compare it to energy deposition as simulated.  $I$ - $V$  curves were taken at each beam position, though only the  $I_{\text{SC}}$  was used in this analysis. The experiment was compared with a GEANT4 simulation, in an attempt to validate the assumption that the whole diamond could be treated as the sensitive volume. As mentioned in Section 3.3.2, the validation criterion was that the simulated deposited energy be linearly related to the measured  $I_{\text{SC}}$ .

### 5.2.1 Simulation details

The simulations were based on that used in the monoenergetic simulation, with the same geometry employed and same basic approach. Two simulations were run, via separate Bash scripts. The first was a pixel mapping-style simulation in which a  $0.5 \times 0.5 \text{ mm}^2$  beam was stepped over the whole face of the device in 0.5 mm increments, to produce a contour map. The second was a match to the actual experiment, with a  $1 \times 1 \text{ mm}^2$  beam moved in 0.5 mm increments along the lines used, so that

energy deposition could be compared directly with measured  $I_{SC}$ . Using a larger beam than step size can be expected to have had a spatial averaging effect.

The Git repository for this simulation can be found at

<https://bitbucket.org/RobbieMackenzie/singlecellsp8/src/main/>

### 5.2.2 Experimental details

Although only the  $I_{SC}$  was used for model validation, full  $I - V$  curves were taken. These  $I - V$  curves were different to those measured in previous experiments in that two points either side of 0 V had to be interpolated to arrive at an  $I_{SC}$  value. Only these  $I_{SC}$  values were used in this analysis, but the full  $I - V$  curves can be found in Appendix B.

### 5.2.3 Results

Figure 5.3 shows the results of the two simulations and the  $I_{SC}$  measurements. The contour map produced by the first simulation, subfigure (a), shows an enhancement in the energy deposited into the device due to the silver epoxy paint, suggesting that from a device design perspective, the epoxy had acted as a form of "scatter shroud". Furthermore, there is a slight, but noticeable, increase in energy deposition due to the copper wire strands, even though the gap between these and the diamond, of 1 mm, can be expected to have attenuated the flux of scatter products from the wires. There is also a much milder effect, visible in the map of the bare contacts, by which more central beam positions deposit more energy. This is as would be expected when considering the fact that photons incident closer to the edges of the cell face are more likely to produce scatter products that escape the edges of the cell, their energy being lost to it. However, the circular imprint in the map, lined up as it is with the outline of the silver epoxy, demonstrates that the scatter shroud effect is more prevalent here.

The second simulation, subfigure (b), in using a larger beam size and in being restricted to only two linear tracks, provided less spatial information but was more directly relevant to the experiment which it mirrored. The measurement heatmap which the simulation heatmap mimics, subfigure (c), showed the measured  $I_{SC}$  values which it had been hypothesized would be proportional to the simulated  $E_{dep}$ . The bar plots in the simulation heatmap and measurement heatmap are equally scaled. It can be seen that there is reasonable overall agreement in these heatmaps/bar charts between simulation and measurement, although the measured  $I_{SC}$  appears to drop off more quickly towards the edges of the device than the simulated  $E_{dep}$ . The relationship between measured  $I_{SC}$  and simulated  $E_{dep}$  was fitted using ODR with

$$(5.1) \quad I_{SC} = \alpha E_{dep},$$

where  $\alpha = 1.6 \pm 0.13$  nA/MeV. In terms of fit quality, the model was linear and so the  $\chi^2_v$  statistic could be used. The orthogonal  $\chi^2_v = 1162$ , indicating an underfitting model. There was one point which appeared as though it could be an outlier, indicated in Figure 5.3 with a pink arrow. It is not clear

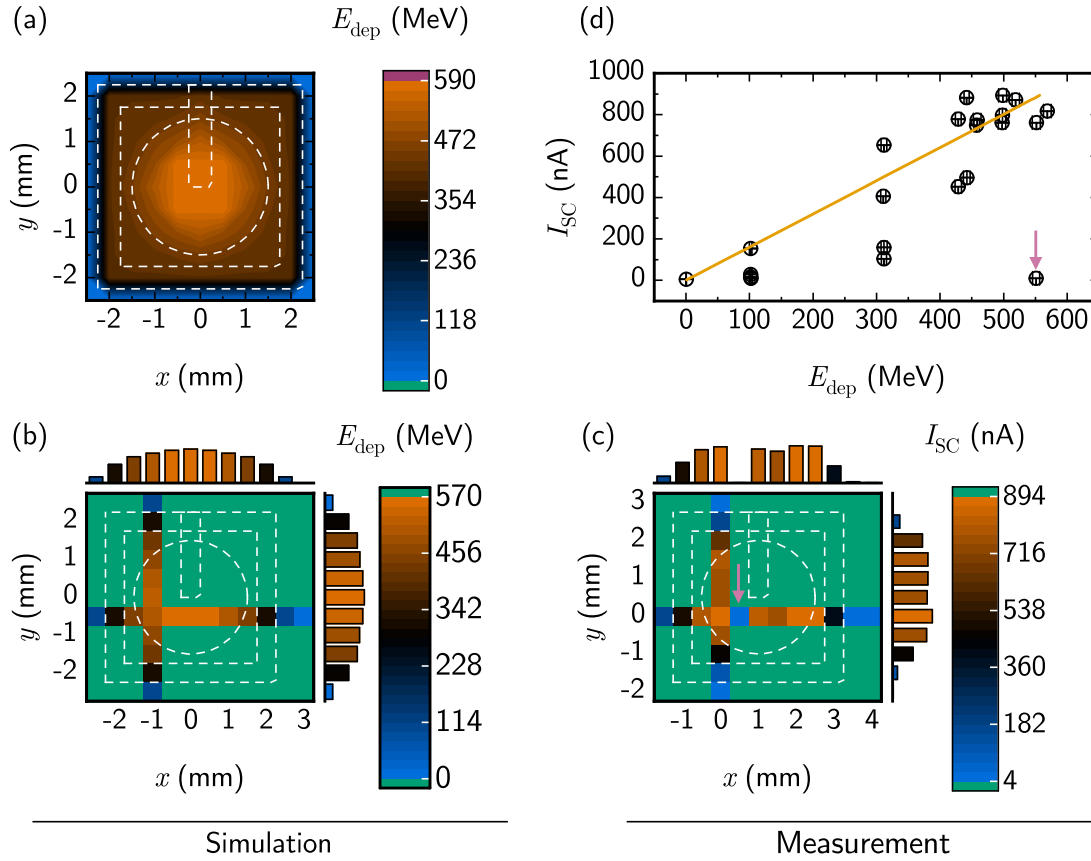


FIGURE 5.3. Simulation and measurement results for the SP8 photoresponse mapping experiment. **(a)** shows the contour map of  $E_{\text{dep}}$  produced by the first simulation. **(b)** shows the  $E_{\text{dep}}$  in the second simulated designed to mimic the experiment, including bar plots for each linear motion of the beam. **(c)** shows the same type of plot but using the measured  $I_{\text{SC}}$  values for the map. The position co-ordinates are slightly different in this subfigure compared to the previous two as they are measured from the initial position of the beam rather than the centre of the face of the DGV. In the three map sub-figures, the white dotted lines are outlines of cell components: the diamond, contact, silver epoxy and copper wire as used in the simulation geometry. Finally, in **(d)**, the measured  $I_{\text{SC}}$  values are plotted against the simulated  $E_{\text{dep}}$  values. Also in this figure is a linear fit according to Equation 5.1, performed with ODR. For this fit,  $\chi^2_{\nu} = 1162$ , indicating an underfitting model. When the point identified in subfigures (c) and (d) with a pink arrow is removed from the fit, the fit remains almost identical but  $\chi^2_{\nu} = 738$ , indicating a better but still poor fit.

what caused this measurement to be so low. It is possible that a combination of irregular tall paint and inhomogeneous concentration of wire strands, not present in the model, combined to create a location of significant shielding on the face of the device. Still, one might expect the spatial averaging of the  $1 \times 1 \text{ mm}^2$  beam to smooth this effect, but that does not appear to have happened. It is possible therefore that this low measurement was the result of a problem with the measurement itself. The fit was performed both with and without this point. The value of  $\alpha$  barely changed between the two (the change not being visible when plotted), but the orthogonal  $\chi_v^2 = 738$ , indicating a better, but still underfitting, model. A modification of the model was also tried which allowed an  $E_{\text{dep}}$  offset corresponding to a threshold energy deposition rate for measurable current generation, but this led to a very similar fit and an increase in  $\chi_v^2$ , suggesting that any additional closeness of fit achieved with the offset was not justified by the increase in model flexibility the offset supplied. All of this suggests that, although there is a positive correlation between the measured  $I_{\text{SC}}$  and the simulated  $E_{\text{dep}}$ , a direct proportionality is not sufficient to explain their relationship, even if it captures the main thrust of the relationship. The SP8 experiment was the only one in this work in which neither energy nor incident flux was changed. As such, the approximate agreement of the measurements with the simulation could suggest that the basic philosophy of the model, in treating the entire diamond volume of a cell as the collection volume, might be approximately correct. Given that a certain amount of inaccuracy is to be expected in simulations where there are idealised components - the silver epoxy being modelled as a truncated cone rather than an irregular blob, the wires being treated as a flat collection of parallel wires rather than a curved and twisted cable - the influence of these discrepancies may be enough to account for the deviation in the data from the model. By avoiding varying photon flux or energy, this paired simulation/measurement experiment was designed to attempt to validate the energy deposition accuracy of the simulation in the hope that this would allow the simulations in experiments later in the work to rest with some confidence on the energy deposition and focus on the influence of other factors. In the final analysis it seems that the validation of the simulation is open to question; the variation between the simulation and the measurements could be due to over-simplified components but a true model, reasonably-simplified components but a false model, or indeed, over-simplified components and a false model. So, energy deposition simulations later in this work should be understood to have the caveat that they may be only approximately correct, despite the effort to simulate the device geometry as closely as possible.

I chose to use silver epoxy in mounting cells into DGVs primarily on the basis that it is robust, conductive, and easily removed. That is to say, for mounting and dismounting prototypical devices which were expected to progress through various permutations and cycles of re-use, silver epoxy was chosen for its practical value for experiments rather than as a candidate for final device packaging. For this latter task, I have always assumed that gold wire bonding would be needed. It is somewhat ironic, therefore, that the presence of silver epoxy seems to have contributed significantly to the output of the cell in this experiment and presumably, by extension, all other experiments in this work. It remains the case that any commercial DGV made according to the presented design would not be

packaged with silver epoxy and that gold wire bonding would likely be required. However, this result emphasizes the need for future research to explore deliberately placing material in front of the DGV as a scatter shroud, to boost power performance.

## 5.3 Probing an interaction crossover region at the Diamond Light Source synchrotron

With the model geometry validated in the previous section, the DLS experiment sought to test the same DGV with a full-frontal irradiation, with photon energies varying from 50 - 150 keV. Any deviation in agreement between simulation and performance could then tentatively be attributed to electrical changes (i.e. those not simulated by GEANT4) brought about by the photon energy.

### 5.3.1 GEANT4 simulation of a single-celled DGV irradiated by the DLS synchrotron

#### 5.3.1.1 Simulation Details

This simulation used the same geometry as shown in Figure 5.1. Rather than simulating monoenergetic photons, this simulation used a Monte Carlo approach, randomly selecting energies from a normal distribution with a standard deviation of 20 eV, to match the energy width of the synchrotron beam. The means of the distribution were the energies as measured during the DLS experiment.

Because the flux was known, and the  $E_{\text{dep}}$  was linear with flux as far as GEANT4 was concerned, the energy and power deposition into the diamond during the synchrotron experiment could be modelled exactly.

The DLS version of the single cell simulation only differed from the monoenergetic case by a few lines in two files, but for administrative reasons the two simulations were kept in separate Git repositories. The Git repository for this simulation can be found at

<https://bitbucket.org/RobbieMackenzie/singlecelldls/src/main/>

#### 5.3.1.2 Simulation Results

Figure 5.4 shows the results of the simulation. Of note is the small but clear rise in the number of hits between the 79.95 and 81.08 keV photon energies. This leads to a rise in the total energy deposited during the simulation. The gold k-absorption edge is at approximately 80 keV [303] (as visible in Figure 1.2), so this sharp rise between the two energies is attributed to the gold in the electrical contacts to the device, despite these only being 100 nm thick each. Other than this rise, the hits consistently decrease with increasing photon energy as the interaction probability decreases. However, the energy deposited by each hit increases with photon energy and increases faster, meaning that overall, the predominant conclusion to be drawn from this simulation is that over the energies used at DLS, a roughly linear rise in device output should be expected for equal flux. Exact power deposition could

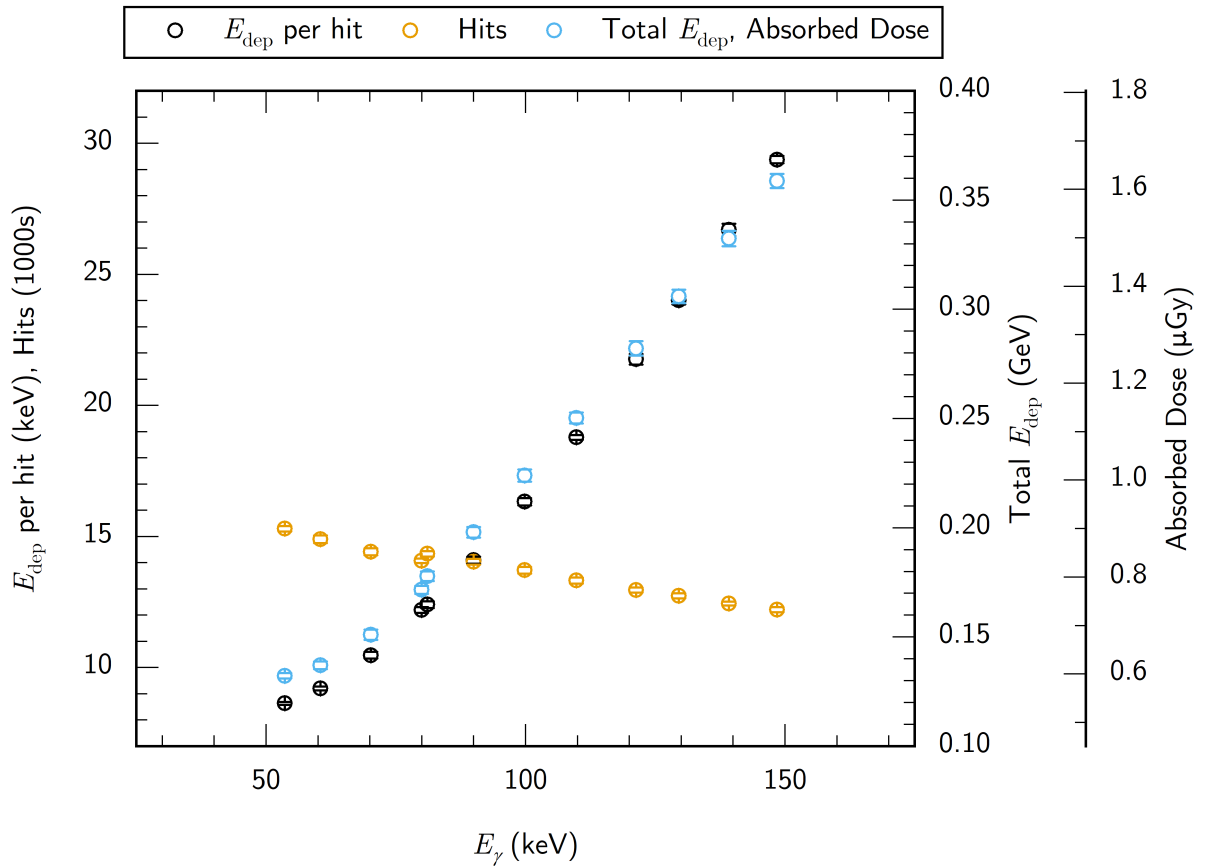


FIGURE 5.4. GEANT4 simulation data of the number of hits, the energy deposited per hit, and the energy deposited in total for a single-celled DGV with 500,000 incident primary gamma rays, with the energy profiles used at the DLS synchrotron. 10 million gamma rays were spread out over 20 threads. An additional ordinate is provided to convert between total energy deposited in GeV and absorbed dose in Gy, taking the mass of the diamond into account.

be calculated from the simulation data, and used to calculate power conversion efficiencies for the device at different energies. These calculations are presented in the next section.

### 5.3.2 Current-voltage and power-voltage curves, power efficiencies and flux-normalised quantities

#### 5.3.2.1 Raw current-voltage and power-voltage curves with photon energy and flux varying

Figure 5.5 shows the  $I$ - $V$  and  $P$ - $V$  curves taken with the single-celled DGV at the DLS synchrotron. The device parameters for the device, extracted from Figure 5.5, are shown in Figure 5.6. At this stage they are plotted against both photon energy and flux. The kinks observable in the otherwise smooth  $I$ - $V$  and  $P$ - $V$  curves were later attributed to auto-ranging errors from the multimeter, leading to the measurement control code to be altered to manual range selection for future experiments. Uncertainty was sometimes greater for specified values and sometimes greater for statistical values, so the larger of the two was used on a point-by-point basis. Both are not really visible in the  $I$ - $V$  trace, but the uncertainty is visible when propagated through to the  $P$ - $V$  curves. Uncertainty was propagated without considering covariance between  $I$  and  $V$ . Fitting of the  $I$ - $V$  curves with the opposing-diodes model has not been attempted here, as the voltage range used was not wide enough to allow a good estimate of the parameters the opposing-diodes model adds to the conventional photovoltaic model. There is an argument for attempting a fit with the conventional model, but as mentioned in Section 2.2, the additional parameters in the opposing-diodes model are covariant with those in the conventional model. So, values for parameters which are shared, such as the  $R_s$ , might change depending on which model was used to estimate them. It may be stated that, as the  $P$ - $V$  curves look quite symmetrical, parasitic resistances are likely to exert a fairly strong influence on the electrical behaviour of the device. The device consistently achieved a  $V_{OC}$  around 0.8 V, although the value changed in a systematic way rather than appearing to vary randomly. Likewise the  $I_{SC}$  rose and then fell, being around 1  $\mu$ A in magnitude. The maximum measured power for each energy was taken as an approximation to the  $P_{MPP}$ , and appeared to be more or less proportional the  $I_{SC}$ . This was because the  $V_{MPP}$  stayed similar across curves, as visible in Figure 5.5. The  $FF$  values were fairly consistent across all curves, varying predominantly within the same band of estimated uncertainty. In each of the four parameters in Figure 5.6 except the  $I_{SC}$ , there is a noticeable deviation at 81.08 keV. This point was taken after all the others in a return to the gold k-absorption edge, where the simulation in Figure 5.4 suggested there should be a small but abrupt bump in energy deposition due to an increase in the number of photons absorbed. The discontinuity in energy deposition here was used as a place to look for degradation. In Figure 5.6 it can be seen that this point was not a small bump, but a small dip. This could be evidence of degradation during the run. Particularly, the  $FF$  looks out of place at 81.02 keV and lends the whole plot an appearance of the  $FF$  not changing in a very systematic way. However, if the points are imagined against time rather than photon energy - meaning the other points stay in the same order but the 81.02 keV point is moved to the end - then the impression is a bit different, and more suggestive that perhaps the  $FF$  was decreasing

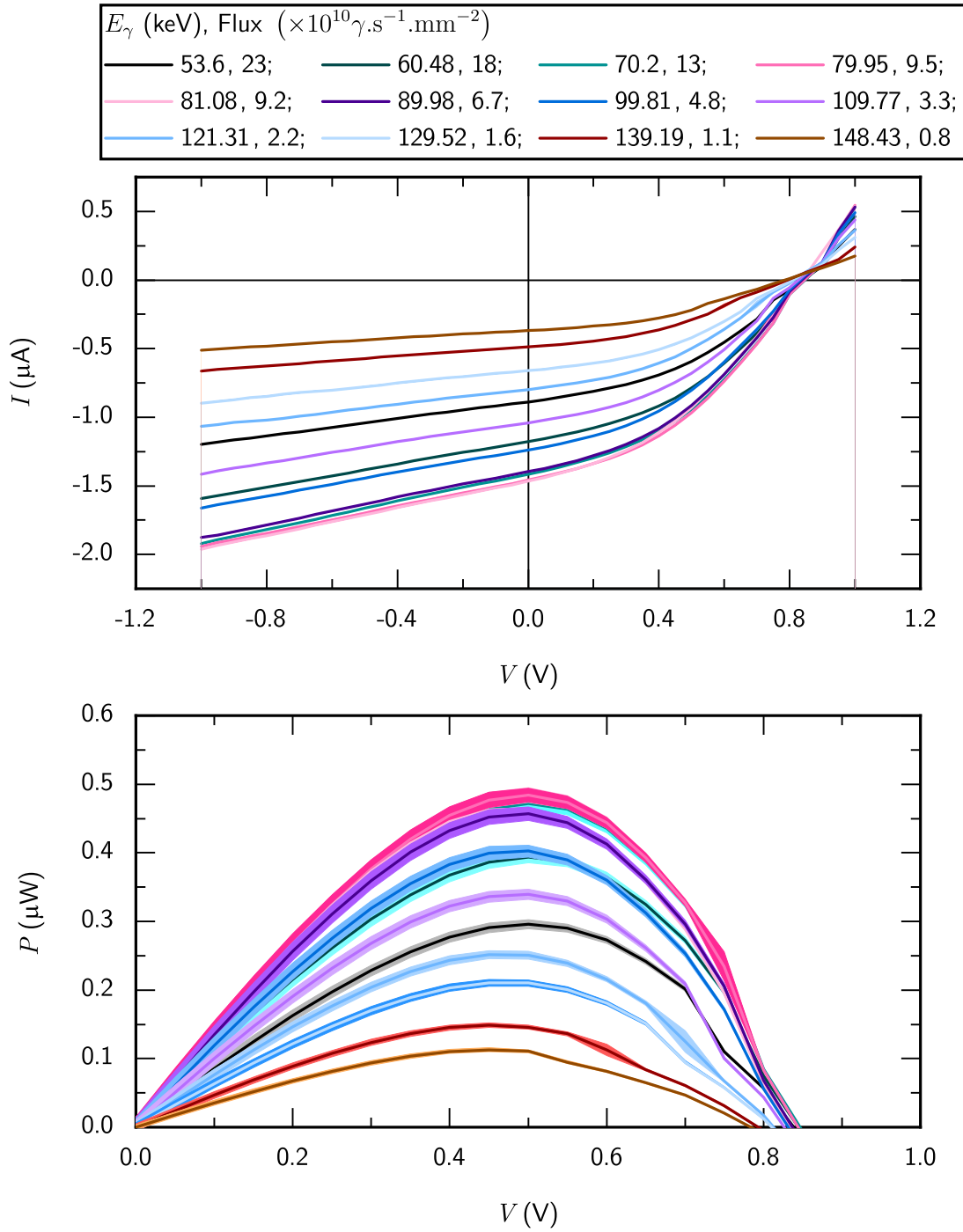


FIGURE 5.5. The raw  $I - V$  and resultant  $P - V$  data taken at the DLS synchrotron, before normalisation by flux.

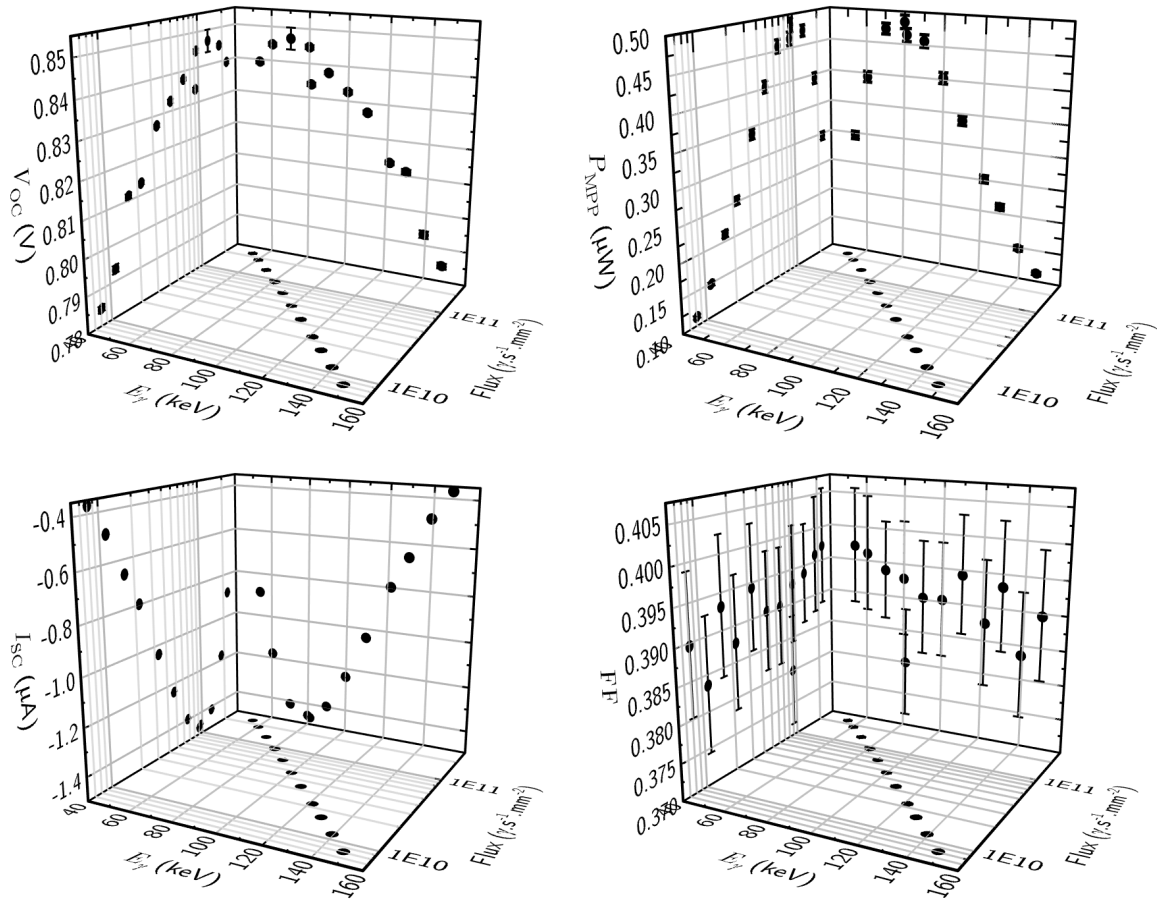


FIGURE 5.6. Parameters extracted from Figure 5.5, shown against both flux and photon energy. Uncertainty values for the  $V_{OC}$  are double-sided as they were found by linear interpolation between error bars, much like the  $V_{OC}$  values themselves were found by interpolation. Uncertainty was propagated to the  $P_{MPP}$  without consideration of covariance.

with time. Each measurement took approximately 15 minutes which was another feature of the auto-ranging issue; the speed of runs was later increased substantially by use of manual ranging. By reference to the simulated absorbed dose rate, this suggests that between the 79.95 and 81.02 keV measurements, the device had absorbed a dose of around 6 kGy. This degradation was therefore relatively minor, although it should be noted that the fact DGVs are eventually envisioned for very long-term deployment, this degradation cannot be written off as negligible. Furthermore, absorbed diamond dose rate is greater than the air KERMA dose rate. All the photon energies employed here are lower than those expected to cause lattice damage in diamond at any dose rate [108]. Whilst little damage occurred to the device during the DLS experiment itself, it failed to operate in later experiments. Performance was later entirely regenerated by re-terminating and remounting. These things taken together, possible sources of degradation are catastrophic resistance increase caused by desorption of surface hydrogen [256, 304], simple manual handling issues, and/or structural damage to the silver epoxy adhesive by x-rays. These latter two issues would be due to the prototypical nature of the test mounting. On hydrogen desorption: researchers have cautioned against using hydrogen terminated diamond surfaces as the basis of transistors in the past due to stability concerns [256]. However more recently, as mentioned in the Introduction, there has been great progress in stabilising the surface for applications in high temperatures [194]. Using the passive electrically depleting effect of a deposited  $\text{HfO}_2$  layer and Ti/Au contact, one group have even created a normally-off MOSFET based on hydrogen-terminated diamond [305], suggesting that the use of an encapsulating layer has distinct potential both for stabilizing and enhancing the DGV. It is of course not logical to use diamond for its bulk radiation hardness if the surface termination is overly sensitive.

### 5.3.2.2 Power efficiencies

Figure 5.7 shows the estimated deposited powers  $P_{\text{dep}}$  for each curve, alongside the  $P_{\text{MPP}}$  values. To calculate the power depositions values, the total energy deposition values from the GEANT4 simulations were multiplied by the flux values from Figure 3.5 and divided by 500,000, the number of events simulated per thread. The figure also shows the maximum power conversion efficiencies,  $\eta$ , and maximum deposited power conversion efficiencies,  $\eta_{\text{dep}}$ . In line with the caveat on energy deposition simulations in Section 5.2, it should be noted that of the four quantities plotted against  $E_\gamma$  in Figure 5.7,  $P_{\text{dep}}$  and  $\eta_{\text{dep}}$  are vulnerable to any inaccuracy in the simulations.

There is a clear difference between the forms of the power deposited into the device and the power extracted from it. This is reflected in the  $\eta_{\text{dep}}$  values, which rise with increasing photon energy between 50 and 100 keV and then stabilise. Because both the flux and  $P_{\text{dep}}$  are decreasing with increasing  $E_\gamma$ , the rise in  $P_{\text{MPP}}$  with  $E_\gamma$  before about 80 keV may be attributed with some confidence to  $E_\gamma$ , in agreement with the overall picture painted by the simulation results of Figure 5.4 which suggests energy deposition should rise with  $E_\gamma$  for equal flux in this range of energy. It seems likely that 80 keV was the point at which the decreasing flux and  $P_{\text{dep}}$  began to overwhelm the effect of increasing  $E_\gamma$ . The increase in deposited power due to the gold k-absorption edge is reduced

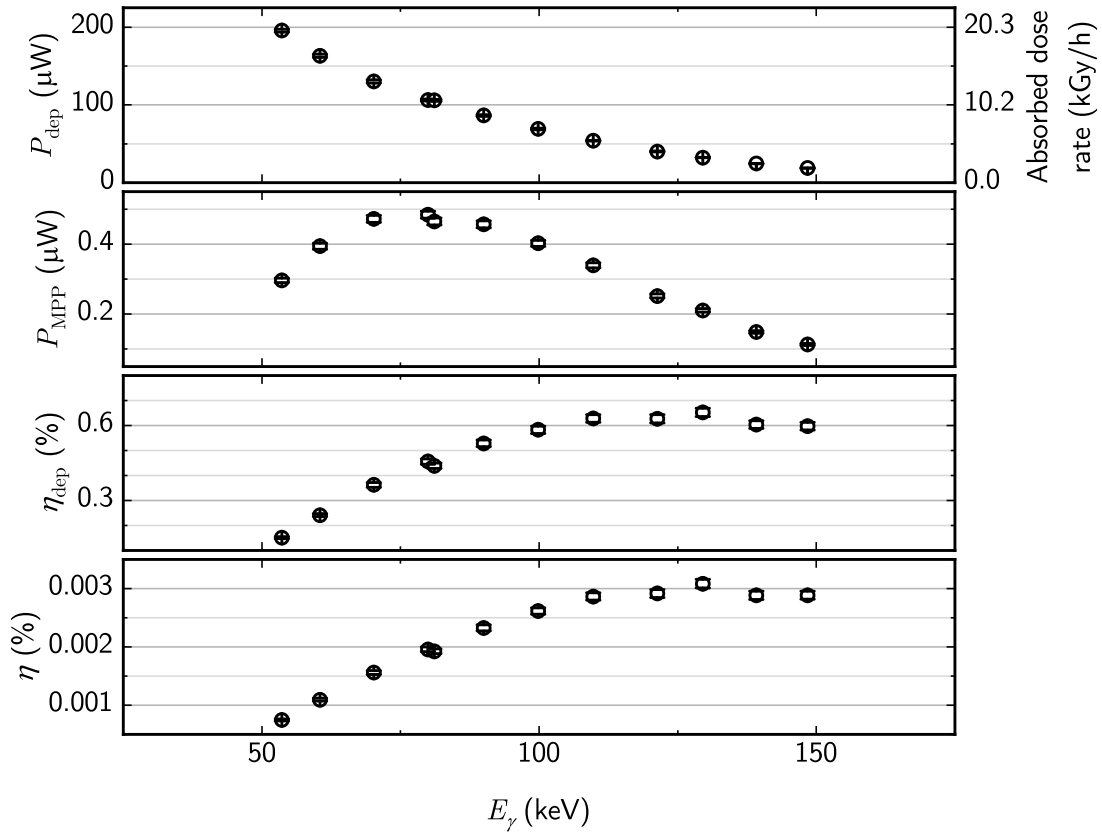


FIGURE 5.7. Various simulated and measured quantities relating to power conversion against photon energy, with flux information incorporated. The quantities are the simulated power deposited  $P_{\text{dep}}$  (and the related quantity of absorbed dose rate, accounting for the diamond mass of 35 mg), the maximum measured power  $P_{\text{MPP}}$ , the maximum deposited power conversion efficiency  $\eta_{\text{dep}}$ , and the maximum incident power conversion efficiency  $\eta$ .

somewhat by convolution with the flux of the synchrotron, but remains a noticeable feature.

Both  $\eta_{\text{dep}}$  and  $\eta$  are low, with  $\eta$  being particularly so. The amount of power generated in this experiment is enough that a low-power circuit could make use of it, but with such low efficiencies it remains the case that a DGV such as this would be useful only in situations where there was really not other source of power and a significant need for sensing. The Am-241 energy was covered and the flux was highly directional, allowing  $\frac{\text{Am-241}}{20,000} \mathfrak{P} = 38907 \text{ nA/cm}^3$  and  $\frac{\text{Am-241}}{20,000} \mathfrak{p} = 1945 \text{ nA/cm}^2$  to be calculated using the approximate conversion between flux and air KERMA of Veinot and Hertel [264]. The specific activity of Am-241 is 129.5 GBq/g [306], so a flux of this magnitude corresponds to what might be expected from somewhat more than 28.7 g of pure Am-241. For comparison, UK law requires ionisation chamber detectors to have no more than 760 kBq of Am-241 inside [307], corresponding to about 6  $\mu\text{g}$ . Domestic smoke detectors contain about 0.29  $\mu\text{g}$  [308]. Also, the conversion is not exact because the flux would be omni-directional and the source would exhibit self-absorption, so in fact, the mass needed would be greater. This does not seem of much use for device design. However it is also of note, with regard to the Am-241 energy, was that the total  $E_{\text{dep}}$  calculated in the GEANT4 simulation was poor relative to other photon energies. Despite being unusually well-matched to Fe-55, and hardly less so to Cs-137 and Co-60, the presented DGV design is almost at its least effective for the Am-241 emission in terms of absorption. This is a result of an "anti-optimisation": at the emission energy of Am-241, photons have too much energy to be predominantly absorbed by the device, as Fe-55 gamma photons are, but too little for those which are absorbed to deposit much energy by comparison to those of Cs-137 or Co-60. This fact, in combination with the fact that the environment of space would rob a bare DGV of the adsorbed water vapour necessary for the surface to conduct, makes the DGV design presented here distinctly unsuited to the kind of space applications where Am-241 is often found. It would seem to be far better suited to its intended application in nuclear waste stores where, Becquerel for Becquerel, the GEANT4 simulation would suggest that  $\eta$  would be ten times greater. In this way this experiment demonstrated the fundamental difficulty with efficiency when working with gammavoltaics which has tended to lend favour to the development of other types of radiovoltaic.

### 5.3.2.3 Flux normalised values

Figure 5.8 shows the  $I_{\text{SC}}$  and  $P_{\text{MPP}}$  values normalised by flux to that of the 53.6 keV curve ( $2.3 \times 10^{11} \text{ } \gamma \cdot \text{s}^{-1} \cdot \text{mm}^{-2}$ ). Normalising in flux in this way relies on the fairly stable  $V_{\text{OC}}$  and is in some sense the same as assuming that the values for  $FF$ ,  $\eta_{\text{dep}}$  and  $\eta$  are constant with flux in this region of the energy-flux space. As mentioned at the start of this chapter, it may be invalid if carrier temperature or concentration effects play a significant role and lead the aforementioned quantities to change. The motivation for performing flux normalisation is to try to isolate the effect of photon energy on the operation of the DGV. For the  $I_{\text{SC}}$  and  $P_{\text{MPP}}$  values at least it would seem that the effect of photon energy is not too far from linear, with a slightly sigmoidal shape that may be attributable to a mixture of the power deposition with photon energy (i.e. Figure 5.4) and the deposited power efficiency

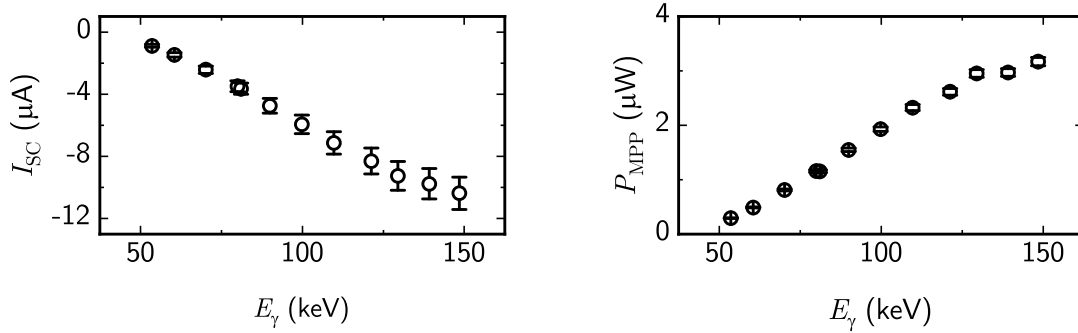


FIGURE 5.8. The short circuit current and maximum power-point power values from Figure 5.6, now normalised by photon flux in an attempt to isolate the effect of photon energy. The flux was normalised to that of the point at 53.6 keV.

(Figure 5.7). There is no obvious qualitative difference between the regions where photoelectric absorption dominates (lower energies) and where Compton scattering dominated (higher energies) for the  $I_{SC}$  and  $P_{MPP}$ . In the paper based on this work which was discussed at the start of the chapter [65], the series resistance appeared to be changing in a manner which was suggestive of a link to Compton scattering. Extraction of equivalent circuit parameters is not presented in the newer treatment of the data here - more work is needed to decide the most reliable way of doing this and of assessing the reliability of the results. It seems likely that a more developed theoretical understanding of the device should be sought first.



## ISOTOPE IRRADIATION STUDIES FOR MORE REALISTIC PERFORMANCE ASSESSMENT

This chapter presents data collected using a triple-celled DGV, made from all three cells fabricated (E6\_ELSC\_2, E6\_ELSC\_3 and E6\_ELSC\_5), under irradiation from radioisotopic gamma sources, with more of a focus on real-world performance than the last chapter. This chapter will predominantly concern **applicability** to nuclear waste stores, **comparability** to literature and **longevity** under the highest dose rate found in a waste store. As with the last chapter, the results of a GEANT4 simulation over the Gamut in 1 keV steps is first presented, with each cell in the DGV treated independently. That is to say, three simulations were run, with one cell treated as the sensitive volume each time. *I-V* curves are then presented, taken at different dose rates using Cs-137 and Co-60 at the facilities mentioned in Section 3.3. The opposing-diodes model is fit and circuit parameters estimated. Finally, a longevity experiment is presented in which 3,192 *I-V* curves were taken over the course of 3.5 wks at 1,350 Gy/h air KERMA of Cs-137 gamma rays, to a total air KERMA dose of over 800 kGy.

At the time of writing, results from this chapter are being prepared for an article entitled *A triple-celled diamond gammavoltaic device tested for performance and longevity under irradiation from Cs-137 and Co-60 gamma rays*. The Co-60 experiment benefited from the help of Dr. Chris Hutson, as did one of the Cs-137 experiments. The long Cs-137 experiment and the simulation work, I arranged and undertook alone.

## 6.1 GEANT4 simulation of a triple-celled DGV irradiated with monoenergetic 1 -2000 keV photons

### 6.1.1 Simulation details

The simulation geometry used for the triple-celled DGV can be seen in Figure 6.1. As would be expected, it is very similar to that used for the single cell case. However, the use of three cells meant silver epoxy was also used to glue the cells together and make electrical contact between them, and these dots of epoxy were modelled as thin discs between cells. As in the previous chapter, ten million primary photons were simulated.

The Git repository for this simulation can be found at

<https://bitbucket.org/RobbieMackenzie/triplecellmono/src/main/>

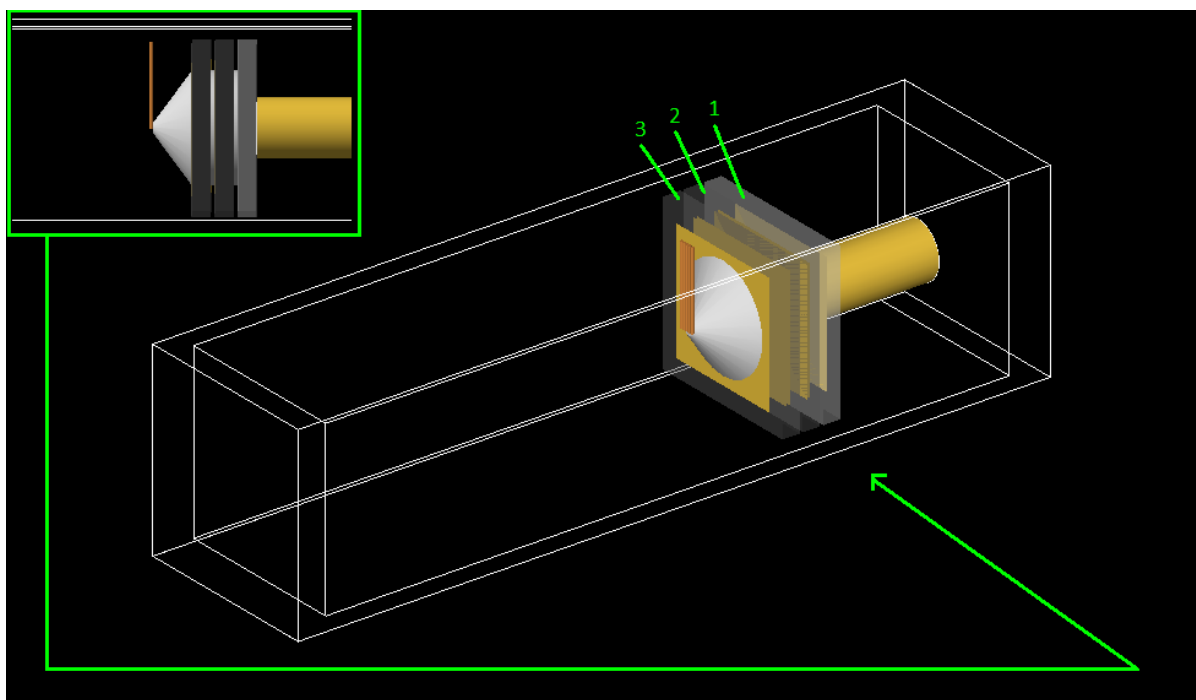


FIGURE 6.1. The GEANT4 geometry used for simulating the triple-celled DGV, showing cell numbers as labelled. Gamma rays originated at randomly-generated positions in a planar square region the same size as the cell cross-section on the left-hand side of the simulation cuboid. **Inset:** a side-on image of the device, showing the silver epoxy in between individual cells, which was modelled as a set of discs. Cell sensitivity was turned on or off for each cell with hard-coding. The figure shows the sensitive cell, in this case Cell1 to the rear, as sensitive by using a lighter shade to colour it.

### 6.1.2 Simulation Results

Figure 6.2 shows the total energy deposited into each cell of the triple-celled DGV during the simulation. Notably, the energy deposition behaviour for the cell closest to the radiation source, Cell3, is very similar to that presented in the previous simulation of a single-celled DGV, in Section 5.1. The result suggests backscatter from the other two cells, and associated silver paint, is not a significant source of energy deposition. At the lowest energies simulated, which are shown at greater magnification in the figure inset, it is clear that photons of the lowest energy do not penetrate through Cell3; they are fully attenuated. Only once the photon energy reaches 4 keV do the photons penetrate to the middle cell, Cell2. Once the photon energy reaches 5 keV, the photons begin to penetrate to the far cell, Cell1.

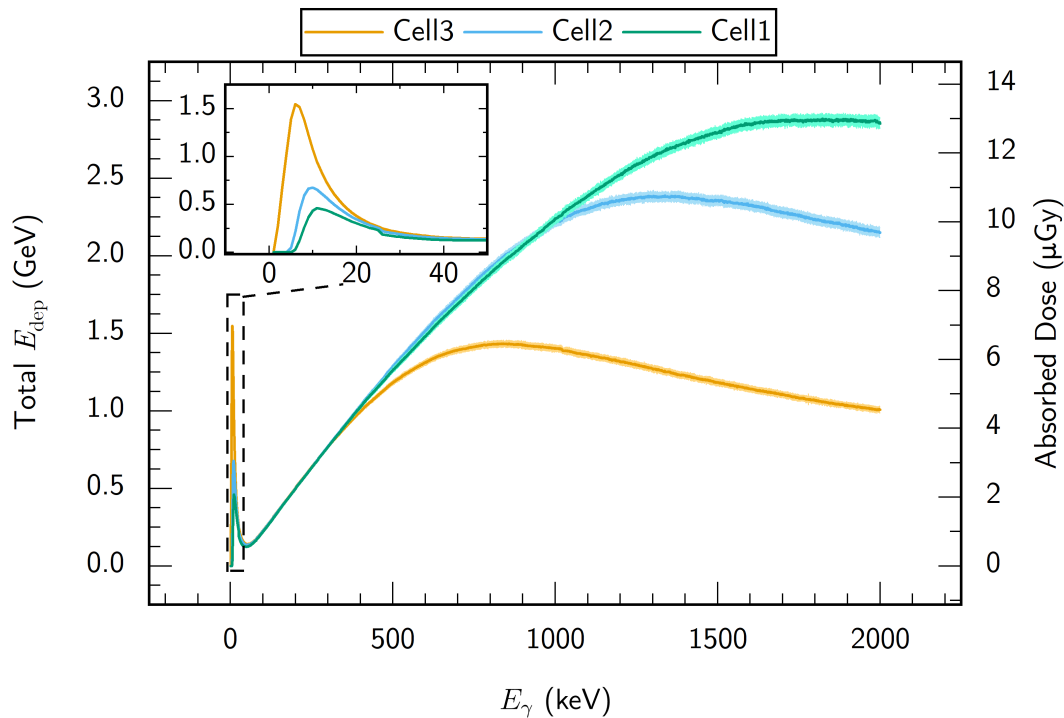


FIGURE 6.2. The total energy deposited into each cell of a triple-celled DGV, and the associated absorbed dose, when the DGV was simulated under 500,000 monoenergetic gamma rays between 1 and 2000 keV in 1 keV steps. **Inset:** a zoomed-in view of the lower-energy section of the data bounded by the dashed line. Cell number labels are as in Figure 6.1.

Because the cells are in series, and therefore must have equal current flowing through them, it might be expected that the triple-celled DGV would not work at all for photon energies below 5 keV due to this self-shielding. This has a certain bearing on the results obtained in Chapter 4.2 with the XRT, as it may mean much of the bremsstrahlung spectrum could not contribute if a triple-celled

DGV were to be used instead of a single-celled DGV under such circumstances. Between 5 and 40 keV, the device would be expected to work, but be throttled by the lower energy depositing into Cell1, much as the power output of a solar panel faces a bottleneck if a portion of the cells in the panel are shaded by the shadow of clouds, tree branches or dust [309]. Between approximately 40 to 400 keV, the energy deposited into the three cells is equal; this region of photon energy represents the best stackwise behaviour, where additional output voltage does not come at the cost of current generating efficiency. At energies greater than approximately 400 keV, the earlier observed relationship has started to reverse, with Cell2 and Cell1 receiving greater energy deposition than Cell3. Because Cell3 receives much the same energy deposition as the cell in the single-celled DGV, stacking cells in this configuration for energies above 400 keV is not expected to reduce the current *generated* compared to the single-celled case (at least in terms of energy deposition; device resistance is another matter). However, it would have lower *generating efficiency*. The effect is not too great at 662 keV, the photon energy of Cs-137 gamma rays [50]. However, at the Co-60 energies of 1170 and 1340 keV [51], the effect is much more substantial. By 2000 keV, the difference in energy deposition between Cell1 and Cell3 is greater than a factor of 3. All things being equal, the device would be losing half of the power it could be generating with the energy deposited into it at 2000 keV, due to Cell3 throttling Cell2 to approximately 50 % and Cell1 to approximately 33 %. So, although the practice of stacking three cells into a DGV to increase voltage is not expected to decrease current generation at Cs-137 and Co-60 energies, it is expected to create a device that uses the energy deposited into it less efficiently.

Looked at another way, however, the results of this simulation naturally raise the suggestion, once again, that the power output of a given cell may be increased substantially if a material is placed in front of it, should the material and thickness be chosen carefully, to increase photon energy deposition without relying on a scintillator whose mechanism may degrade under irradiation. This echoes the effect exhibited by the silver paint in the last chapter and strengthens the case for future study. Of course, Horiuchi *et al* found that scintillators, by producing light at wavelengths for which solar photovoltaics are optimised, improved the power output of their voltaics by several orders of magnitude [35] over their base line; it is unlikely that even an optimised scatter shroud could do this for a diamond gammavoltaic. Another interpretation might suggest simply presenting the DGV side-on to the radiation rather than involving a scatter shroud, so that it might present a deeper collection volume at the expense of surface area. This was not pursued in this work, but it is given some attention in Section 7.2.3.

Based purely on energy deposition considerations from this simulation, irradiation of a triple-celled DGV with Cs-137 radiation is expected to produce slightly higher power than with Co-60 radiation, due to the device in both circumstances being throttled by Cell3. The Co-60 energies are above the pair production threshold at 1022 keV [310], but there is no distinguishing feature in the energy deposition in this region.

## 6.2 Irradiation of a triple-celled DGV with Cs-137 and Co-60 gamma rays

Figure 6.3 shows the  $I-V$  and  $P-V$  curves for the Cs-137 irradiation together, first, so that their relation to each other can be seen. The measurement uncertainty is propagated through from the  $I-V$  to the  $P-V$  curves without accounting for correlation between the variables. Each  $I-V$  curve is then plotted separately so that its individual features may be observed, alongside a fit obtained using ODR and the opposing-diodes model, as well as line plots and histograms of the instrumentally-weighted current and voltage residuals. These are plotted as Figures 6.4 to 6.9 on pages 127 to 132.

Likewise, Figure 6.10 on page 133 shows the  $I-V$  and  $P-V$  curves for the Co-60 irradiation, with the same caveat about the uncertainty values used in the  $P-V$  plot, and the individual curves with their fits are shown in Figures 6.11 to 6.22 on pages 134 to 145. The  $I-V$  trace for 591 Gy/h of Co-60 gamma radiation is truncated in Figure 6.10. This is believed to be because the automation software halted recording due to computer hibernation during a lunch break. This was not known until after the experimental session. As such, fitting has not been performed for this dataset. When measurement uncertainty is taken into account, the two lowest Co-60 dose rate cases, 13 and 17 Gy/h (shown in Figures 6.11 and 6.12 on pages 134 and 135), do not pass the basic "third quadrant"  $I-V$  test: it cannot be said the DGV was definitely producing power at these dose rates, despite the shape of the curves. The fits of the opposing-diodes model for these dose rates of Co-60 gamma rays are also visibly worse than any of the others, with obvious trends in both the current and voltage residual line plots. That the electrical noise is notably greater for the Co-60 data than the Cs-137 data may be due to the manner in which Co-60 gamma rays deposit energy into the crystal. However, it seems more likely that, as the Cs-137 irradiator chamber was lead-lined it was more effective at shielding electromagnetic interference from the device. The bounds used when fitting the opposing-diodes model were  $1 \leq n_1, n_2 \leq 2$ , and all other parameters bound to be positive. The residual line plots look reasonable for most fits, with the exception of the lowest doses of Co-60 as mentioned above, although there is a common tendency for them to spike in voltage and sometimes current near the  $V_{OC}$ . A good demonstration on the influence of the instrumental weighting can be found by comparing the power-producing quadrant with the higher-voltage areas of the curves for higher dose rates under either isotope: the fit deviates from the measured data in both areas, but in the higher-voltage area the instrumentally weighed current residuals stay very small, due to the uncertainty at these points being greater. By contrast, there is a marked increase in the residuals in the power-producing quadrant. It is unfortunate that the power-producing quadrant should, as a rule of thumb, be the region in which the model deviates most from the data, as this is the most important area for engineering purposes. This region is quite strongly affected by the values of the ideality factors, and it may be that restricting them to between 1 and 2 is not suitable for the DGV. Diamond is, after all, a wide band gap material, and the structure of the device does suggest something similar to Frenkel-Poole conduction if the band diagram in Figure 2.14 is valid, so allowing one or both ideality factors to take values larger

than 2 may be justified in light of the references and discussion in Section 2.2. Indeed, preliminary attempts to fit the data whilst allowing the ideality factors to change over a broader range do lead to closer fits, but without a more solid theoretical foundation for allowing this, there is a risk of falling into the trap of a spurious fit.

Despite the deviation of the model in the power-producing region, visual inspection of the residual histograms suggests they are much more tightly distributed around the mean than they would be if normally distributed, and much more so for voltage residuals than current residuals. The Kolmogorov-Smirnov test with Lilliefors correction returns  $p \approx 0$  for the residuals being normally distributed for every set. In the case of voltage residuals, it is worth remembering that the uncertainty values chosen came from the multimeter specification, and take the form of legal statements. They are therefore likely to overestimate the uncertainty in the applied voltage (so that their specification is always met), and this is consistent with the very tight residual distribution. The voltage residuals are in fact so tightly distributed around zero compared to the current residuals that it may be argued that use of ODR over OLS is not necessary in future. In the case of the current residuals, the taking of ten measurements at each voltage is quite a reliable method of uncertainty estimation and so the tight error margins are assumed to be as a result of over-fitting on the part of the ODR algorithm. That said, it is noteworthy that all of the fits terminated due to reaching the iteration limit rather than due to reaching parameter convergence or sum-of-squares convergence. Ironically it may be the case that reducing the iteration limit in future might lead to fits which, whilst less close, provide more physically reliable parameters estimates.

When performing the two-sample KS test between all the permutations of possible pairs of fit residuals across all the data, some patterns in the  $p$ -values did seem to emerge, but not strongly enough to discount the possibility that the patterns had arisen randomly. For example, whilst the vast majority of the  $p$  values were very small (between  $10^{-42}$  and  $10^{-5}$ ), the fits for the Cs-137 data produced the two-sample KS test  $p$ -values between their current residuals shown in Table 6.1.

Air KERMA dose rate (Gy/h)	15	95	273	520	1070	3200
15	1.0	0.55	0.23	3.6E-5	5.6E-5	1.4E-5
95	-	1.0	0.40	8.4E-6	2.2E-5	1.4E-5
273	-	-	1.0	8.9E-5	8.9E-5	3.6E-5
520	-	-	-	1.0	0.15	9.1E-3
1070	-	-	-	-	1.0	0.12

TABLE 6.1.  $p$ -values from the two-sample Kolmogorov-Smirnov test between instrumentally-weighted current residuals from fits to  $I$ - $V$  curves taken under different dose rates of Cs-137 gamma rays. For clarity,  $p$ -values greater than  $\alpha = 0.05$  are shaded in orange.

There are some reasonable  $p$ -values in clusters at the three lower dose rates and the two higher dose rates, meaning the test did not give sufficient reason to reject the hypothesis that the residuals from the 15, 95 and 273 Gy/h tests were drawn from the same distribution, and likewise for the

1070 and 3200 Gy/h tests. On the surface of it this may give some reason to suspect that a similarity exists between the tests in the two groups, and a difference exists between the groups themselves. However, by comparison, there is an even larger value of  $p = 0.72$  between the 15 Gy/h Cs-137 case and the 374 Gy/h Co-60 case, which appears to have arisen randomly as there is no thematic link with other dose rates, other runs with the same isotopes, or other surrounding  $p$ -values. Overall, the safest working conclusion to draw seems to be that the fits are all, or predominantly, overfits, and all relate to their respective datasets in different ways despite the qualitative similarity some of them share to the eye. Both the one-sample and two-sample KS tests strongly rejected the null hypothesis in the overwhelming proportion of cases. Caution should therefore be applied when assessing the parameters extracted by this method.

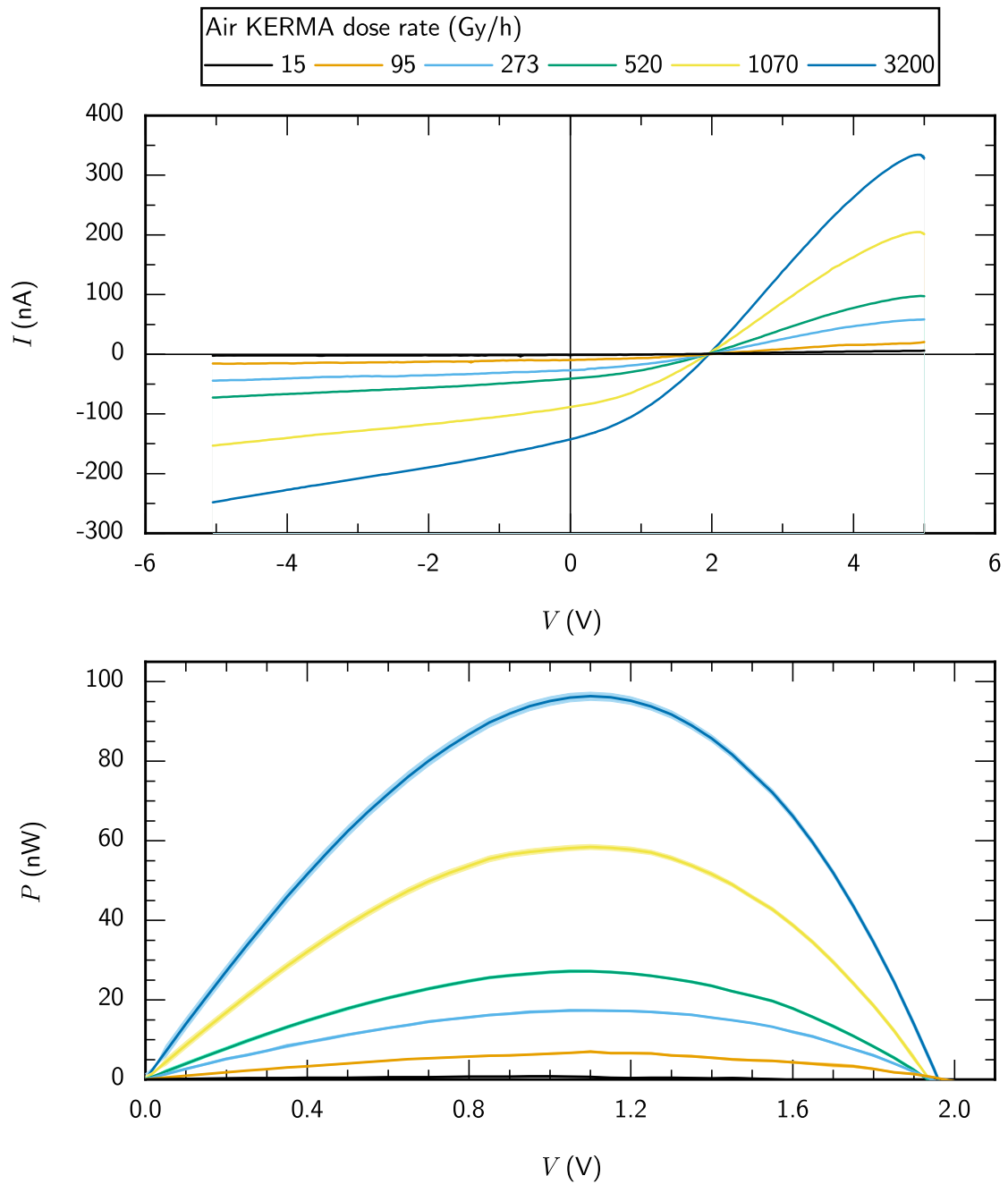


FIGURE 6.3.  $I$ - $V$  and  $P$ - $V$  data from a triple-celled DGV irradiated with dose rates between 15 Gy/h and 3200 Gy/h air KERMA of Cs-137 gamma rays. Uncertainties have been propagated from the  $I$ - $V$  data into the  $P$ - $V$  data without accounting for correlation.

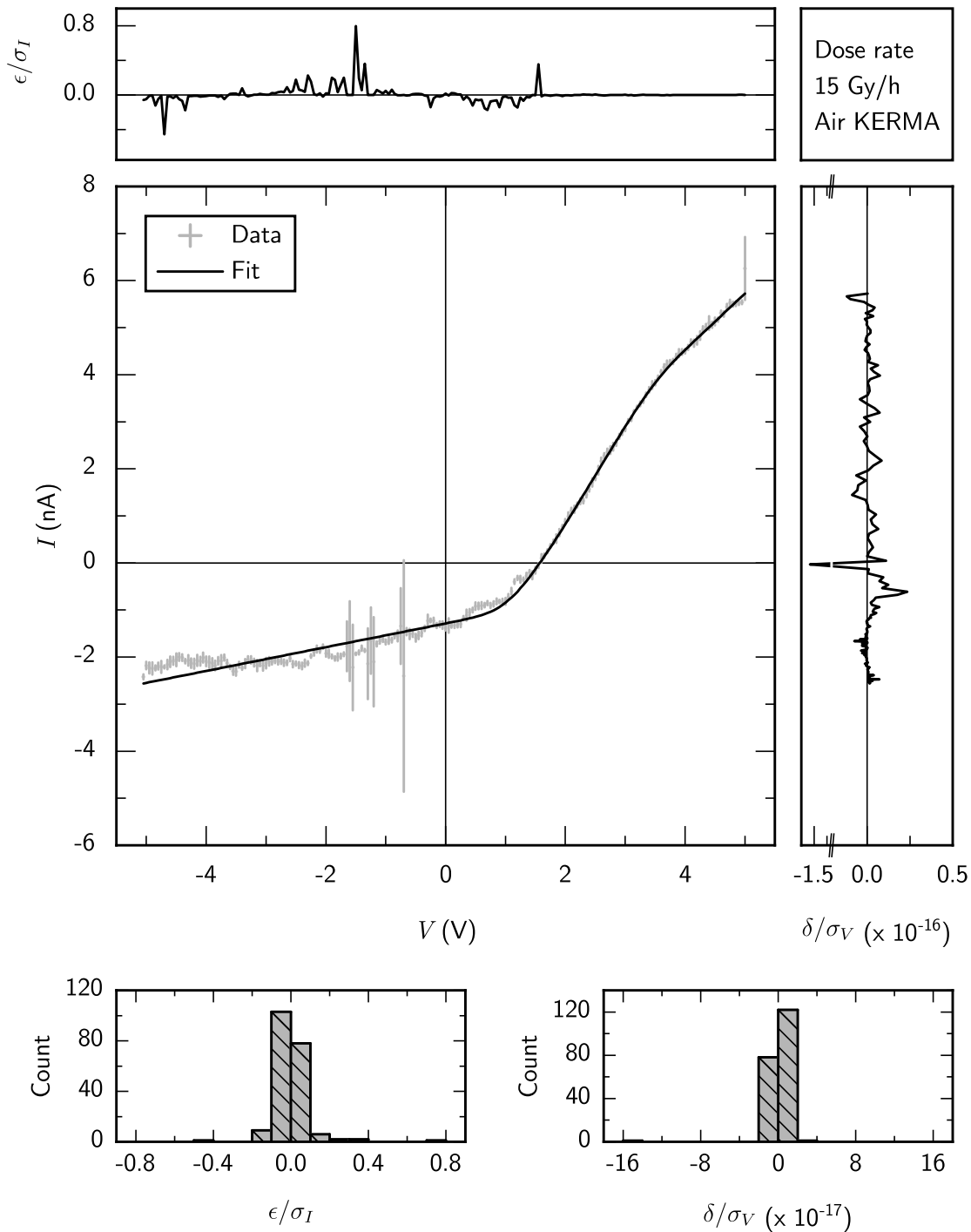


FIGURE 6.4.  $I$ - $V$  data from a triple-celled DGV irradiated with 15 Gy/h air KERMA of Cs-137 gamma rays, fitted with the opposing-diodes model. Also shown are current and voltage residuals  $\epsilon$  and  $\delta$ , scaled at each point by the measurement uncertainty at that point, and histograms of the same. N.B. there is an axis break on the line plot of voltage residuals.

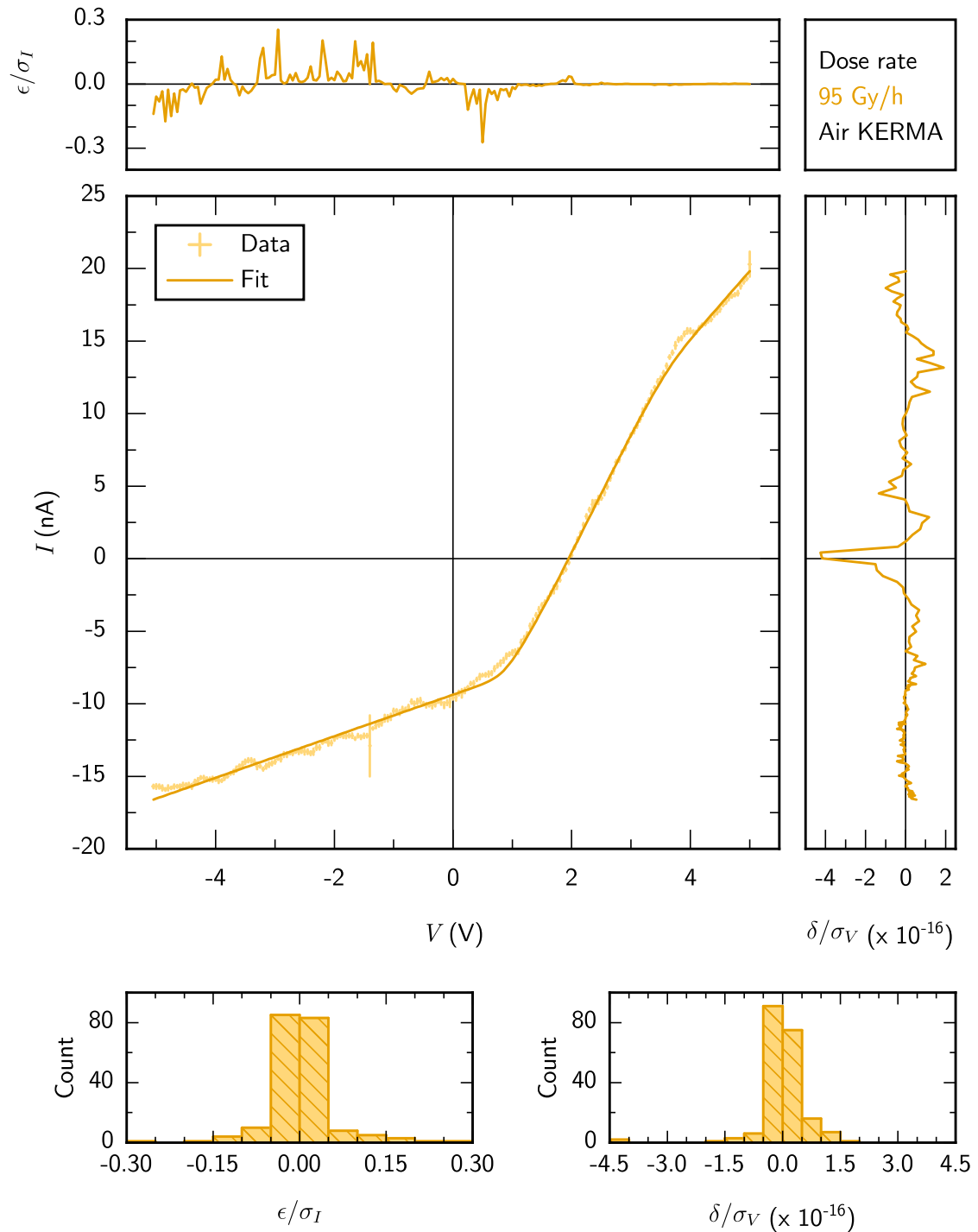


FIGURE 6.5.  $I$ - $V$  data from a triple-celled DGV irradiated with 95 Gy/h air KERMA of Cs-137 gamma rays, fitted with the opposing-diodes model. Also shown are current and voltage residuals  $\epsilon$  and  $\delta$ , scaled at each point by the measurement uncertainty at that point, and histograms of the same.

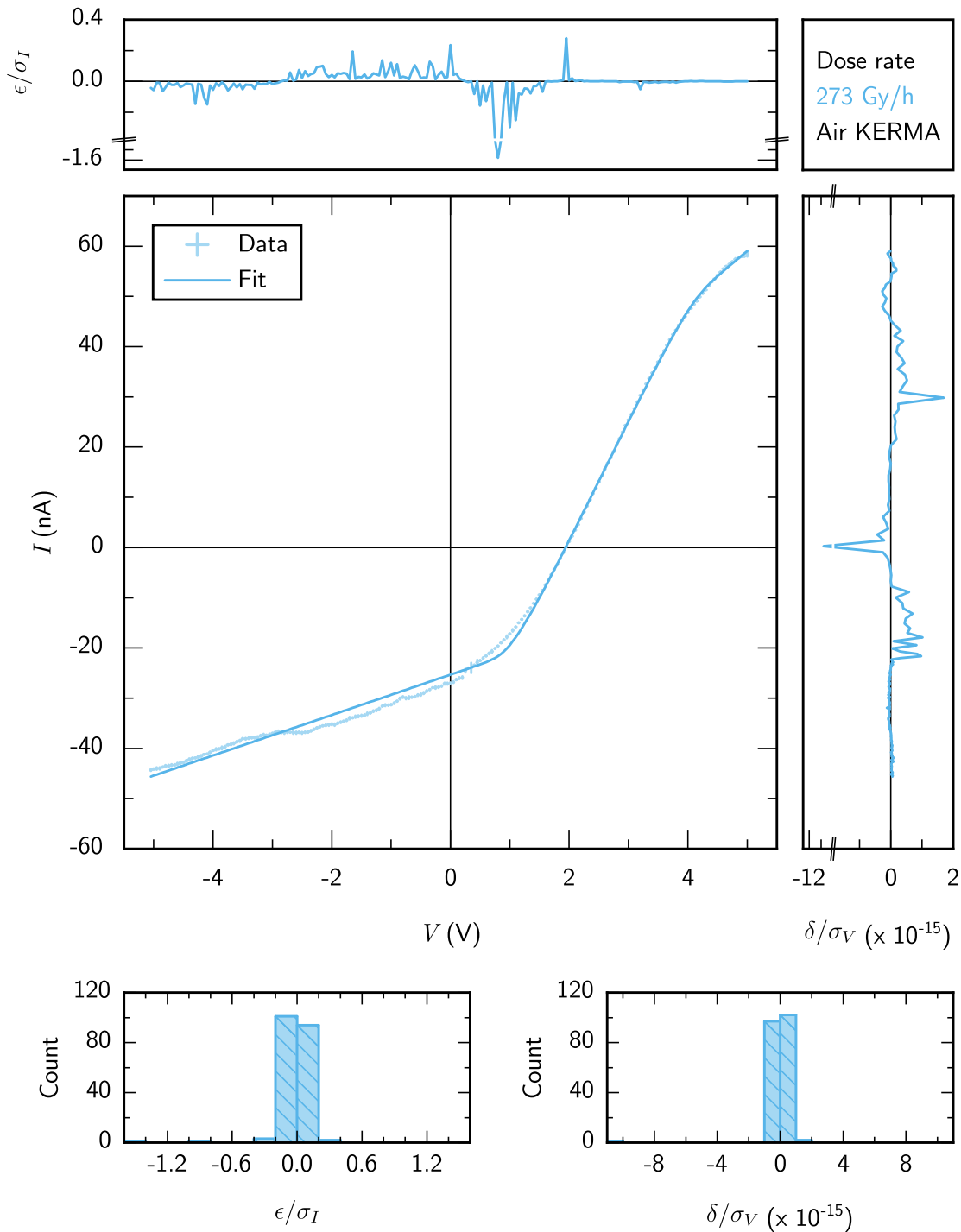


FIGURE 6.6.  $I$ - $V$  data from a triple-celled DGV irradiated with 273 Gy/h air KERMA of Cs-137 gamma rays, fitted with the opposing-diodes model. Also shown are current and voltage residuals  $\epsilon$  and  $\delta$ , scaled at each point by the measurement uncertainty at that point, and histograms of the same. N.B. there are axis breaks on the line plots of the residuals.

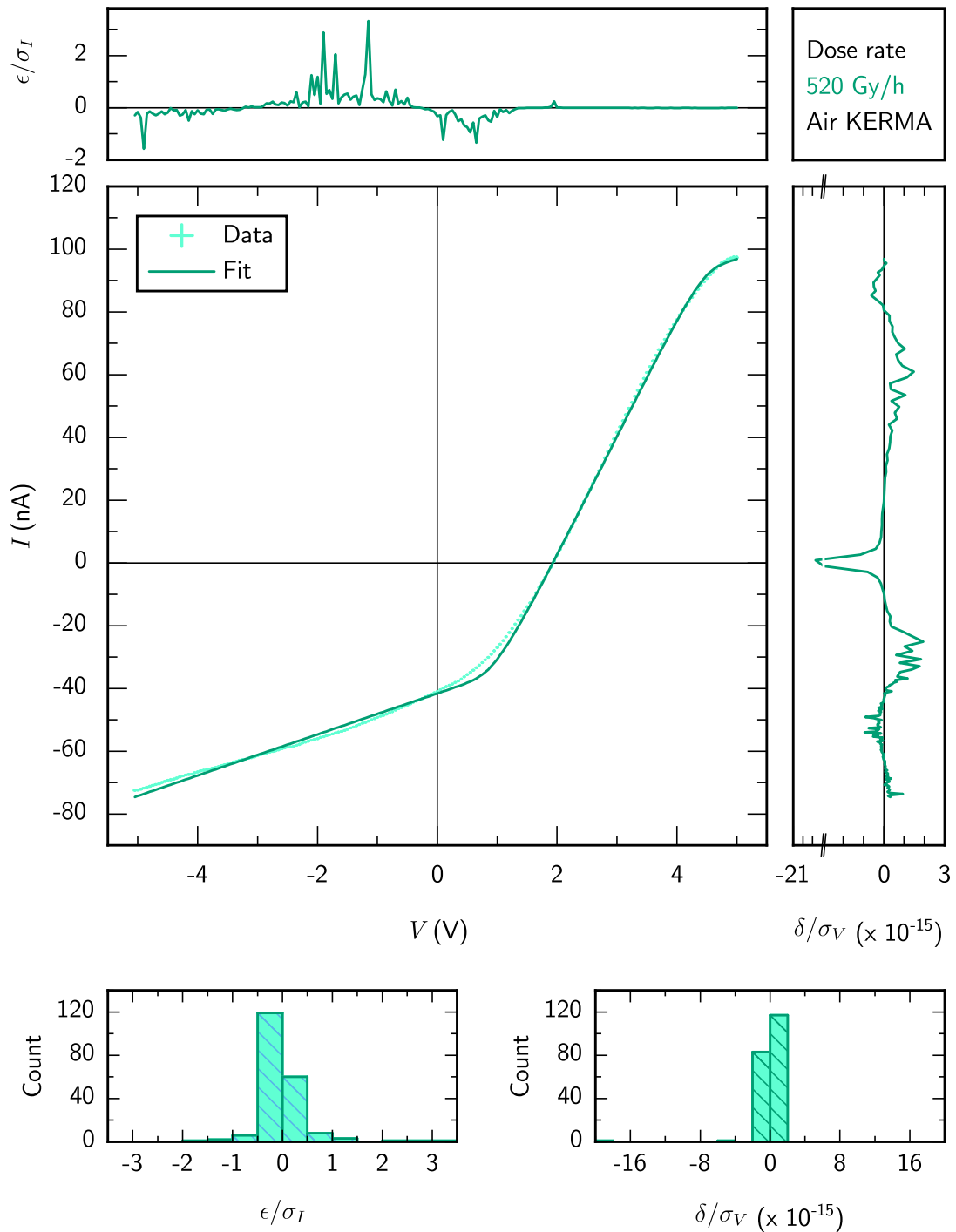


FIGURE 6.7.  $I$ - $V$  data from a triple-celled DGV irradiated with 520 Gy/h air KERMA of Cs-137 gamma rays, fitted with the opposing-diodes model. Also shown are current and voltage residuals  $\epsilon$  and  $\delta$ , scaled at each point by the measurement uncertainty at that point, and histograms of the same. N.B. there is an axis break on the line plot of voltage residuals.

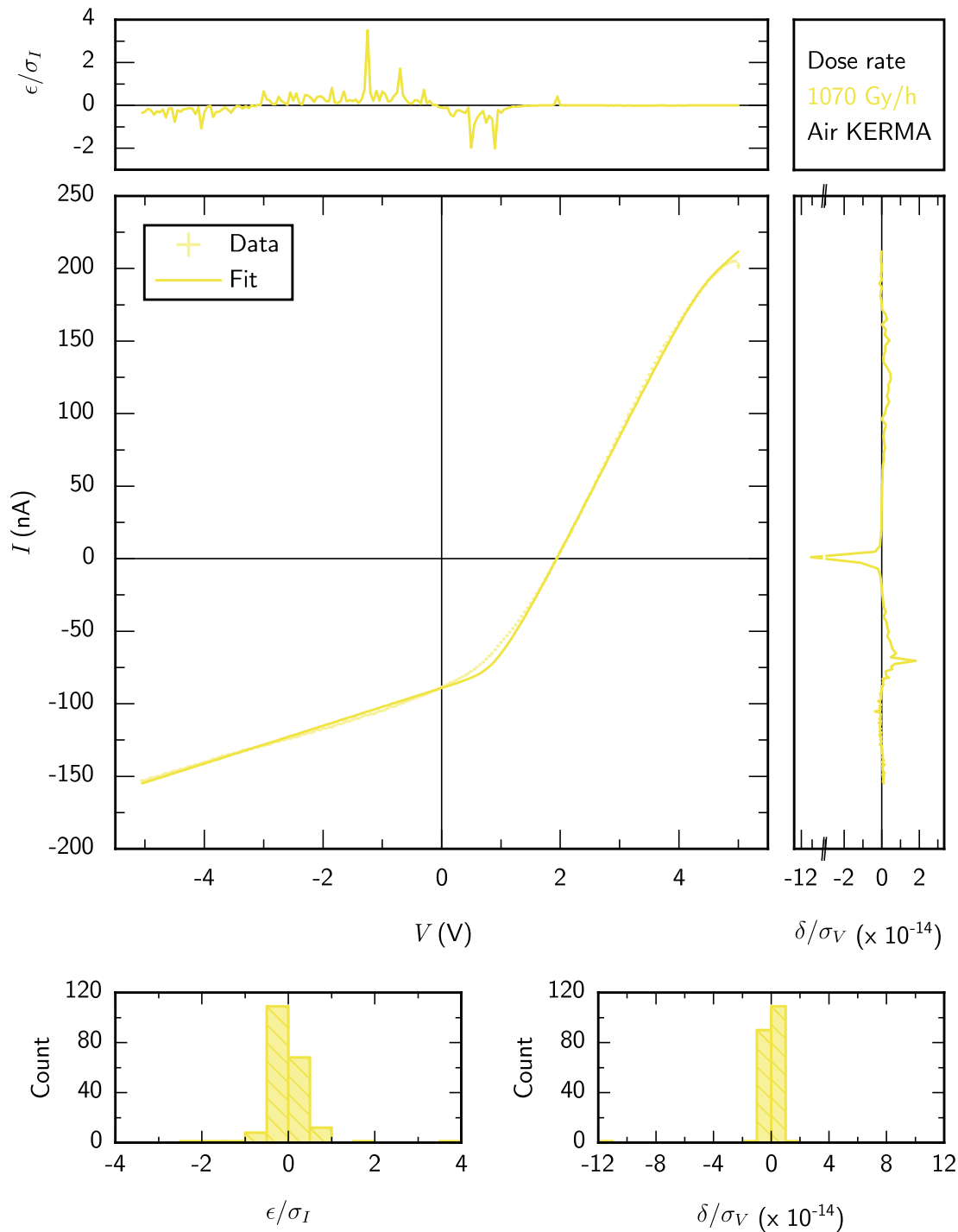


FIGURE 6.8.  $I$ - $V$  data from a triple-celled DGV irradiated with 1070 Gy/h air KERMA of Cs-137 gamma rays, fitted with the opposing-diodes model. Also shown are current and voltage residuals  $\epsilon$  and  $\delta$ , scaled at each point by the measurement uncertainty at that point, and histograms of the same. N.B. there is an axis break on the line plot of voltage residuals.

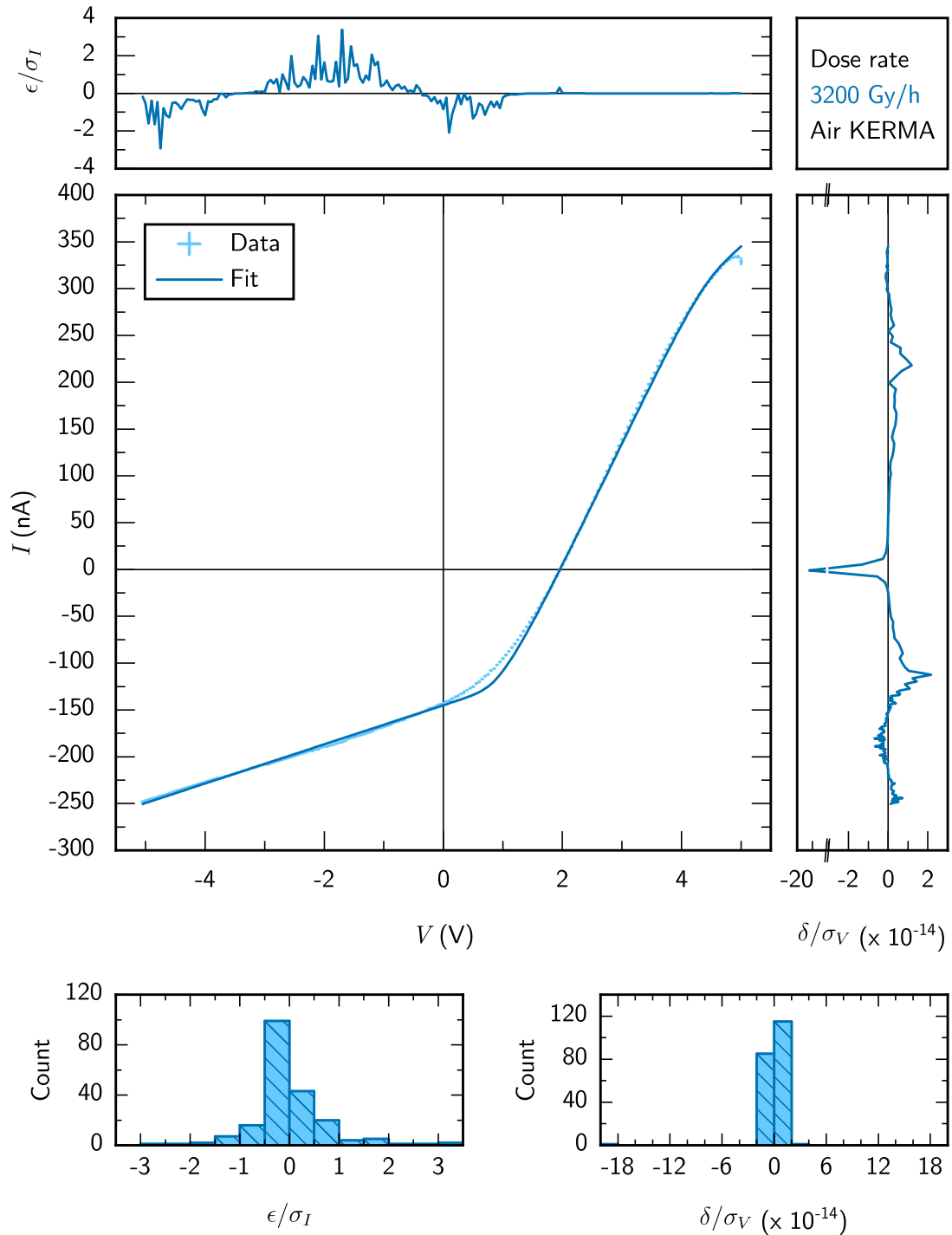


FIGURE 6.9.  $I$ - $V$  data from a triple-celled DGV irradiated with 3200 Gy/h air KERMA of Cs-137 gamma rays, fitted with the opposing-diodes model. Also shown are current and voltage residuals  $\epsilon$  and  $\delta$ , scaled at each point by the measurement uncertainty at that point, and histograms of the same. N.B. there is an axis break on the line plot of voltage residuals.

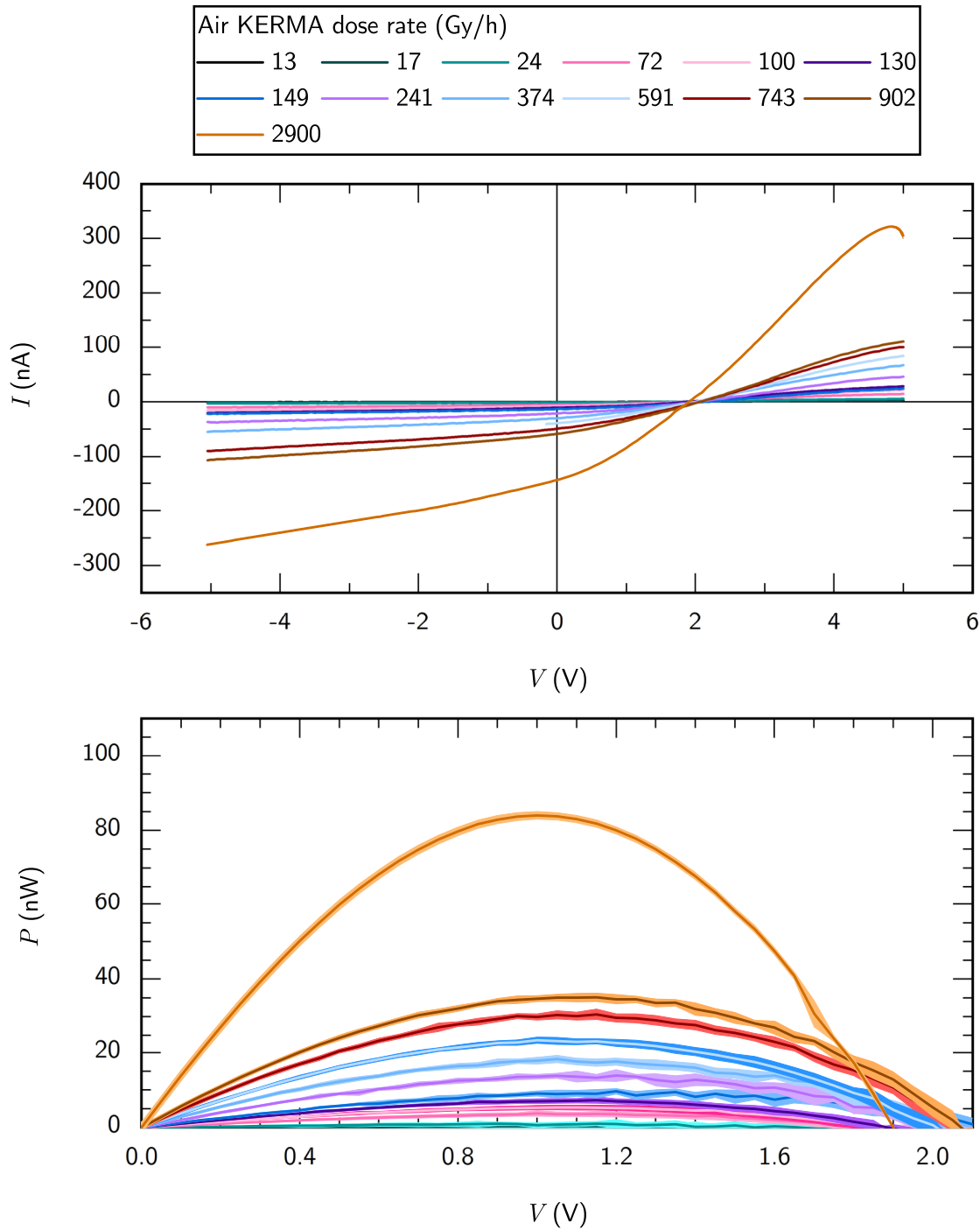


FIGURE 6.10.  $I$ - $V$  and  $P$ - $V$  data from a triple-celled DGV irradiated with dose rates between 13 Gy/h and 2900 Gy/h air KERMA of Cs-137 gamma rays. Uncertainties have been propagated from the  $I$ - $V$  data into the  $P$ - $V$  data without accounting for correlation.

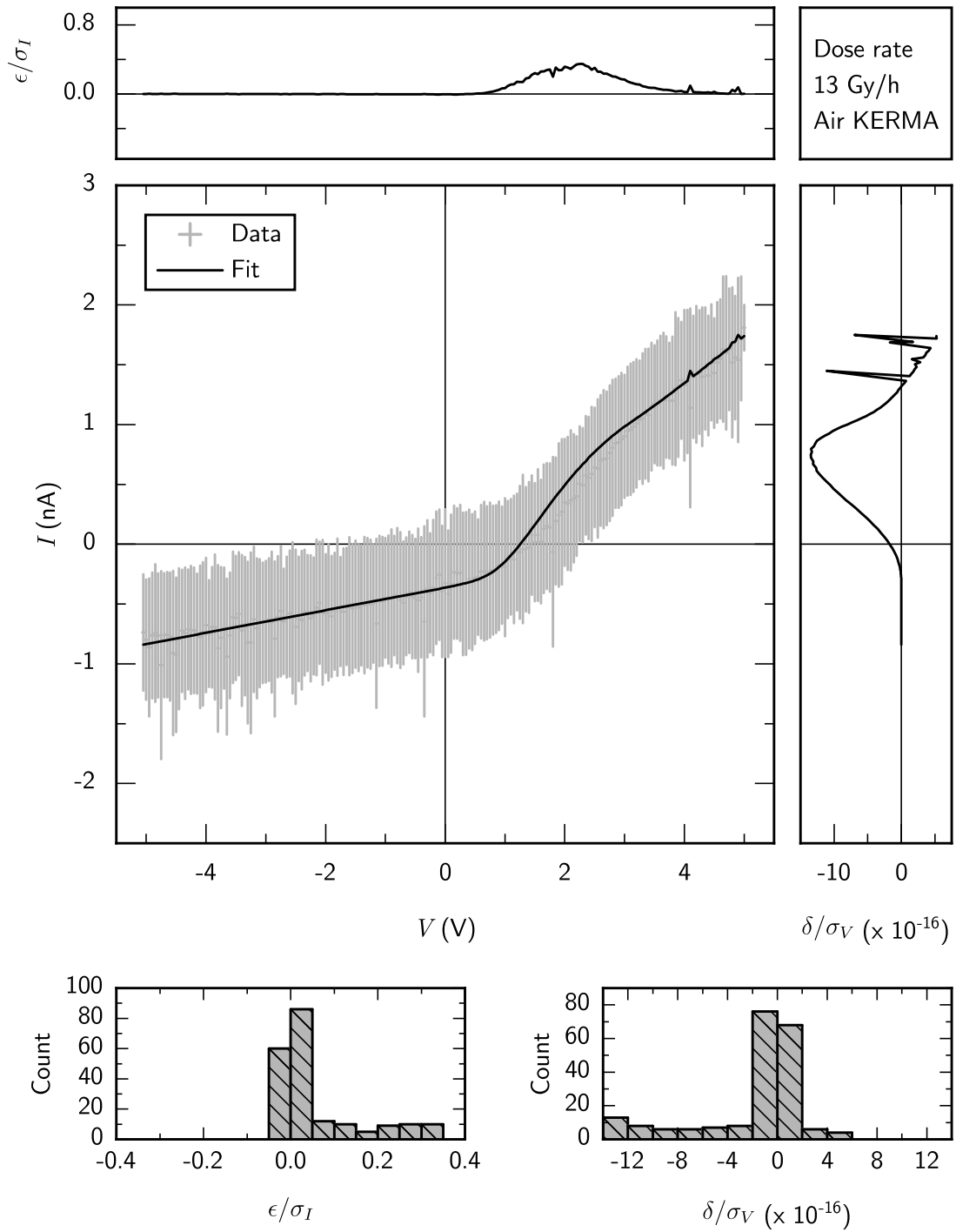


FIGURE 6.11.  $I$ - $V$  data from a triple-celled DGV irradiated with 13 Gy/h air KERMA of Co-60 gamma rays, fitted with the opposing-diodes model. Also shown are current and voltage residuals  $\epsilon$  and  $\delta$ , scaled at each point by the measurement uncertainty at that point, and histograms of the same.

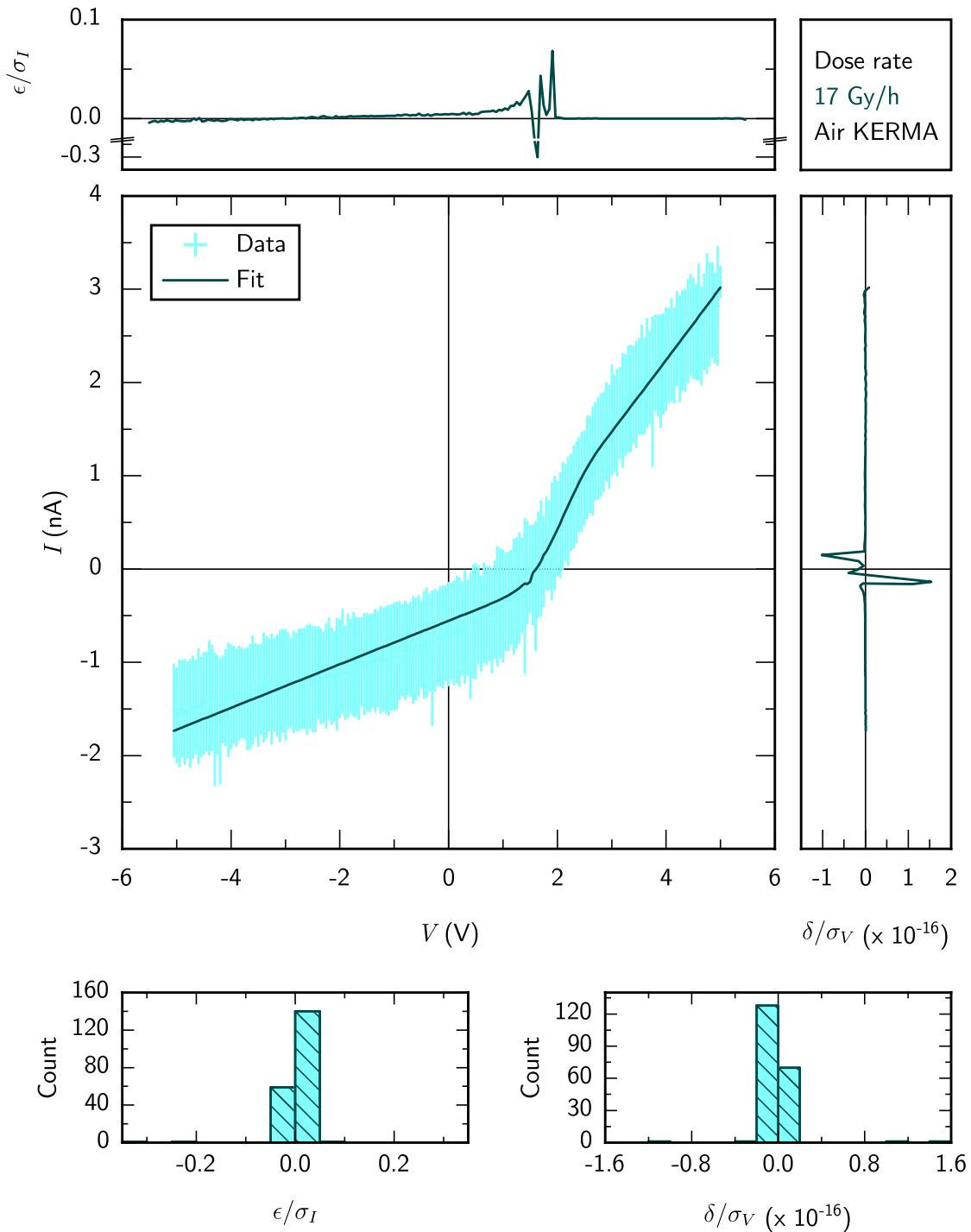


FIGURE 6.12.  $I$ - $V$  data from a triple-celled DGV irradiated with 17 Gy/h air KERMA of Co-60 gamma rays, fitted with the opposing-diodes model. Also shown are current and voltage residuals  $\epsilon$  and  $\delta$ , scaled at each point by the measurement uncertainty at that point, and histograms of the same. N.B. there is an axis break on the line plot of current residuals.

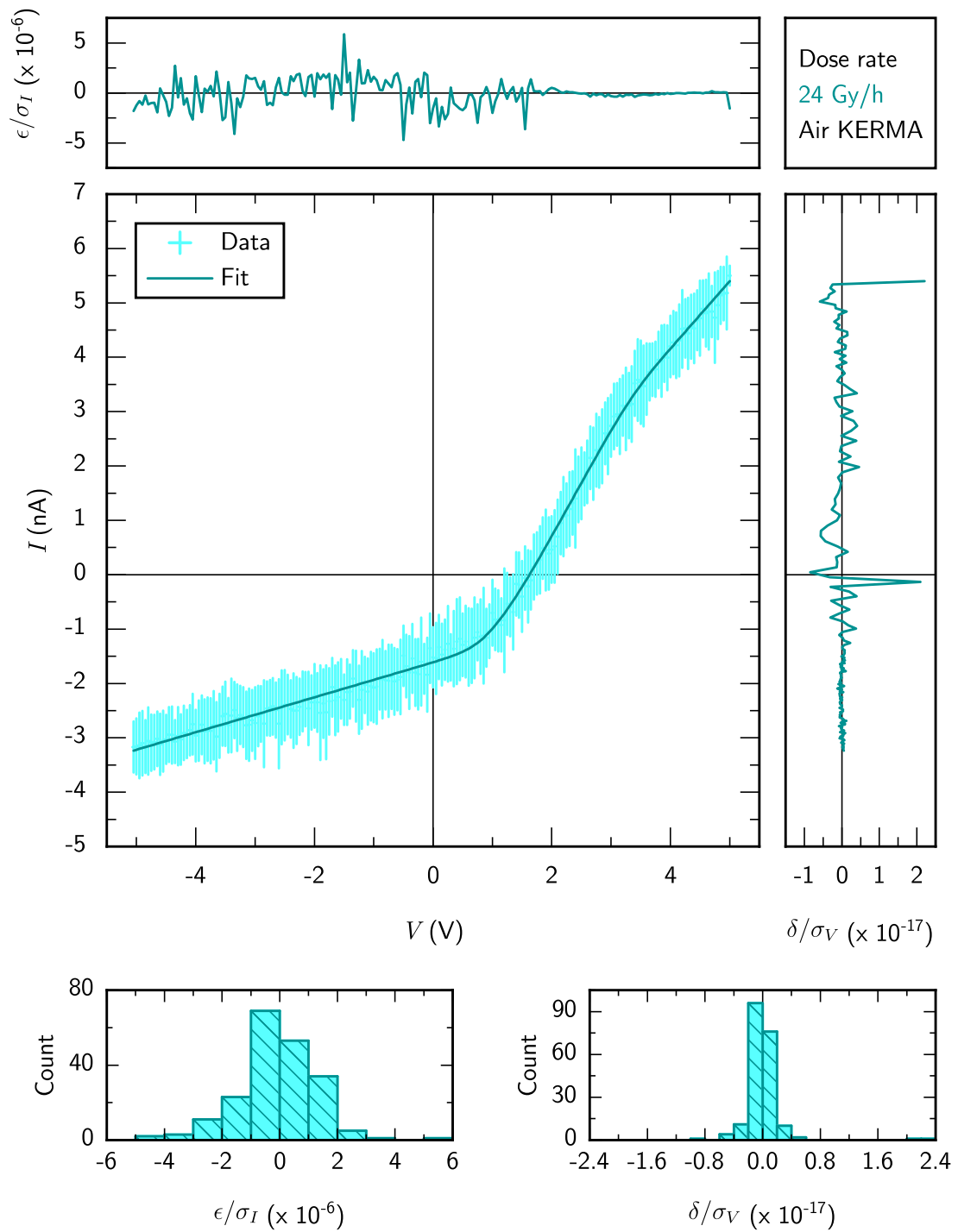


FIGURE 6.13.  $I$ - $V$  data from a triple-celled DGV irradiated with 24 Gy/h air KERMA of Co-60 gamma rays, fitted with the opposing-diodes model. Also shown are current and voltage residuals  $\epsilon$  and  $\delta$ , scaled at each point by the measurement uncertainty at that point, and histograms of the same.

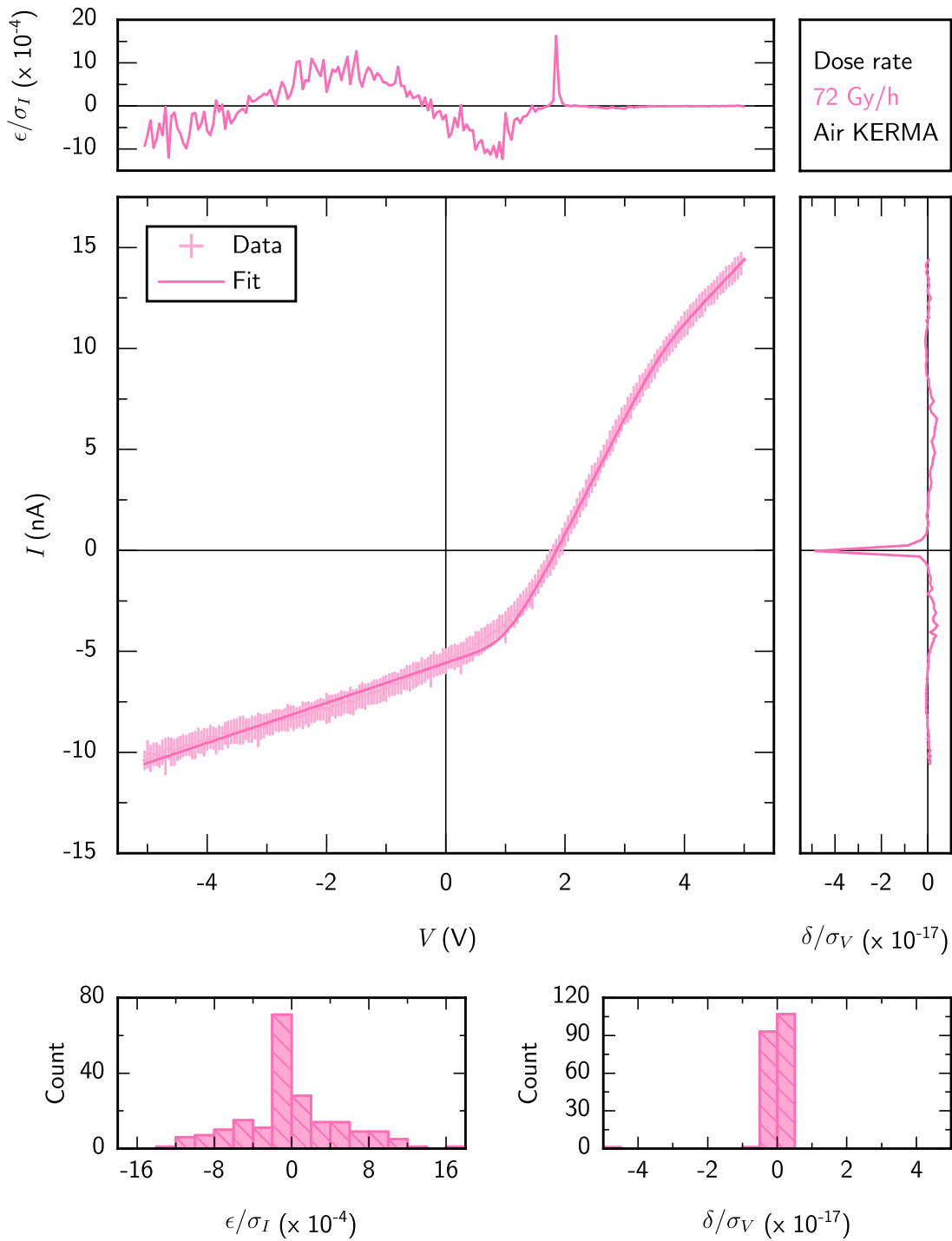


FIGURE 6.14.  $I$ - $V$  data from a triple-celled DGV irradiated with 72 Gy/h air KERMA of Co-60 gamma rays, fitted with the opposing-diodes model. Also shown are current and voltage residuals  $\epsilon$  and  $\delta$ , scaled at each point by the measurement uncertainty at that point, and histograms of the same.

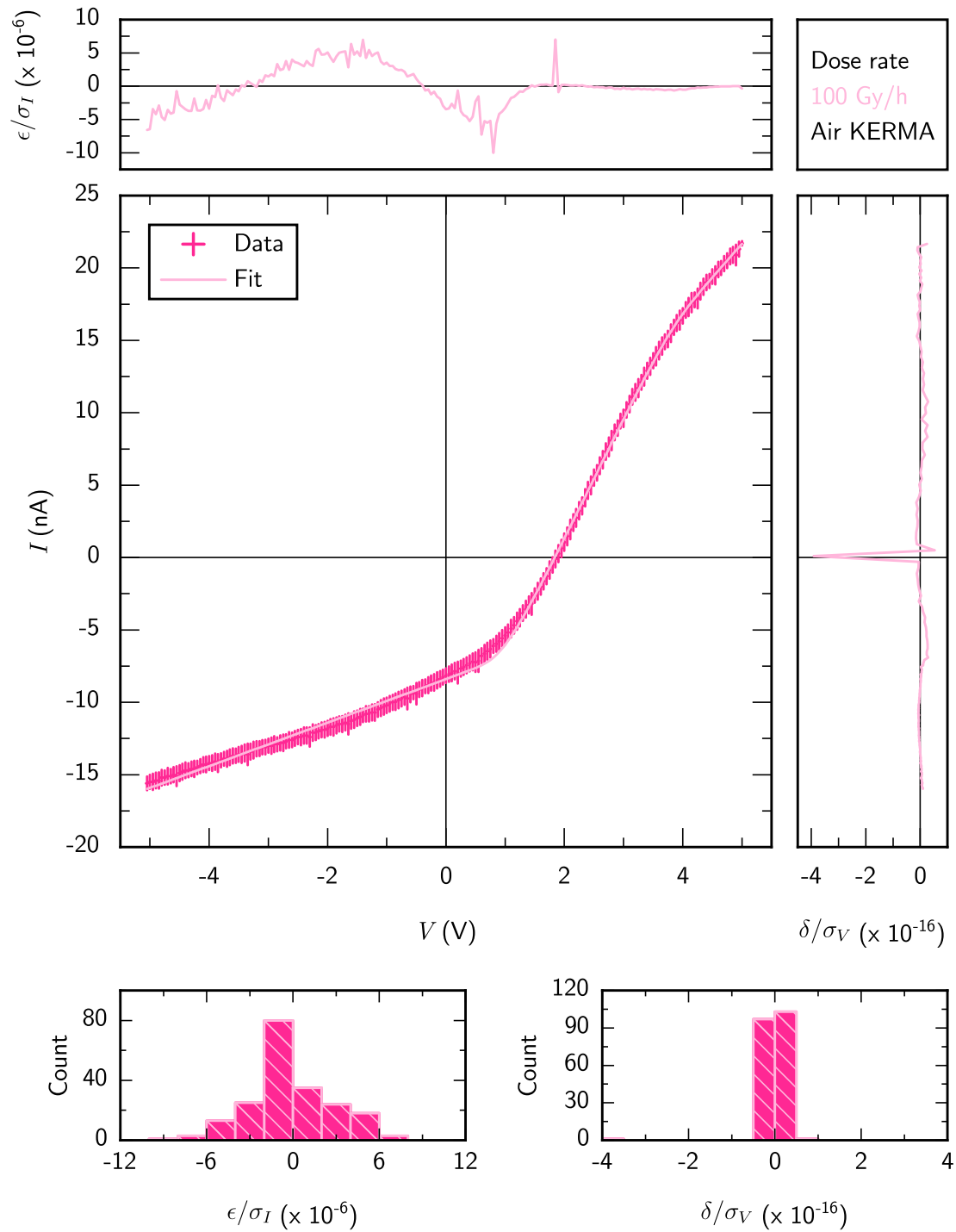


FIGURE 6.15.  $I$ - $V$  data from a triple-celled DGV irradiated with 100 Gy/h air KERMA of Co-60 gamma rays, fitted with the opposing-diodes model. Also shown are current and voltage residuals  $\epsilon$  and  $\delta$ , scaled at each point by the measurement uncertainty at that point, and histograms of the same.

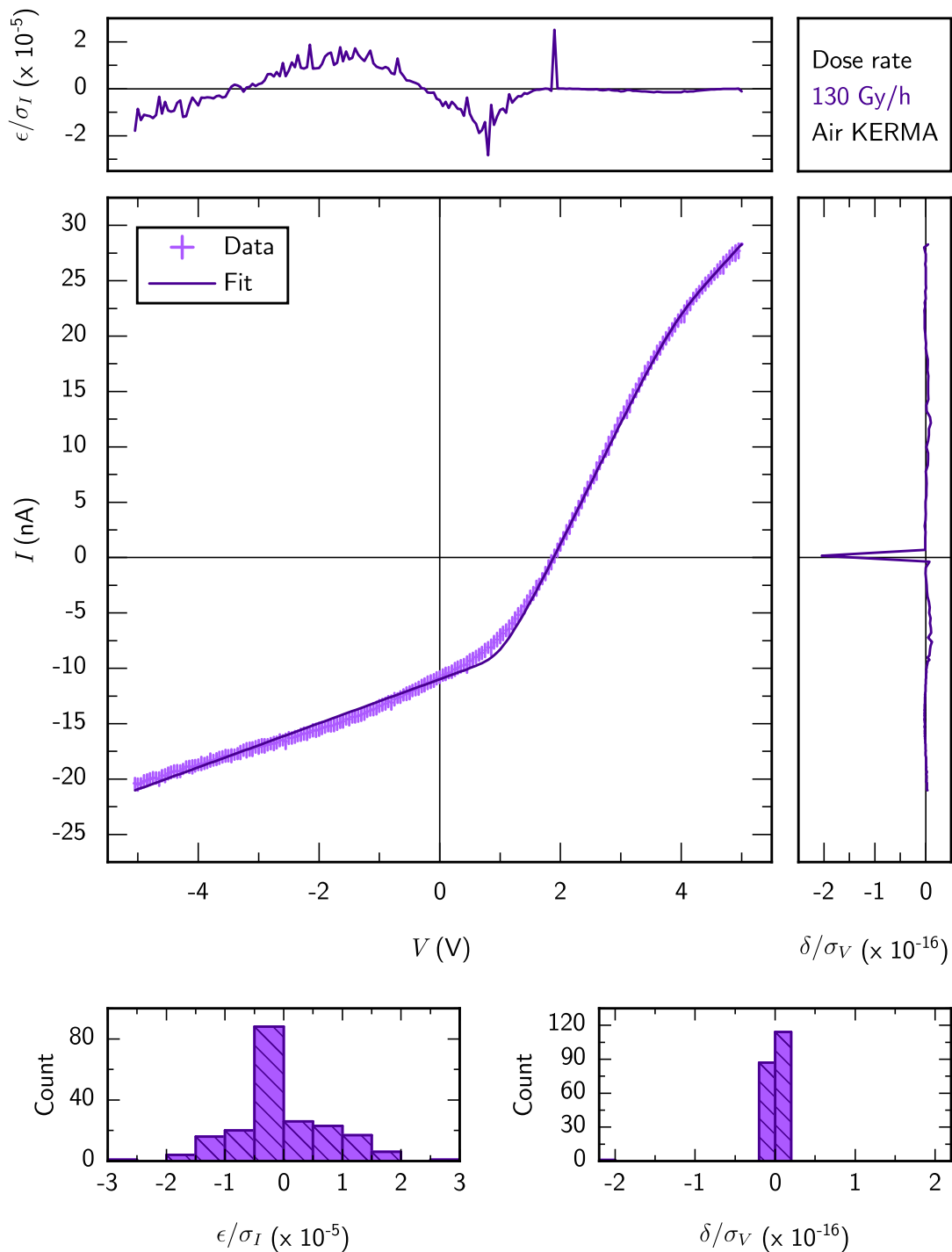


FIGURE 6.16.  $I$ - $V$  data from a triple-celled DGV irradiated with 130 Gy/h air KERMA of Co-60 gamma rays, fitted with the opposing-diodes model. Also shown are current and voltage residuals  $\epsilon$  and  $\delta$ , scaled at each point by the measurement uncertainty at that point, and histograms of the same.

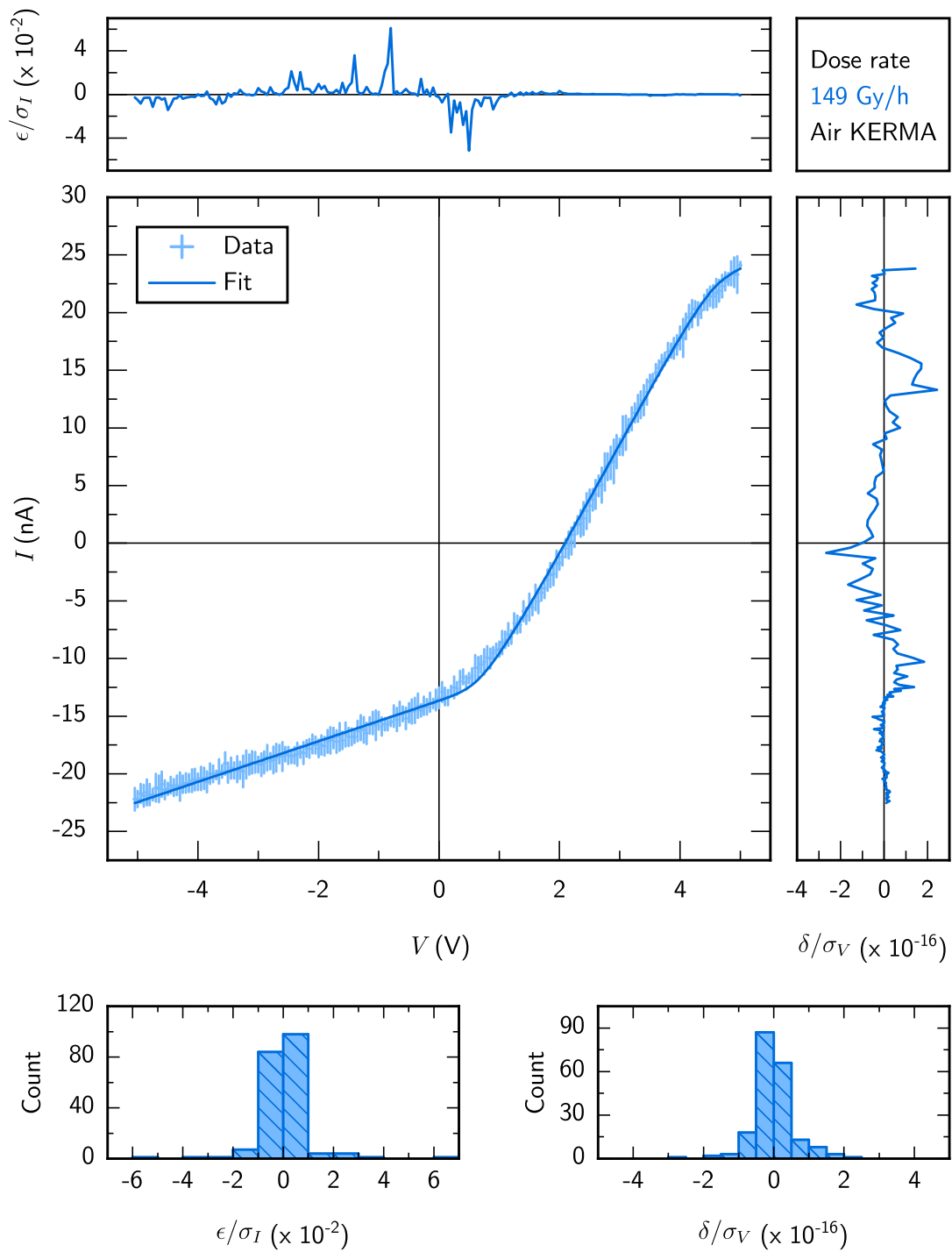


FIGURE 6.17.  $I$ - $V$  data from a triple-celled DGV irradiated with 149 Gy/h air KERMA of Co-60 gamma rays, fitted with the opposing-diodes model. Also shown are current and voltage residuals  $\epsilon$  and  $\delta$ , scaled at each point by the measurement uncertainty at that point, and histograms of the same.

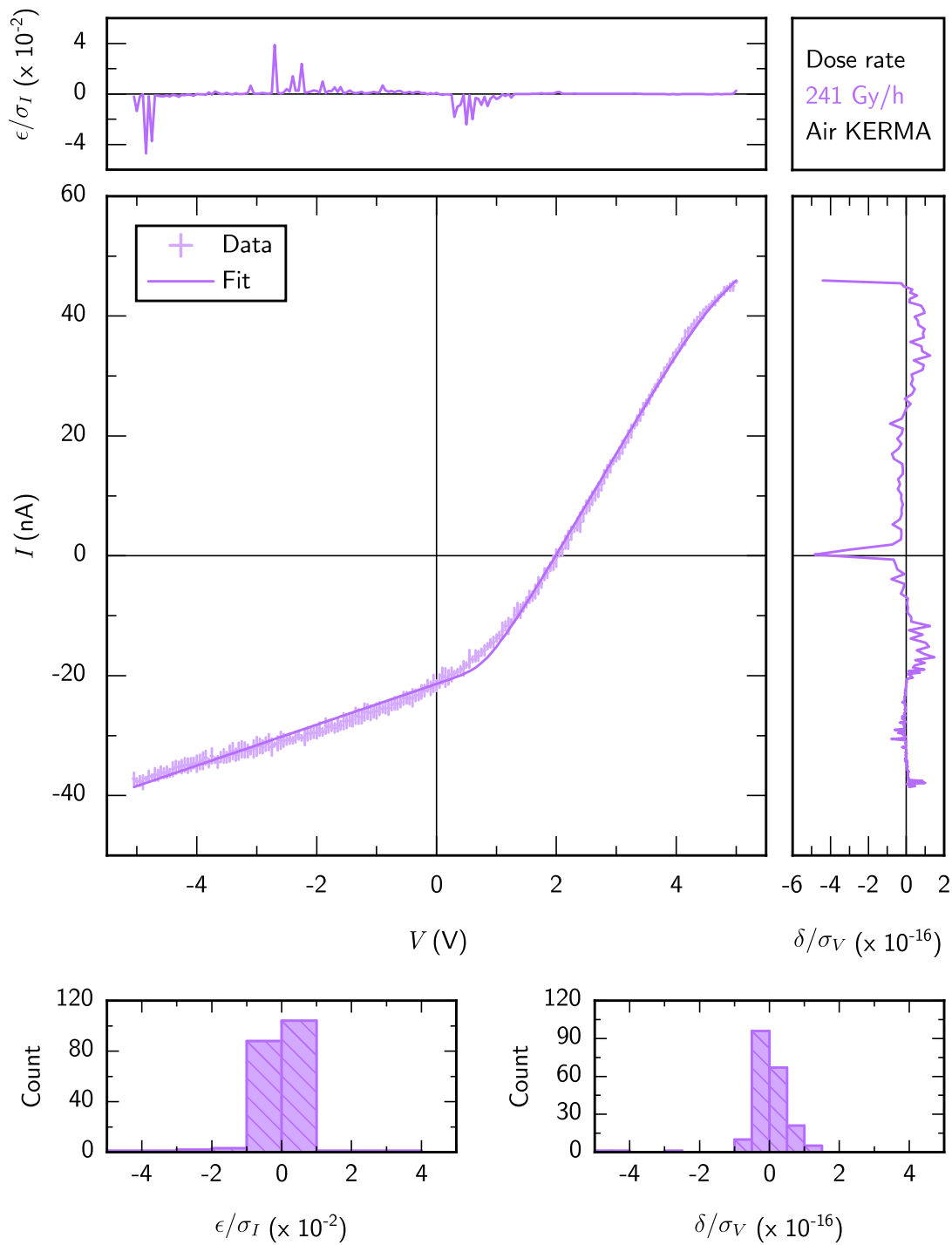


FIGURE 6.18.  $I$ - $V$  data from a triple-celled DGV irradiated with 241 Gy/h air KERMA of Co-60 gamma rays, fitted with the opposing-diodes model. Also shown are current and voltage residuals  $\epsilon$  and  $\delta$ , scaled at each point by the measurement uncertainty at that point, and histograms of the same.

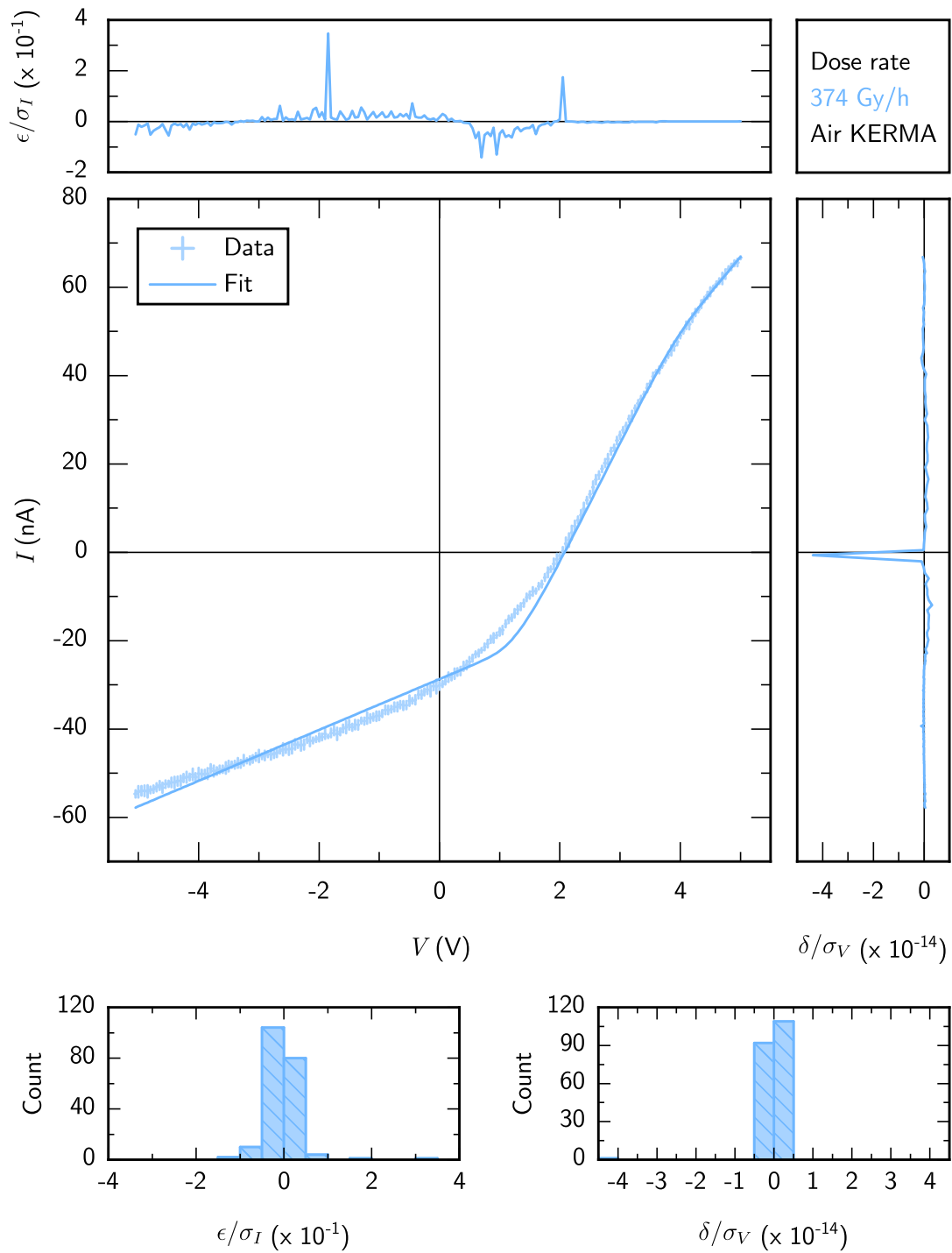


FIGURE 6.19.  $I$ - $V$  data from a triple-celled DGV irradiated with 374 Gy/h air KERMA of Co-60 gamma rays, fitted with the opposing-diodes model. Also shown are current and voltage residuals  $\epsilon$  and  $\delta$ , scaled at each point by the measurement uncertainty at that point, and histograms of the same.

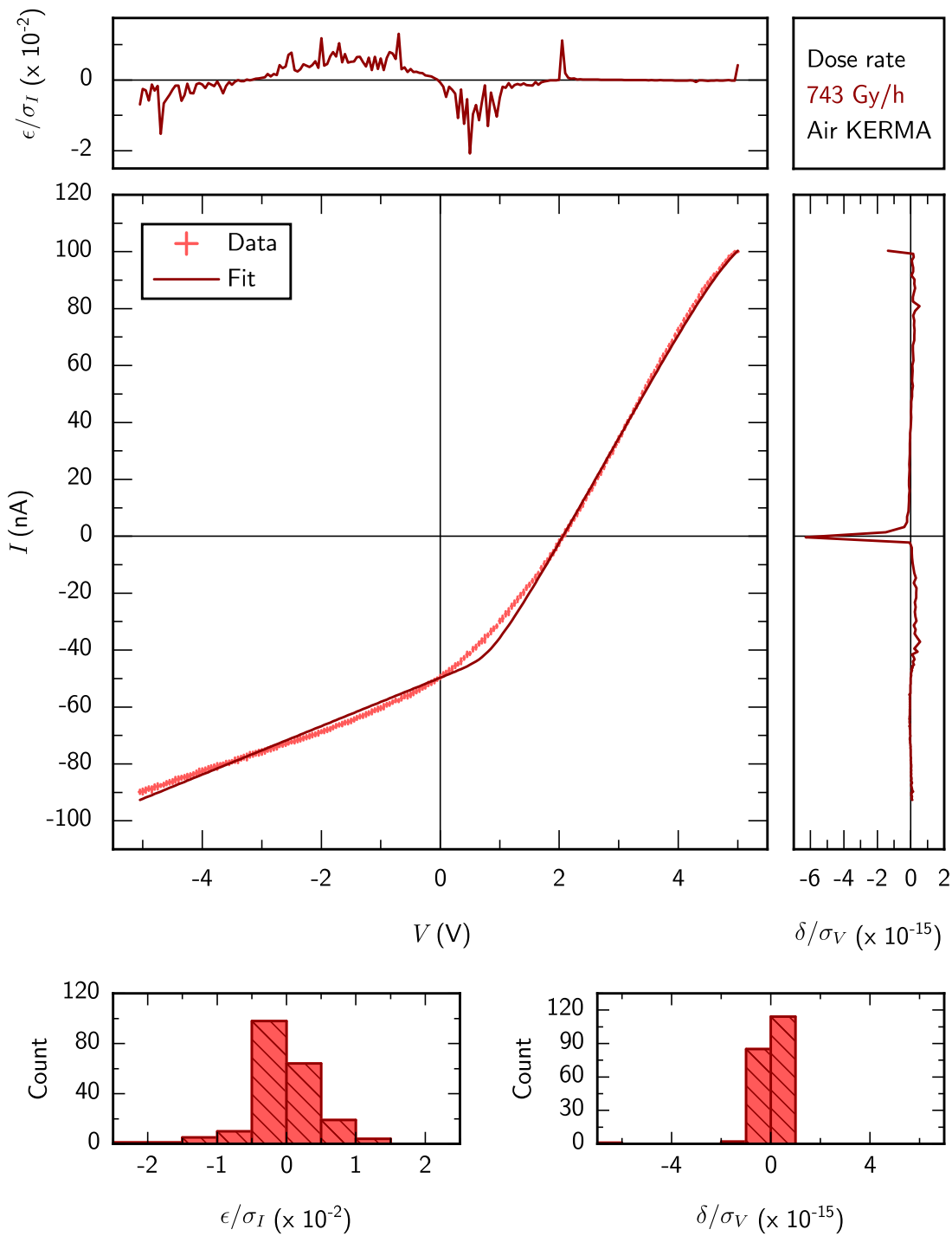


FIGURE 6.20.  $I$ - $V$  data from a triple-celled DGV irradiated with 743 Gy/h air KERMA of Co-60 gamma rays, fitted with the opposing-diodes model. Also shown are current and voltage residuals  $\epsilon$  and  $\delta$ , scaled at each point by the measurement uncertainty at that point, and histograms of the same.

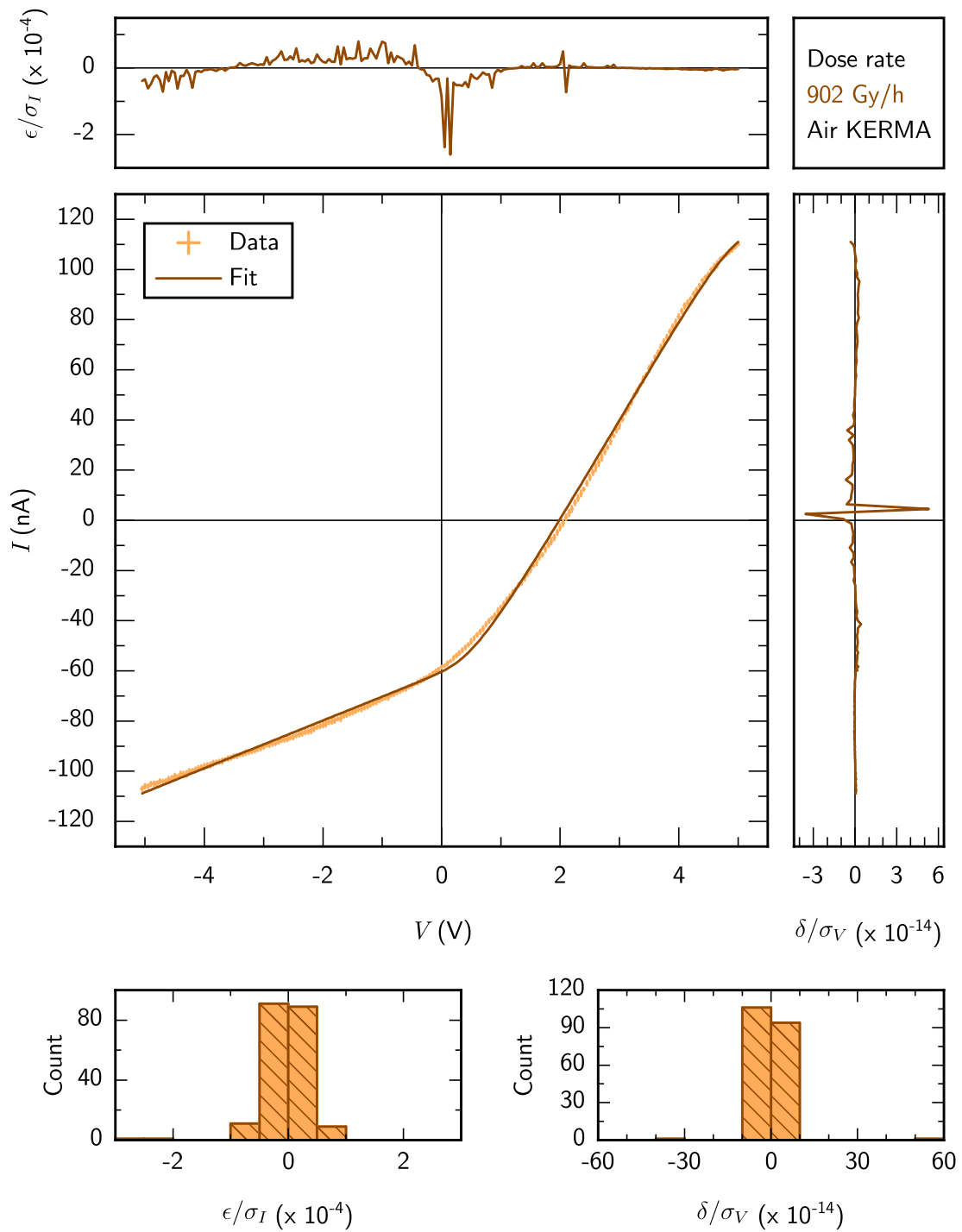


FIGURE 6.21.  $I$ - $V$  data from a triple-celled DGV irradiated with 902 Gy/h air KERMA of Co-60 gamma rays, fitted with the opposing-diodes model. Also shown are current and voltage residuals  $\epsilon$  and  $\delta$ , scaled at each point by the measurement uncertainty at that point, and histograms of the same.

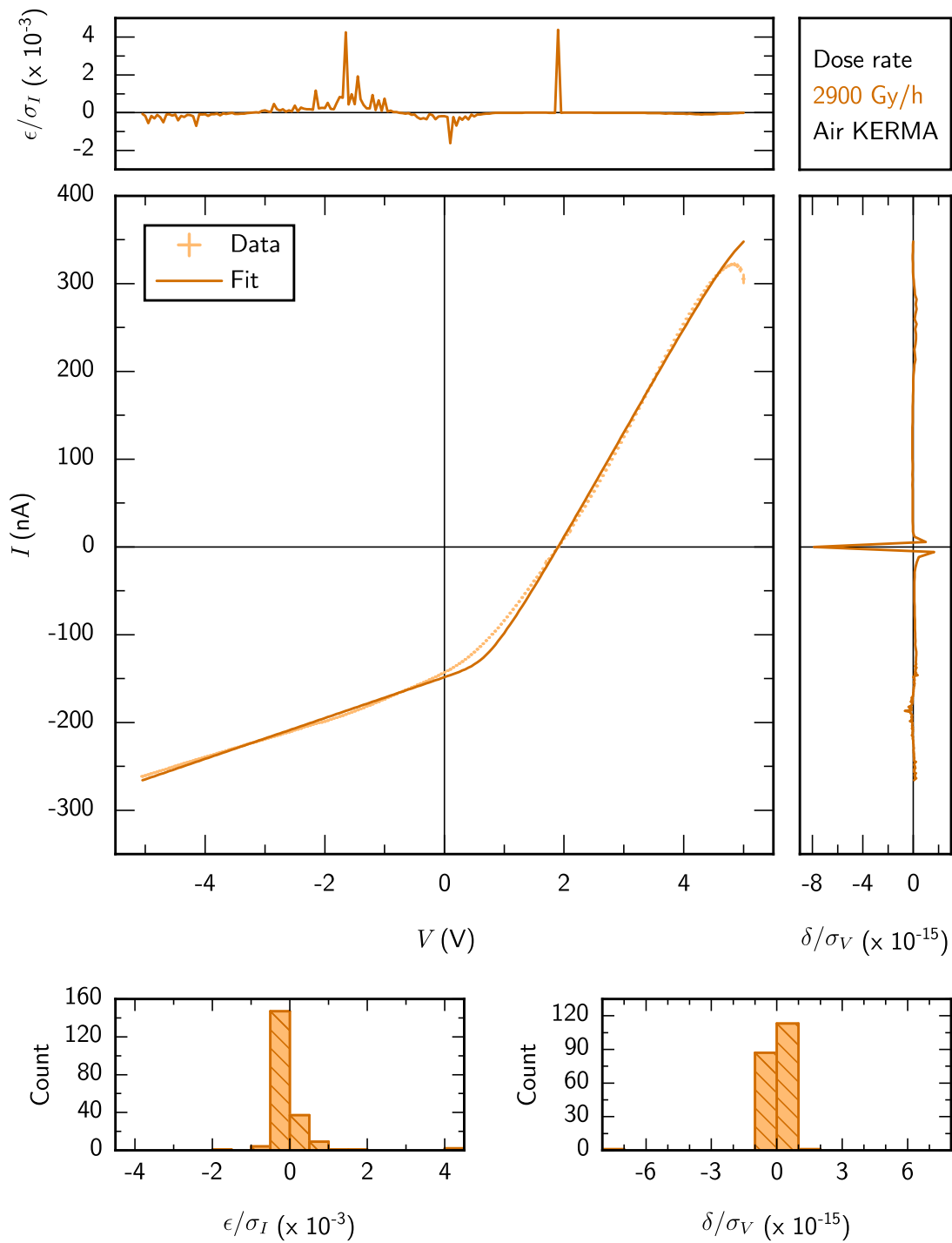


FIGURE 6.22.  $I$ - $V$  data from a triple-celled DGV irradiated with 2900 Gy/h air KERMA of Co-60 gamma rays, fitted with the opposing-diodes model. Also shown are current and voltage residuals  $\epsilon$  and  $\delta$ , scaled at each point by the measurement uncertainty at that point, and histograms of the same.

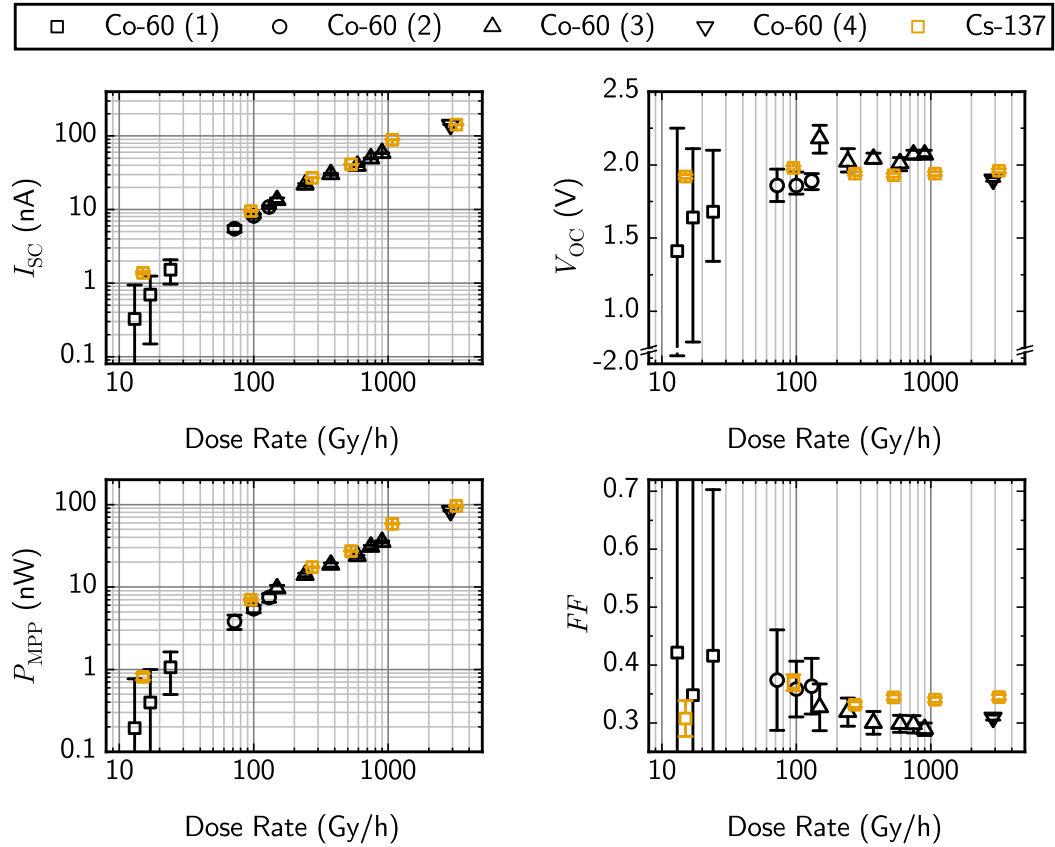


FIGURE 6.23.  $I_{SC}$ ,  $V_{OC}$ ,  $P_{MPP}$  and  $FF$  for the Cs-137 data from Figure 6.3 and the Co-60 data from Figure 6.10. For the Co-60 data, points are distinguished by position number. In the current and power data, error bars which took negative values are truncated due to the logarithmic scales. In the fill factor data, three points have had their error bars truncated for clarity and because they took unphysical values: from left to right these were upper bounds of 2.2 and 1.0, and lower bounds of -1.3, -0.3 and 0.1. Uncertainty was propagated to  $FF$  without considering correlation of variables.

Figure 6.23 shows the  $I_{SC}$ ,  $V_{OC}$ ,  $P_{MPP}$  and  $FF$  extracted from Figures 6.3 and 6.10. With the exception of the lowest three Co-60 dose rates (13, 17 and 24 Gy/h), the  $V_{OC}$  remains relatively stable between approximately 1.8 to 2 V, with no clear relationship between dose rate and  $V_{OC}$ . Indeed, the positions at which the measurements were taken - not presented in Figure 6.10 but presented in Figure 6.23 - would appear to have more of a relationship with  $V_{OC}$  than the dose rate. The  $V_{OC}$  is far more stable for the Cs-137 experiment, but of essentially the same value as in the Co-60 case. This approximate constancy in the  $V_{OC}$ , as with the DLS case, meant that the  $P_{MPP}$  followed the  $I_{SC}$  by relation with a roughly constant factor. Compared to that of the single-celled DGV in the DLS irradiation,  $V_{MPP} \approx 0.5V_{OC}$ , which is consistent with a greater influence from parasitic resistances.

The fill factor  $FF$  is also correspondingly low, with the values for the lowest Co-60 dose rates having very large uncertainty. Uncertainty was propagated without considering correlation between the variables. To the eye there is a difference in the behaviour of  $FF$  between the Cs-137 and Co-60 experiments. It seems to stay roughly constant between 0.3 and 0.4 for Cs-137, whilst declining with increasing dose rate for Co-60. It is not known why this might be, and no prediction is made on whether this apparent trend would persist in a repeat experiment.

The power generated by the DGV under Cs-137 irradiation was very slightly higher than under Co-60 irradiation. This is as would be expected from the simulation.

Figure 6.24 shows values of the opposing-diodes fit parameters arrived at by ODR for both the Cs-137 and Co-60 experiments. Also shown is the quantity  $k_b T \ln(I_{01}/I_{02})$ , which in the case of equal-area opposing Schottky diodes in which thermionic emission dominates would equal the difference in barrier heights<sup>1</sup>. The results are quite mixed in terms of the certainty of parameters. Every dataset, regardless of dose rate or isotope, converges to  $n_1 = 1$ , and it may be that in future experiments, this parameter can be set as such rather than used for fitting. With occasional exceptions, the results for  $R_{Sh2}$ ,  $R_S$ ,  $I_{Ph}$  and  $I_{01}$  are all quite certain, and it may be that these parameters have converged to their global minimum for each fit. The certainty in  $R_{Sh1}$  decreases with increasing dose rate, which is consistent with the fact that curves taken under higher dose rates contain less of the region in which  $R_{Sh1}$  exerts a prominent influence, if the voltage sweep range is kept the same. Future experiments would likely benefit from using a wider voltage range for this reason. The worst certainty was obtained for  $I_{02}$ , which had uncertainty roughly an order of magnitude greater than its value for all data. Qualitatively it follows a similar pattern to  $n_2$  with dose rate, and it seems likely that there is some interference from local minima in these axes of the parameter space. The quantity  $k_b T \ln(I_{01}/I_{02})$  falls within the expected range of values for two barriers under contacts of equal area, subject to Fermi level pinning at or below 1.2eV above the valence band maximum. But, is not constant with dose rate. It is only an approximate measure of barrier difference because current crowding may affect the relative sizes of the contacts from an electrical perspective, and barriers may have effective heights different to their zero-bias, cold-carrier heights for a DGV  $I-V$  curve. Nevertheless, the fact that it takes reasonable values for barrier difference suggest that the fits are of some value. It seems probably that the photon energy difference between Cs-137 and Co-60 gamma irradiations do not make much difference, although transforming this from air KERMA dose rate to flux may change this interpretation and would be suitable future analysis. It seems reasonably clear that  $I_{Ph}$  does not change linearly with dose rate, nor is it the only equivalent circuit parameter to change substantially with dose rate with fair certainty. At this stage it would seem that the parameters extracted by the ODR fits of the opposing-diodes model are of varying reliability depending on the parameter, and whilst the model does a better job of accounting for the shape of the  $I-V$  curves than the conventional solar cell model, more theoretical work is needed to refine it before proper mechanistic conclusions can be drawn from the data. The fits were performed before the explicit

<sup>1</sup>The reverse saturation current of a Schottky diode is given by  $I_0 = AA \exp(\phi_B/k_b T)$ , so if the two contacts have equal area, dividing the two saturation currents and re-arranging for  $\phi_{B1} - \phi_{B2}$  gives the expression in the main text.

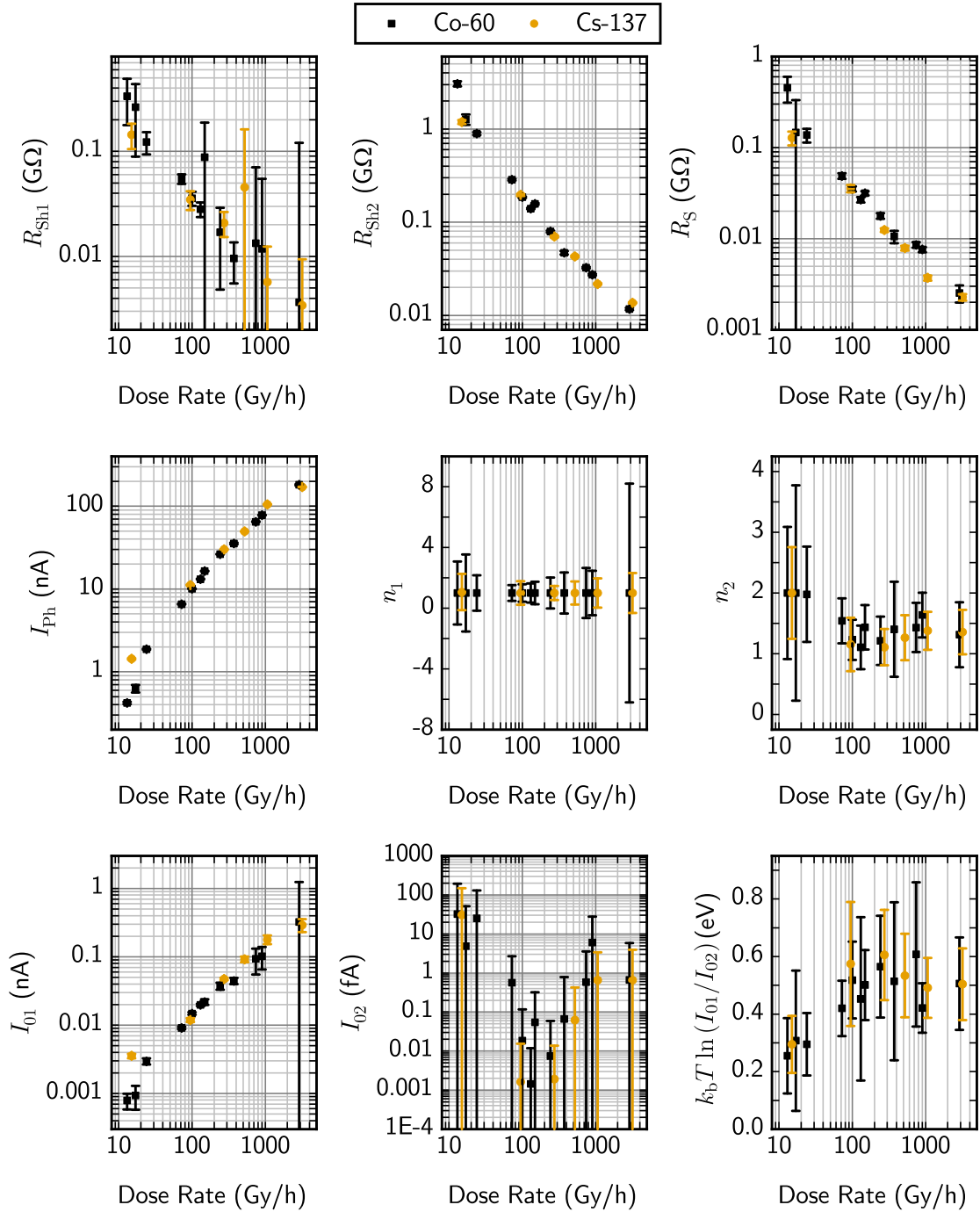


FIGURE 6.24. Fitting parameter values for the opposing-diodes model, as fit to the data in Figures 6.4 to 6.22. Where error bars are truncated, it is because they go to negative values and so cannot be shown on the logarithmic scale. Also plotted is the quantity  $k_b T \ln(I_{O1}/I_{O2})$ , which in the case of equal-area opposing Schottky diodes in which thermionic emission dominates would equal the difference in barrier heights.

$V$ - $I$  relation of Equation 2.26 was derived, and this latter achievement should make it more feasible (if still very computationally expensive) to do a brute search of the parameter space to attain more confidence that the fits found have fallen into their global minima.

Because of the range of dose rates and the triple-celled DGV employed, it can be seen that the device performance attained in these experiments is approaching that necessary for micropower devices. At the maximum Co-60 dose rate employed, of approximately 2,900 Gy/h, the device had  $P_{MPP} \approx 80$  nW, via an  $I_{MPP} \approx 80$  nA and a  $V_{MPP} \approx 1$  V. At the maximum Cs-137 dose rate employed, of approximately 3200 Gy/h, the device had  $P_{MPP} \approx 100$  nW, via an  $I_{MPP} \approx 100$  nA and a  $V_{MPP} \approx 1$  V. In both cases, performance was too low for any known energy harvesting circuit, and the dose rate is three times too high for any known region of a waste store. However, it is on the right order of magnitude in both cases, suggesting simple methods such as modestly increasing the number of cells in a device (e.g. creating a "gammavoltaic panel") or optimising a scatter shroud will improve the performance to useful levels. Alternatively, no scatter shroud could be used, but cells could be arranged to optimise between self-scattering and bottleneck reduction.

In terms of **applicability** to a nuclear waste store, at 1070 Gy/h air KERMA of Cs-137 irradiation, the device produced a  $P_{MPP} = 57$  nW. This corresponds to  ${}_{1070}^{Cs-137} p = 281$  nW/cm<sup>2</sup>, and  ${}_{1070}^{Cs-137} \mathfrak{P} = 1873$  nW/cm<sup>3</sup>.

In terms of **comparability**, there was  ${}_{100}^{Co-60} p = 27$  nW/cm<sup>2</sup> and  ${}_{100}^{Co-60} \mathfrak{P} = 179$  nW/cm<sup>3</sup>. There is almost, but not quite, sufficient information to compare to the previously-mentioned 1997 work of Horiuchi *et al*: because the best device tested in that work used a caesium iodide scintillator crystal, but the dimensions of that scintillator were not given<sup>2</sup>, it is not possible to determine  $\mathfrak{P}$  and  $p$  even though Co-60 measurements were performed at 72 Gy/h for both that work and this work. There *would* seem to be a direct comparison that can be drawn between this work and the devices tested *without* scintillators in the Horiuchi paper, as the silicon cell dimensions were reported, but this would give an undue benefit to this work, as the scintillators were found to be responsible for an increase in power of several orders of magnitude in the Horiuchi work, and ultimately in these early stages of gammavoltaic development, the volumetric figure-of-merit is of less importance than overall **applicability** - the ability to produce sufficient power under the correct circumstances. Furthermore, in that work, only the  $I_{SC}$  and  $V_{OC}$  were measured, and their product used as the power output (i.e. the theoretical  $P_{MAX}$ , not the real  $P_{MPP}$ ). As  $I$ - $V$  curves were not provided, the  $FF$ , hence the  $P_{MPP}$ , is unknown. Comparison must be restricted to saying: when these dissimilar and only partially-known quantities are compared by the use of estimation, conversion, etc., it appears the DGV presented here worked roughly as well as the Horiuchi cell when coupled to its caesium iodide scintillator. As the Horiuchi cell without a scintillator was roughly one order of magnitude smaller in volume but several orders of magnitude weaker in power output than when coupled to the scintillator,

<sup>2</sup>It seems fair to assume it was a few centimeters to a side: caesium iodide crystal scintillators generally are, and the caesium iodide scintillator they used in their 2005 work was  $5 \times 3 \times 1.5$  cm<sup>3</sup> [37]. Such dimensions, were they used in the 1997 work, would lead to an order of magnitude lower volumetric-to-areal figure-of-merit ratio than in this work, though it raises the question of whether in this work, the silver paint should be taken into consideration within the dimensions of the device.

it may be said that the bare DGV performed notably better than the bare Horiuchi cell. Of course, the Horiuchi cell was not designed to be used bare.

In some works, performance metrics are given in terms of areal power density per unit dose rate. The results in this chapter and the previous chapter show that, at least for this work and possibly for other gammavoltaics too, this is not suitable unless a linear performance with dose rate is known to exist. That is not the case here - comparison must be kept to specific dose rates.

The difficulty of performing this comparison, even when much of the experimental setup and units used in that work were comparable to this work, re-emphasizes the need for the application-oriented philosophy adopted here, and the efforts for greater comparability which the field of gammavoltaics would benefit from. Still, it would seem that in terms of device comparison, the most prescient test is from this point the longevity of the DGV under high dose-rate conditions. This is because reasonable longevity would be required to meet the standard set by the Horiuchi cell, the weakest point of which was the caesium iodide scintillator. Caesium iodide is known to suffer radiation damage, and at some of the dose rates considered in this work, certainly so. Some researchers have found significant degradation after an absorbed dose of around 4 Gy [311], meaning a short lifetime and therefore limited usefulness to the nuclear waste store application considered in this work, for which monitoring deployments ought to last years or decades. Longevity will be assessed in the next section.

### **6.3 Assessment of the durability of a single-celled DGV under Cs-137 gamma irradiation**

This section presents results taken with a single-celled DGV under Cs-137 irradiation, at 1,350 Gy/h air KERMA, over the course of three and a half weeks. The method for this, which included the concurrent measurement of temperature and humidity variation, is described in Section 3.3.4. A single-celled DGV was used to simplify the interpretation of results. The DGV was built using E6\_ELSC\_2.

#### **6.3.1 $I$ - $V$ and $P$ - $V$ curves taken over 600 hours at 1,350 Gy/h Cs-137 irradiation.**

Figure 6.25 shows the  $I$ - $V$  and  $P$ - $V$  data for the long irradiation. It can be seen that there was a clear decrease in  $I_{SC}$  and  $V_{OC}$  over the duration of exposure, but that there was no catastrophic failure of the device. In the latter case, the  $I$ - $V$  curves may have been expected to collapse to near-zero magnitude, in line with how the DGV performed prior to hydrogen termination in Chapters 4. The bulk of the  $I_{SC}$  values fall between 100 and 150 nA with  $I$ - $V$  curves taken later being more likely to have lower values. Likewise for the  $V_{OC}$  values falling predominantly between 0.4 and 0.55 V, with later curves more likely to have lower values. However, in the case of the  $V_{OC}$ , some of the earliest curves visibly have the lowest values.

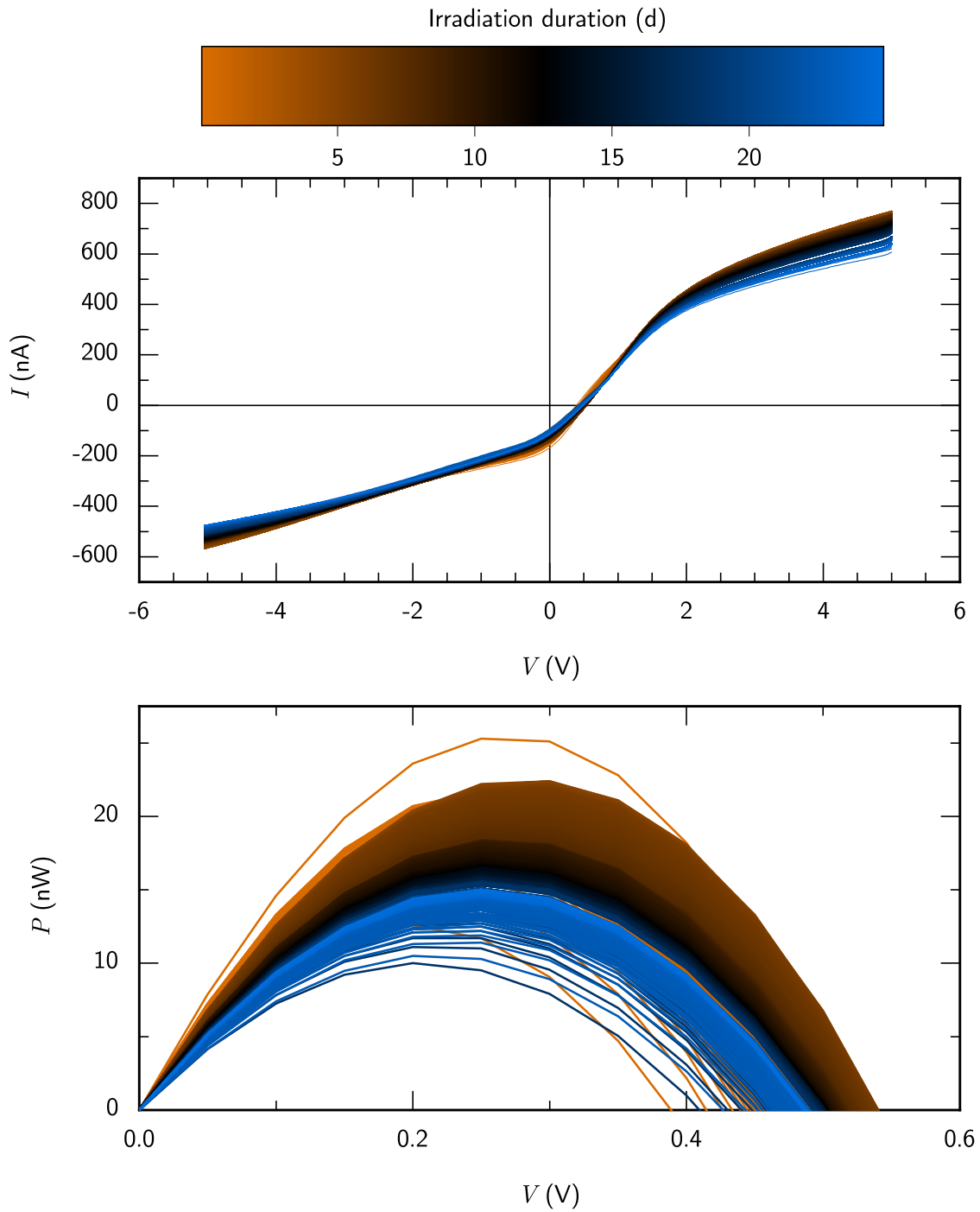


FIGURE 6.25. 3,192  $I$ - $V$  and  $P$ - $V$  curves taken under constant irradiation at 1,350 Gy/h air KERMA of Cs-137 gamma irradiation over the course of 600 h/3.5 wks. Uncertainty margins have been omitted for clarity but were of similar size to those found in previous  $I$ - $V$  curves for similar dose rates.

### 6.3.2 Parameter behaviour with irradiation time

Parameter extraction was performed to allow more detailed analysis of how key parameters from the  $I$ - $V$  and  $P$ - $V$  curves behaved with irradiation time. Due to the large number of separate curves, manual data handling was not feasible and much had to be done programmatically: as with previous experiments, the  $I_{SC}$  values already existed in the data and could be extracted directly; a Julia script was used to interpolate to the  $V_{OC}$  for each trace. Fitting the data with the opposing-diodes model was not attempted for the longevity experiment, as currently the fitting process is quite unpredictable with regards to convergence from starting values, and it is not clear that automating the process will be trivial. More work on this front may be possible with the brute search employed in future.

Figure 6.26 shows the  $P_{MPP}$ ,  $I_{SC}$ ,  $V_{OC}$ , temperature  $T$  and relative humidity  $H$  with irradiation duration and cumulative air KERMA dose. The  $P_{MPP}$  shows the decrease over time. By inspection of the  $I_{SC}$  and  $V_{OC}$  it is clear that many of the finer features in the  $P_{MPP}$  are related to the current generated in the device, and that both  $I_{SC}$  and  $V_{OC}$  appear to be decreasing with dose over all. However, by comparison to the temperature and humidity data, it is not clear that it is the irradiation time that has caused the decrease. Indeed, the temperature and humidity varied more than was expected at the outset of the experiment, and qualitatively speaking, there are features in the temperature and humidity data which clearly correspond with features in the  $I_{SC}$  data. There is a hump feature between approximately 50 to 150 h which occurs most clearly in the humidity trace, but can be seen in all traces. The temperature and humidity data share certain peak and trough features. This is consistent with influxes of warmer, more humid air, and is likely due to facility checks by security personnel during the building closure. The points at which the  $I$ - $V$  measurement was started or re-started are marked by Roman numerals on the figure, and show that there is a stabilisation period for the device whenever it is turned on having been off for some time. However, it is notable that performance returns to a level that may be expected. These re/start features explain the anomalous curves visible in Figure 6.26, particularly in the  $P$ - $V$  data. It is likely that all previous tests fell within such re-start features, which does not invalidate them, but which must be borne in mind. Power increases of around one third were evident after the dips in each re/start feature, which stabilised within less than 24 h. Dr. Hutson's dosimeter exhibited a similar "priming" effect, hinting that it is the diamond crystal type, which the dosimeter shares in common with the DGV, that is responsible. That said, in the dosimeter, the effect tended to last weeks rather than days. Whilst these priming effects show a clear dependence of performance on irradiation time in the short-term, it is no longer clear whether irradiation time affects device performance in the long-term and, if it does, to what extent. There are two options for analysis of the full long irradiation data: creation of a full mechanistic model, or finding a statistical model.

The system in this experiment is simple enough, despite the temperature and humidity changes, that a mechanistic model could be considered. Such a model would have to account for the effect of temperature and humidity on adsorbed water coverage,  $\theta_{H_2O}$ , and the effect of irradiation duration on the terminating hydrogen coverage,  $\theta_H$ . The combination of a water molecule adsorbed to a

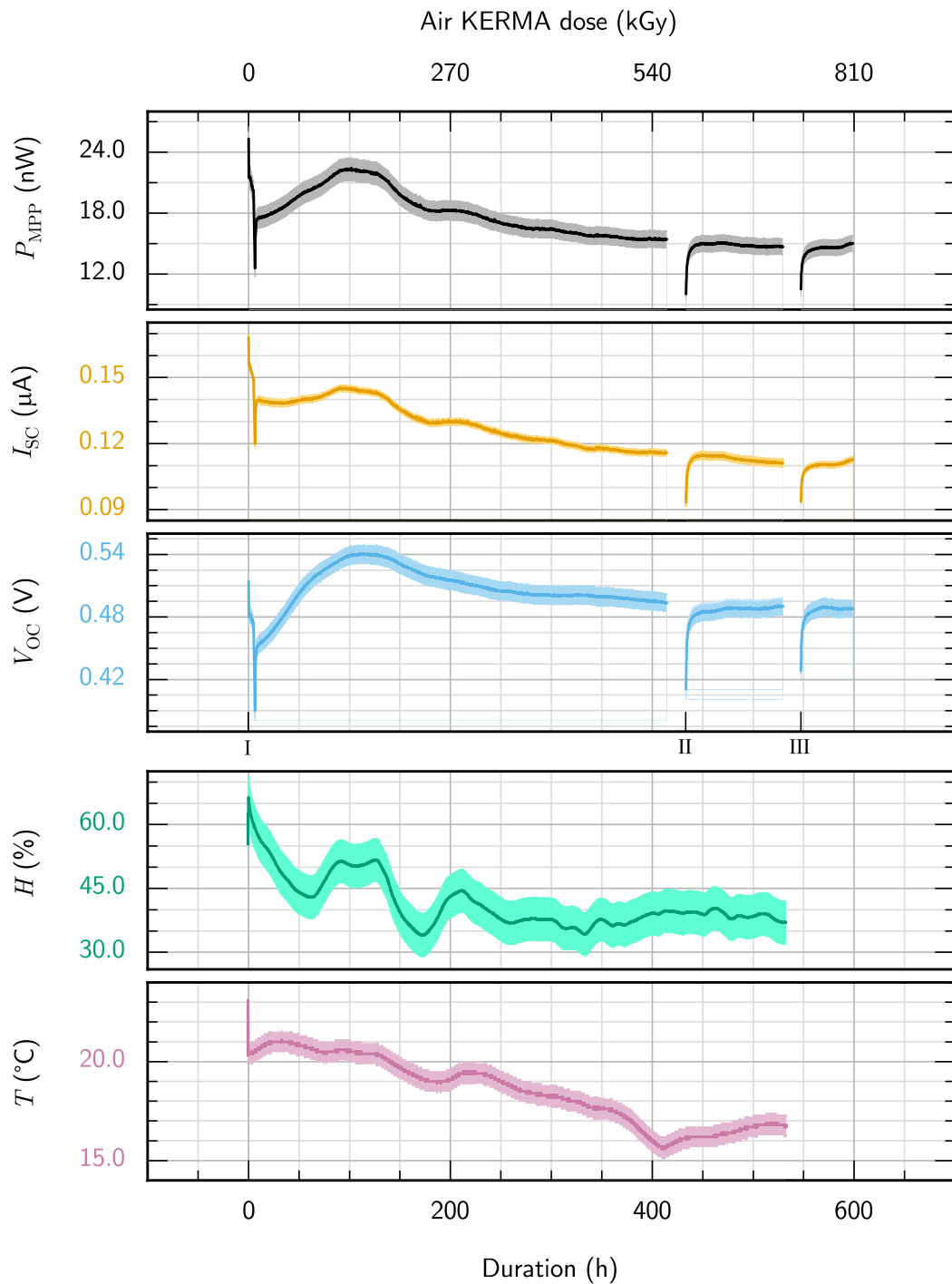


FIGURE 6.26.  $P_{MPP}$ ,  $I_{SC}$ ,  $V_{OC}$ ,  $H$  and  $T$  with irradiation duration, and the first three of these also with and air KERMA dose. Roman numerals correspond to electrical measurement session starts. The aliasing in the subfigure for  $T$  is a symptom of the measurement resolution, not the figure resolution.

hydrogen site could then be referred to in terms of an "activated coverage",  $\Theta$ . A relationship between this coverage and the device resistance and other such electrical parameters would then need to be sought. A model for the activated coverage can be arrived at by reference to literature and the introduction of a small number of fitting, parameters: -

$$(6.1) \quad \Theta(t) = -\theta_{H,0} \left( \frac{1}{2} \right)^{\frac{t}{\tau_{1/2}}} \ln \left( \frac{RT(t) \ln(0.01H(t))}{E_a} \right),$$

where  $t$  is the time spent under irradiation at a given dose rate;  $\tau_{1/2}$  is the desorption half life of the hydrogen coverage under that dose rate;  $\theta_{H,0} = 0.3$  is the initial coverage, which is known *via* the XPS measurements in Chapter 4;  $R$  is the ideal gas constant;  $E_a$  is the molar energy of adsorption for the first adsorbed water molecule; and  $T(t)$  and  $H(t)$  are the temperature and humidity at time  $t$ . For the reasoning behind, and derivation of, Equation 6.1, see Appendix C.  $E_a$  and  $\tau_{1/2}$  are unknown, but bounds and reasonable value ranges for each are available and could be used to fit both. It is here that the trail goes cold, however, as relating  $\Theta$  to the electrical properties seems impossible. One reason for this is that the surface conductivity of diamond can take tens of hours to stabilise [265], as elaborated on in Appendix C. A given  $\Theta$  therefore does not always correspond directly to a set of electrical parameters. Sample history must be considered.

Failing a mechanistic model, one may attempt a statistical model, which would allow the inclusion of such history by, for example, treating the previous ten humidity values for any given time as predictors for the surface conductivity, and hence  $P_{MPP}$ , at that time. There are many conceivable statistical models which could be argued for the data presented here, and also model selection processes. For example, one might begin with a linear model such as

$$(6.2) \quad P_{MPP} \sim t + H(t) + H(t-1) + \dots + H(t-10),$$

then use stepwise regression to whittle the model down to one in which all terms were considered significant [312]. This model would not describe the underlying processes like a mechanistic model, but would allow a decision to be made on whether degradation had occurred, and if so, how severe it was. Alternatively, all the models could be compared with an instrument such as Akaike's Information Criterion, in which relative scores are given to models which optimise between goodness-of-fit and the number of predictors used [313]. What both of these approaches, and indeed all statistical model approaches, sacrifice is that, as the data is known before the model, any model found to fit in this way cannot be used to draw conclusions at this stage. Rather, it must be re-applied to new data taken during a repeat experiment. The reason for this is that so called *post-hoc* analysis, wherein a model is fitted to known data, is liable to various errors [314]. Most prominently, increasing the number of models assessed increases the chance of finding incorrect but successful-looking models. It is worth noting, however, that criticism against this approach is usually tied to the fact that researchers are themselves biased towards finding significance in the variables they are studying. Finding false significance of predictors is therefore biased for twice. In the case of this work, the situation is reversed; a better gammavoltaic is one for which irradiation time is *not* a significant

predictor. On the assumption that I harbour at least some unconscious bias towards results which paint a favourable picture of the DGV, my experimenter bias opposes multimodel bias. The deciding factor for not pursuing a statistical approach, however, is pragmatic. Regardless of whether or not the device suffered degradation due to irradiation, it did suffer significant instability due to the bare surface being exposed to changing ambient conditions. Because encapsulation of the device, such as with transition metal oxides, is the natural next step to attempt to address both issues, there is not so much to gain from a device development perspective. How the device performs when bare is unlikely to carry much relevance to such a DGV in future. Whilst the data remains for use as pilot data should such a statistical approach be pursued in future it would be better, if another long experiment slot could be obtained, to use a device which is known to not respond to environmental humidity and temperature changes - a conclusion that could be obtained from a much shorter session.

A restrictive but less complex third approach would be to use the substantial size of the dataset to control for temperature and humidity, and indeed it can be shown that there is a run of approximately 15 h, between 286 and 301 h of irradiation, when both the temperature and humidity stay stable at the same time. Plotting of the  $I-V$  and  $P-V$  curves has shown that they do not change with dose in this time, to within measurement precision and possibly also measurement resolution (these curves are not plotted as a figure here as not much can be gleaned beyond the simple statement that the curves look more or less identical). Promising though this is, a window of 15 h is a substantially smaller cumulative dose than the experiment set out to attempt - only 20.25 kGy - and does not take us much further to answering whether a DGV could be deployed into a waste store long-term.

The scientific conclusions that may be drawn from this experiment are of a lower order of precision than the measurements. Nevertheless, they are useful: it is conservative to assume that the device degraded on its way to 800 kGy air KERMA dose, and as such, the DGV cannot be said to have passed the test of **longevity**. However, any degradation it did suffer was not catastrophic, and compared favourably to the 90 % degradation reported for a similar dose by Hashizume *et al* [38]. This is very promising, and to my mind, justifies further development of the technology.



## CONCLUSIONS

This work was spawned by the noticing of a very small gammavoltaic effect in a device which was not expected to exhibit it. Starting with the intention to explain this phenomenon, efforts quickly became diverted towards the creation of a commercially useful gammavoltaic device. This happened when it was realised that surface transfer doping might allow a very unconventional photovoltaic device design to improve greatly on the accidental gammavoltaic effect observed in the dosimeter. Concrete steps have been taken towards the creation of a useful gammavoltaic device. The work has generated perhaps more questions than it has answered, but there are substantive conclusions that may be drawn. This chapter will summarise the results of previous chapters, discuss the many avenues for future work and DGV improvement, and finish with the report of a proof-of-concept demonstration undertaken to clarify how close, exactly, to "useful" this DGV design has come.

### 7.1 Summary of this work

Each experiment in this thesis aimed to work within at least one of the five factors of comparability, accountability, capability, applicability, and longevity. These factors were each identified in the introduction as important for the research of gammavoltaic technology towards viability, with comparability and accountability being factors of standards within gammavoltaic research, and capability, applicability and longevity being factors of gammavoltaic device performance. Within each chapter, the factors at hand were made explicit in an attempt to give as clear and complete a picture as possible of the diamond gammavoltaic cell concept under study, but I do believe the attempt I have made in this work has several flaws, particularly insofar as accountability is concerned. Summaries of the results, the conclusions, and the flaws identified so far are given in the following subsections.

### 7.1.1 Capability and accountability: XRT and XPS experiments in Chapter 4

The first and most natural research question in this work was whether the gammavoltaic concept presented here was capable of actually working, and whether it indeed worked in the manner intended. This was tested by fabricating a DGV up to the point just before hydrogen termination - seen as the key facilitating step - and testing it under a high flux of broadband x-rays in the XRT. The behaviour of the device in the dark was different when not terminated and when partially terminated to a hydrogen monolayer coverage  $\theta_H \approx 0.3$ , but in both cases the device permitted only picoamperes of current to flow when  $I$ - $V$  curves between -50 and 50 V were applied. The device actually appeared to conduct better with no termination, which is a confusing result. When illuminated, the response of the device when unterminated was effectively the same, small gammavoltaic effect as seen in Dr. Hutson's dosimeter under Co-60 irradiation. When the device was completed with its partial hydrogen coverage, this greatly increased the gammavoltaic effect. Whilst no direct comparison could be made to literature due to the relative lack of gammavoltaic literature and the experimental variability inherent in the field, the voltages, currents and attendant powers attainable by a single,  $0.01 \text{ cm}^3$  cell compared favourably in a general sense to those reported in the literature, even with none of the parameters of the design optimised. This was a surprise. The rest of the work kept the same cell design for this reason, although it should be noted that probably, insufficient weight was given to the fact that the XRT radiation was quite different in some respects to that used in other experiments in the work. This is a flaw in the method and fails to work within the framework outlined in the introduction in terms of comparability.

Due to the idiosyncratic method of hydrogen termination employed - a modified coating system - it was next desirable to measure the hydrogen coverage present on a DGV. This was done through the proxy of a set of XPS measurements performed on a single crystal diamond with a boron doped diamond epilayer. It was expected that the coater system might not achieve a full hydrogen coverage due to being a less intense process than the microwave enhanced termination process usually used. This expectation was proved correct. Because there remains some suspicion that a full hydrogen coverage may in fact short the device, the coverage of 0.3 found in these measurements had no value judgement associated with it. However, it is not an optimised value, and it is likely that further exploring and optimising the hydrogen coverage is one important avenue for further improving the DGV presented here. As noted above, the device did not really conduct when not irradiated, so a proper 2DHG is unlikely to have formed.

### 7.1.2 Further accountability: synchrotron studies and validation of a GEANT4 model in Chapter 5

With the capability and the primary mechanism of action of the DGV design accounted for, more advanced experiments to try to account for other mechanisms taking place within a DGV were made with synchrotrons, and these also allowed the opportunity to pair well-controlled experimental conditions with GEANT4 simulations. GEANT4 is only capable of the high-energy component of

gammavoltaic physics, but was a good place to start in transforming a largely qualitative theoretical understanding of the device into a quantitative one. The basic assumption of the model used in the GEANT4 simulations was that the entire diamond region of a cell could be considered a sensitive volume for the sake of energy deposition. That is, that energy deposited anywhere in the diamond could be harvested, with some constant efficiency for a given photon flux and photon energy. That is, a linear relationship  $I_{SC} \propto E_{dep}$  was sought for validation. Other sensible hypotheses existed, such as the sensitive volume only occupying a space within a certain distance of the diamond surface, but this one was tested first for the pragmatic reason that simulating gamma ray interactions requires more and more computer time the smaller the sensitive volume becomes. With it desirable to keep photon flux and energy constant, a photoresponse mapping experiment was chosen and performed at the SP8 synchrotron in Japan. The  $I_{SC}$  at each point of the map was compared to the  $E_{dep}$  as simulated with GEANT4. Whilst a positive correlation was found, and the data were noisy enough that a linear fit did not appear out of the question, a fit using ODR gave  $\chi^2_v = 1162$ , indicating a linear model did not fully account for the shape of the data. Possible reasons presented for this include the mismatch between idealised components in the simulation and their real counterparts, and genuine electrical differences in how the device handles illumination in different regions of its surface. As the latter were what the validation experiment were trying to eliminate, this experiment had only moderate success. The conclusion drawn was that simulated energy deposition should be treated as an estimate rather than a well-determined property.

A second experiment was performed at the DLS synchrotron in the UK, with a complimentary simulation which carried the caveats of the previous attempt at validation. The DLS experiment was performed to probe how the electrical behaviour of the device might change with internal scattering mechanism, as it was performed over the energy range in which the mechanism changed from photoelectric absorption to Compton scattering inside the diamond. The analysis of these results is presented differently to how it was presented in a previously published article [65], in light of questions raised when this work was examined *viva voce*. In the article, a series resistance extraction technique adapted from one found in the literature [159, p. 157][302] was used and the series resistances extracted in this way compared to the prevalence of Compton scattering over the range of photon energy, seeming to show a correspondence between series resistance and the prevalence of Compton scattering. The adaptation of the series resistance extraction technique may be too blunt in terms of accuracy, or invalid - work is ongoing to understand this. The opposing-diodes model, presented in Section 2.2, was also not suitable because the  $I$ - $V$  curves had been taken over too narrow a voltage range. As such, the conclusions drawn from this experiment are of a more basic nature than in the paper. Photon flux decreased with photon energy in the DLS measurement. It would appear that the increase in photon energy led to an increase in power output up to a point, after which the decreasing photon flux overwhelmed this effect. With deposited power estimated using a GEANT4 simulation, maximum deposited power efficiency could be estimated as well as maximum incident power efficiency. Both were low. A very large proportion of the incident

energy was estimated to have not been deposited into the device, and of that which was, only a small fraction was turned into electrical power. This was expected to some degree, as one of the GEANT4 simulations had suggested that the DGV would be at its least efficient in terms of absorbing power in this region of photon energy. In particular this was the case for the photon energy corresponding to the emission of Am-241, for which power density values were found of  ${}_{20,000}^{Am-241}\mathfrak{P} = 38907 \text{ nA/cm}^3$  and  ${}_{20,000}^{Am-241}\mathfrak{p} = 1945 \text{ nA/cm}^2$ . These were compared in dose rate to the mass of Am-241 found in domestic smoke detectors, to illustrate the fact that the power densities themselves were unlikely to be of much use for device design. The experimental design did not take into consideration the fact that the charge injection from such a beam, likely to be so much greater than in the XRT case, may have led the DGV to operate in a different regime in which the surface may have played a less significant enabling role.

As a last calculation, the short-circuit current and maximum power-point power were normalised in flux and found to rise nearly linearly with photon energy, the data in both cases having a slightly sigmoidal shape. No obvious qualitative difference emerged between the regimes of photoelectric absorption and Compton scattering in these two parameters. It may be the case in the future that a more thorough theoretical understanding of the device will allow these data to be re-used for better mechanistic conclusions. As it stands the data are mainly of interest for their magnitude.

### 7.1.3 Comparability, applicability and longevity: Isotope irradiation experiments in Chapter 6

Further work could have been, and can be, performed to investigate the current generation mechanisms within the DGV cell design, and how they contribute to the overall accountability of the performance of the cells. However, with the work also wanting to address applicability, it was important to also test devices made of more than one DGV cell, under irradiation from gamma rays from prominent isotopes. A triple-celled DGV device was created out of all three fabricated cells, with the cells mounted stackwise in a series connection. The triple-celled DGV was tested under Co-60 and then Cs-137 gamma irradiation, over three orders of magnitude in dose rate, from tens to thousands of Grays per hour. Benchmark areal and volumetric maximum power-point power density values, presented in the hope that it would aid comparability between this work and future works in gammavoltaics, were found, of  ${}_{100}^{Co-60}\mathfrak{p} = 27 \text{ nW/cm}^2$  and  ${}_{100}^{Co-60}\mathfrak{P} = 179 \text{ nW/cm}^3$  respectively. At this level of hundreds of Grays per hour, equivalent to the ambient dose rates found in nuclear waste stores, the power output was reasonable for a gammavoltaic. But, it was not at the level of applicability, in the sense that many such devices, or physically larger cells, would have to be used together to produce useful quantities of power. The numbers required in such circumstances would be completely technically reasonable, but not financially so. This gammavoltaic cell design is not yet applicable to deployments into the ambient field of a waste store. However, at the level of thousands of Grays per hour, on the order of dose rates found at the surface of waste canisters in such a store, power outputs were such that only a few such devices would breach the 4 V, 200 nA threshold

requirement used as a benchmark in this work. The device was thus considered to pass *this* test of applicability, at least in a qualified sense. The relevant areal and volumetric maximum power-point power densities were  ${}_{1070}^{Cs-137} p = 281 \text{ nW/cm}^2$ , and  ${}_{1070}^{Cs-137} \mathfrak{P} = 1873 \text{ nW/cm}^3$ , respectively. Whilst this is a promising achievement, the arrangement of material around a DGV has not yet been optimised, and it is suspected that some changes here could capitalise on the "scatter shroud" effect by increasing the energy deposited into the DGV for a given photon flux.

The opposing-diodes model was found to be capable of fitting the  $I-V$  data in this section, and inspection of the instrumentally-weighted residuals of the fit suggested that in each case the fit was an over-fit. That said, the model appeared to deviate the most precisely where a close fit would be most useful - in the power-producing quadrant of the curves. For the fits attempted in this work, the ideality factors were bounded between 1 and 2. It may be that allowing one or both ideality factors to be larger would improve the closeness of the fit, and there is some suggestion in the literature that this may be a suitable course of action, but more work is needed to understand this before it is attempted. That said, one of the ideality factors was fit to a value of 1 for every fit, so it might be possible to remove this parameter entirely in future and thus shrink the complexity of the model and the size of the fitting parameter space. Fitting the opposing-diodes model gave much greater certainty for some of the equivalent-circuit parameters than others, which is consistent with the way the fitting parameter space can behave for the less-complicated models used to model conventional photovoltaics with, and without, parasitic resistances. It seems possible that some of the parameters took their values at the global minimum whereas others were more prone to falling into local minimum values. Nevertheless, with the fits likely over-fits and the Kolmogorov-Smirnov test also supporting the notion that the residuals were not drawn from normal distributions, only so much weight should be attached to the equivalent circuit parameters estimated in this fashion. There does appear to be strong reason to believe at this stage that the cell does not respond with a simple change in the photocurrent with increasing air KERMA dose rate, and thus with increasing flux. An additional test was performed in which the quantity  $k_b T \ln(I_{01}/I_{02})$  was calculated and plotted. This quantity would be equal to the difference in barrier heights if both contacts had equal effective areas and conducted purely *via* thermionic emission. As the barrier of the high-barrier contact was expected to be pinned at around 1.2 eV, this quantity should be less than that. And indeed, it was found to vary, across the curves, between about 0.2 and 0.6 eV.

Finally, with a level of applicability demonstrated, work turned to longevity. Whilst work from this point could have focused on increasing power outputs through hydrogen coverage or scatter shroud optimisation, the longevity test was considered to be of higher priority. That is because increased power outputs would be in vain if the device ultimately degraded too quickly. Gammavoltaic devices in a nuclear waste store would need to work for many years or decades. As mentioned at the beginning of this work, the three performative factors of capability, applicability and longevity must all be met, probably in sequence, for any gammavoltaic to become industrially useful. The longevity test for the waste store application is a particularly tricky one, and in a sense it is here that the gammavoltaic

must pay for the low bar of power output it must achieve to be useful in such a context. Because it was only at the level of thousands of Grays per hour that the DGV had passed the test of applicability under isotope irradiation, it was at this dose rate that the test for longevity was made. A single-celled DGV was irradiated at 1,350 Gy/h air KERMA for just over 3.5 wks, for a total air KERMA dose of over 800 kGy. The circumstances that led to such a test being possible were unusual, to say the least, and the temperature and humidity fluctuations during the experiment appeared to dominate performance fluctuations, due to the choice to leave the terminated diamond surface bare of encapsulants. The data proved resistant to mechanistic modelling due to the fact that the conductivity of diamond surfaces can take many hours to stabilise even when temperature and humidity are constant. A statistical model was discussed as a possibility, although I am of the opinion that repeating the experiment would provide too little extra information, relative to the resources it would cost, to be worthwhile. The two important results are: -

1. that as expected, any future diamond gammavoltaic cells of the design presented in this work need encapsulation, to ensure that surface hydrogen termination is maintained and electrical behaviour does not vary with ambient factors; and,
2. the surface hydrogen termination appears to be quite robust in the face of such a high Cs-137 dose rate.

This latter conclusion is based on the fact that no catastrophic degradation occurred, and that even ignoring the effect of humidity and temperature, the observed drop in performance from stable start to end regions of the  $P_{MPP}$  trace is only about 16 %. This compares favourably against the previous reports of more rapid degradation in the gammavoltaic literature. However, the DGV did not pass the test of longevity here. It would need to survive far longer at the same dose rate to do so. Future work will need to investigate how surface encapsulation can improve the stability of the device under irradiation, and to run long duration testing in real nuclear sites. The administrative arrangements for these tests have been made. Also of benefit would be finding a way to reliably fit the opposing-diodes model to many curves automatically, as currently it is too sensitive to starting parameters to be able to fit the thousands of  $I-V$  curves generated by longevity experiments like this.

## 7.2 Avenues for future work

This has been the start of the device development journey for DGVs, and hopefully not too close to the end of it, too. At time of writing, funding has been secured to continue development in short term. Much like for the development of early, 1 % - efficient photovoltaics, the prototypical DGVs presented herein are very small and crudely optimised, but show promise for substantial further improvement. Whilst it is therefore gratifying that the performance of the DGV has been competitive, it leaves several significant avenues open for future research.

### 7.2.1 Diamond type

Diamond type could present a significant avenue for device improvement in the right circumstances. Cell thickness is the most obvious parameter to vary, but perhaps the most difficult without the backing of a commercial project partner able to supply custom wafers with specified qualities in addition to different thicknesses. Crystallinity is another, though it is not clear that a move to polycrystalline diamond would be successful, even if it were detector-grade. Were it possible to make capable and applicable DGVs with lower-purity polycrystalline diamond, this would represent an abrupt increase in the viability of the technology: thermal grade polycrystalline diamonds are available at quadruple the size of electronic grade single crystals for a twentieth of the cost from the same supplier (Element Six). Until internal processes within the DGV are better understood, polycrystalline diamond remains an unattractive research avenue due to the likelihood that grain boundaries would reduce the proportion of charge carriers collected.

However, the ability of researchers to grow larger single crystals is improving all the time; consider the 92 mm - diameter wafer grown in 2017 by Schreck *et al* [315]. Such crystal may not yet be of high enough quality for a DGV, but this avenue ought to open up with time. A wafer of such a size would present 328 times the surface area to a gamma field. As power output may be expected to rise linearly with surface area, this could push the performance of a triple-celled device from 57 nW to 19  $\mu$ W under 1070 Gy/h air KERMA of Cs-137 radiation. Such a power increase would push the DGV from a device which is limited to sporadic power *via* on-chip energy storage, to one which could operate some circuits continuously. For example, gas sensors now exist which operate on 6  $\mu$ W [316]. It is likely that single crystal growth technology and low-power sensor technology, the progress of each of which is driven strongly by fields other than gammavoltaics, will increasingly meet in the middle in a way which increases the applicability of DGVs. In a similar vein, the increasing ability to thread fine, conductive paths of lattice damage through single crystal diamond [163] may offer an alternative to hydrogen termination altogether, side-stepping the issues of surface instability found in this work. Of course, both of these steps would likely increase the embodied financial and carbon cost of devices significantly, so this would need to be taken into account.

### 7.2.2 Termination optimisation

Neglecting the possibility of avoiding it altogether, two approaches could be taken to optimising the hydrogen termination, depending on how much emphasis is applied to the engineering side *versus* the scientific side of device development. It would be straightforward to repeatedly terminate the same DGV cell for varying lengths of time in the coater system to find the optimum recipe for power output. The most scientific route, which would also be more labour and resource intensive, would seem to be to follow the above procedure whilst also performing further XPS measurements with the NanoESCA II, such that performance could be tied to hydrogen monolayer coverage rather than just termination duration. Given the latter is likely quite specific to the setup used in this work, attributing

changes to the process but not the result of said process would present a replication problem to other researchers.

There is also a second type of termination to be considered - the under-contact termination. It was known that an oxygen-termination under the aluminium high-barrier contact would lead dependably to a high-barrier contact, but probably not the highest barrier possible. With the core DGV design concept validated to some degree in this work, attempting to use a fluorine or nitrogen termination instead of oxygen, with the attendant challenges, seems justified.

### **7.2.3 Mounting: Scatter shrouds and backplates**

Much like a concentrated solar power installation uses mirrors to focus light onto an optimised solar photovoltaic, the penetrating nature of gamma rays and their immediate scatter products suggests that the mounting and housing of a gammavoltaic cell may be quite important for the power generated by the cell. Indeed, it may be exploited, as hinted at by the influence of the silver epoxy paint in the energy deposition heat-map simulated in Figure 5.2 (Chapter 5), or the increased energy deposition into the other two cells due to the cell facing the radiation as simulated in Figure 6.1 (Chapter 6). Optimising the device housing materials - the backplate and the scatter shroud - for increasing energy deposition into the device is a relatively small parameter space which may be explored with simulations first, bringing the development of the DGV closer to the normal mode of device development. A backplate must simply scatter as much radiation back into the DGV as possible, whereas a scatter shroud must optimise between interacting with as much primary gamma radiation as possible, whilst impeding scatter products as little as possible so that they reach the device. Assuming a constant diamond thickness for now, that would be a four-dimensional parameter space: backplate material, backplate thickness, scatter shroud material and scatter shroud thickness. Probably, using  $Z$  as an analogy quantity for material in each case. To simulate this parameter space for a single photon energy, such as the 662 keV of Cs-137, would be a simple extension of the simulations presented in this work, if time-consuming.

To illustrate the potential of such an approach, I have performed an exploratory set of simulations in which a lead backplate is paired with a diamond scatter shroud, which could be highly boron-doped so as to also act as an electrode and mounting clip in place of silver epoxy paint. These simulations are shown in Figure 6.2, using 662 keV photons. First the base case is presented, using the simulation geometry used in this work. All other cases are normalised to this one. Removing the silver paint, copper wires and SMA pin from the simulation leads to a decrease in energy deposition of around 10 %. Adding in a lead backplate of 0.5 mm thickness increases the energy deposition substantially. Adding a diamond scatter shroud, also 0.5 mm thick, leads to another substantial increase. These simple changes, using fairly arbitrary but reasonable materials and thicknesses, leads to an energy deposition of 150 % of the base case. With suitable diamonds costing in the region of £2,000 each, power density increases due to backplates and scatter shrouds offer not just the appeal of increased power output, but also of substantial cost decreases because less diamond could be

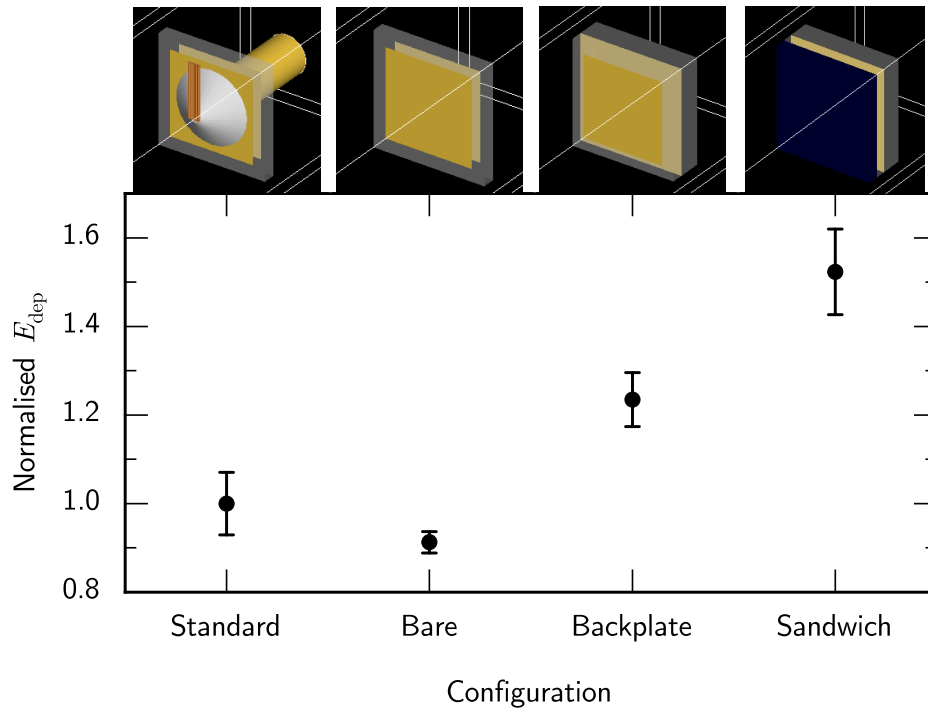


FIGURE 7.1. The total energy deposited into a single-celled DGV in various configurations, normalised to the configuration used throughout this work.

used.

A simpler technique, as alluded to in Section 6.1, might be to present the DGV sideways to the radiation, sacrificing surface area for the sake of collection volume depth. This kind of technique lends itself well to simulation, although some consideration of what such a batch of simulations would entail shows it is a large parameter space to explore - particularly when additional considerations like scatter shrouds, backplates, and the fact that different dimensions in the individual diamond crystals may become relevant in future. Nevertheless, basic exploratory work has been conducted, using the simple technique of simulating just a single slab of diamond at two rotations (face-on as standard, and side-on), and with dimensions corresponding to either single- or triple-celled DGV devices. The results are shown in Table 7.1.

As might be expected, turning a DGV side-on makes the most difference for thinner diamonds (i.e. fewer cells), and higher photon energies. Furthermore, for higher photon energies, each cell would be receiving the same energy deposition, so current throttling would not apply. However, as may be drawn from other conclusions in this work, energy deposition does not always related to power output in a straightforward manner, and the clearest cause for concern when turning a DGV side-on would be the greater inhomogeneity in energy deposition across the device. Whilst diffusion

Dimensions	Isotope	$E_{\text{dep}}$ (%)	$A$ (%)
Single cell	Cs-137	116	11
Single cell	Co-60	154	11
Triple cell	Cs-137	104	33
Triple cell	Co-60	111	33

TABLE 7.1. Simulated energy deposition for diamonds placed side-on to radiation, with energy deposition and surface area presented given as percentages of the front-on cases.

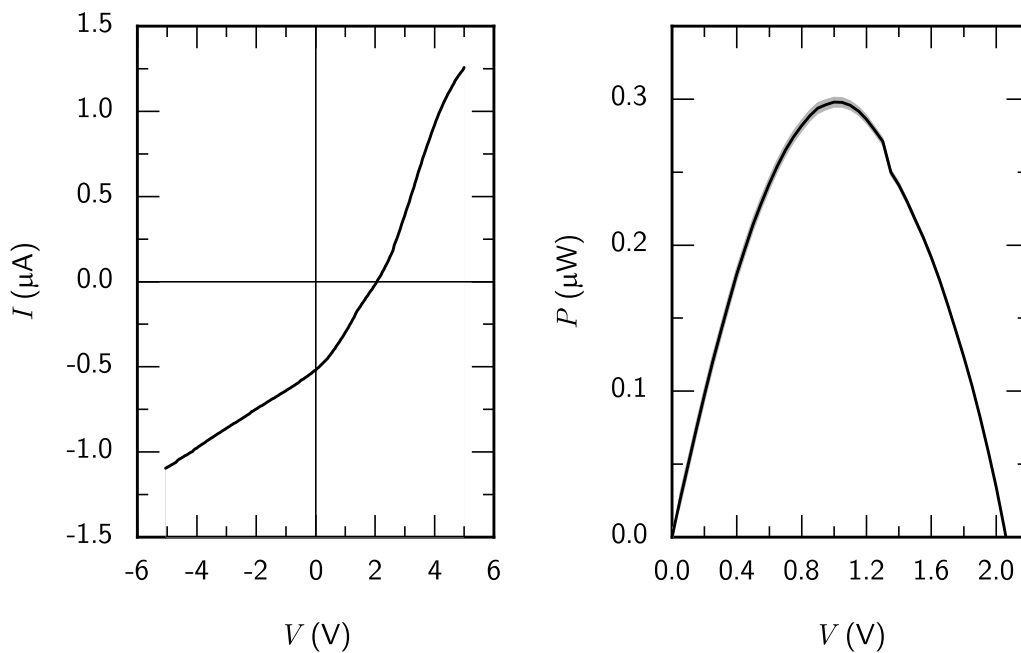


FIGURE 7.2. The  $I$ - $V$  curve of the triple-celled DGV under irradiation in the XRT, operating at 160 kVp and 10 W source power.

currents would no doubt rectify some of this by their nature, the fact that a drop in resistance would likely be seen in one region of the device more than the other might lead to throttling of a different kind - of voltage. Ultimately, answering the question of what combination of device rotation, scatter shroud and backplate, diamond size and electrical configuration is optimal would depend strongly on the radiation type, availability of diamonds, and practical concerns around fabrication, and would require a didactic research effort in which simulation, practical concerns and experimental work all inform one another.

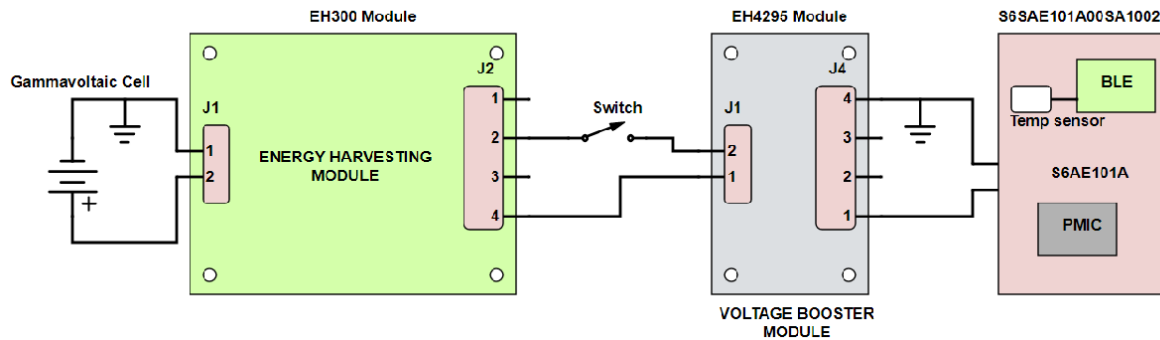


FIGURE 7.3. The circuit attached to the triple-celled DGV for demonstration purposes, designed by Dr. Suresh Kaluvan, University of Bristol. This figure was produced by Dr. Kaluvan.

### 7.3 A final demonstration

Throughout this work, the goal has been 200 nA and 4V, in line with the specifications of the EH300 by Advanced Linear Devices. This was six million times more power than the dosimeter had produced, and the device has not yet progressed all the way there. Success has been had, with the majority of that gap having been closed though fairly simple changes, each of which provides avenues for further improvement. It is known now that the triple-celled DGV in its present form could pass the test of applicability, given that several such devices could be used together. However, this focus on the DGV itself obscures the fact that the circuit will exert some influence on the device whilst it is in operation. It might be the case, for example, that the DGV would never be held at the maximum power-point. This is a capability issue, at its root. To address this, a stripped-down energy harvesting circuit was created, based upon the EH300 operating sub-optimally. It was coupled with the triple-celled DGV under an irradiation of x-rays in the XRT, operating at 160 kVp and 10 W. The  $I$ - $V$  curve from this irradiation can be seen in Figure 7.2, whilst a schematic of the circuit can be found in Figure 7.3. A manual switch was used in the circuit, in place of the "powerless switch", the UB20M by Sensor Driven [317], earmarked for future circuits, which would consume 5.4 pW to trigger. The output of the triple-celled DGV in the XRT produced an  $I_{SC} = 518$  nA, a  $V_{OC} = 2.06$  V, and a resultant  $P_{MAX} = 1067$  nW. At the maximum power-point, it produced an  $I_{MPP} = 292$  nA, a  $V_{MPP} = 1.02$  V, and a  $P_{MPP} = 298$  nW. The  $I$ - $V$  curve form was not good; the  $FF = 0.28$ .

However, when connected to the circuit, and left to run for 10 h before the switch was thrown, the circuit powered up for a sufficient period (around 10 s) that a reading of temperature and humidity could be recorded and transmitted *via* Bluetooth to a nearby receiving laptop. This is a crude demonstration, but it shows that a triple-celled DGV passes a higher test of capability than previously believed - the capability to power a sensor pod, and perhaps to be useful. To my knowledge, this is

the first time a gammavoltaic has been used to power anything.

There are several important speculative uses for gammavoltaics in general - the safety of nuclear reactors when shut down, the supplementation of their operation when working, the powering of satellite components, the creation of set-and-forget power sources for distributed applications. But I hope that this final demonstration shows that this thesis has brought one use - the notion of powering sensor units in nuclear waste stores - from the speculative realm towards the concrete. Diamond gammavoltaic devices, of the type presented in this thesis, may greatly increase the information we have about the evolving interiors of such stores in future, and I hope may therefore make a contribution to our safety.



## REFERENCES FOR DIAMOND-METAL CONTACTS

This appendix contains tables of references for Figure 1.5, in which contact barrier heights are displayed for a range of metals and surface termination on diamond. In the tables, contacts are arranged alphabetically by contact metal, then alphabetically by termination species (with "clean" referring to no intentional termination), then by barrier height, smallest to largest. Entries have been split over multiple tables for the purposes of space.

It should be noted that several other factors influence barrier height, such as the crystal orientation of the surface on which the contact is formed; whether or not the contact was annealed, and if so, at what temperature and for how long; the presence or lack of encapsulating metals; and, the deposition method. However, as the figure was stripped of this information to make clear the overriding dependence on surface termination, that information is not included in these tables either. It has, however, been collected and can be made available on request. A similar table has also been compiled for diamond ohmic contact research, which is not included here as I did not consider it suitably relevant to this work. However, it too can be made available on request. I do not presume that these tables come close to a full survey of the literature - in fact I know that they do not - but they are considered sufficiently thorough that they give a reasonable account of trends.

Contact metal	Termination	Barrier height (eV)	Reference
Ag	O	1.65	[147]
Al	H	0.59	[153]
Al	H	0.86	[151]
Al	H	0.9	[318]
Al	O	1.05	[131]
Al	O	1.2	[150]
Al	O	1.3	[154]
Al <sub>2</sub> O <sub>3</sub>	O	1.34	[140]
Au	F	2.29	[169]
Au	F	2.38	[319]
Au	H	-0.19	[169]
Au	N	2.37	[152]
Au	N	2.39	[169]
Au	O	1.2	[150]
Au	O	1.57	[137]
Au	O	1.58	[25]
Au	O	1.7	[150]
Au	O	1.71	[169]
Au	O	1.75	[319]
Au	O	2.2	[138]
Co	Clean	0.35	[144]
Co	Clean	0.4	[144]
Co	Clean	0.4	[144]
Co	H	0.27	[153]
Co	H	0.45	[144]
Co	H	0.45	[144]
Co	H	0.5	[144]
Co	O	1.4	[144]
Cr	Clean	1.05	[136]
Cr	O	0.75	[154]
Cr	O	1.2	[150]

TABLE A.1. References for Schottky contact barrier heights, as shown in Figure 1.5. Metals Ag to Cr. "Clean" here means no termination process used.

Contact metal	Termination	Barrier height (eV)	Reference
Cu	Clean	0.3	[155]
Cu	Clean	0.6	[155]
Cu	Clean	0.7	[155]
Cu	Clean	0.75	[155]
Cu	F	2.31	[319]
Cu	H	0.49	[318]
Cu	H	0.5	[155]
Cu	H	0.9	[155]
Cu	H	0.9	[155]
Cu	N	1.84	[152]
Cu	O	1.4	[146]
Cu	O	1.6	[155]
Cu	O	1.69	[319]
Fe	H	0.51	[318]
In	H	0.8	[318]
Ir	N	2.2	[152]
ITO	O	2.45	[135]
Mg	H	0.87	[318]
Mg	H	0.94	[318]
Mo	O	1.2	[142]
Mo	O	1.2	[143]
Mo	O	1.4	[320]
Mo	O	1.85	[141]
Ni	H	0.19	[153]
Ni	H	0.59	[318]
Ni	H	0.7	[318]
Ni	O	0.61	[147]
Ni	O	1.2	[150]
Ni	O	1.55	[154]
Ni	O	1.7	[150]

TABLE A.2. References for Schottky contact barrier heights, as shown in Figure 1.5. Metals Cu to Ni. "Clean" here means no termination process used. ITO here is the popular initialism for indium tin oxide.

Contact metal	Termination	Barrier height (eV)	Reference
Pb	H	0.51	[153]
Pb	H	0.79	[318]
Pb	H	0.82	[318]
Pd	F	2.3	[319]
Pd	N	1.78	[152]
Pd	O	1.7	[319]
Pt	Clean	1.39	[321]
Pt	N	2.14	[152]
Pt	O	1.2	[150]
Pt	O	2	[21]
Ru	O	1.16	[143]
Ta	H	0.8	[318]
Ti	H	0.39	[153]
W	H	0.51	[318]
W	O	1.65	[154]
WC	O	0.8	[149]
WC	O	1.48	[149]
WC	O	1.5	[149]
Zn	H	0.36	[153]
Zn	H	0.79	[318]
Zn	H	0.92	[318]
Zn	O	2.1	[150]
Zr	Clean	0.7	[144]
Zr	Clean	0.7	[144]
Zr	Clean	0.85	[144]
Zr	H	0.7	[144]
Zr	H	0.75	[144]
Zr	H	0.95	[144]
Zr	O	0.9	[144]
Zr	O	0.93	[139]
Zr	O	1	[149]
Zr	O	1.4	[135]
Zr	O	1.4	[135]
Zr	O	1.4	[149]
Zr	O	1.57	[139]
Zr	O	1.9	[149]
Zr	O	1.93	[139]
Zr	O	1.97	[135]

TABLE A.3. References for Schottky contact barrier heights, as shown in Figure 1.5. Metals Pb to Zr. "Clean" here means no termination process used.

## *I-V* CURVES TAKEN AT THE SPRING-8 SYNCHROTRON IN FULL

In the experiment at the SP8 synchrotron, only the  $I_{SC}$  values were taken for use when validating the GEANT4 model in Figure 5.3, Section 5.2. This appendix presents the rest of the *I-V* curves, in Figure B.1. For the sake of clarity, the *I-V* curves are separated out over a number of panes, firstly in directional order (the order they were taken as the beam was scanned vertically or horizontally) and secondly, grouped by magnitude. For ease of reference, there is a colourmap in the figure which is laid out how the  $I_{SC}$  values are in Figure 5.3, which is coloured the same as the trace as it appears Figure B.1.

Two things are notable from the full *I-V* data. The first thing is that many of the *I-V* curves do not present with the normal form. There are a number of potential reasons that suggest themselves for this, but it seems most likely that these "double-dip" *I-V* curves are due to there being substantially different levels of shading within the cross-sectional area of the beam. For example, the traces between that labelled C and that labelled G in Figure B.1 show a gradual transition from the standard form, to the "double-dip" form, and back to the standard form. At C, which was taken with the beam centrally positioned on the device, the beam may have had roughly equal shading across the cross-sectional area due to silver paint being at its thickest. Conversely at G, there will have been no silver paint. In between, the quantity of silver paint will have been changing throughout the cross-sectional area, and this difference - equivalent in some sense to partial shading - may be enough to explain the form of the *I-V* curves. All other experiments in this work focused on irradiating the whole device and did not show, at least to the eye, much in the way of shading effects. It may be that the finer precision and flux of the SP8 experiment threw this effect into sharper relief, or it may be that the inherently unpredictable nature of applying silver paint with a brush was the cause, and the device for this test simply had a less uniform and/or thicker application. Silver paint has proved useful for its relative ease of use, low cost and reversibility, but future work may benefit from avoiding it.

The second thing notable in Figure B.1 is that even when the beam was nominally not hitting

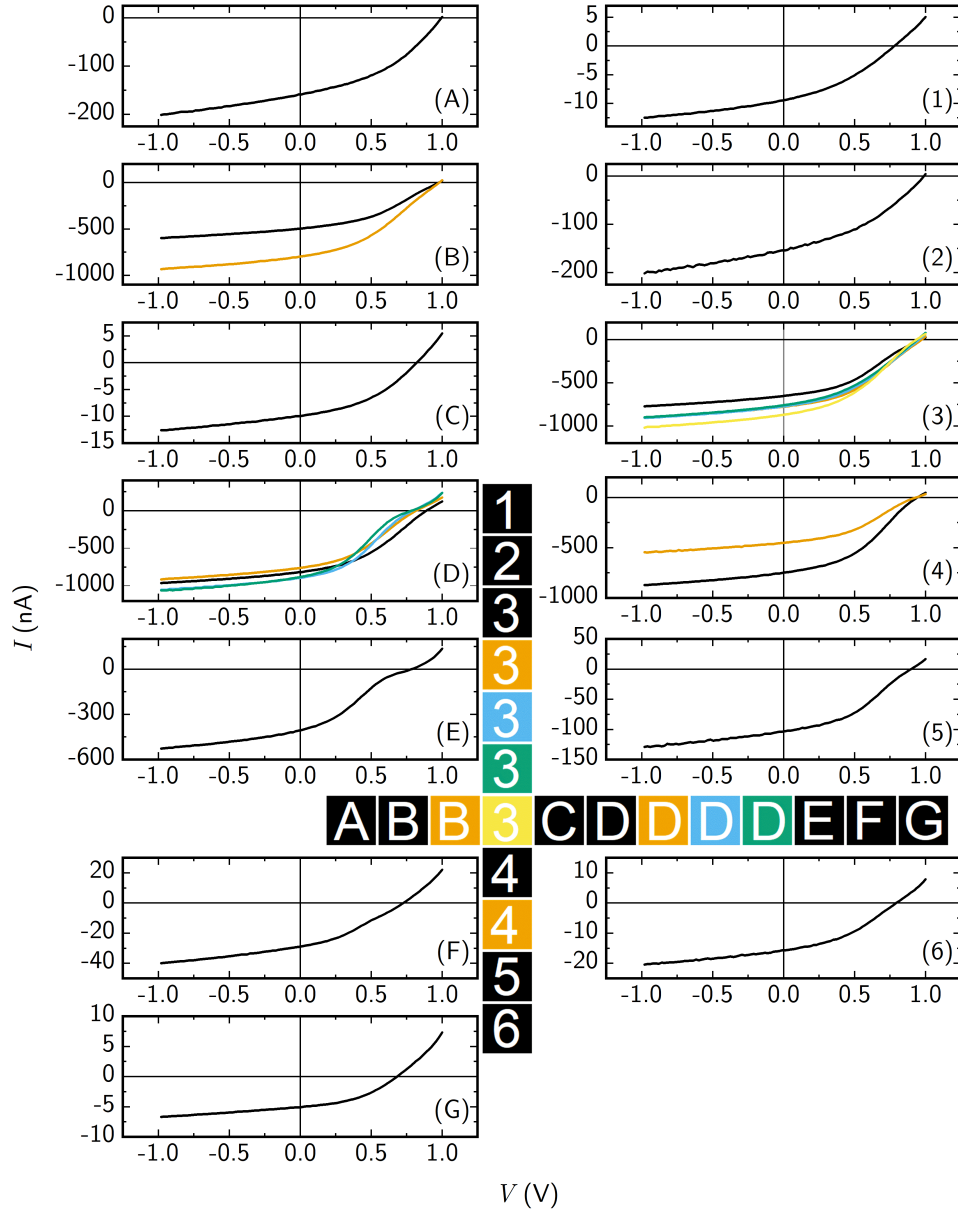


FIGURE B.1. The full  $I-V$  curves from the SP8 mapping experiment. Lettered sub-figures correspond to the horizontal axis whilst numbered ones correspond to the vertical, in terms of beam position. Set amid the plots is a map key, coloured in correspondence to the traces in this figure, annotated in correspondence to the plot that trace is displayed in, and laid out in the same relative positions as the co-ordinates in Figure 5.3.

---

the face of the device at all, at position  $(x, y) = (4.0, 0.0)$  (plot G in Figure B.1), there was a small photo-current measured. Because multiple measurements were not made and the instrumental error was small, it is not clear whether this trace in truth would pass the third-quadrant test when error bars were taken into account. Positioning was done by measuring the onset of current, so uncertainty here may also have played a role - though any displacement made at this end would require a corresponding displacement at the other, so by the larger response at  $(-1.5, 0.0)$ , we can be reasonably sure that the position uncertainty was not great. Secondary scatter from the air, in such an intense beam, provides some justification for the possibility of power being generated.



## TOWARDS MECHANISTIC MODELLING OF THE LONG Cs-136 IRRADIATION

This appendix deals with the progress made towards a mechanistic model for the behaviour seen in the long Cs-137 irradiation experiment, the results of which are shown in Section 6.3.2. Mechanisms tied to temperature such as carrier concentration and mobility tend to be cast in terms of absolute temperature, and as such the temperature variations seen during the long irradiation might safely be set aside for a simple model, with their average used instead. This would leave two major environmental considerations for device performance: irradiation duration and humidity. Irradiation (as opposed to irradiation duration) will cause two effects: photo-dissociation of adsorbed water, and desorption of termination hydrogen. The former will be compensated for by the reservoir of water molecules in the humid air; irradiation will shift the average water molecule concentration in what is a dynamic equilibrium of monolayer coverage. The hydrogen desorption, meanwhile, will not be compensated for. The irradiation duration (as opposed to irradiation) might therefore be expected to only be observed in its affect on hydrogen monolayer coverage:

$$(C.1) \quad \theta_H = \theta_H(t).$$

A reasonable form seems to be a decay relationship, which may either be cast as an exponential or, with a view to future communication of device performance, as a half-life equation:

$$(C.2) \quad \theta_H(t) = \theta_{H,0} \left( \frac{1}{2} \right)^{\frac{t}{\tau_{1/2}}},$$

where  $\tau_{1/2}$  is the half life of the hydrogen coverage under a given dose rate, and  $\theta_{H,0} = 0.3$  is the initial coverage, which is known via the XPS measurements in Chapter 4. Meanwhile, humidity ought not affect the hydrogen monolayer coverage, but will directly affect the coverage of adsorbed water, which is also a key component in the surface transfer doping mechanism. There are a number of approximations for adsorbate coverage based on gas pressure, but perhaps the simplest to apply,

which also introduces the fewest unknown quantities and is among the more accurate, is the chi hypothesis [322]:

$$(C.3) \quad \theta_{\text{H}_2\text{O}} = \begin{cases} \chi - \chi_c & (\chi - \chi_c) > 0 \\ 0 & (\chi - \chi_c) < 0 \end{cases},$$

where

$$(C.4) \quad \chi = -\ln\left(-\ln\left(\frac{P}{P_{\text{vap}}}\right)\right) = -\ln(-\ln(0.01H)),$$

$$(C.5) \quad \chi_c = -\ln\left(\frac{-E_a}{RT}\right),$$

$P$  is the partial pressure of water vapour in the air,  $P_{\text{vap}}$  is the saturation vapour pressure of water,  $R$  is the ideal gas constant, and  $E_a$  is the molar energy of adsorption for the first adsorbed water molecule. When considering water vapour rather than other gases, the relative humidity  $H = 100 \times P/P_{\text{vap}}$ . In practise, it is known that there is always some quantity of water on any surface in standard conditions, so the piecewise nature of Equation C.3 is reduced to only its top term. Substituting Equations C.4 and C.5 into this allows a final equation for water monolayer coverage to be given:

$$(C.6) \quad \theta_{\text{H}_2\text{O}} = -\ln\left(\frac{RT\ln(0.01H)}{E_a}\right).$$

Hydrogen termination sites must have adsorbed water vapour on them for the surface transfer doping effect to activate [256]. The conductivity of the surface,  $\sigma$  is therefore a function of both coverages - hence leading to Equation 6.1 in the main text. The resultant function would be  $\sigma = \sigma(\theta_{\text{H},0}, t, t_{1/2}, H, E_a, T)$ . This would not be a bad place to attempt a mechanistic fit from, as there are only two unknown quantities, both of which benefit from there being some information from which to draw upon when choosing bounds for the fit [323]. However, it has been shown that, although water molecule sorption may be a fast process, the stabilisation of surface conductivity due to that sorption is not: for example, as mentioned in the main text, in 2019 Piña-Salazar *et al* showed that the surface conductivity of hydrogen-terminated nanodiamonds, which had been stripped of their adsorbate layer and kept under vacuum, took tens of hours to stabilise once exposed to humid air [265]. The situation is further complicated by the fact that the DGV is not fully hydrogen terminated, and the fact that the humidity continues to change, so the stabilisation of the surface is constantly disrupted. It may be that the much smaller relative changes in water adsorption expected when a device sits in ambient air with changing relative humidity may negate this long stabilisation time, but it remains uncertain how a mechanistic model could adequately address the issue without further experimental evidence to draw upon.

## BIBLIOGRAPHY

- [1] C. Hutson; *Diamond-based dosimetry for measurements in highly radioactive nuclear environments*; Ph.D. thesis; University of Bristol (2018).
- [2] R. Kalish;  
“Doping of diamond”; *Carbon*; **37**, pp. 781–785 (1999);  
DOI 10.1016/S0008-6223(98)00270-X.
- [3] E. A. Burgemeister;  
“Dosimetry with a diamond operating as a resistor”; *Physics in Medicine and Biology*; **26**,  
pp. 269–275 (1981);  
DOI 10.1088/0031-9155/26/2/006.
- [4] “EH300 Datasheet (PDF) - Advanced Linear Devices”; .  
URL <https://pdf1.alldatasheet.com/datasheet-pdf/view/206196/ALD/EH300.html>
- [5] L. Szabó;  
“The history of using solar energy”; in: *International Conference on Modern Power Systems, MPS 2017*; Institute of Electrical and Electronics Engineers Inc. (2017); ISBN 9781509065653;  
DOI 10.1109/MPS.2017.7974451.
- [6] A. N. Caruso, R. B. Billa, S. Balaz, J. I. Brand, and P. A. Dowben;  
“The heteroisomeric diode”; *Journal of Physics: Condensed Matter*; **16**, p. L139 (2004);  
DOI 10.1088/0953-8984/16/10/L04.
- [7] M. R. Khan, J. R. Smith, R. P. Tompkins, S. Kelley, M. Litz, J. Russo, J. Leathersich, F. S. Shahedipour-Sandvik, K. A. Jones, and A. Iliadis;  
“Design and characterization of GaN p-i-n diodes for betavoltaic devices”; *Solid-State Electronics*; **136**, pp. 24–29 (2017);  
DOI 10.1016/J.SSE.2017.06.010.
- [8] C. E. Munson, Q. Gaimard, K. Merghem, S. Sundaram, D. J. Rogers, J. d. Sanoit, P. L. Voss, A. Ramdane, J. P. Salvestrini, and A. Ougazzaden;

- “Modeling, design, fabrication and experimentation of a GaN-based,  $^{63}\text{Ni}$  betavoltaic battery”; *Journal of Physics D: Applied Physics*; **51**, p. 035101 (2017);  
DOI 10.1088/1361-6463/AA9E41.
- [9] C. Haiyang, Y. Jianhua, and L. Darang;  
“Electrode pattern design for GaAs betavoltaic batteries”; *Journal of Semiconductors*; **32**, p. 084006 (2011);  
DOI 10.1088/1674-4926/32/8/084006.
- [10] H. Chen, L. Jiang, and X. Chen;  
“Design optimization of GaAs betavoltaic batteries”; *Journal of Physics D: Applied Physics*; **44**, p. 215303 (2011);  
DOI 10.1088/0022-3727/44/21/215303.
- [11] S. Butera, M. D. C. Whitaker, A. B. Krysa, and A. M. Barnett;  
“Investigation of a temperature tolerant InGaP (GaInP) converter layer for a  $^{63}\text{Ni}$  betavoltaic cell”; *Journal of Physics D: Applied Physics*; **50**, p. 345101 (2017);  
DOI 10.1088/1361-6463/aa7bc5.
- [12] M. V. Chandrashekhar, C. I. Thomas, H. Li, M. G. Spencer, and A. Lal;  
“Demonstration of a 4H SiC betavoltaic cell”; *Applied Physics Letters*; **88**, pp. 1–3 (2006);  
DOI 10.1063/1.2166699.
- [13] D.-Y. Qiao, W.-Z. Yuan, G. Peng, Y. Xian-Wang, B. Zang, Z. Lin, G. Hui, and H.-J. Zhang;  
“Demonstration of a 4H SiC Betavoltaic Nuclear Battery Based on Schottky Barrier Diode \*”; *Chinese Physics Letters*; **25**, p. 3798 (2008);  
DOI 10.1088/0256-307X/25/10/076.
- [14] M. Wu and J. Zhang;  
“Design and simulation of high conversion efficiency betavoltaic battery based on a stacked multilayer structure”; *AIP Advances*; **9**, p. 075124 (2019);  
DOI 10.1063/1.5094826.
- [15] B. Ulmen, P. D. Desai, S. Moghaddam, G. H. Miley, and R. I. Masel;  
“Development of diode junction nuclear battery using  $^{63}\text{Ni}$ ”; *Journal of Radioanalytical and Nuclear Chemistry*; **282**, pp. 601–604 (2009);  
DOI 10.1007/S10967-009-0320-3.
- [16] M. A. Polikarpov and E. B. Yakimov;  
“Study of the properties of silicon-based semiconductor converters for betavoltaic cells”; *Semiconductors*; **49**, pp. 746–748 (2015);  
DOI 10.1134/S1063782615060202.

- [17] H. Wang, X. B. Tang, Y. P. Liu, Z. H. Xu, M. Liu, and D. Chen;  
“Temperature effect on betavoltaic microbatteries based on Si and GaAs under  $^{63}\text{Ni}$  and  $^{147}\text{Pm}$  irradiation”; *Nuclear Instruments and Methods in Physics Research Section B: Beam Interactions with Materials and Atoms*; **359**, pp. 36–43 (2015);  
DOI 10.1016/J.NIMB.2015.07.046.
- [18] Y. Liu, R. Hu, Y. Yang, G. Wang, S. Luo, and N. Liu;  
“Investigation on a radiation tolerant betavoltaic battery based on Schottky barrier diode”;  
*Applied Radiation and Isotopes*; **70**, pp. 438–441 (2012);  
DOI 10.1016/J.APRADISO.2011.10.013.
- [19] “Products CityLabs”; .  
URL <https://citylabs.net/products/>
- [20] L. Olsen, D. Serralta, and P. Cabauy; *Betavoltaic Batteries: A Historical Review*; City Labs, Inc.;  
Homestead, FL.  
URL <https://citylabs.net/wp-content/uploads/2017/08/BetavoltaicHistory.pdf>
- [21] V. Bormashov, S. Troschiev, A. Volkov, S. Tarelkin, E. Korostylev, A. Golovanov, M. Kuznetsov,  
D. Teteruk, N. Kornilov, S. Terentiev, S. Buga, and V. Blank;  
“Development of nuclear microbattery prototype based on Schottky barrier diamond  
diodes”; *physica status solidi (a)*; **212**, pp. 2539–2547 (2015);  
DOI 10.1002/pssa.201532214.
- [22] S. Tarelkin, V. Bormashov, E. Korostylev, S. Troschiev, D. Teteruk, A. Golovanov, A. Volkov,  
N. Kornilov, M. Kuznetsov, D. Prikhodko, and S. Buga;  
“Comparative study of different metals for Schottky barrier diamond betavoltaic power  
converter by EBIC technique”; *physica status solidi (a)*; **213**, pp. 2492–2497 (2016);  
DOI 10.1002/pssa.201533060.
- [23] V. S. Bormashov, S. Y. Troschiev, S. A. Tarelkin, A. P. Volkov, D. V. Teteruk, A. V. Golovanov, M. S.  
Kuznetsov, N. V. Kornilov, S. A. Terentiev, and V. D. Blank;  
“High power density nuclear battery prototype based on diamond Schottky diodes”; *Dia-  
mond and Related Materials*; **84**, pp. 41–47 (2018);  
DOI 10.1016/j.diamond.2018.03.006.
- [24] A. A. Krasnov and S. A. Legotin;  
“Advances in the Development of Betavoltaic Power Sources (A Review)”; *Instruments and  
Experimental Techniques 2020*; **63**, pp. 437–452 (2020);  
DOI 10.1134/S0020441220040156.

- [25] B. Liu, B. Dai, K. Liu, L. Yang, J. Zhao, G. Shu, Z. Lv, G. Gao, K. Yao, M. Bi, J. Xue, W. Wang, V. Ralchenko, J. Han, and J. Zhu;  
“Alpha-voltaic battery on diamond Schottky barrier diode”; *Diamond & Related Materials*; **87**, pp. 35–42 (2018);  
DOI 10.1016/j.diamond.2018.05.008.
- [26] C. D. Cress, B. J. Landi, R. P. Raffaele, and D. M. Wilt;  
“InGaP alpha voltaic batteries: Synthesis, modeling, and radiation tolerance”; *Journal of Applied Physics*; **100**, p. 114519 (2006);  
DOI 10.1063/1.2390623.
- [27] S. G. Bailey, D. M. Wilt, S. L. Castro, C. D. Cress, and R. P. Raffaele;  
“Photovoltaic development for alpha voltaic batteries”; *Conference Record of the IEEE Photovoltaic Specialists Conference*; pp. 106–109 (2005);  
DOI 10.1109/PVSC.2005.1488080.
- [28] J. K. Liakos;  
“Gamma ray driven photovoltaic cells: an interface between nuclear and semiconductor physics”; *Semiconductor Science and Technology*; **23**, pp. 85001–10 (2008);  
DOI 10.1088/0268-1242/23/8/085001.
- [29] J. K. Liakos;  
“Thorium-229m1/m2-powered heterojunction GRPVCs: an interface between nuclear and semiconductor physics”; *Semiconductor Science and Technology*; **24**, p. 065001 (2009);  
DOI 10.1088/0268-1242/24/6/065001.
- [30] J. K. Liakos;  
“Gamma-Ray-Driven Photovoltaic Cells via a Scintillator Interface”; *Journal of Nuclear Science and Technology*; **48**, pp. 1428–1436 (2011);  
DOI 10.1080/18811248.2011.9711836.
- [31] S. Butera, G. Lioliou, A. B. Krysa, and A. M. Barnett;  
“Al<sub>0.52</sub>In<sub>0.48</sub>P 55Fe x-ray-photovoltaic battery”; *Journal of Physics D: Applied Physics*; **49**, p. 355601 (2016);  
DOI 10.1088/0022-3727/49/35/355601.
- [32] Z. R. Zhang, Y. P. Liu, X. B. Tang, Z. H. Xu, Z. C. Yuan, K. Liu, and W. Chen;  
“GaAs low-energy X-ray radioluminescence nuclear battery”; *Nuclear Instruments and Methods in Physics Research Section B: Beam Interactions with Materials and Atoms*; **415**, pp. 9–16 (2018);  
DOI 10.1016/J.NIMB.2017.10.033.

- [33] J. R. White, D. Kinsman, T. M. Regan, and L. M. Bobek; *Novel Nuclear Powered Photocatalytic Energy Conversion*; Technical report; UMass-Lowell Radiation Laboratory, University of Massachusetts Lowell (2005).  
URL <https://www.osti.gov/servlets/purl/850408>
- [34] K. Scharf;  
“Photovoltaic Effect Produced in Silicon Solar Cells by x-and Gamma Rays J”; *Journal of Research of the National Bureau of Standards A. Physics and Chemistry*; **64**, pp. 297–307 (1960);  
DOI 10.6028/jres.064A.029.
- [35] N. Horiuchi, K. Taniguchi, M. Kamiki, T. Kondo, and M. Aritomi;  
“The characteristics of solar cells exposed to  $\gamma$ -radiation”; *Nuclear Instruments and Methods in Physics Research, Section A: Accelerators, Spectrometers, Detectors and Associated Equipment*; **385**, pp. 183–188 (1997);  
DOI 10.1016/S0168-9002(96)01046-7.
- [36] J. T. Bushberg, J. A. Seibert, E. M. Leidholdt, and J. M. Boone; *The Essential Physics of Medical Imaging*; Lippincott Williams & Wilkins, Philadelphia; 3rd edition (2011); ISBN 9781469821559.
- [37] N. Horiuchi, N. Iijima, S. Hayashi, and I. Yoda;  
“Proposal of utilization of nuclear spent fuels for gamma cells”; *Solar Energy Materials & Solar Cells*; **87**, pp. 287–297 (2005);  
DOI 10.1016/j.solmat.2004.07.029.
- [38] K. Hashizume, H. Kimura, T. Otsuka, T. Tanabe, and T. Okai;  
“Direct Energy Conversion From Gamma Ray to Electricity Using Silicon Semiconductor Cells”; *MRS Proceedings*; **1264**, p. 1264BB0501 (2010);  
DOI 10.1557/PROC-1264-BB05-01.
- [39] S. Almagora, M. Marinelli, E. Milani, A. Tucciarone, G. Verona-Rinati, R. Consorti, A. Petrucci, F. De Notaristefani, and I. Ciancaglioni;  
“Synthetic single crystal diamond diodes for radiotherapy dosimetry”; *Nuclear Instruments and Methods in Physics Research Section A: Accelerators, Spectrometers, Detectors and Associated Equipment*; **594**, pp. 273–277 (2008);  
DOI 10.1016/j.nima.2008.06.028.
- [40] S. Almagora, M. Marinelli, E. Milani, G. Prestopino, A. Tucciarone, C. Verona, G. Verona-Rinati, M. Angelone, M. Pillon, I. Dolbnya, K. Sawhney, and N. Tartoni;  
“Chemical vapor deposition diamond based multilayered radiation detector: Physical

- analysis of detection properties”; *Journal of Applied Physics*; **107**, p. 014511 (2010); DOI 10.1063/1.3275501.
- [41] B. Náfrádi, G. Náfrádi, F. László, and E. Horváth;  
“Methylammonium Lead Iodide for Efficient X-ray Energy Conversion”; *Journal of Physical Chemistry C*; **119**, pp. 25204–25208 (2015); DOI 10.1021/acs.jpcc.5b07876.
- [42] G. Náfrádi, E. Horváth, M. Kollár, A. Horváth, P. Andričević, A. Sienkiewicz, L. Forró, and B. Náfrádi;  
“Radiation detection and energy conversion in nuclear reactor environments by hybrid photovoltaic perovskites”; *Energy Conversion and Management*; **205**, p. 112423 (2020); DOI 10.1016/j.enconman.2019.112423.
- [43] Q. Dong, Y. Fang, Y. Shao, P. Mulligan, J. Qiu, L. Cao, and J. Huang;  
“Electron-hole diffusion lengths > 175  $\mu\text{m}$  in solution-grown  $\text{CH}_3\text{NH}_3\text{PbI}_3$  single crystals”; *Science*; **347**, pp. 967–970 (2015); DOI 10.1126/science.aaa5760.
- [44] S. Yakunin, D. N. Dirin, Y. Shynkarenko, V. Morad, I. Cherniukh, O. Nazarenko, D. Kreil, T. Nauser, and M. V. Kovalenko;  
“Detection of gamma photons using solution-grown single crystals of hybrid lead halide perovskites”; *Nature Photonics*; **10**, pp. 585–589 (2016); DOI 10.1038/nphoton.2016.139.
- [45] R. G. Helmer and C. W. Reich;  
“An excited state of Th 229 at 3.5 eV”; *Physical Review C*; **49**, pp. 1845–1858 (1994); DOI 10.1103/PhysRevC.49.1845.
- [46] M. M. Bé, V. Chisté, C. Dullieu, E. Browne, C. Baglin, V. Chechev, N. Kuzmenko, R. Helmer, F. Kondev, D. MacMahon, and K. Lee;  
“Fe-55”; in: *A = 3 to 244*, volume 3 of *Monographie BIPM-5 - Table of Radionuclides*; pp. 5–10; Bureau International des Poids et Mesures, Sèvres (2006); ISBN 92-822-2218-7.  
URL [https://www.bipm.org/utils/common/pdf/monographieRI/Monographie\\_BIPM-5\\_Tables\\_Vol3.pdf](https://www.bipm.org/utils/common/pdf/monographieRI/Monographie_BIPM-5_Tables_Vol3.pdf)
- [47] M. M. Bé, V. Chisté, C. Dullieu, E. Browne, V. Chechev, N. Kuzmenko, R. Helmer, A. Nichols, E. Schönfeld, and R. Dersch;  
“Am-241”; in: *A = 151 to 242*, volume 2 of *Monographie BIPM-5 - Table of Radionuclides*; pp. 257–276; Bureau International des Poids et Mesures, Sèvres (2004); ISBN 92-822-2207-1.  
URL [https://www.bipm.org/utils/common/pdf/monographieRI/Monographie\\_BIPM-5\\_Tables\\_Vol2.pdf](https://www.bipm.org/utils/common/pdf/monographieRI/Monographie_BIPM-5_Tables_Vol2.pdf)

- [48] M. M. Bé, V. Chisté, C. Dulieu, X. Mougeot, E. Browne, V. Chechev, N. Kuzmenko, F. Kondev, A. Luca, M. Galán, A. Nichols, A. Arinc, and X. Huang; “Am-241\*”; in: *A = 22 to 244*, volume 5 of *Monographie BIPM-5 - Table of Radionuclides*; pp. 175–198; Bureau International des Poids et Mesures, Sèvres (2010); ISBN 978-92-822-2234-8.  
URL [https://www.bipm.org/utils/common/pdf/monographieRI/Monographie\\_BIPM-5\\_Tables\\_Vol15.pdf](https://www.bipm.org/utils/common/pdf/monographieRI/Monographie_BIPM-5_Tables_Vol15.pdf)
- [49] L. A. Popeko, G. V. Val'skii, D. M. Kaminker, and G. A. Petrov; “Delayed gamma emission in the fission of 235U”; *Journal of Nuclear Energy. Parts A/B. Reactor Science and Technology*; **20**, pp. 811–814 (1966);  
DOI 10.1016/0368-3230(66)90162-5.
- [50] M. M. Bé, V. Chisté, C. Dulieu, E. Browne, C. Baglin, V. Chechev, N. Kuzmenko, R. Helmer, F. Kondev, D. MacMahon, and K. Lee; “Cs-137”; in: *A = 3 to 244*, volume 3 of *Monographie BIPM-5 - Table of Radionuclides*; pp. 91–98; Bureau International des Poids et Mesures, Sèvres (2006); ISBN 92-822-2218-7.  
URL [http://www.bipm.org/utils/common/pdf/monographieRI/Monographie\\_BIPM-5\\_Tables\\_Vol13.pdf](http://www.bipm.org/utils/common/pdf/monographieRI/Monographie_BIPM-5_Tables_Vol13.pdf)
- [51] M. M. Bé, V. Chisté, C. Dulieu, E. Browne, C. Baglin, V. Chechev, N. Kuzmenko, R. Helmer, F. Kondev, D. MacMahon, and K. Lee; “Co-60”; in: *A = 3 to 244*, volume 3 of *Monographie BIPM-5 - Table of Radionuclides*; pp. 23–28; Bureau International des Poids et Mesures, Sèvres (2006); ISBN 92-822-2218-7.  
URL [https://www.bipm.org/utils/common/pdf/monographieRI/Monographie\\_BIPM-5\\_Tables\\_Vol13.pdf](https://www.bipm.org/utils/common/pdf/monographieRI/Monographie_BIPM-5_Tables_Vol13.pdf)
- [52] J. R. Ashton, J. L. West, and C. T. Badea; “In vivo small animal micro-CT using nanoparticle contrast agents”; *Frontiers in Pharmacology*; **6**, p. 256 (2015);  
DOI 10.3389/fphar.2015.00256.
- [53] J. W. Strutt; “LVIII. On the scattering of light by small particles”; *The London, Edinburgh and Dublin Philosophical Magazine and Journal of Science*; **41**, pp. 447–454 (1871);  
DOI 10.1080/14786447108640507.
- [54] D. P. Riley; “Lattice Constant of Diamond and the CC Single Bond”; *Nature*; **153**, pp. 587–588 (1944);  
DOI 10.1038/153587b0.

- [55] C. F. Bohren and D. R. Huffman; *Absorption and Scattering of Light by Small Particles*; Wiley-VCH, Weinheim (2004); ISBN 978-047-129-3408.
- [56] A. Einstein;  
“Über die von der molekularkinetischen Theorie der Wärme geforderte Bewegung von in ruhenden Flüssigkeiten suspendierten Teilchen”; *Annalen der Physik*; **322**, pp. 549–560 (1905);  
DOI 10.1002/andp.19053220806.
- [57] A. H. Compton;  
“A quantum theory of the scattering of X-rays by light elements”; *Physical Review*; **21**, pp. 483–502 (1923);  
DOI 10.1103/PhysRev.21.483.
- [58] K. Wojciech Fornalski;  
“Total Cross Section Phenomenological Formulas for X-Ray and Gamma Radiation Interaction With Matter for Different Energies and Absorber Types”; *Journal of Nuclear Engineering and Radiation Science*; **7**, pp. 011501–1 (2021);  
DOI 10.1115/1.4045806.
- [59] J. H. Hubbell;  
“Electron-positron pair production by photons: A historical overview”; *Radiation Physics and Chemistry*; **75**, pp. 614–623 (2006);  
DOI 10.1016/j.radphyschem.2005.10.008.
- [60] M. J. Berger, J. S. Coursey, M. A. Zucker, and J. Chang; *Stopping-Power & Range Tables for Electrons, Protons, and Helium Ions*; Technical report; NIST Physical Measurement Laboratory;  
DOI 10.18434/T4NC7P.  
URL <https://www.nist.gov/pml/stopping-power-range-tables-electrons-protons-and-h>
- [61] F. Tuomisto;  
“Defect identification in semiconductors with positron annihilation: Experiment and theory”; *Reviews of Modern Physics*; **85**, pp. 1583–1631 (2013);  
DOI 10.1103/revmodphys.85.1583.
- [62] S. Dannefaer, P. Mascher, and D. Kerr;  
“Defect characterization in diamonds by means of positron annihilation”; *Diamond and Related Materials*; **1**, pp. 407–410 (1992);  
DOI 10.1016/0925-9635(92)90138-E.
- [63] S. Dannefaer, T. Bretagnon, and D. Kerr;  
“Positron lifetime investigations of diamond films”; *Diamond and Related Materials*; **2**, pp.

- 1479–1482 (1993);  
DOI 10.1016/0925-9635(93)90016-U.
- [64] M. J. Berger, J. H. Hubbell, S. M. Seltzer, J. Chang, J. S. Coursey, R. Sukumar, D. S. Zucker, and K. Olsen;  
“NIST XCOM: Photon Cross Sections Database”;  
DOI 10.18434/T48G6X.  
URL <https://www.nist.gov/pml/xcom-photon-cross-sections-database>
- [65] G. Mackenzie, S. Kaluvan, P. Martin, C. Hutson, T. Connolley, M. Cattelan, H. Dominguez-Andrade, T. Martin, N. Fox, and T. Scott;  
“A diamond gammavoltaic cell utilizing surface conductivity and its response to different photon interaction mechanisms”; *Materials Today Energy*; **21**, p. 100688 (2021);  
DOI 10.1016/j.mtener.2021.100688.
- [66] J. Nelson; *The Physics of Solar Cells*; Imperial College Press, London; 1st edition (2003); ISBN 978-1-86094-349-2;  
DOI 10.1142/p276.
- [67] M. J. Berger, M. Inokuti, H. H. Anderson, H. Bichsel, J. A. Dennis, D. Powers, S. M. Seltzer, and J. E. Turner;  
“ICRU Report 37: Stopping Powers for Electrons and Positrons”; *Journal of the ICRU*; **os-19** (1984);  
DOI 10.1093/jicru\_os19.2.1.
- [68] C. Leroy and P.-G. Rancoita;  
“Particle interaction and displacement damage in silicon devices operated in radiation environments”; *Reports on Progress in Physics*; **70**, p. 493 (2007);  
DOI 10.1088/0034-4885/70/4/R01.
- [69] C. Baur, M. Gervasi, P. Nieminen, S. Pensotti, P. G. Rancoita, and M. Tacconi;  
“NEIL dose dependence for solar cells irradiated with electrons and protons”; *Astroparticle, Particle, Space Physics and Detectors for Physics Applications* (2014);  
DOI 10.1142/9789814603164\_0111.
- [70] W. Nakel;  
“The elementary process of bremsstrahlung”; *Physics Reports*; **243**, pp. 317–353 (1994);  
DOI 10.1016/0370-1573(94)00068-9.
- [71] F. Tessier and I. Kawrakow;  
“Calculation of the electron-electron bremsstrahlung cross-section in the field of atomic electrons”; *Nuclear Instruments and Methods in Physics Research B*; **266**, pp. 625–634 (2008);  
DOI 10.1016/j.nimb.2007.11.063.

- [72] M. J. B. et al.; *{ESTAR}, {PSTAR}, and {ASTAR}: Computer Programs for Calculating Stopping-Power and Range Tables for Electrons, Protons, and Helium Ions (version 1.2.3)*; Technical report; National Institute of Standards and Technology, Gaithersburg, MD, USA (2005).
- [73] C. R. Company; *CRC handbook of chemistry and physics*; Cleveland OH, USA, CRC Press; 59th edition (1978); ISBN 978-0849304590.
- [74] V. A. Dmitriev and M. G. Spencer;  
“SiC materials and devices”; in: Y.-S. Park, R. K. Willardson, and E. R. Weber (editors), *Semiconductors and Semimetals*, volume 52; pp. 20–60; Academic Press, San Diego (1998); ISBN 978-0-12-752160-2.
- [75] C. Kittel;  
“Semiconductor Crystals”; in: *Introduction to Solid State Physics*; chapter 8, pp. 187–219; John Wiley & Sons, Inc.; 8th edition (2005); ISBN 0-471-41526-X.
- [76] S. M. Sze and K. K. Ng; *Physics of Semiconductor Devices*; Wiley India Pvt. Ltd., New Dehli; 3rd edition (2006); ISBN 978-81-265-1702-2.
- [77] D. A. Neamen;  
“Carrier Transport Phenomena”; in: *Semiconductor Physics And Devices: Basic Principles*; chapter 5, pp. 154–188; McGraw Hill, New York; 3rd edition (2003); ISBN 0-07-232107-5.
- [78] S. L. Howell, S. Padalkar, K. Yoon, Q. Li, D. D. Koleske, J. J. Wierer, G. T. Wang, and L. J. Lauhon;  
“Spatial mapping of efficiency of GaN/InGaN nanowire array solar cells using scanning photocurrent microscopy”; *Nano Letters*; **13**, pp. 5123–5128 (2013);  
DOI 10.1021/nl402331u.
- [79] G. Davies; *Diamond*; Ada Hilger Ltd., Bristol; 1st edition (1984); ISBN 0-85274-512-5.
- [80] F. P. Bundy, H. T. Hall, H. M. Strong, and R. H. Wentorf;  
“Man-Made Diamonds”; *Nature*; **176**, pp. 51–55 (1955);  
DOI 10.1038/176051a0.
- [81] M. N. R. Ashfold, J. P. Goss, B. L. Green, P. W. May, M. E. Newton, and C. V. Peaker;  
“Nitrogen in Diamond”; *Chemical Reviews*; **120**, pp. 5745–5794 (2020);  
DOI 10.1021/ACS.CHEMREV.9B00518.
- [82] S. Matsumoto, M. Tsutsumi, and N. Setaka;  
“Growth of diamond particles from methane-hydrogen gas”; *Journal of Materials Science*; **17**, pp. 3106–3112 (1982);  
DOI 10.1007/BF01203472.

- [83] “Corporate Information | Element Six - Element Six”; .  
URL <https://www.e6.com/en/about/corporate-information>
- [84] A. V. Lysenko;  
“Interatomic Bond Energy and Analytical Scale of Hardness”; *Journal of Superhard Materials*; **39**, pp. 25–33 (2017);  
DOI 10.3103/S1063457617010038.
- [85] T. Behnke, M. Doucet, N. Ghodbane, A. Imhof, C. Martínez, and W. Zeuner;  
“Electromagnetic radiation hardness of diamond detectors”; *Nuclear Instruments and Methods in Physics Research, Section A: Accelerators, Spectrometers, Detectors and Associated Equipment*; **489**, pp. 230–240 (2002);  
DOI 10.1016/S0168-9002(02)00572-7.
- [86] R. S. Balmer, J. R. Brandon, S. L. Clewes, H. K. Dhillon, J. M. Dodson, I. Friel, P. N. Inglis, T. D. Madgwick, M. L. Markham, T. P. Mollart, N. Perkins, G. A. Scarsbrook, D. J. Twitchen, A. J. Whitehead, J. J. Wilman, and S. M. Woollard;  
“Chemical vapour deposition synthetic diamond: materials, technology and applications”; *Journal of Physics: Condensed Matter*; **21**, p. 364221 (2009);  
DOI 10.1088/0953-8984/21/36/364221.
- [87] B. Caiffi, I. Coffey, M. Pillon, M. Osipenko, G. Prestopino, M. Ripani, M. Taiuti, C. Verona, and G. Verona-Rinati;  
“Analysis of the response of CVD diamond detectors for UV and sX-ray plasma diagnostics installed at JET”; in: *Physics Procedia*, volume 62; pp. 79–83; Elsevier B.V. (2015);  
DOI 10.1016/j.phpro.2015.02.014.
- [88] C. S. Bodie, G. Lioliou, G. Lefevre, and A. M. Barnett;  
“A single crystal chemical vapour deposition diamond soft X-ray spectrometer”; *Nuclear Instruments and Methods in Physics Research, Section A: Accelerators, Spectrometers, Detectors and Associated Equipment*; **989** (2021);  
DOI 10.1016/J.NIMA.2020.164950.
- [89] M. Marinelli, E. Milani, G. Prestopino, C. Verona, G. Verona-Rinati, M. Angelone, M. Pillon, V. Kachkanov, N. Tartoni, M. Benetti, D. Cannatà, F. D. Pietrantonio, and F. Di Pietrantonio;  
“Synchrotron Radiation X-ray beam monitor made by thin-film CVD single-crystal diamond”; *Journal of Synchrotron Radiation*; **19**, pp. 1015–1020 (2012);  
DOI 10.1107/S0909049512038186.
- [90] G. Prestopino, M. Marinelli, E. Milani, C. Verona, and G. Verona-Rinati;  
“Transient lateral photovoltaic effect in synthetic single crystal diamond”; *Applied Physics*

- Letters*; **111**, p. 143504 (2017);  
DOI 10.1063/1.4994120.
- [91] C. Verona, G. Magrin, P. Solevi, V. Grilj, M. Jakšić, R. Mayer, M. Marinelli, and G. Verona-Rinati; “Spectroscopic properties and radiation damage investigation of a diamond based Schottky diode for ion-beam therapy microdosimetry”; *Journal of Applied Physics*; **118**, p. 184503 (2015);  
DOI 10.1063/1.4935525.
- [92] S. Rollet, M. Angelone, G. Magrin, M. Marinelli, E. Milani, M. Pillon, G. Prestopino, C. Verona, and G. Verona-Rinati; “A novel microdosimeter based upon artificial single crystal diamond”; *IEEE Transactions on Nuclear Science*; **59**, pp. 2409–2415 (2012);  
DOI 10.1109/TNS.2012.2209677.
- [93] J. Damodar, D. Odgers, D. Pope, and R. Hill; “A study on the suitability of the PTW microDiamond detector for kilovoltage x-ray beam dosimetry”; *Applied Radiation and Isotopes*; **135**, pp. 104–109 (2018);  
DOI 10.1016/j.apradiso.2018.01.025.
- [94] A. Chalkley and G. Heyes; “Evaluation of a synthetic single-crystal diamond detector for relative dosimetry measurements on a CyberKnife”; *British Journal of Radiology*; **87** (2014);  
DOI 10.1259/bjr.20130768.
- [95] “CVD Diamond Radiation Detector Development: RD42 Collaboration”; .  
URL <http://rd42.web.cern.ch/rd42/>
- [96] M. Reichmann, A. Alexopoulos, M. Artuso, F. Bachmair, L. Bäni, M. Bartosik, J. Beacham, H. Beck, V. Bellini, V. Belyaev, B. Bentele, A. Bes, J. M. Brom, M. Bruzzi, G. Chiodini, D. Chren, V. Cindro, G. Claus, J. Collot, J. Cumalat, A. Dabrowski, R. D’Alessandro, D. Dauvergne, W. de Boer, S. Dick, C. Dorfer, M. Dünser, G. Eigen, V. Eremin, G. T. Forcolin, J. Forneris, L. Gallin-Martel, M. L. Gallin-Martel, K. K. Gan, M. Gastal, C. Giroletti, M. Goffe, J. Goldstein, A. Golubev, A. Gorišek, E. Grigoriev, J. Grosse-Knetter, A. Grummer, B. Gui, M. Guthoff, B. Hiti, D. Hits, M. Hoeferkamp, T. Hofmann, J. Hosselet, J. Y. Hostachy, F. Hügging, C. Hutton, J. Janssen, H. Kagan, K. Kanxheri, G. Kasiieczka, R. Kass, M. Kis, G. Kramberger, S. Kuleshov, A. Lacoste, S. Lagomarsino, A. L. Giudice, I. L. Paz, E. Lukosi, C. Mazzouzi, I. Mandic, A. Marino, C. Mathieu, M. Menichelli, M. Mikuž, A. Morozzi, J. Moss, R. Mountain, A. Oh, P. Olivero, D. Passeri, H. Pernegger, R. Perrino, M. Piccini, F. Picollo, M. Pomorski, R. Potenza, A. Quadt, F. Rarbi, A. Re, S. Roe, D. A. Becerra, M. Scaringella, C. J. Schmidt, E. Schioppa, S. Schnetzer, S. Sciortino, A. Scorzoni, S. Seidel, L. Servoli, D. S. Smith,

- B. Sopko, V. Sopko, S. Spagnolo, S. Spanier, K. Stenson, R. Stone, B. Stugo, C. Sutura, B. Tannenwald, M. Traeger, W. Trischuk, D. Tromson, M. Truccato, C. Tuve, J. Velthuis, N. Venturi, S. Wagner, R. Wallny, J. C. Wang, J. Weingarten, C. Weiss, N. Wermes, M. Yamouni, M. Zalieckas, M. Zavrtanik, P. S. Salter, M. Chmeissani, S. Grinstein, and D. V. Furelos;  
“New test beam results of 3D and pad detectors constructed with poly-crystalline CVD diamond”; *Nuclear Instruments and Methods in Physics Research, Section A: Accelerators, Spectrometers, Detectors and Associated Equipment*; **958**, p. 162675 (2020);  
DOI 10.1016/j.nima.2019.162675.
- [97] J. Janssen;  
“Test beam results of ATLAS DBM pCVD diamond detectors using a novel threshold tuning method”; *Journal of Instrumentation*; **12**, p. C03072 (2017);  
DOI 10.1088/1748-0221/12/03/C03072.
- [98] L. Liu, X. Ouyang, J. Zhang, X. Zhang, and Y. Zhong;  
“Polycrystalline CVD diamond detector: Fast response and high sensitivity with large area”; *AIP Advances*; **4**, p. 017114 (2014);  
DOI 10.1063/1.3275501.
- [99] G. Conte, M. Girolami, S. Salvatori, and V. Ralchenko;  
“X-ray diamond detectors with energy resolution”; *Applied Physics Letters*; **91**, p. 183515 (2007);  
DOI 10.1063/1.2805221.
- [100] D. Tromson, A. Brambilla, F. Foulon, C. Mer, B. Guizard, R. Barrett, and P. Bergonzo;  
“Geometrical non-uniformities in the sensitivity of polycrystalline diamond radiation detectors”; *Diamond and Related Materials*; **9**, pp. 1850–1855 (2000);  
DOI 10.1016/S0925-9635(00)00334-4.
- [101] A. Matsushita, N. Fujimori, Y. Tsuchida, N. Ohtani, D. Dojima, K. Koide, T. Kaneko, and S. Shikata;  
“Evaluation of diamond mosaic wafer crystallinity by electron backscatter diffraction”; *Diamond and Related Materials*; **101**, p. 107558 (2020);  
DOI 10.1016/j.diamond.2019.107558.
- [102] L. Rubin;  
“Crystalline Silicon Solar Cells and Modules”; in: L. M. Fraas and L. D. Partain (editors), *Solar Cells and Their Applications*; p. 115; John While & Sons; 2nd edition (2010); ISBN 978-0-470-44633-1.
- [103] R. M. Shipley; *Famous diamonds of the world*; Gemmological Institute of America, Los Angeles (1939).

- [104] W. Koeppe and A. M. Donefer-Hickle;  
“Steadfast and Pure: How the "Dresden Green" Diamond Became a Symbol of Saxon Rule | The Metropolitan Museum of Art”; (2020).  
URL <https://www.metmuseum.org/blogs/now-at-the-met/2020/dresden-green-diamond>
- [105] R. Schirhagl, K. Chang, M. Loretz, and C. L. Degen;  
“Nitrogen-Vacancy Centers in Diamond: Nanoscale Sensors for Physics and Biology”; *Annual Review of Physical Chemistry*; **65**, pp. 83–105 (2014);  
DOI 10.1146/annurev-physchem-040513-103659.
- [106] C. D. Clark, R. W. Ditchburn, and H. B. Dyer;  
“The absorption spectra of irradiated diamonds after heat treatment”; *Proceedings of the Royal Society of London A*; **237**, pp. 75–89 (1956);  
DOI 10.1098/RSPA.1956.0163.
- [107] A. T. Collins;  
“Colour centres in diamond”; *Journal of Gemmology*; **18**, pp. 37–75 (1982);  
DOI 10.15506/JOG.1982.18.1.37.
- [108] B. Campbell and A. Mainwood;  
“Radiation Damage of Diamond by Electron and Gamma Irradiation”; *phys. stat. sol. (a)*; **181**, pp. 99–108 (2000);  
DOI 10.1002/1521-396X(200009)181:13.0.CO;2-5.
- [109] J. Koike, D. M. Parkin, and T. E. Mitchell;  
“Displacement threshold energy for type IIa diamond”; *Applied Physics Letters*; **60**, p. 1452 (1998);  
DOI 10.1063/1.107267.
- [110] H. A. Hoff, G. L. Waytena, C. L. Vold, J. S. Suehle, I. P. Isaacson, M. L. Rebbert, D. I. Ma, and K. Harris;  
“Ohmic contacts to semiconducting diamond using a Ti/Pt/Au trilayer metalization scheme”; *Diamond and Related Materials*; **5**, pp. 1450–1456 (1996);  
DOI 10.1016/S0925-9635(96)00566-3.
- [111] C. A. Hewett and J. R. Zeidler;  
“Ohmic contacts to epitaxial and natural diamond”; *Diamond & Related Materials*; **2**, pp. 1319–1321 (1993);  
DOI 10.1016/0925-9635(93)90176-3.
- [112] M. Mertens, M. Mohr, N. Wiora, K. Brühne, and H.-J. Fecht;  
“N-Type Conductive Ultrananocrystalline Diamond Films Grown by Hot Filament CVD”;

- Journal of Nanomaterials*; **2015**, p. 527025 (2015);  
DOI 10.1155/2015/527025.
- [113] G. Kawaguchi, J. Nakanishi, A. Otsuki, T. Oku, and M. Murakami;  
“Dependence of contact resistance on metal electronegativity for B-doped diamond films”;  
*Journal of Applied Physics*; **75**, pp. 5165–5170 (1994);  
DOI 10.1063/1.357009.
- [114] Y. G. Chen, M. Ogura, S. Yamasaki, and H. Okushi;  
“Investigation of specific contact resistance of ohmic contacts to B-doped homoepitaxial diamond using transmission line model”; *Diamond & Related Materials*; **13**, pp. 2121–2124 (2004);  
DOI 10.1016/j.diamond.2004.07.001.
- [115] J. Nakanishi, A. Otsuki, T. Oku, O. Ishiwata, and M. Murakami;  
“Formation of ohmic contacts to p-type diamond using carbide forming metals”; *Journal of Applied Physics*; **76**, pp. 2293–2298 (1994);  
DOI 10.1063/1.357649.
- [116] M. Yokoba, Y. Koide, A. Otsuki, F. Ako, T. Oku, and M. Murakami;  
“Carrier transport mechanism of Ohmic contact to p-type diamond”; *Journal of Applied Physics*; **81**, pp. 6815–6821 (1997);  
DOI 10.1063/1.365240.
- [117] V. Venkatesan, D. M. Malta, K. Das, and A. M. Belu;  
“Evaluation of ohmic contacts formed by B+implantation and Ti-Au metallization on diamond”; *Journal of Applied Physics*; **74**, pp. 1179–1187 (1993);  
DOI 10.1063/1.354918.
- [118] Y. Chen, M. Ogura, S. Yamasaki, and H. Okushi;  
“Ohmic contacts on p-type homoepitaxial diamond and their thermal stability”; *Semiconductor Science and Technology*; **20**, pp. 860–863 (2005);  
DOI 10.1088/0268-1242/20/8/041.
- [119] G. Civrac, S. Msolli, J. Alexis, O. Dalverny, and H. Schneider;  
“Electrical and mechanical characterisation of Si/Al ohmic contacts on diamond”; *Electronics Letters*; **46**, p. 791 (2010);  
DOI 10.1049/el.2010.0803.
- [120] H. J. Looi, L. Y. S. Pang, M. D. Whitefield, J. S. Foord, and R. B. Jackman;  
“Engineering Low Resistance Contacts on p-type Hydrogenated Diamond Surfaces”; *Diamond Relat. Mater.*; **9**, pp. 975–981 (2000);  
DOI 10.1016/S0925-9635(00)00240-5.

- [121] G. R. Brandes, C. P. Beetz, C. F. Feger, R. W. Wright, and J. L. Davidson; “Ion implantation and anneal to produce low resistance metal-diamond contacts”; *Diamond and Related Materials*; **8**, pp. 1936–1943 (1999); DOI 10.1016/S0925-9635(99)00161-2.
- [122] T. Tachibana, B. E. Williams, and J. T. Glass; “Correlation of the electrical properties of metal contacts on diamond films with the chemical nature of the metal-diamond interface. I. Gold contacts: A non-carbide-forming metal”; *Physical Review B*; **45**, pp. 11968–11974 (1992); DOI 10.1103/PhysRevB.45.11968.
- [123] T. Tachibana, B. E. Williams, and J. T. Glass; “Correlation of the electrical properties of metal contacts on diamond films with the chemical nature of the metal-diamond interface. II. Titanium contacts: A carbide-forming metal”; *Physical Review B*; **45**, pp. 11975–11981 (1992); DOI 10.1103/PhysRevB.45.11975.
- [124] M. Werner, O. Dorsch, H.-u. Baerwind, E. Obermeier, C. Johnston, P. R. Chalker, and S. Romani; “The Effect of Metallization on the Ohmic Contact Resistivity to Heavily B-doped Polycrystalline Diamond Films”; *IEEE Transactions on Electron Devices*; **42**, pp. 1344–1351 (1995); DOI 10.1109/16.391217.
- [125] M. Davydova, A. Taylor, P. Hubík, L. Fekete, L. Klimša, D. Trémouilles, A. Soltani, and V. Mortet; “Characteristics of zirconium and niobium contacts on boron-doped diamond”; *Diamond and Related Materials*; **83**, pp. 184–189 (2018); DOI 10.1016/j.diamond.2018.02.009.
- [126] Y. Jingu, K. Hiram, and H. Kawarada; “Ultrashallow TiC source/drain contacts in diamond MOSFETs formed by hydrogenation-last approach”; *IEEE Transactions on Electron Devices*; **57**, pp. 966–972 (2010); DOI 10.1109/TED.2010.2043311.
- [127] T. Ichibha, K. Hongo, I. Motochi, N. W. Makau, G. O. Amolo, and R. Maezono; “Adhesion of the electrodes on diamond device surfaces”; *arXiv: Condensed Matter and Materials Science*; p. 1709.03200 (2017).
- [128] C. Zhen, Y. Wang, S. He, Q. Guo, Z. Yan, and Y. Pu; “Ohmic contacts to boron-doped diamond”; *Optical Materials*; **23**, pp. 117–121 (2003); DOI 10.1016/S0925-3467(03)00071-5.
- [129] K. L. Moazed, J. R. Zeidler, and M. J. Taylor; “A thermally activated solid state reaction process for fabricating ohmic contacts to semi-

- conducting diamond”; *Journal of Applied Physics*; **68**, pp. 2246–2254 (1990);  
DOI 10.1063/1.346529.
- [130] Y. Koide, M. Yokoba, A. Otsuki, F. Ako, T. Oku, and M. Murakami;  
“Carrier transport mechanisms through the metal/p-type diamond semiconductor inter-  
face”; *Diamond and Related Materials*; **6**, pp. 847–851 (1997);  
DOI 10.1016/S0925-9635(96)00632-2.
- [131] D. A. Evans, O. R. Roberts, G. T. Williams, A. R. Vearey-Roberts, F. Bain, S. Evans, D. P. Langstaff,  
and D. J. Twitchen;  
“Diamond-metal contacts: Interface barriers and real-time characterization”; *Journal of  
Physics: Condensed Matter*; **21**, p. 364223 (2009);  
DOI 10.1088/0953-8984/21/36/364223.
- [132] Y. F. Wang, X. Chang, S. Li, D. Zhao, G. Shao, T. Zhu, J. Fu, P. Zhang, X. Chen, F. Li, Z. Liu, S. Fan,  
R. Bu, F. Wen, J. Zhang, W. Wang, and H. X. Wang;  
“Ohmic contact between iridium film and hydrogen-terminated single crystal diamond”;  
*Scientific Reports*; **7**, pp. 1–8 (2017);  
DOI 10.1038/s41598-017-09380-1.
- [133] W. Wang, C. Hu, F. N. Li, S. Y. Li, Z. C. Liu, F. Wang, J. Fu, and H. X. Wang;  
“Reprint of iridium Ohmic contact on hydrogen-terminated single crystal diamond  
film”; *Diamond and Related Materials*; **63**, pp. 175–179 (2016);  
DOI 10.1016/j.diamond.2016.01.019.
- [134] T. Teraji, S. Koizumi, and Y. Koide;  
“Ohmic contact for p -type diamond without postannealing”; *Journal of Applied Physics*;  
**104**, pp. 10–13 (2008);  
DOI 10.1063/1.2936371.
- [135] A. Traoré, P. Muret, A. Fiori, D. Eon, E. Gheeraert, and J. Pernot;  
“Zr/oxidized diamond interface for high power Schottky diodes”; *Applied Physics Letters*;  
**104**, pp. 52105–141601 (2014);  
DOI 10.1063/1.3520140.
- [136] J. E. Butler, M. W. Geis, K. E. Krohn, J. Lawless Jr, S. Deneault, T. M. Lyszczarz, D. Flechtner, and  
R. Wright;  
“Exceptionally high voltage Schottky diamond diodes and low boron doping”; *Semicond.  
Sci. Technol.*; **18**, pp. 67–71 (2003).
- [137] T. Aoki, T. Teraji, Y. Koide, and K. Shiojima;  
“Displacement current of Au/p-diamond Schottky contacts”; *Materials Science in Semicon-*

- ductor Processing*; **70**, pp. 207–212 (2017);  
DOI 10.1016/j.mssp.2016.12.012.
- [138] T. Teraji, Y. Garino, Y. Koide, and T. Ito;  
“Low-leakage-type diamond Schottky diodes prepared using vacuum ultraviolet light/  
ozone treatment”; *Journal of Applied Physics*; **105**, p. 126109 (2009);  
DOI 10.1063/1.3153986.
- [139] P. Muret, A. Traoré, A. Maréchal, D. Eon, J. Pernot, J. C. Piñero, M. P. Villar, and D. Araujo;  
“Potential barrier heights at metal on oxygen-terminated diamond interfaces”; *Journal of Applied Physics*; **118**, p. 204505 (2015);  
DOI 10.1063/1.4936317.
- [140] A. Maréchal, M. Aoukar, C. Vallée, C. Rivière, D. Eon, J. Pernot, and E. Gheeraert;  
“Energy-band diagram configuration of Al<sub>2</sub>O<sub>3</sub> / oxygen-terminated p-diamond metal-oxide-  
semiconductor”; *Applied Physics Letters*; **107**, p. 141601 (2015);  
DOI 10.1063/1.4931123.
- [141] H. Umezawa, S.-I. Shikata, and T. Funaki;  
“Diamond Schottky barrier diode for high-temperature, high-power, and fast switching  
applications”; *Japanese Journal of Applied Physics*; **53**, p. 05FP06 (2014);  
DOI 10.7567/JJAP.53.05FP06.
- [142] T. Funaki, M. Hirano, H. Umezawa, and S. Shikata;  
“High temperature switching operation of a power diamond Schottky barrier diode”; *IEEE Transactions on Power Electronics*; **9**, pp. 960–962 (2012);  
DOI 10.1587/elex.9.1835.
- [143] K. Ikeda, H. Umezawa, K. Ramanujam, and S.-I. Shikata;  
“Thermally Stable Schottky Barrier Diode by Ru/Diamond”; *Applied Physics Express*; **2**, p. 11202 (2009);  
DOI 10.1143/APEX.2.011202.
- [144] P. K. Baumann and R. J. Nemanich;  
“Electron affinity and Schottky barrier height of metal-diamond (100), (111), and (110)  
interfaces”; *Journal of Applied Physics*; **83**, p. 1940 (1998);  
DOI 10.1063/1.366940.
- [145] Y. Li, S. Li, M. Song, Y. She, Q. Wang, and X. Guan;  
“Synthesis of n-type semiconductor diamond single crystal under high pressure and high  
temperature”; *IOP Conference Series: Materials Science and Engineering*; **274** (2017);  
DOI 10.1088/1757-899X/274/1/012131.

- [146] K. Ueda, K. Kawamoto, and H. Asano;  
“High-temperature and high-voltage characteristics of Cu/diamond Schottky diodes”;  
*Diamond & Related Materials*; **57**, pp. 28–31 (2015);  
DOI 10.1016/j.diamond.2015.03.006.
- [147] K. Ueda, K. Kawamoto, T. Soumiya, and H. Asano;  
“High-temperature characteristics of Ag and Ni/diamond Schottky diodes”; *Diamond & Related Materials*; **38**, pp. 41–44 (2013);  
DOI 10.1016/j.diamond.2013.06.007.
- [148] V. A. Kukushkin;  
“Simulation of a perfect CVD diamond Schottky diode steep forward current-voltage characteristic”; *Physica B: Condensed Matter*; **498**, pp. 1–6 (2016);  
DOI 10.1016/j.physb.2016.06.011.
- [149] J. Piñero, D. Araújo, A. Fiori, A. Traoré, M. Villar, D. Eon, P. Muret, J. Pernot, and T. Teraji;  
“Atomic composition of WC/ and Zr/O-terminated diamond Schottky interfaces close to ideality”; *Applied Surface Science*; **395**, pp. 200–207 (2017);  
DOI 10.1016/j.apsusc.2016.04.166.
- [150] D. Takeuchi, S. Yamanaka, H. Watanabe, and H. Okushi;  
“Device Grade B-Doped Homoepitaxial Diamond Thin Films”; *physica status solidi (a)*; **186**, pp. 269–280 (2001);  
DOI 10.1002/1521-396X(200108)186:2<269::AID-PSSA269>3.0.CO;2-Z.
- [151] H. Kawarada, M. Aoki, and M. Ito;  
“Enhancement mode metal-semiconductor field effect transistors using homoepitaxial diamonds”; *Applied Physics Letters*; **65**, pp. 1563–1565 (1994);  
DOI 10.1063/1.112915.
- [152] F. N. Li, Y. Li, D. Y. Fan, and H. X. Wang;  
“Barrier heights of Au, Pt, Pd, Ir, Cu on nitrogen terminated (1 0 0) diamond determined by X-ray photoelectron spectroscopy”; *Applied Surface Science*; **456**, pp. 532–537 (2018);  
DOI 10.1016/j.apsusc.2018.06.184.
- [153] K. Tsugawa, H. Noda, K. Hirose, and H. Kawarada;  
“Schottky barrier heights, carrier density, and negative electron affinity of hydrogen-terminated diamond”; *Physical Review B - Condensed Matter and Materials Physics*; **81**, p. 045303 (2010);  
DOI 10.1103/PhysRevB.81.045303.
- [154] S. Koné, H. Schneider, K. Isoird, F. Thion, J. Achard, R. Issaoui, S. Msolli, and J. Alexis;  
“An assessment of contact metallization for high power and high temperature diamond

- Schottky devices”; *Diamond & Related Materials*; **27-28**, pp. 23–28 (2012);  
DOI 10.1016/j.diamond.2012.05.007.
- [155] P. K. Baumann and R. J. Nemanich;  
“Characterization of copper-diamond (100), (111), and (110) interfaces: Electron affinity and Schottky barrier”; *Physical Review B*; **58**, pp. 1643–1654 (1998);  
DOI 10.1103/PhysRevB.58.1643.
- [156] N. F. Mott;  
“Note on the contact between a metal and an insulator or semi-conductor”; *Mathematical Proceedings of the Cambridge Philosophical Society*; **34**, pp. 568–572 (1938);  
DOI 10.1017/S0305004100020570.
- [157] R. T. Tung;  
“The physics and chemistry of the Schottky barrier height”; *Applied Physics Reviews*; **1**, pp. 11304–1522 (2014);  
DOI 10.1116/1.591472.
- [158] S. Kurtin, T. C. McGill, and C. A. Mead;  
“Fundamental Transition in The Electronic Nature of Solids”; *Physical Review Letters*; **22**, pp. 91–94 (1969);  
DOI 10.1007/978-94-009-0657-0\_10.
- [159] D. K. Schröder; *Semiconductor Material and Device Characterization*; John Wiley & Sons, Inc. (1990); ISBN 0-471-51104-8.
- [160] K. L. Moazed, R. Nguyen, and J. R. Zeidler;  
“Ohmic Contacts to Semiconducting Daimond”; *IEEE Electron Device Letters*; **9**, pp. 350–354 (1988);  
DOI 10.1109/55.740.
- [161] W. Trischuk;  
“Diamond Particle Detectors for High Energy Physics”; *Nuclear and Particle Physics Proceedings*; **273-275**, pp. 1023–1028 (2016);  
DOI 10.1016/j.nuclphysbps.2015.09.160.
- [162] M. Girolami, L. Criante, F. Di Fonzo, S. Lo Turco, A. Mezzetti, A. Notargiacomo, M. Pea, A. Bellucci, P. Calvani, V. Valentini, and D. M. Trucchi;  
“Graphite distributed electrodes for diamond-based photon-enhanced thermionic emission solar cells”; *Carbon*; **111**, pp. 48–53 (2017);  
DOI 10.1016/j.carbon.2016.09.061.

- [163] I. Haughton, I. L. Paz, M. McGowan, A. Oh, A. Porter, P. S. Salter, and O. Allegre;  
“Barrier potential for laser written graphitic wires in diamond”; *Diamond and Related Materials*; **111**, p. 108164 (2020);  
DOI 10.1016/j.diamond.2020.108164.
- [164] C. Bloomer, M. E. Newton, G. Rehm, and P. S. Salter;  
“A single-crystal diamond X-ray pixel detector with embedded graphitic electrodes”; *Journal of Synchrotron Radiation*; **27**, pp. 599–607 (2020);  
DOI 10.1107/S160057752000140X.
- [165] K. Xing, A. Tsai, S. Rubanov, D. L. Creedon, S. A. Yianni, L. Zhang, W. C. Hao, J. Zhuang, J. C. McCallum, C. I. Pakes, and D. C. Qi;  
“Palladium forms Ohmic contact on hydrogen-terminated diamond down to 4 K”; *Applied Physics Letters*; **116**, p. 111601 (2020);  
DOI 10.1063/1.5141775.
- [166] M. C. James, F. Fogarty, R. Zulkarnay, N. A. Fox, and P. W. May;  
“A review of surface functionalisation of diamond for thermionic emission applications”;  
*Carbon*; **171**, pp. 532–550 (2021);  
DOI 10.1016/J.CARBON.2020.09.019.
- [167] K. G. Crawford, A. Tallaire, X. Li, D. A. Macdonald, D. Qi, and D. A. Moran;  
“The role of hydrogen plasma power on surface roughness and carrier transport in transfer-doped H-diamond”; *Diamond and Related Materials*; **84**, pp. 48–54 (2018);  
DOI 10.1016/j.diamond.2018.03.005.
- [168] G. Wan, M. Cattelan, and N. A. Fox;  
“Electronic Structure Tunability of Diamonds by Surface Functionalization”; *The Journal of Physical Chemistry C*; **123**, pp. 4168–4177 (2019);  
DOI 10.1021/acs.jpcc.8b11232.
- [169] F. Li, J. Zhang, X. Wang, M. Zhang, and H. Wang;  
“Barrier Heights of Au on Diamond with Different Terminations Determined by X-ray Photoelectron Spectroscopy”; *Coatings*; **7**, p. 88 (2017);  
DOI 10.3390/coatings7070088.
- [170] B. J. Baliga;  
“Power Semiconductor Device Figure of Merit for High-Frequency Applications”; *IEEE Electron Device Letters*; **10**, pp. 455–457 (1989);  
DOI 10.1109/55.43098.
- [171] Q. Wang, A. Puntambekar, and V. Chakrapani;  
“Co-adsorption of water and oxygen on GaN: Effects of charge transfer and formation of

- electron depletion layer”; *The Journal of Chemical Physics*; **147**, p. 104703 (2017);  
DOI 10.1063/1.4991322.
- [172] W. Chen, D. Qi, X. Gao, and A. T. S. Wee;  
“Surface transfer doping of semiconductors”; *Progress in Surface Science*; **84**, pp. 279–321  
(2009);  
DOI 10.1016/j.progsurf.2009.06.002.
- [173] W. Chen, S. Chen, D. C. Qi, X. Y. Gao, and A. Thye Shen Wee;  
“Surface Transfer p-Type Doping of Epitaxial Graphene”; *Journal of the American Chemical  
Society*; **129**, pp. 10418–10422 (2007);  
DOI 10.1021/JA071658G.
- [174] T. Ohta, A. Bostwick, T. Seyller, K. Horn, and E. Rotenberg;  
“Controlling the Electronic Structure of Bilayer Graphene”; *Science*; **313**, pp. 951–954 (2006);  
DOI 10.1126/SCIENCE.1130681.
- [175] W. Chen, X. Gao, D. Qi, S. Chen, Z. Chen, and A. Wee;  
“Surface-Transfer Doping of Organic Semiconductors Using Functionalized Self-Assembled  
Monolayers”; *Advanced Functional Materials*; **17**, pp. 1339–1344 (2007);  
DOI 10.1002/ADFM.200601029.
- [176] M. I. Landstrass and K. V. Ravi;  
“Hydrogen passivation of electrically active defects in diamond”; *Applied Physics Letters*;  
**55**, p. 1391 (1989);  
DOI 10.1063/1.101604.
- [177] M. I. Landstrass and K. V. Ravi;  
“Resistivity of chemical vapor deposited diamond films”; *Applied Physics Letters*; **55**, p. 975  
(1989);  
DOI 10.1063/1.101694.
- [178] K. G. Crawford, I. Maini, D. A. Macdonald, and D. A. Moran;  
“Surface transfer doping of diamond: A review”; *Progress in Surface Science*; **96**, p. 100613  
(2021);  
DOI 10.1016/J.PROGSURE.2021.100613.
- [179] F. Maier, M. Riedel, B. Mantel, J. Ristein, and L. Ley;  
“Origin of Surface Conductivity in Diamond”; *Physical Review Letters*; **85**, pp. 3472–3475  
(2000);  
DOI 10.1103/PhysRevLett.85.3472.

- [180] J. Ristein;  
“Surface transfer doping of diamond”; *Journal of Physics D: Applied Physics*; **39**, p. R71 (2006);  
DOI 10.1088/0022-3727/39/4/R01.
- [181] S. J. Sque, R. Jones, S. Öberg, and P. R. Briddon;  
“Transfer doping of diamond: The use of C60 and C60F36 to effect p-type surface conductivity”; *Physica B: Condensed Matter*; **376-377**, pp. 268–271 (2006);  
DOI 10.1016/J.PHYSB.2005.12.069.
- [182] S. J. Sque, R. Jones, S. Öberg, and P. R. Briddon;  
“Transfer doping of diamond: Buckminsterfullerene on hydrogenated, hydroxylated, and oxygenated diamond surfaces”; *Journal of Materials Science: Materials in Electronics*; **17**, pp. 459–465 (2006);  
DOI 10.1007/S10854-006-8092-9.
- [183] S. J. Sque, R. Jones, J. P. Goss, P. R. Briddon, and S. Öberg;  
“First principles study of C60 and C60F36 as transfer dopants for p-type diamond”; *Journal of Physics: Condensed Matter*; **17**, p. L21 (2004);  
DOI 10.1088/0953-8984/17/2/L03.
- [184] P. Strobel, M. Riedel, J. Ristein, and L. Ley;  
“Surface transfer doping of diamond”; *Nature*; **430**, pp. 439–441 (2004);  
DOI 10.1038/nature02751.
- [185] P. Strobel, J. Ristein, L. Ley, K. Seppelt, I. V. Goldt, and O. Boltalina;  
“Surface conductivity induced by fullerenes on diamond: Passivation and thermal stability”; *Diamond and Related Materials*; **15**, pp. 720–724 (2006);  
DOI 10.1016/J.DIAMOND.2005.10.034.
- [186] Y. Takagi, K. Shiraishi, M. Kasu, and H. Sato;  
“Mechanism of hole doping into hydrogen terminated diamond by the adsorption of inorganic molecule”; *Surface Science*; **609**, pp. 203–206 (2013);  
DOI 10.1016/J.SUSC.2012.12.015.
- [187] T. Wade, M. Geis, T. Fedynyshyn, S. Vitale, J. Varghese, D. Lennon, T. Grotjohn, R. Nemanich, and M. Hollis;  
“Effect of surface roughness and Htermination chemistry on diamond’s semiconducting surface conductance”; *Diamond and Related Materials*; **76**, pp. 79–85 (2017);  
DOI 10.1016/j.diamond.2017.04.012.
- [188] M. Geis, T. Fedynyshyn, M. Plaut, T. Wade, C. Wuorio, S. Vitale, J. Varghese, T. Grotjohn, R. Nemanich, and M. Hollis;

- “Chemical and semiconducting properties of NO<sub>2</sub>-activated H-terminated diamond”; *Diamond and Related Materials*; **84**, pp. 86–94 (2018);  
DOI 10.1016/j.diamond.2018.03.002.
- [189] H. Sato and M. Kasu;  
“Maximum hole concentration for Hydrogen-terminated diamond surfaces with various surface orientations obtained by exposure to highly concentrated NO<sub>2</sub>”; *Diamond and Related Materials*; **31**, pp. 47–49 (2013);  
DOI 10.1016/j.diamond.2012.10.007.
- [190] M. Tordjman, K. Weinfeld, and R. Kalish;  
“Boosting surface charge-transfer doping efficiency and robustness of diamond with WO<sub>3</sub> and ReO<sub>3</sub>”; *Applied Physics Letters*; **111**, p. 111601 (2017);  
DOI 10.1063/1.4986339.
- [191] K. G. Crawford, L. Cao, D. Qi, A. Tallaire, E. Limiti, C. Verona, A. T. S. Wee, and D. A. J. Moran;  
“Enhanced surface transfer doping of diamond by V<sub>2</sub>O<sub>5</sub> with improved thermal stability”; *Applied Physics Letters*; **108**, p. 042103 (2016);  
DOI 10.1063/1.4940749.
- [192] S. A. O. Russell, L. Cao, D. Qi, A. Tallaire, K. G. Crawford, A. T. S. Wee, and D. A. J. Moran;  
“Surface transfer doping of diamond by MoO<sub>3</sub>: A combined spectroscopic and Hall measurement study”; *Applied Physics Letters*; **103**, p. 202112 (2013);  
DOI 10.1063/1.4832455.
- [193] M. Tordjman, C. Saguy, A. Bolker, and R. Kalish;  
“Superior Surface Transfer Doping of Diamond with MoO<sub>3</sub>”; *Advanced Materials Interfaces*; **1**, p. 1300155 (2014);  
DOI 10.1002/ADMI.201300155.
- [194] C. Verona, W. Ciccognani, S. Colangeli, E. Limiti, M. Marinelli, and G. Verona-Rinati;  
“Comparative investigation of surface transfer doping of hydrogen terminated diamond by high electron affinity insulators”; *Journal of Applied Physics*; **120**, p. 25104 (2016);  
DOI 10.1063/1.4955469.
- [195] Element Six Ltd;  
“The Element Six CVD Diamond Handbook”;  
URL [https://e6-prd-cdn-01.azureedge.net/mediacontainer/medialibraries/element6/documents/brochures/element\\_six\\_cvd\\_diamond\\_handbook.pdf?ext=.pdf](https://e6-prd-cdn-01.azureedge.net/mediacontainer/medialibraries/element6/documents/brochures/element_six_cvd_diamond_handbook.pdf?ext=.pdf)
- [196] H. Morimoto, Y. Hazama, K. Tanaka, and N. Naka;  
“Exciton lifetime and diffusion length in high-purity chemical-vapor-deposition diamond”;

- Diamond and Related Materials*; **63**, pp. 47–50 (2016);  
DOI 10.1016/J.DIAMOND.2015.11.010.
- [197] T. Malinauskas, K. Jarašiūnas, E. Ivakin, N. Tranchant, and M. Nesladek;  
“Determination of carrier diffusion coefficient and lifetime in single crystalline CVD diamonds by light-induced transient grating technique”; *physica status solidi (a)*; **207**, pp. 2058–2063 (2010);  
DOI 10.1002/pssa.201000100.
- [198] P. Forster, V. Ramaswamy, P. Artaxo, T. Berntsen, R. Betts, D. W. Fahey, J. Haywood, J. Lean, D. C. Lowe, G. Myhre, J. Nganga, R. Prinn, G. Raga, M. Schulz, and R. Van Dorland;  
“Changes in Atmospheric Constituents and in Radiative Forcing”; in: S. Solomon, D. Qin, M. Manning, Z. Chen, M. Marquis, K. Averyt, M. Tignor, and H. L. Miller (editors), *Climate Change 2007: The Physical Science Basis. Contribution of Working Group I to the Fourth Assessment Report of the Intergovernmental Panel on Climate Change*; p. 212; Cambridge University Press, Cambridge, UK (2007).  
URL <https://www.ipcc.ch/site/assets/uploads/2018/02/ar4-wg1-chapter2-1.pdf>
- [199] “Transport and environment statistics: 2021”; .  
URL <https://www.gov.uk/government/statistics/transport-and-environment-statistics-2021>
- [200] R. Griffith and R. Ouvrard; *Calibration of Radiation Protection Monitoring Instruments*; Technical report; International Atomic Energy Agency; Vienna (2000).  
URL [www.iaea.org/ns/coordinet](http://www.iaea.org/ns/coordinet)
- [201] A. Jain and A. Kapoor;  
“Exact analytical solutions of the parameters of real solar cells using Lambert W-function”; *Solar Energy Materials & Solar Cells*; **81**, pp. 269–277 (2004);  
DOI 10.1016/j.solmat.2003.11.018.
- [202] P. T. Boggs, R. H. Byrd, and R. B. Schnabel;  
“A Stable and Efficient Algorithm for Nonlinear Orthogonal Distance Regression”; *SIAM Journal on Scientific and Statistical Computing*; **8**, pp. 1052–1078 (1987);  
DOI 10.1137/0908085.
- [203] P. T. Boggs, J. R. Donaldson, R. h. Byrd, and R. B. Schnabel;  
“Algorithm 676: ODRPACK: software for weighted orthogonal distance regression”; *ACM Transactions on Mathematical Software (TOMS)*; **15**, pp. 348–364 (1989);  
DOI 10.1145/76909.76913.

- [204] J. W. Zwolak, P. T. Boggs, and L. T. Watson;  
“User’s guide to ODRPACK95 version 1.0 software for weighted orthogonal distance regression with bound constraints”; (2006).
- [205] C. Wagner;  
“Theory of current rectifiers”; *Physikalische Zeitschrift*; **32**, pp. 641–645 (1931).
- [206] “Physikalische Zeitschrift. v.32 1931. - Limited View | HathiTrust Digital Library”; .  
URL <https://babel.hathitrust.org/cgi/pt?id=mdp.39015020111368>
- [207] J. L. Moll;  
“The Evolution of the Theory for the Voltage-Current Characteristic of P-N Junctions”;  
*Proceedings of the IRE*; **46**, pp. 1076–1082 (1958);  
DOI 10.1109/JRPROC.1958.286846.
- [208] B. Davydov;  
“The rectifying action of semiconductors”; *Technical Physics of the USSR*; **5**, pp. 87–95  
(1938).
- [209] W. Shockley;  
“The Theory of pn Junctions in Semiconductors and pn Junction Transistors”; *Bell System  
Technical Journal*; **28**, pp. 435–489 (1949);  
DOI 10.1002/j.1538-7305.1949.tb03645.x.
- [210] N. Mizuochi, T. Makino, H. Kato, D. Takeuchi, M. Ogura, H. Okushi, M. Nothaft, P. Neumann,  
A. Gali, F. Jelezko, J. Wrachtrup, and S. Yamasaki;  
“Electrically driven single-photon source at room temperature in diamond”; *Nature Pho-  
tonics 2012 6:5*; **6**, pp. 299–303 (2012);  
DOI 10.1038/nphoton.2012.75.
- [211] M. G. Rosul, M. S. Akhanda, and M. Zebarjadi;  
“Thermionic energy conversion”; *Nanoscale Energy Transport*; pp. 14–1 (2020);  
DOI 10.1088/978-0-7503-1738-2CH14.
- [212] C. Melnick and M. Kaviany;  
“Phonovoltaic. I. Harvesting hot optical phonons in a nanoscale p-n junction”; *Physical  
Review B*; **93**, p. 094302 (2016);  
DOI 10.1103/PHYSREVB.93.094302/FIGURES/10/MEDIUM.
- [213] C. Melnick and M. Kaviany;  
“Phonovoltaic. II. Tuning band gap to optical phonon in graphite”; *Physical Review B*; **93**  
(2016);  
DOI 10.1103/PHYSREVB.93.125203.

- [214] R. Feynman, R. B. Leighton, and M. Sands; *The Feynman Lectures on Physics*; volume 2; Basic Books, New York; new millen edition (2010); ISBN 978-0-465-02416-2.
- [215] J. M. Shah, Y. L. Li, T. Gessmann, and E. F. Schubert;  
“Experimental analysis and theoretical model for anomalously high ideality factors (n2.0) in AlGaIn/GaN p-n junction diodes”; *Journal of Applied Physics*; **94**, p. 2627 (2003);  
DOI 10.1063/1.1593218.
- [216] C. X. Wang, G. W. Yang, H. W. Liu, Y. H. Han, J. F. Luo, C. X. Gao, and G. T. Zou;  
“Experimental analysis and theoretical model for anomalously high ideality factors in ZnO/diamond p-n junction diode”; *Applied Physics Letters*; **84**, p. 2427 (2004);  
DOI 10.1063/1.1689397.
- [217] M. Brötzmann, U. Vetter, and H. Hofsäss;  
“BN/ZnO heterojunction diodes with apparently giant ideality factors”; *Journal of Applied Physics*; **106**, p. 63704 (2009);  
DOI 10.1063/1.3212987.
- [218] J. H. Lambert;  
“Observationes variae in mathesin puram”; *Acta Helvetica physico-mathematico-anatomico-botanico-medica*; **3**, pp. 128–168 (1758).
- [219] L. Euler;  
“De serie Lambertina plurimisque eius insignibus proprietatibus”; *Acta Academiae Scientiarum Imperialis Petropolitanae*; **1779:2**, pp. 29–51 (1783).
- [220] L. Euler;  
“De serie Lambertina plurimisque eius insignibus proprietatibus”; .  
URL [https://scholarlycommons.pacific.edu/euler-works/532/?utm\\_source=scholarlycommons.pacific.edu%2Feuler-works%2F532&utm\\_medium=PDF&utm\\_campaign=PDFCoverPages](https://scholarlycommons.pacific.edu/euler-works/532/?utm_source=scholarlycommons.pacific.edu%2Feuler-works%2F532&utm_medium=PDF&utm_campaign=PDFCoverPages)
- [221] S. Gallagher;  
“Euler’s De Serie Lambertina, Translated from Latin to English With Supplementary Notes”; *Euleriana*; **1**, p. 272 (2021);  
DOI 10.56031/2693-9908.1015.
- [222] R. M. Corless, G. H. Gonnet, D. E. Hare, D. J. Jeffrey, and D. E. Knuth;  
“On the LambertW function”; *Advances in Computational Mathematics 1996 5:1*; **5**, pp. 329–359 (1996);  
DOI 10.1007/BF02124750.

- [223] M. Bronstein, R. M. Corless, J. H. Davenport, and D. J. Jeffrey;  
“Algebraic properties of the Lambert W function from a result of Rosenlicht and of Liouville”;  
*Integral Transforms and Special Functions*; **19**, pp. 709–712 (2008);  
DOI 10.1080/10652460802332342.
- [224] T. C. Banwell and A. Jayakumar;  
“Exact analytical solution for current flow through diode with series resistance”; *Electronics Letters*; **36**, pp. 291–292 (2000);  
DOI 10.1049/EL:20000301.
- [225] B. Pelz, A. Belkadi, and G. Moddel;  
“Avoiding erroneous analysis of MIM diode current-voltage characteristics through exponential fitting”; (2018);  
DOI 10.1016/j.measurement.2018.01.054.
- [226] K. Bobrov, G. Comtet, G. Dujardin, P. Bergonzo, and C. Mer;  
“Surface electronic states of the partially hydrogenated diamond C(100) - (2 × 1) : H surface”;  
*Physical Review B*; **63**, p. 165421 (2001);  
DOI 10.1103/PhysRevB.63.165421.
- [227] H. Dominguez-Andrade, J. Anaya, A. Croot, M. Cattelan, D. J. Twitchen, M. Kuball, and N. A. Fox;  
“Correlating Thermionic Emission with Specific Surface Reconstructions in a <100> Hydrogenated Single-Crystal Diamond”; *Cite This: ACS Appl. Mater. Interfaces*; **12** (2020);  
DOI 10.1021/acsami.0c01677.
- [228] M. W. Geis, M. A. Hollis, G. W. Turner, J. Daulton, J. O. Varghese, K. Klyukin, J. Wang, B. Yildiz, and B. Zhang;  
“Controlling the carrier density of surface conductive diamond”; *Diamond and Related Materials*; **122**, p. 108775 (2022);  
DOI 10.1016/J.DIAMOND.2021.108775.
- [229] M. W. Geis, J. O. Varghese, A. Vardi, J. Kedzierski, J. Daulton, D. Calawa, M. A. Hollis, C. H. Wuorio, G. W. Turner, S. M. Warnock, T. Osadchy, J. Mallek, A. Melville, J. A. del Alamo, and B. Zhang;  
“Hydrogen and deuterium termination of diamond for low surface resistance and surface step control”; *Diamond and Related Materials*; **118**, p. 108518 (2021);  
DOI 10.1016/J.DIAMOND.2021.108518.
- [230] M. Nesládek, M. Vaněček, J. Rosa, C. Quaeys, and L. M. Stals;  
“Subgap optical absorption in CVD diamond films determined from photothermal deflec-

- tion spectroscopy”; *Diamond and Related Materials*; **4**, pp. 697–701 (1995);  
DOI 10.1016/0925-9635(94)05248-4.
- [231] J. W. Zwolak, P. T. Boggs, and L. T. Watson;  
“Algorithm 869: ODRPACK95: A weighted orthogonal distance regression code with bound constraints”; *ACM Transactions on Mathematical Software (TOMS)*; **33** (2007);  
DOI 10.1145/1268776.1268782.
- [232] R. Andrae, T. Schulze-Hartung, and P. Melchior; *Dos and don'ts of reduced chi-squared*; Technical report.
- [233] T. W. Anderson and D. A. Darling;  
“Asymptotic Theory of Certain "Goodness of Fit" Criteria Based on Stochastic Processes”;  
*The Annals of Mathematical Statistics*; **23**, pp. 193–212 (1952);  
DOI 10.1214/AOMS/1177729437.
- [234] S. S. Shapiro and A. M. B. Wilk;  
“An analysis of variance test for normality (complete samples)”; *Biometrika*; **52**, pp. 591–611 (1965);  
DOI 10.1093/BIOMET/52.3-4.591.
- [235] A. Kolmogorov;  
“Sulla Determinazione Empirica di una Legge di Distribuzione”; *Giornale dell'Istituto Italiano degli Attuari*; **4**, pp. 83–91 (1933).
- [236] N. Smirnov;  
“On the estimation of the discrepancy between empirical curves of distribution for two independent samples”; *Bulletin Mathématique de l'Université de Moscou*; **2** (1939).
- [237] R. B. D'Agostino, A. Belanger, and R. B. D'Agostino;  
“A Suggestion for Using Powerful and Informative Tests of Normality”; *The American Statistician*; **44**, p. 316 (1990);  
DOI 10.2307/2684359.
- [238] M. Baker;  
“Statisticians issue warning over misuse of P values”; *Nature*; **531**, p. 151 (2016);  
DOI 10.1038/NATURE.2016.19503.
- [239] H. W. Lilliefors;  
“On the Kolmogorov-Smirnov Test for Normality with Mean and Variance Unknown”;  
*Journal of the American Statistical Association*; **62**, pp. 399–402 (1967);  
DOI 10.1080/01621459.1967.10482916.

- [240] I. V. Shpilevaya and J. S. Foord;  
“Electrochemistry of nanocrystalline and microcrystalline diamond”; in: O. A. Williams (editor), *Nanodiamond*; Nanoscience & Nanotechnology Series; chapter 15, pp. 354–384; Royal Society of Chemistry (2014); ISBN 9781849736398.
- [241] N. H. Turner and J. A. Schreifels;  
“Surface Analysis: X-ray Photoelectron Spectroscopy and Auger Electron Spectroscopy”; *Analytical Chemistry*; **66**, pp. 163–185 (1994);  
DOI 10.1021/ac00084a008.
- [242] C. S. Fadley;  
“Atomic-level characterization of materials with core- and valence-level photoemission: basic phenomena and future directions”; *Surface and Interface Analysis*; **40**, pp. 1579–1605 (2008);  
DOI 10.1002/sia.2902.
- [243] T. A. Carlson;  
“Photoelectron Spectroscopy”; *Annual Review of Physical Chemistry*; **26**, pp. 211–233 (1975);  
DOI 10.1146/annurev.pc.26.100175.001235.
- [244] P. van der Heide; *X-Ray Photoelectron Spectroscopy: An Introduction to Principles and Practices*; John Wiley & Sons, Inc.; 1st edition (2011); ISBN 9781118162927.
- [245] D. Roy and D. Tremblay;  
“Design of electron spectrometers”; *Reports on Progress in Physics*; **53**, pp. 1621–1674 (1990);  
DOI 10.1088/0034-4885/53/12/003.
- [246] D. R. Baer, K. Artyushkova, H. Cohen, C. D. Easton, M. Engelhard, T. R. Gengenbach, G. Greczynski, P. Mack, D. J. Morgan, and A. Roberts;  
“XPS guide: Charge neutralization and binding energy referencing for insulating samples”; *Journal of Vacuum Science & Technology A*; **38**, p. 031204 (2020);  
DOI 10.1116/6.0000057.
- [247] A. Pélisson-Schecker, H. J. Hug, and J. Patscheider;  
“Charge referencing issues in XPS of insulators as evidenced in the case of Al-Si-N thin films”; *Surface and Interface Analysis*; **44**, pp. 29–36 (2012);  
DOI 10.1002/sia.3765.
- [248] T. L. Barr and S. Seal;  
“Nature of the use of adventitious carbon as a binding energy standard”; *Journal of Vacuum Science & Technology A: Vacuum, Surfaces, and Films*; **13**, pp. 1239–1246 (1995);  
DOI 10.1116/1.579868.

- [249] P. Swift;  
“Adventitious carbon the panacea for energy referencing?”; *Surface and Interface Analysis*; **4**, pp. 47–51 (1982);  
DOI 10.1002/sia.740040204.
- [250] G. H. Major, N. Fairley, P. M. A. Sherwood, M. R. Linford, J. Terry, V. Fernandez, and K. Artyushkova;  
“Practical guide for curve fitting in x-ray photoelectron spectroscopy”; *Journal of Vacuum Science & Technology A*; **38**, p. 061203 (2020);  
DOI 10.1116/6.0000377.
- [251] P. M. Sherwood;  
“The use and misuse of curve fitting in the analysis of core X-ray photoelectron spectroscopic data”; *Surface and Interface Analysis*; **51**, pp. 589–610 (2019);  
DOI 10.1002/sia.6629.
- [252] J.-Q. Zhong, M. Wang, W. H. Hoffmann, M. A. v. Spronsen, D. Lu, and J. A. Boscoboinik;  
“Synchrotron-based ambient pressure X-ray photoelectron spectroscopy of hydrogen and helium”; *Applied Physics Letters*; **112**, p. 091602 (2018);  
DOI 10.1063/1.5022479.
- [253] “NanoESCA - Scienta Omicron”; .  
URL <https://scientaomicron.com/en/productDetailPages/system-solutions/electron-spectroscopy/NanoESCA>
- [254] M. Escher, K. Winkler, O. Renault, and N. Barrett;  
“Applications of high lateral and energy resolution imaging XPS with a double hemispherical analyser based spectromicroscope”; *Journal of Electron Spectroscopy and Related Phenomena*; **178-179**, pp. 303–316 (2010);  
DOI 10.1016/j.elspec.2009.06.001.
- [255] “Bristol NanoESCA Laboratory | School of Physics | University of Bristol”; .  
URL <http://www.bristol.ac.uk/physics/facilities/nanoesca/>
- [256] O. A. Williams and R. B. Jackman;  
“Surface conductivity on hydrogen terminated diamond”; *Semiconductor Science and Technology*; **18**, pp. S34–S40 (2003);  
DOI 10.1088/0268-1242/18/3/305.
- [257] M. F. Koenig and J. T. Grant;  
“An evaluation of the bremsstrahlung contribution to specimen damage in XPS using Auger peak intensities”; *Applied Surface Science*; **25**, pp. 455–468 (1986);  
DOI 10.1016/0169-4332(86)90088-7.

## BIBLIOGRAPHY

---

- [258] R. D. Deslattes, E. G. Kessler Jr., P. Indelicato, L. de Billy, E. Lindroth, J. Anton, J. S. Coursey, D. J. Schwab, J. Chang, R. Sukumar, K. Olsen, and R. A. Dragoset; “X-Ray Transition Energies Database”; (2005); DOI 10.18434/T4859Z. URL <https://www.nist.gov/pml/x-ray-transition-energies-database>
- [259] “Spring-8”; . URL <http://www.spring8.or.jp/en/>
- [260] “Remote participation in user experiments at SACLA under the COVID-19 influence (Updated on Feb 8, 2021) | SACLA User Information”; . URL <http://sacra.xfel.jp/?p=14408&lang=en>
- [261] “Diamond Light Source”; . URL <https://www.diamond.ac.uk/Home.html;jsessionid=64F637D2C80692BEFAFAB2D335D7F1D6>
- [262] M. Drakopoulos, T. Connolley, C. Reinhard, R. Atwood, O. Magdysyuk, N. Vo, M. Hart, L. Connor, B. Humphreys, G. Howell, S. Davies, T. Hill, G. Wilkin, U. Pedersen, A. Foster, N. De Maio, M. Basham, F. Yuan, and K. Wanelik; “I12: The Joint Engineering, Environment and Processing (JEEP) beamline at Diamond Light Source”; *Journal of Synchrotron Radiation*; **22**, pp. 828–838 (2015); DOI 10.1107/S1600577515003513.
- [263] K. W. Fornalski; “Simple empirical correction functions to cross sections of the photoelectric effect, Compton scattering, pair and triplet production for carbon radiation shields for intermediate and high photon energies”; *Journal of Physics Communications*; **2**, p. 035038 (2018); DOI 10.1088/2399-6528/aab408.
- [264] K. G. Veinot and N. E. Hertel; “Personal dose equivalent conversion coefficients for photons to 1 GeV”; *Radiation Protection Dosimetry*; **145**, pp. 28–35 (2011); DOI 10.1093/RPD/NCQ380.
- [265] E. Z. Piña-Salazar, K. Sagisaka, Y. Hattori, T. Sakai, R. Futamura, E. Ōsawa, and K. Kaneko; “Electrical conductivity changes of water-adsorbed nanodiamonds with thermal treatment”; *Chemical Physics Letters: X*; **2**, p. 100018 (2019); DOI 10.1016/j.cpletx.2019.100018.
- [266] S. Agostinelli, J. Allison, K. Amako, J. Apostolakis, H. Araujo, P. Arce, M. Asai, D. Axen, S. Banerjee, G. Barrand, F. Behner, L. Bellagamba, J. Boudreau, L. Broglia, A. Brunengo, H. Burkhardt,

- S. Chauvie, J. Chuma, R. Chytracek, G. Cooperman, G. Cosmo, P. Degtyarenko, A. Dell'acqua, G. Depaola, D. Dietrich, R. Enami, A. Feliciello, C. Ferguson, H. Fesefeldt, G. Folger, F. Foppiano, A. Forti, S. Garelli, S. Giani, R. Giannitrapani, D. Gibin, J. J. Gómez Cadenas, I. González, G. G. Abril, G. Greeniaus, W. Greiner, V. Grichine, A. Grossheim, S. Guatelli, P. Gumplinger, R. Hamatsu, K. Hashimoto, H. Hasui, A. Heikkinen, A. Howard, V. Ivanchenko, A. Johnson, F. W. Jones, J. Kallenbach Aa, N. Kanaya, M. Kawabata, Y. Kawabata, M. Kawaguti, S. Kelner, P. Kent, A. Kimura, T. Kodama, R. Kokoulin, M. Kossov, H. Kurashige, E. Lamanna, T. Lampén, V. Lara, V. Lefebure, F. Lei, M. Liendl, W. Lockman, F. Longo, S. Magni, M. Maire, E. Medernach, K. Minamimoto, P. Mora De Freitas, Y. Morita, K. Murakami, M. Nagamatu, R. Nartallo, P. Nieminen, T. Nishimura, K. Ohtsubo, M. Okamura, S. O'neale, Y. Oohata, K. Paech, J. Perl, A. Pfeiffer, M. G. Pia, F. Ranjard, A. Rybin, S. Sadilov, E. Di Salvo, G. Santin, T. Sasaki, N. Savaas, Y. Sawada, S. Scherer, S. Sei, V. Sirotenko, D. Smith, N. Starkov, H. Stoecker, J. Sulkimo, M. Takahata, S. Tanaka, E. Tcherniaev, E. Safai Tehrani, M. Tropeano, P. Truscott, H. Uno, L. Urban, P. Urban, M. Verderi, A. Walkden, W. Wander, H. Weber, J. P. Wellisch, T. Wenaus, D. C. Williams, D. Wright, T. Yamada, H. Yoshida, and D. Zschiesche;  
 “Geant4a simulation toolkit”; *Nuclear Instruments and Methods in Physics Research A*; **506**, pp. 250–303 (2003);  
 DOI 10.1016/S0168-9002(03)01368-8.
- [267] S. Banerjee and M. Hildreth;  
 “Validation and Tuning of the CMS Full Simulation”; in: *International Conference on Computing in High Energy and Nuclear Physics 2010*; CERN, Geneva (2011).  
 URL [https://twiki.cern.ch/twiki/pub/CMSPublic/SWGuideSimulation/CR2011\\_019.pdf](https://twiki.cern.ch/twiki/pub/CMSPublic/SWGuideSimulation/CR2011_019.pdf)
- [268] “The Standard : Standard C++”; .  
 URL <https://isocpp.org/std/the-standard>
- [269] J. Baró, J. Sempau, J. M. Fernández-Varea, and F. Salvat;  
 “PENELOPE: An algorithm for Monte Carlo simulation of the penetration and energy loss of electrons and positrons in matter”; *Nuclear Inst. and Methods in Physics Research, B*; **100**, pp. 31–46 (1995);  
 DOI 10.1016/0168-583X(95)00349-5.
- [270] J. A. Davis, K. Ganesan, A. D. C Alves, S. Guatelli, M. Petasecca, A. A. Jeremy Davis, J. Livingstone, M. L. F Lerch, D. A. Prokopovich, M. I. Reinhard, R. M. Siegele, S. Prawer, D. Jamieson, Z. Kuncic, V. L. Pisacane, J. F. Dicello, J. Ziegler, M. Zaider, and A. B. Rosenfeld;  
 “Characterization of a novel diamond-based microdosimeter prototype for radioprotection applications in space environments”; *IEEE Transactions on Nuclear Science*; **59**, pp. 3110–3116 (2012);  
 DOI 10.1109/TNS.2012.2218131.

- [271] J. Allison, K. Amako, J. Apostolakis, P. Arce, M. Asai, T. Aso, E. Bagli, A. Bagulya, S. Banerjee, G. Barrand, B. R. Beck, A. G. Bogdanov, D. Brandt, J. M. Brown, H. Burkhardt, P. Canal, D. Cano-Ott, S. Chauvie, K. Cho, G. A. Cirrone, G. Cooperman, M. A. Cortés-Giraldo, G. Cosmo, G. Cuttone, G. Depaola, L. Desorgher, X. Dong, A. Dotti, V. D. Elvira, G. Folger, Z. Francis, A. Galoyan, L. Garnier, M. Gayer, K. L. Genser, V. M. Grichine, S. Guatelli, P. Guèye, P. Gumplinger, A. S. Howard, I. Hřivnáčová, S. Hwang, S. Incerti, A. Ivanchenko, V. N. Ivanchenko, F. W. Jones, S. Y. Jun, P. Kaitaniemi, N. Karakatsanis, M. Karamitrosi, M. Kelsey, A. Kimura, T. Koi, H. Kurashige, A. Lechner, S. B. Lee, F. Longo, M. Maire, D. Mancusi, A. Mantero, E. Mendoza, B. Morgan, K. Murakami, T. Nikitina, L. Pandola, P. Paprocki, J. Perl, I. Petrović, M. G. Pia, W. Pokorski, J. M. Quesada, M. Raine, M. A. Reis, A. Ribon, A. Ristić Fira, F. Romano, G. Russo, G. Santin, T. Sasaki, D. Sawkey, J. I. Shin, I. I. Strakovsky, A. Taborda, S. Tanaka, B. Tomé, T. Toshito, H. N. Tran, P. R. Truscott, L. Urban, V. Uzhinsky, J. M. Verbeke, M. Verderi, B. L. Wendt, H. Wenzel, D. H. Wright, D. M. Wright, T. Yamashita, J. Yarba, and H. Yoshida;  
“Recent developments in GEANT4”; *Nuclear Instruments and Methods in Physics Research, Section A: Accelerators, Spectrometers, Detectors and Associated Equipment*; **835**, pp. 186–225 (2016);  
DOI 10.1016/j.nima.2016.06.125.
- [272] R. Iacono and J. P. Boyd;  
“New approximations to the principal real-valued branch of the Lambert W-function”; *Advances in Computational Mathematics*; **43**, pp. 1403–1436 (2017);  
DOI 10.1007/s10444-017-9530-3.
- [273] “Ngspice, the open source Spice circuit simulator”; .  
URL <https://ngspice.sourceforge.io/>
- [274] A. Signorell and contributors;  
“DescTools: Tools for Descriptive Statistics”; .  
URL <https://cran.r-project.org/package=DescTools>
- [275] “GNU Fortran - GNU Project”; .  
URL <https://gcc.gnu.org/fortran/>
- [276] “Orthogonal distance regression (scipy.odr) SciPy v0.14.0 Reference Guide”; .  
URL <https://docs.scipy.org/doc/scipy-0.14.0/reference/odr.html#id1>
- [277] “Origin”; .  
URL <https://www.originlab.com/index.aspx?go=PRODUCTS/Origin>

- [278] J. Bezanson, A. Edelman, S. Karpinski, and V. B. Shah;  
“Julia: A fresh approach to numerical computing”; *SIAM Review*; **59**, pp. 65–98 (2017);  
DOI 10.1137/141000671.
- [279] “HypothesisTests package · HypothesisTests.jl”; .  
URL <https://juliastats.org/HypothesisTests.jl/stable/>
- [280] F. van der Plas, M. Dral, P. Berg, Γεωργακπουλ, R. Huijzer, N. Bochenski, A. Mengali, B. Lungwitz, C. Burns, H. Priyashan, J. Ling, E. Zhang, F. S. S. Schneider, I. Weaver, Rogerluo, S. Kadowaki, Z. Wu, J. Gerritsen, R. Novosel, Supanat, Z. Moon, pupuis, M. Abbott, N. Bauer, P. Bouffard, S. Terasaki, S. Polasa, and TheCedarPrince;  
“fonsp/Pluto.jl: v0.19.11”; (2022);  
DOI 10.5281/ZENODO.6916713.
- [281] “PyVISA: Control your instruments with Python”; .  
URL <https://pyvisa.readthedocs.io/en/latest/index.html>
- [282] “The Raspberry Pi Foundation”; .  
URL <https://www.raspberrypi.org/>
- [283] “VNC® Connect”; .  
URL <https://www.realvnc.com/en/connect/>
- [284] “Overleaf”; .  
URL [www.overleaf.com](http://www.overleaf.com)
- [285] C. Feuersänger, H. Menke, T. Tantau, and The PGF/TikZ team;  
“CTAN: Package pgf”; .  
URL <https://www.ctan.org/pkg/pgf>
- [286] S. Erhardt, R. Giannetti, S. Lindner, and M. Redaelli;  
“CTAN: Package CircuiTikZ”; .  
URL <https://www.ctan.org/pkg/circuitikz>
- [287] A. V. Naumkin, A. Kraut-Vass, S. W. Gaarenstroom, and C. J. Powell;  
“NIST X-ray Photoelectron Spectroscopy Database”; (2012);  
DOI 10.18434/T4T88K.  
URL <http://srdata.nist.gov/xps/Default.aspx>
- [288] Y. Liu, Y. Zheng, B. Du, R. R. Nasaruddin, T. Chen, and J. Xie;  
“Golden Carbon Nanotube Membrane for Continuous Flow Catalysis”; *Industrial and Engineering Chemistry Research*; **56**, pp. 2999–3007 (2017);  
DOI 10.1021/acs.iecr.7b00357.

- [289] V. Bondarenka, Z. Martunas, S. Kaciulis, and L. Pandolfi;  
“Sol-gel synthesis and XPS characterization of sodium-vanadium oxide bronze thin films”;  
*Journal of Electron Spectroscopy and Related Phenomena*; **131-132**, pp. 99–103 (2003);  
DOI 10.1016/S0368-2048(03)00110-5.
- [290] “Handbook of the Elements and Native Oxides”; (1999).  
URL [https://www.xpsdata.com/XI\\_BE\\_Lookup\\_table.pdf](https://www.xpsdata.com/XI_BE_Lookup_table.pdf)
- [291] “XPS Reference Table of Elements (Thermo Scientific)”; .  
URL <https://xpssimplified.com/periodictable.php>
- [292] G. P. Lopez, D. G. Castner, and B. D. Ratner;  
“XPS O 1s Binding Energies for Polymers Containing Hydroxyl, Ether, Ketone and Ester  
Groups”; *Surface and Interface Analysis*; **17**, pp. 267–272 (1991);  
DOI 10.1002/sia.740170508.
- [293] G. Conte, E. Giovine, M. Girolami, S. Salvatori, A. Bolshakov, V. Ralchenko, and V. Konov;  
“Polycrystalline diamond UV-triggered MESFET receivers”; *Nanotechnology*; **23**, p. 6 (2012);  
DOI 10.1088/0957-4484/23/7/075202.
- [294] C.-H. Chiang and C.-G. Wu;  
“Bulk heterojunction perovskite-PCBM solar cells with high fill factor”; *Nature Photonics*;  
**10**, pp. 196–201 (2016);  
DOI 10.1038/NPHOTON.2016.3.
- [295] M. Wang, H. Wang, W. Li, X. Hu, K. Sun, and Z. Zang;  
“Defect passivation using ultrathin PTAA layers for efficient and stable perovskite solar cells  
with a high fill factor and eliminated hysteresis”; *Journal of Materials Chemistry A*; **7**, pp.  
26421–26428 (2019);  
DOI 10.1039/c9ta08314f.
- [296] F. Bachmair, L. Bäni, P. Bergonzo, B. Caylar, G. Forcolin, I. Haughton, D. Hits, H. Kagan, R. Kass,  
L. Li, A. Oh, S. Phan, M. Pomorski, D. Smith, V. Tyzhnevyyi, R. Wallny, and D. Whitehead;  
“A 3D diamond detector for particle tracking”; *Nuclear Instruments and Methods in Physics  
Research Section A: Accelerators, Spectrometers, Detectors and Associated Equipment*; **786**,  
pp. 97–104 (2015);  
DOI 10.1016/j.nima.2015.03.033.
- [297] I. Lopez Paz, O. Allegre, Z. Li, A. Oh, A. Porter, and D. Whitehead;  
“Study of Electrode Fabrication in Diamond with a FemtoSecond Laser”; *physica status  
solidi (a)*; **216**, p. 1900236 (2019);  
DOI 10.1002/pssa.201900236.

- [298] B. Caylar, M. Pomorski, and P. Bergonzo;  
“Laser-processed three dimensional graphitic electrodes for diamond radiation detectors”;  
*Applied Physics Letters*; **103**, p. 43504 (2013);  
DOI 10.1063/1.4816328.
- [299] S. Lagomarsino, M. Bellini, C. Corsi, F. Gorelli, G. Parrini, M. Santoro, and S. Sciortino;  
“Three-dimensional diamond detectors: Charge collection efficiency of graphitic electrodes”;  
*Applied Physics Letters*; **103**, p. 233507 (2013);  
DOI 10.1063/1.4839555.
- [300] M. J. Booth, G. T. Forcolin, V. Grilj, B. Hamilton, I. Haughton, M. McGowan, S. A. Murphy, A. Oh,  
P. S. Salter, I. Sudić, and N. Skukan;  
“Study of cubic and hexagonal cell geometries of a 3D diamond detector with a proton  
micro-beam”; *Diamond and Related Materials*; **77**, pp. 137–145 (2017);  
DOI 10.1016/j.diamond.2017.06.014.
- [301] M.-L. Hicks, A. C. Pakpour-Tabrizi, and R. B. Jackman;  
“Diamond Etching Beyond 10 $\mu$ m with Near-Zero Micromasking”; *Scientific Reports 2019*  
*9:1*; **9**, pp. 1–6 (2019);  
DOI 10.1038/s41598-019-51970-8.
- [302] R. J. Handy;  
“Theoretical analysis of the series resistance of a solar cell”; *Solid State Electronics*; **10**, pp.  
765–775 (1967);  
DOI 10.1016/0038-1101(67)90159-1.
- [303] A. Kurtolu and A. B. Turul;  
“Gold analysis by the gamma absorption technique”; *Applied Radiation and Isotopes*; **58**,  
pp. 5–8 (2003);  
DOI 10.1016/S0969-8043(02)00237-3.
- [304] A. Hoffman and A. Laikhtman;  
“Photon stimulated desorption of hydrogen from diamond surfaces via core-level exci-  
tations: fundamental processes and applications to surface studies”; *Journal of Physics:*  
*Condensed Matter*; **18**, pp. 1517–1546 (2006);  
DOI 10.1088/0953-8984/18/30/S08.
- [305] C. Sun, T. Hao, J. Li, H. Ye, and C. Gu;  
“The design and performance of hydrogen-terminated diamond metal-oxide-  
semiconductor field-effect transistors with high k oxide HfO<sub>2</sub>”; *Micro and Nano*  
*Engineering*; **6**, p. 100046 (2020);  
DOI 10.1016/j.mne.2020.100046.

## BIBLIOGRAPHY

---

- [306] “Americium | Am - PubChem”; .  
URL <https://pubchem.ncbi.nlm.nih.gov/compound/americium>
- [307] “Radiation and The Health and Safety Act”; .  
URL <https://www.hse.gov.uk/radiation/ionising/apparatus/ta1.htm>
- [308] “Smoke Detectors and Americium - World Nuclear Association (Archived via WaybackMachine)”; (2010).  
URL <https://web.archive.org/web/20101112082137/http://www.world-nuclear.org/info/inf57.html>
- [309] J. C. Teo, R. H. G. Tan, V. H. Mok, V. K. Ramachandaramurthy, and C. Tan;  
“Impact of bypass diode forward voltage on maximum power of a photovoltaic system under partial shading conditions”; *Energy*, **191**, p. 116491 (2020);  
DOI 10.1016/j.energy.2019.116491.
- [310] W. S. C. Williams; *Nuclear and Particle Physics*; Oxford University Press, Oxford; 1st edition (1991); ISBN 978-0-19-852046-7.
- [311] K. Hyun Kim, Y. Soo Kim, and J. Soo Kim;  
“Signal and noise performance of large-area PIN photodiodes and charge-sensitive preamplifiers for gamma radiography”; *Nuclear Instruments and Methods in Physics Research A*; **591**, pp. 63–66 (2008);  
DOI 10.1016/j.nima.2008.03.025.
- [312] X. Yan and X. Su; *Linear regression analysis : theory and computing*; World Scientific Pub. Co., Singapore (2009); ISBN 9789812834119.
- [313] H. Akaike;  
“A New Look at the Statistical Model Identification”; *IEEE Transactions on Automatic Control*; **19**, pp. 716–723 (1974);  
DOI 10.1109/TAC.1974.1100705.
- [314] S. Derksen and H. J. Keselman;  
“Backward, forward and stepwise automated subset selection algorithms: Frequency of obtaining authentic and noise variables”; *British Journal of Mathematical and Statistical Psychology*; **45**, pp. 265–282 (1992);  
DOI 10.1111/j.2044-8317.1992.tb00992.x.
- [315] M. Schreck, S. Gsell, R. Brescia, and M. Fischer;  
“Ion bombardment induced buried lateral growth: The key mechanism for the synthesis of single crystal diamond wafers”; *Scientific Reports*; **7**, pp. 1–8 (2017);  
DOI 10.1038/srep44462.

- [316] L. Fan, N. Xu, H. Chen, J. Zhou, and S. Deng;  
“A millisecond response and microwatt power-consumption gas sensor: Realization based on cross-stacked individual Pt-coated WO<sub>3</sub> nanorods”; *Sensors and Actuators B: Chemical*; **346**, p. 130545 (2021);  
DOI 10.1016/J.SNB.2021.130545.
- [317] “UB20M High-Voltage, Low-Threshold, Ultra-Low Power Voltage Detector for Energy Harvesting, RF Power Transfer, and Event-Driven Sensing”; .  
URL [http://www.bris.ac.uk/media-library/sites/engineering/research/eem-group/zero-standby/UB20M\\_Datasheet\\_Rev.1.5.pdf](http://www.bris.ac.uk/media-library/sites/engineering/research/eem-group/zero-standby/UB20M_Datasheet_Rev.1.5.pdf)
- [318] H. Kawarada, M. Aoki, H. Sasaki, and K. Tsugawa;  
“Characterization of hydrogen-terminated CVD diamond surfaces and their contact properties”; *Diamond and Related Materials*; **3**, pp. 961–965 (1994);  
DOI doi.org/10.1016/0925-9635(94)90309-3.
- [319] F. Li, J. Zhang, X. Wang, Z. Liu, W. Wang, S. Li, and H.-X. Wang;  
“X-ray photoelectron spectroscopy study of Schottky junctions based on oxygen-/fluorine-terminated (100) diamond”; *Diamond & Related Materials*; **63**, pp. 180–185 (2016);  
DOI 10.1016/j.diamond.2015.12.007.
- [320] R. Kumaresan, H. Umezawa, and S. Shikata;  
“Vertical structure Schottky barrier diode fabrication using insulating diamond substrate”; *Diamond and Related Materials*; **19**, pp. 1324–1329 (2010);  
DOI 10.1016/J.DIAMOND.2010.06.019.
- [321] H. Umezawa, T. Saito, N. Tokuda, M. Ogura, S.-G. Ri, H. Yoshikawa, and S.-I. Shikata;  
“Leakage current analysis of diamond Schottky barrier diode”; *Applied Physics Letters*; **90**, p. 73506 (2007);  
DOI 10.1063/1.2643374.
- [322] J. B. Condon;  
“Equivalency of the DubininPolanyi equations and the QM based sorption isotherm equation. A. Mathematical derivation”; *Microporous and Mesoporous Materials*; **38**, pp. 359–376 (2000);  
DOI 10.1016/S1387-1811(00)00157-8.
- [323] O. Manelli, S. Corni, and M. C. Righi;  
“Water adsorption on native and hydrogenated diamond (001) surfaces”; *Journal of Physical Chemistry C*; **114**, pp. 7045–7053 (2010);  
DOI 10.1021/jp910971e.

